UNIVERSITY OF SOUTHAMPTON

A Study of Be/X-Ray Binaries in the SMC and the Milky Way

José Luis Galache Vielba

SCHOOL OF PHYSICS AND ASTRONOMY
FACULTY OF SCIENCE

July 26, 2006

Light, where there is Darkness
Laughter, where there is Silence
Motion in the still of Night
A flame of Life, burning Bright.

To Karina.

UNIVERSITY OF SOUTHAMPTON

ABSTRACT

FACULTY OF SCIENCE

SCHOOL OF PHYSICS AND ASTRONOMY

Doctor of Philosophy

A Study of Be/X-Ray Binaries in the SMC and the Milky Way

by José Luis Galache Vielba

This thesis presents the results of monitoring of 14 Be/X-ray binary systems in the Galaxy over $\sim$9 years with the *BATSE* instrument on-board *CGRO*, and 46 in the SMC over $\sim$8 years using PCA-*RXTE*data from a weekly survey program. The reduction pipeline for these data was perfected and new code was written to analyse the products. A technique is presented for subtracting the contribution of pulsations to a light curve, enabling the cleaning of power spectra with many sources and the precise measurement of power for all the harmonic components of a pulsar's profile. Application of these techniques has permitted the production of pulse amplitude light curves for the SMC systems, timing analysis of which has returned a large number of orbital ephemerides, which in turn has allowed for a better estimate of the spin/orbit relationship parameters. Two new quantities are defined for transient outburst systems: $\delta_{\rm orb}$ is the difference between the predicted and actual orbital periods expressed as a percentage, and is found to be inversely proportional to the magnetic fields of the pulsars in the SMC, but no such relation is seen for the Galactic systems. $X_{\rm od}$ is the number of outbursts per orbit, which we find to be strongly correlated with the orbital period for both galaxies. Based on the distribution of $X_{\rm od}$ we propose a classification scheme that would categorize Be/X-ray binary systems as Class Ia, Ib or II. A dependence of the X-ray luminosity on $X_{\rm od}$ is also found for SMC systems, but is weaker for Galactic ones. We present 21 possible new pulsars in the SMC for which orbital ephemerides have also been calculated. A multi-set technique for folding light curves is discussed and used to create pulse profiles for all the SMC pulsars, qualitatively showing that in most cases both fan and pencil beams are required together in order to explain the observed shapes. Lastly, two pulsars: SXP46.4 and SXP165 were found to be missidentifications of SXP46.6 and SXP169 respectively.

Contents

List of Figures

List of Tables

Acknowledgements

This thesis would not be in your hands if it were not for the help, however small, of a large number of people; I will do my best to honour them:

First and foremost, I cannot give enough thanks to my supervisor, Prof Malcolm Coe, who took me on as his student despite Spain having just been kicked out of the World Cup by Korea and the refs. I felt you were always on my side, even when you didn't agree with my graphs. You pulled funding and a new thesis project out of thin air when SMART-1 went bust, and always supported me. I apologise for the many hours of waiting time you no doubt accumulated over these years of BeX Group meetings. But I still think 09:30 is too early.

Thanks to Dr Robin Corbet, my shadow e-supervisor, who thought I would have time to complete the *RXTE* survey project in 12 months. Well, it took me 18; I hope you're not disappointed! Thanks also to Silas Laycock, my older academic brother, whose scripts I inherited and had to answer many e-mails about them, even after he had trained me for a week. It's over now, mate; you can stop hiding.

Thank you to Drs Mike Garcia and Danny Steeghs, who blindly (it seems to me) offered me a great job and have been so patient and supportive during the time it took me to finish. Now I can finally work for you guys!

Thank you to the people I have shared an office with, you made late evenings and weekends at work much less difficult; in roughly chronological order: Nick Haigh, Luisa Morales-Rueda (I know I always had too many questions), Matt North, Carolyn Brinkworth (I miss you girl!), Dave Russell and Elmar Körding (enjoy my desk!). 4075 was also home to my fellow BeXers: William Edge, whose keen sense of humour and quick wit always had me smiling (why did you retire so early?); Vanessa McBride, who was always up for a good discussion on any subject and whom I shared many a brainstorming session with in order to figure out what these rude pulsars were doing, and who always came asking questions thinking I knew the answer ... I rarely did (thanks for being a friend, and for providing enough protein

during the great *Dinners at the Godfrey's* that kept us all that little bit saner); the new kid, Matt Schurch, who exchanged the camera for the telescope (I don't know if that was a wise choice, but I hope I taught you and Herschel how to drive the 1.9m well enough); Katie McGowan, comrade in long-distance relationship, who has always been all too happy to answer any questions, be they on astronomy, visas, freight or other related subjects (it's a shame you didn't arrive earlier!).

I have to say "hi" to my fellow yearmates Adam Hill and Andy Barnes, who decided to finish ahead and before me. Thanks for not letting me feel overly (un)successful. Special thanks to Edward(o) Pope for all those brilliant films we enjoyed, and all the wacky conversations we had on who-can-remember-what (I miss them already, mate!). Big thanks to Liz Palmer (sorry, Barlow), fellow knee-pain and LaTeX sufferer, for being a friend with a big smile and for making sure I caught the aeroplane to Boston (good luck with the wedding!). To Tony "Ralph" Bird, for (almost) always having a book with the answer I was looking for. To Christian Knigge, for many useful discussions on the ever-fascinating topic of statistics, and for more entertaining talks on other subjects in Tenerife. To Izaro López-García, my partner in kebabs and fellow expatriate, whom I have more in common with than is healthy (¡y ya era hora de que acabaras, macho!).

A multi-thanks goes out to the rest of the Astro group at Southampton, past and present, who are definitely the most sociable astronomers I've ever come across. In no particular order: Retha, Ross, Dave (Mr Google Videos), Katrine, O.J., Stephen, Remon (enjoy the sun ye who can); the symmetrical boys: Matt Dallimore (ever the sarky lad), Grant (save the trees, not yourself) and Colin; Will Clarkson, Shaggy, Katherine, Vito, Manuela, Web Czar Giorgi ... and all those who didn't fit. A special thanks to Simon Harris, who had the envious task of keeping the astro computers ticking away for us.

Gracias a mis padres, que tanto en la lejanía como en la cercanía me apoyaron en mi sueño astronómico, aunque siempre me preguntaban cuándo encontraría un trabajo de verdad. Bueno, por fin llego el momento. Gracias también a mi preciosa hermana, a quien echo tantísimo de menos. Myrta, siento perderme como te conviertes en mujer, pero sé que lo estás haciendo muy bien. Os quiero mucho a los tres y espero que consideréis que vuestro sacrificio ha merecido la pena.

Last of all, but first in all, I thank my wife: Karina. She has pushed me up the steepest hills and braced me on the highest cliffs. My pole star in the night, an oasis of life in the day, you took me when I was nothing and from across the ocean made every breath of hard work oh-so worth it. We made it through the thorns together, and this thesis is as much your success as it might be mine. From the deepest of my heart: thank you.

Chapter 1

Be/X-Ray Binaries and the Magellanic Clouds

But do not despise the lore that has come down from distant years; for oft it may chance that old wives keep in memory word of things that once were needful for the wise to know.

—Celeborn (in *The Fellowship of the Ring*)

1.1 X-rays in astronomy

X-rays are electromagnetic radiation with frequencies in the range $\sim 10^{16} - 10^{20}$ Hz, corresponding to energies of $\sim 0.5 - 500$ keV. Unfortunately, the Earth's atmosphere completely absorbs them; while a balloon can ascend to $\sim 30 - 40$ km allowing the observation of X-rays down to ~ 30 keV, it is necessary to send an instrument higher than ~ 200 km to observe 1 keV X-rays, the region favoured by cosmic X-rays.

When the first rockets were launched into the upper atmosphere to study X-rays in the 1940 – 50s, scientists only expected to detect such radiation from the Sun as even the nearest stars were much too far away to be detected by the rudimentary instrumentation of the time. So it came as a surprise when in 1962 the AS&E

(American Science and Engineering) group, led by Riccardo Giacconi, discovered the first cosmic X-ray source, Sco X-1, located in the constellation of Scorpius (Giacconi and Gursky 1965).

After this initial discovery, sources continued to be found as both rockets and detectors improved, thus fuelling the growing field of X-ray astronomy. By the end of the 1970s, after the conclusion of the HEAO-1 satellite all-sky survey mission, over 800 sources, both galactic and extragalactic, were known. At present X-rays have been detected from a variety of sources (black holes, binary systems, AGN...) scattered throughout the Universe, as can be seen in the all-sky survey (see Fig. 1) conducted in 1990 – 91 by the imaging X-ray telescope aboard the *ROSAT* satellite; it detected more than 60 000 X-ray sources.

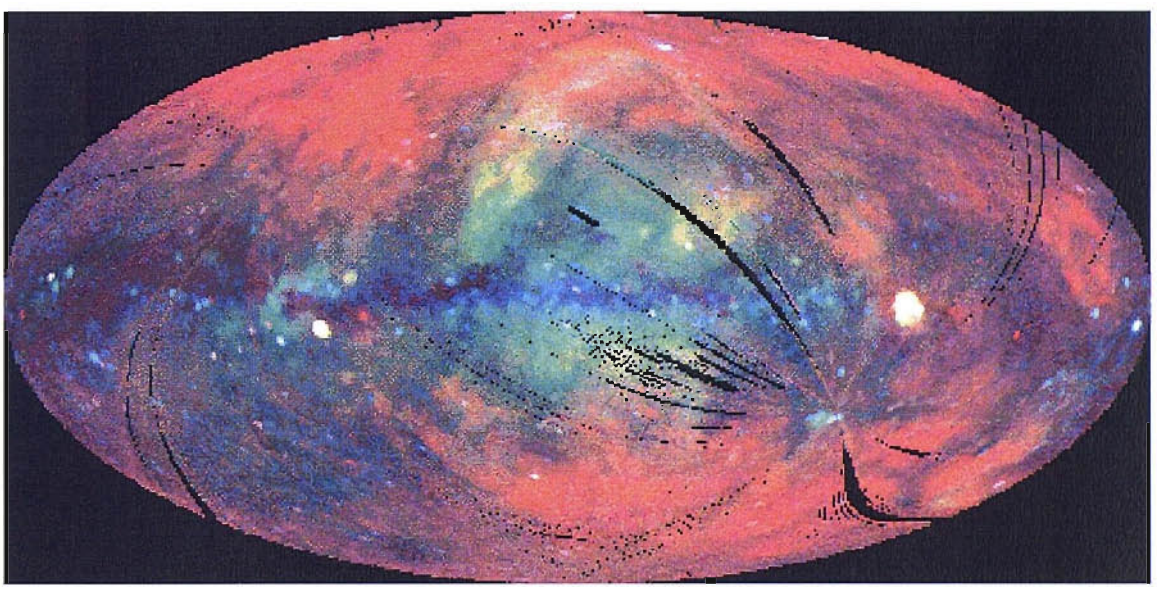

Figure 1.1: *ROSAT* image of the X-ray sky in the 0.1 – 2.4 keV band; it was created from data taken over 6 months between 1990 and 1991 as part of the *ROSAT* All Sky Survey (RASS). The image shows only the 50 000 sources detected in the first round of the data processing. The map is in galactic coordinates, and the colours represent different energy bands. These are, in keV, red: 0.1 – 0.4; green: 0.4 – 0.9: blue: 0.9 – 2.0.

1.2 X-ray binaries

One of the most powerful sources of X-rays (with luminosities up to $10^{38}\,\mathrm{erg\,s^{-1}}$) are binary systems in which one of the two constituent stars (the companion) is losing matter that is then accreted onto the other (the primary star), typically a compact object such as a white dwarf, a neutron star or a black hole. In general, only systems with a neutron star or a black hole are termed X-ray binaries (XRBs), while those with a white dwarf (usually accompanying a low mass star) are known as cataclysmic variables (CVs) as they exhibit large variations in their brightness due to different types of nova outbursts. Amongst the XRB systems we find two classifications: LMXBs (low mass X-ray binaries), where the companion star is of mass comparable to the Sun; and HMXBs (high mass X-ray binaries), where the companion's mass is much larger than the Sun's, typically $10-40\,M_{\odot}$ (Lewin et al. 1997).

1.3 Be/X-ray binaries

Of all the HMXB systems discovered and optically identified up to date (Liu et al. 2000), $\sim 72\%$ have a Be counterpart. Be stars are class III – V stars that show, or have shown, emission lines in the Balmer series (Collins 1987). Be stars are located on or near the main sequence in the Hertzsprung-Russell diagram, indicating that they still burn core hydrogen, with $T_{\mathrm{eff}} = 10^4 - 3 \times 10^4\,\mathrm{K}$ (Jaschek and Jaschek 1990). They possess extremely rapid rotation ($\sim 60\%$ of the critical break-up rotation velocity (Slettebak 1982; Porter 1996; Townsend et al. 2004) and can be variable in both brightness (Doazan et al. 1986) and spectra (Dachs et al. 1986). The observed emission arises from the material surrounding the Be star in a disc-like formation, whose origin is still not well understood, but is most likely due to mass ejection from the Be star due to its rapid rotation in the form of a high-velocity, low density wind that escapes quickly through the polar regions but becomes a slow, higher-density outflow in the equatorial regions, thus giving rise to a disc (Lamers and Waters 1987). However, contributions from other phenomena, such as non-radial pulsation or magnetic loops, seem also to play a role in this phenomenon (Hanuschik et al.

1993; Smith and Robinson 1998; Smith et al. 1998). There is also a significant infrared excess associated with the circumstellar disc of these stars (Porter 1999; Howells et al. 2001), and their Hα emission is of special interest for optical studies as it is an indicator of disc size. The disc structure is not yet fully understood, but it is known to be optically thick, this implies that changes in Hα emission are correlated with changes in the geometry (surface area) of the circumstellar disc (or at least of its emitting region).

1.3.1 Outburst characteristics and behaviour

Because in the majority of these systems there is not a continuous and substantial supply of matter for the compact object to accrete (as we shall see in § 1.3.3), X-ray emission is intermittent at best, with some systems having shown only one or two outbursts in a decade (Bildsten et al. 1997); these are known as Be/X-ray transients (e.g., A 0535+26 or XTE J0111.2-7317). In fact, most Be systems exhibit this behaviour, while some go through phases of recurring outbursts interspersed by periods of inactivity (EXO 2030+375).

The different types of X-ray activity where classified by Stella et al. (1986) into the following categories:

- Persistent low-luminosity X-ray emission ($L_{\rm x} \lesssim 10^{36}\,{\rm erg\,s^{-1}}$) or none detectable (in which case the system is said to be in quiescence).
- Type I outbursts: Outbursts of moderate intensity ($L_{\rm x} \simeq 10^{36}-10^{37}\,{\rm erg\,s^{-1}}$) and short duration (a few days) generally recurring with the orbital period of the system and taking place at, or close to the time of periastron passage.
- Type II outbursts: Giant X-ray outbursts ($L_{\rm x} \gtrsim 10^{37}\,{\rm erg\,s^{-1}}$) lasting for weeks or months that generally begin around periastron but otherwise show no other correlation with orbital parameters.

It has become common to sometimes refer to the behaviour of a system as Type I or II, when many systems can undergo outbursts of both types at different times

during their lifetime. We therefore suggest that it would be more appropriate to separate the nomenclature for the type of outburst from that of the type of system, as they are not necessarily interchangeable. A look at the type of activity exhibited by Be/X-ray systems finds 3 broad groups that we classify as follows:

- Class Ia: Exhibits regular Type I outbursts, associated with periastron passage.
- Class Ib: Mixes periods of quiescence with periods of regular, Type I outbursts associated with periastron passage, often set off by an initial Type II outburst not necessarily coincident with periastron.
- Class II: X-ray activity is infrequent, but very bright when it happens, generally consisting of long Type II outbursts.

This is an appropriate point to introduce the *X-ray outburst density*, $X_{\rm od}$. It is simply defined as the number of outbursts that occur per orbit and will be useful in comparing pulsars across varying orbital periods. It is clear that a perfect Class Ia system would have $X_{\rm od} = 1$; a Class Ib would be $X_{\rm od} \simeq 0.5$; while a Class II system would have $X_{\rm od} \simeq 0.2$[1]. The $X_{\rm od}$ is not concerned with the brightness or duration of the outbursts, only with the number of them occurring during the period of observation. This parameter will be discussed further in § 4.3.

1.3.2 The spin/orbit connection

As the number of Be/X-ray systems with known orbital periods grew, a relationship was observed between the spin period, $P_{\rm s}$, of the neutron star and its orbital period, $P_{\rm orb}$, around its companion Corbet (1984). A different relationship between spin periods and orbital periods was later found for other types of high mass X-ray binaries Corbet (1986). Fig. 1.2 shows the spin/orbit, or Corbet, diagram. Fitting

[1]Note that a system exhibiting occasional apastron outbursts could have $X_{\rm od} > 1$!

a line to the Milky Way and SMC systems gives the following empirical relations (Corbet 2006, private communication):

$$P_{\rm orb} = 20.32\, P_{\rm s}^{0.3243}, \quad \text{Milky Way} \tag{1.1}$$

$$P_{\rm orb} = 17.94\, P_{\rm s}^{0.3118}, \quad \text{SMC} \tag{1.2}$$

Although there is a lot of spread in the graph, both lines are quite consistent with each other and point towards a real dependence of the orbital period on spin. In fact, it is probably the opposite, in Be/X-ray systems the orbital period will determine (in general) how often a system can accrete material, and as the rate of spin up is determined by the amount of matter accreted, eventually a system will reach equilibrium when the spin down in between outbursts is counterbalanced by the spin up during outbursts.

1.3.3 Outburst mechanisms

Fig. 1.3 shows the classical view of a Be/X-ray binary system, in which outbursts occur when the neutron star passes through the disc of the Be star. It this were correct, then the only parameters governing outbursts would be the presence of a circumstellar disc and the size of the neutron star's orbit. The larger the disc, and the smaller the periastron distance, the more likely it would be to see outbursts. This turned out to be a rather oversimplified model; while the extent of the Be disc and the neutron star orbit are indeed important, there are other factors influencing and triggering outbursts.

Okazaki (1998) presents some results from numerical simulations of Be discs based on the viscous disc model of Lee et al. (1993). He shows how a viscous, truncated disc, with a one-armed spiral perturbation can explain the behaviour of many Be/X-ray systems. It is also suggested that discs with circular or eccentric orbits will exhibit different X-ray behaviour. Further simulations, presented in Okazaki and Negueruela (2001), assume a near-Keplerian, isothermal disc which is governed pri-

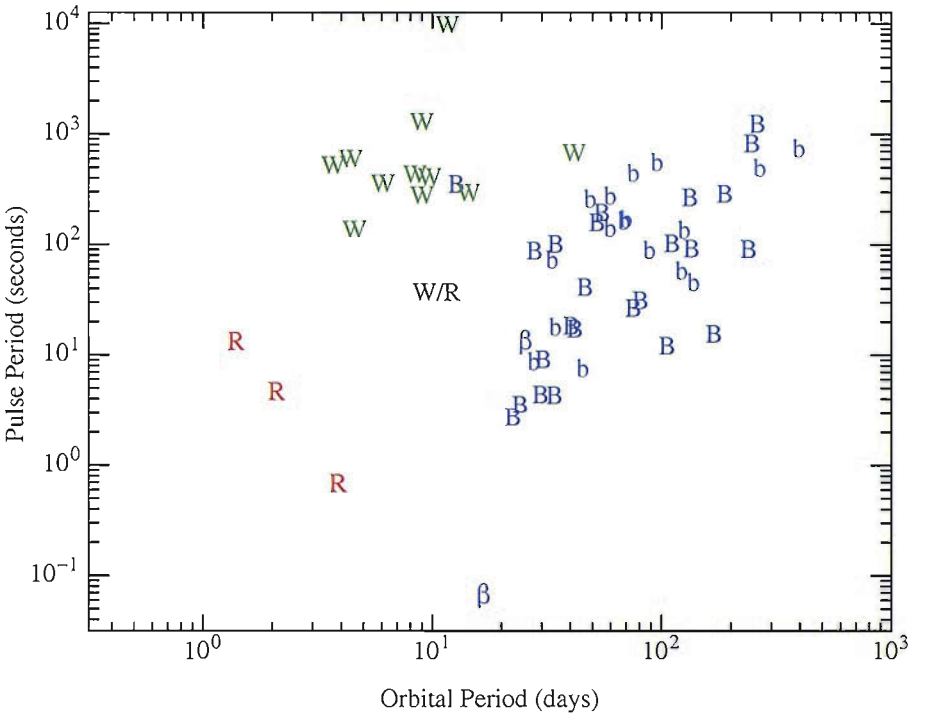

Figure 1.2: The spin/orbit relation diagram, also known as the Corbet diagram. The Be/X-ray binaries are denoted in blue, with B representing the Galactic, b the SMC and β the LMC systems. W represents the underfilled Roche lobe (wind accreting) supergiants, while R denotes the Roche lobe filling supergiants. Figure courtesy of Robin Corbet (2006, private communication).

marily by pressure and viscosity. The scenario that emerges is that of a truncated disc, whose truncation radius is at a distance resonant with the neutron star's orbital period. The truncation radius will depend on the temperature and viscosity of the disc, with higher values of either (or both) driving the disc to be larger. The model predicts that matter ejected by the Be star will continue to accumulate onto the disc, without making it any larger. Hence the disc becomes a reservoir of matter, becoming increasingly denser until it either accretes onto the neutron star or falls back onto its parent star. Fig. 1.4 shows the predicted truncation radii at different disc densities for a number of Galactic Be/X-ray systems. Another consequence of

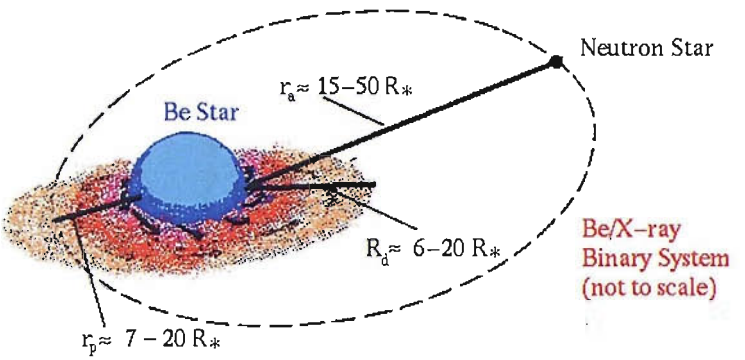

Figure 1.3: Classical view of a Be/X-ray binary system (from Slettebak (1988)).

the truncated disc is that the Hα-emitting region probably coincides with the actual disc size.

Because the truncation is affected (indeed induced) by the neutron star's passage, the only way for material in such a confined disc to be accreted is by passing through the L_1 point, akin to a disc Roch-lobe overflow. This material will have a low velocity relative to the neutron star but carry significant angular momentum such that the formation of an accretion disc around the neutron star is very likely.

Based on the predictions of this model made by Okazaki and Negueruela (2001) one would expect systems with a highly eccentric ($e > 0.5$) orbiting neutron star to primarily exhibit Type I outbursts and belong to Class Ia; systems with a low/mild eccentricity ($e \simeq 0.5$) would belong to Class Ib (with outbursts being triggered by instabilities in the disc making it temporarily asymmetric); while systems with very low eccentricity ($e \lesssim 0.2$) would belong to Class II, exhibiting mainly Type II outbursts (when the Be disc grows sufficiently large to reach the L_1 point). This classification is made with one caveat: it does not include the actual size of the orbit. Undoubtedly, a neutron star with $e = 0.3$ will not pass as close to its companion Be star if it is in a 300 day orbit as it would in a 10 day orbit. It would be desireable to combine both the orbital period and the eccentricity of a system to produce a figure that would be indicative of the type of behaviour exhibited by it. More systems need to be studied and the mechanisms behind the Be star's mass ejection must be better understood. It is also probable that the spin period and magnetic field of the neutron

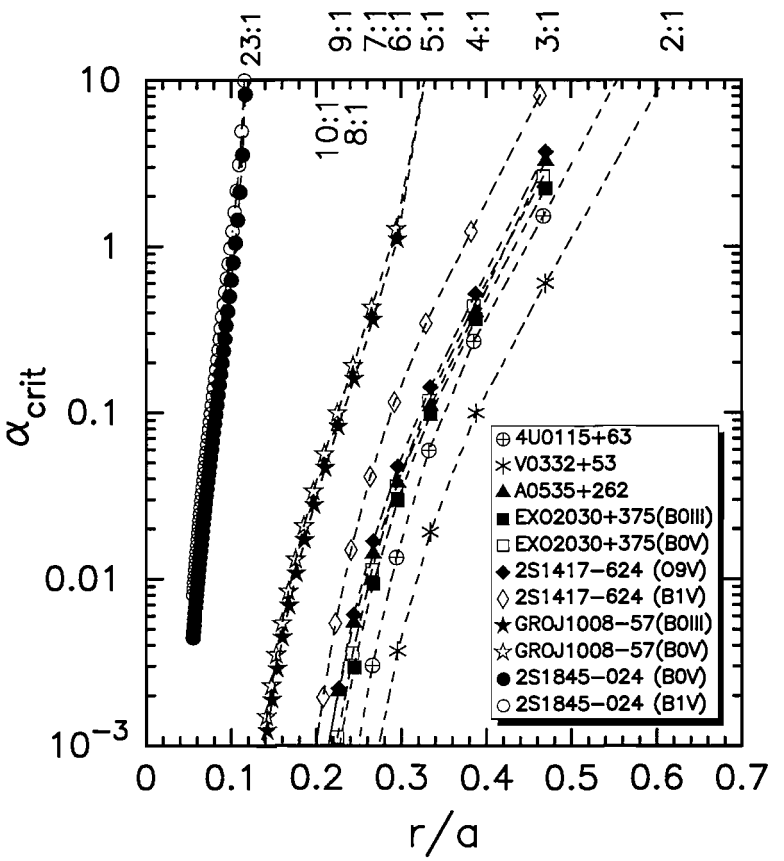

Figure 1.4: Critical values of α (the Shakura-Sunyaev viscosity parameter (Shakura and Sunyaev 1973)) at some resonance radii for a number of Galactic systems. $T_{\rm disc} = \frac{1}{2}T_{\rm eff}$ is adopted for all models (where $T_{\rm eff}$ is the effective temperature of the parent star). Figure taken from Okazaki and Negueruela (2001).

star are factors that should be taken into consideration. For example, the propeller effect (Illarionov and Sunyaev 1975) exhibited by the faster spinning neutron stars would significantly inhibit accretion, while high magnetic fields facilitate it.

As an example, A 0535+26 has been monitored over a long period of X-ray inactivity by Coe et al. (2005) (of which the present author was a contributor). Its Hα emission profile has provided estimates of the size of the disc, which has been found to be consistent with the 7:1 truncation radius for the last $\sim$3 years. Shortly after the end of 2003 the disc began expanding until it underwent a Type II outburst in May/June 2005, the first outburst in $\sim$10 years. Three further outbursts, of a lower intensity followed the initial one and were separated by the orbital period,

coinciding with the periastron ephemeris proposed by Coe et al. (2006).

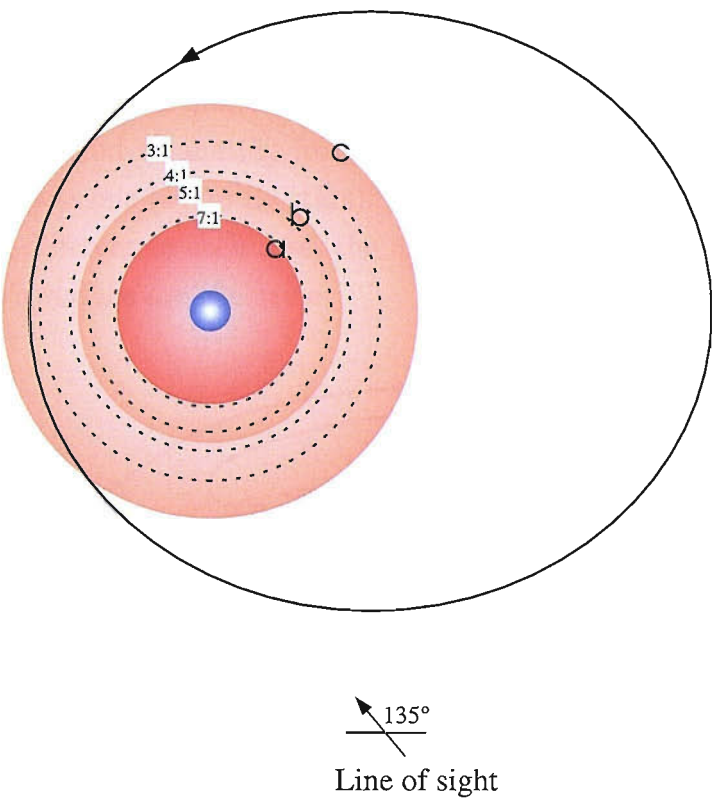

Figure 1.5: Estimate of the radius of the Hα emitting region of the circumstellar disc of A 0535+26 compared to the neutron star orbit (solid black line). The three disc sizes shown correspond to the following radii and epoch values: a) 4.8×10^{10} m, $\sim$2001 – 03; b) 6.8×10^{10} m, March 2005; c) 10.7×10^{10} m, August 2005. The Be-to-NS distance at periastron is 9.33×10^{10} m. Four truncation radii are shown in dashed lines for comparison (6:1 has been left out for clarity). The Be star is drawn to scale. Picture based on data provided by Vanessa McBride (2005, private communication).

Okazaki and Negueruela (2001) predict the circumstellar disc to be at the 4:1 or 5:1 truncation radius (they assume a value of $\alpha \simeq 0.1$). From our study the Hα emitting region appears to have been in the 7:1 radius for the $\sim$3 years before it began to extend outwards; if we are to assume that this is indicative of the physical radius of the disc, then it would imply a very low viscosity of $\alpha \lesssim 0.02$.

1.3.4 Neutron star accretion

"When I eat a biscuit," said Arthur, "it stays eaten."

—The Hitchhiker's Guide to the Galaxy

A neutron star orbiting its massive companion may accrete matter from one of two sources: the stellar wind emanating from the companion, or from its circumstellar disc, should it possess one (as for Be stars). Although the dynamic properties of the captured gas are different in each case, the mechanisms required to deposit it onto the neutron star's surface are the same.

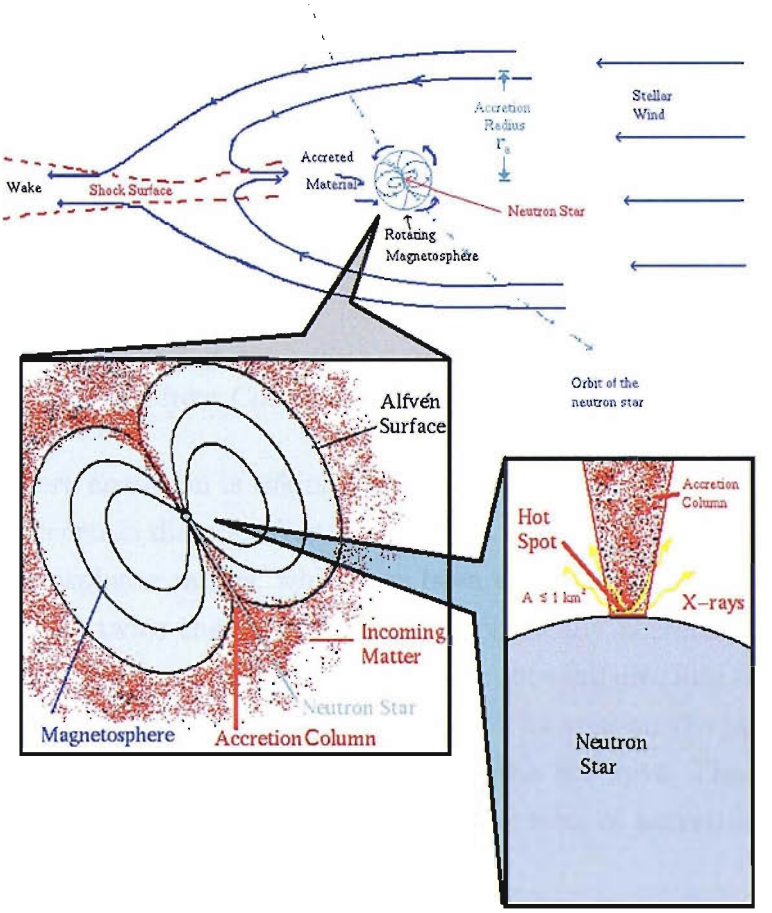

Figure 1.6: Accretion onto a neutron star from a stellar wind; see text for details. Diagram from Davidson and Ostriker (1973); Ventura and Pines (1991).

As the neutron star passes through the stellar wind (as in Fig. 1.6) its gravity

attracts gasses towards it. Because the neutron star has a strong magnetic field ($\gtrsim 10^{12}$ G) the gas particles will follow the field lines to one of the neutron star's poles. Of course, the velocity of the incoming gas will determine at what distance from the neutron star's surface it will start to follow a field line. In general, a mass of in-falling gas will posses a certain ram pressure; the distance at which it is equaled by the magnetic pressure (which is exerted outwards) is called the Alfvén radius ($R_{\text{Alfvén}}$). Once within this radius the trajectory of the gas will be magnetically dominated (Toropina et al. 2003).

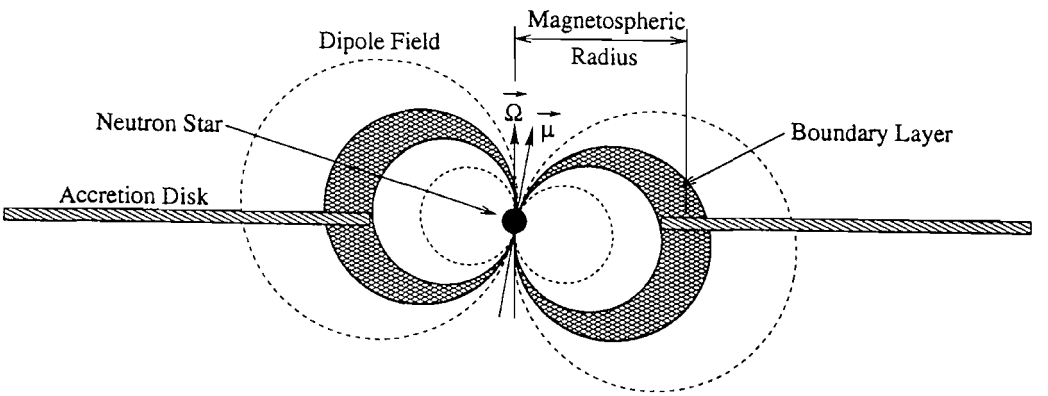

Figure 1.7: Side view of the accretion flow around a neutron star; see text for details. Diagram from Coburn (2001).

In the case where accretion is taking place from a disc, as in Fig. 1.7, the disc will be truncated at a certain distance from the surface, $R_{\text{mag}} < R_{\text{Alfvén}}$. This distance is called the magnetospheric radius, which has been estimated as the radius for which magnetic pressure is twice the ram pressure of spherically accreting matter (Lamb et al. 1973). At this radius the magnetosphere disrupts the disc and forces matter to move along the field lines towards the closest pole. The area on the pole of a neutron star where matter is falling onto is referred to as the *hot spot.* The characteristics of the hot spot differ greatly depending on the type type of accretion taking place:

Stellar wind accretion: The in-falling material most likely undergoes spherical accretion and is probably stopped by a collisionless shock outside the magnetosphere, penetrating it through the Rayleigh-Taylor instability. This implies that matter will literally rain through the magnetosphere until it becomes attached to a field line. For low luminosities (i.e., low mass accretion) it is

possible for material to fall directly onto the neutron star surface without following a field line. The conclusion is that the size of the hot spot is inversely proportional to L_x (to $\sqrt{L_x}$, in fact) (White et al. 1983).

Disc accretion: If in-falling material has sufficient angular momentum to form an accretion disc, it will pinch the magnetosphere and penetrate via a transition zone where field lines thread it such that Kelvin-Helmholtz instabilities or magnetic flux reconnection force it to follow the field lines. As the amount of in-falling material increases (thus increasing the ram pressure) the field lines it will follow get closer and closer to the neutron star's surface, such that matter will fall increasingly further from the poles. Hence we reach the opposite conclusion in this case, the size of the hot spot will increase with L_x (and is proportional to $L_x^{2/7}$ (Baan and Treves 1973)).

We will concentrate on the disc scenario, as that is the most likely mechanism by which neutron stars in Be/X-ray binaries accrete matter (Hayasaki and Okazaki 2004, 2005). After leaving the disc, the in-falling gas is accelerated by the magnetic field to extremely high speeds, $\sim 0.1-0.3\,c$, and it is believed to not reach the actual surface of the star, but be stopped by a standing shock maintained by radiation pressure (Davidson and Ostriker 1973; Burnard et al. 1991). This structure is called the accretion mound (a schematic view of which is shown in Fig. 1.8) and simulations suggest it can be as high as 600 m with a radius of up to 1 km (Burnard et al. 1991).

This model would be able to explain the two types of X-ray beams observed from pulsars: pencil and fan beams. Pencil beams, as the name suggests, are thin beams emanating from the poles of the neutron star that are observed as the pole(s) cross the viewer's line of sight. Fan beams, on the other hand, are characterised by emitting photons at relatively large angles to the magnetic axis, even perpendicular to it; in this case, X-rays will be observed when the magnetic equator of the neutron star crosses the line of sight. A mound with a vertical geometry could be responsible for this type of beam, while a flatter mound could produce pencil beams. Many pulsars are seen to exhibit either type at different times, sometimes changing from one to another during the course of an outburst. What is most likely is that both types of beams are always present, albeit at different intensities. A cylindrical slab of varying height could be responsible for this. From observations of a number

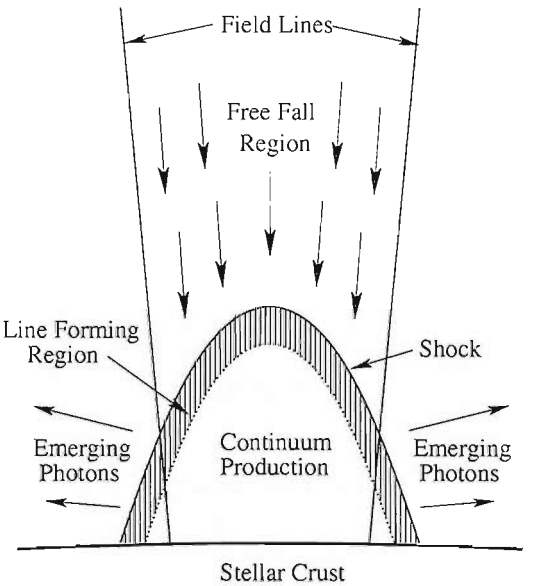

Figure 1.8: Schematic diagram of the accretion mound on a neutron star. Diagram from Heindl et al. (2004).

of different systems it would appear that at low luminosities, $L_x \lesssim 10^{36} - 10^{37}$, no pressure shock is formed and the accretion mound is flat, leading to a pencil beam. At higher luminosities, $L_x \gtrsim 10^{37} - 10^{38}$, a high mound would form and create a fan beam. Some systems exhibit phase reversals in their pulse profiles at different energies, indicative that a) both types of beam are present and, b) that the fan beam dominates the hard band while the pencil beam the soft band (White et al. 1983). Such pulse profile changes at different luminosities have been observed in a number of systems, e.g., EXO 2030+375 (Parmar et al. 1989a) and GX 1+4 (Makishima et al. 1988).

1.3.5 Pulsar profiles

The shape of the pulse profile of a rotating neutron star will depend on a number of factors:

Position of the emitting region(s): Fig. 1.9 shows the position of magnetic poles on a neutron star. That the magnetic axis does not coincide with the spin axis is

the reason it is possible to see pulsars at all. The angles between the two axes and the angle between them and the line of sight will determine how strong the detected emission will be. The smaller the angle between the magnetic axis and the line of sight, the more X-rays will be incident on our detectors. Also, these angles determine whether one or two poles will be seen. It is important to note that it is not necessary for the magnetic poles to be at 180° opposite each other.

Structural geometry of the emitting region(s): Depending on the morphology of the emitting region the hot spot will produce a pencil or fan beam, or even both types. Fig. 1.10 shows the shape of these beams, and the type of profiles they produce.

Energy range observed: In general, profiles are simpler at higher energies, showing less structure. Because the fan beams generally dominate the higher energies, profiles can look very different from those of lower energies, where we are more likely to observe the emission due to the pencil beam. For this reason, profiles will often be out of phase by 180° between the low and high energy bands.

Luminosity of the emission: Profiles are seen to change with luminosity, as it depends on the amount of material being accreted onto the neutron star, which in turn will dictate the size and shape of the emitting region, thus affecting the pulse profile.

Presence of accretion disc: A disc might obscure part of the emission or hide one of the poles.

For an overview of changes in profile shape with varying luminosities and energy ranges, see White et al. (1983); Nagase (1989).

Although a pulse profile can provide clues as to the geometry and nature of the emitting region, there is a certain degeneracy associated with it. In the case of the pencil beam profile in Fig. 1.10, the asymmetric peaks could be due to 4 causes: both hot spots are emitting with the same strength, but due to the position of the various axes one of the magnetic poles is viewed preferentially; both poles are viewed equally, but one pole is emitting stronger than the other; one of the magnetic poles

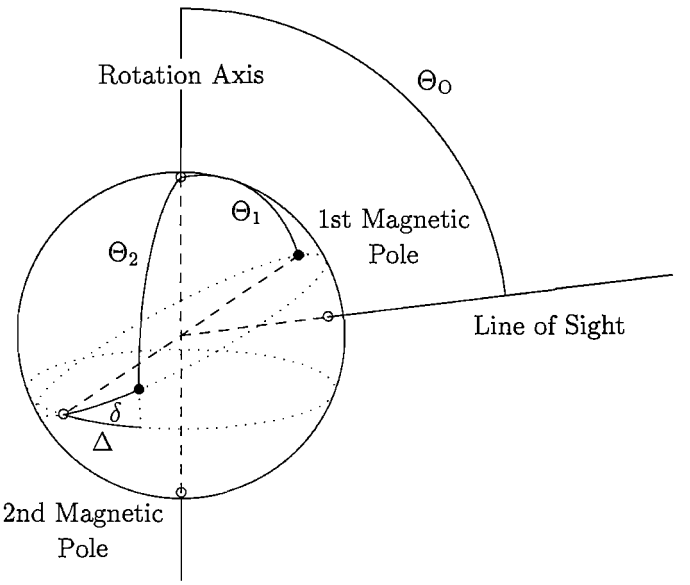

Figure 1.9: Schematic diagram of the location of magnetic poles on a neutron star (from Blum and Kraus (2000)).

is offset and is viewed at a different angle to the other; one of the poles is being viewed through the accretion disc and its emission is attenuated. Of course, this shape could also be due to a combination of two or more of the above factors.

It should be noted that double-peaked profiles are rather rare, Bulik et al. (2003) show that the available pulse profiles (using mostly Galactic sources) are inconsistent with a model of random axis alignment, but consistent with a model where the line of sight and the spin axis are randomly aligned, but the magnetic axis is constrained to lie within a certain angle of the spin axis. They argue that there is some mechanism which tends to align these axes and they set an upper limit of 50° on the rotation-magnetic axis angle.

In the case of a fan beam, both peaks will be symmetrical whatever the axes configuration and/or beam strength; however, an offset magnetic pole will result in unequal peaks in the profile, as would obstruction of the line of sight towards one of the poles by the accretion disk. Another consideration are the relativistic effects suffered by photons leaving the hot spot. These will vary depending on the dispostion of the axes and will affect pencil and fan beams differently (for a given pulsar); their main effect is the distortion of the profile making the individual peaks

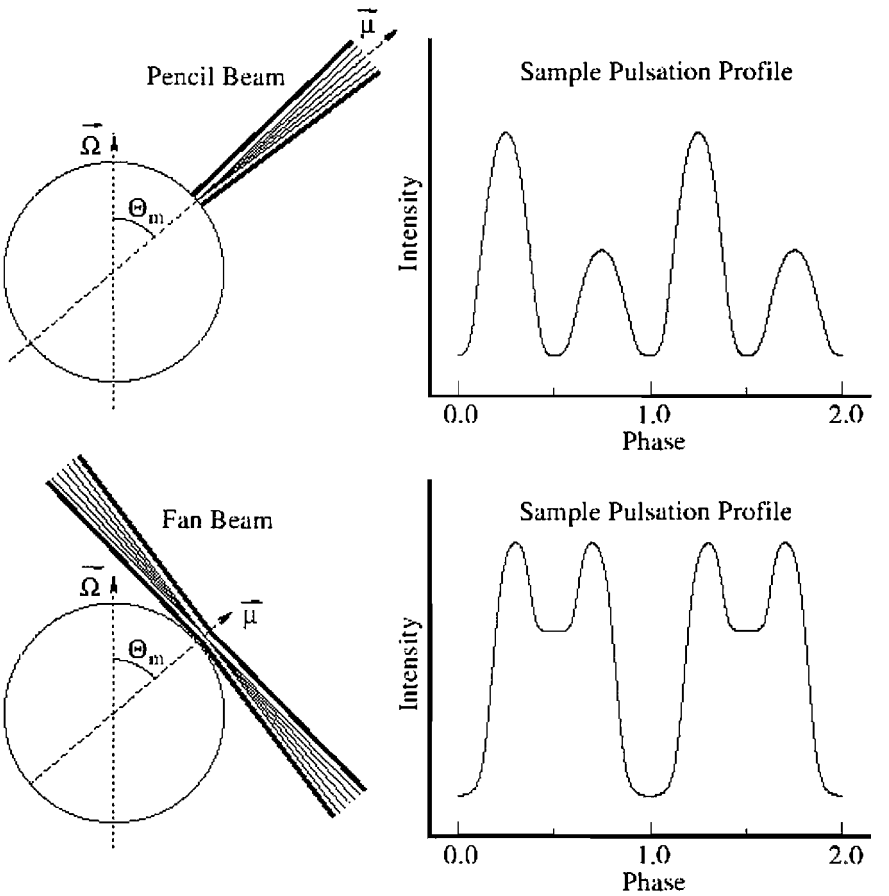

Figure 1.10: Types of beams produced and the profiles observed for an X-ray pulsar from a pencil beam (*top*) and a fan beam (*bottom*). Only one pole is shown emitting, but the profiles correspond to two emission poles, which have been set 180° apart. Diagram from Coburn (2001).

lopsided.

A number of studies have been carried out to recreate the shape of the pulse based on models of rotating hot spots and/or hot mounds. Parmar et al. (1989a) fit the pulse profile of EXO 2030+375 at different times using fan and pencil beam components; they find that an offset pole is likely present. Burnard et al. (1991) study the emission from a theoretical mound and model the expected flux at different viewing angles. Blum and Kraus (2000) analyse the profiles of Her X-1 and find that they can be reproduced by the superposition of two single-pole profiles.

1.3.6 Energy in accretion

Let us consider a neutron star accreting mass at a certain rate, $\dot{M}$. The luminosity that will result is simply the gravitational energy lost by the in-falling mass:

$$L_{\mathrm{x}} = \frac{GM\dot{M}}{R} \tag{1.3}$$

Some manipulation and substitution can provide a more manageable expression:

$$L_{\mathrm{x}37} = 8.4 \times 10^{9} \left(\frac{M_n \dot{M}}{R_n} \right) \tag{1.4}$$

which will give us the luminosity in terms of $10^{37}\,\mathrm{erg\,s^{-1}}$, and where M_n is the mass of the neutron star in units of $M_\odot$, $\dot{M}$ is the mass accretion rate in units of $M_\odot\,\mathrm{yr}^{-1}$, and R_n is the radius of the neutron star in km. Substituting reasonable values for the neutron star parameters ($1.4M_\odot$ and a 10 km radius) tells us that a relatively small accretion rate of $\dot{M} \approx 10^{-8}\,M_\odot$ is all that is required to achieve a luminosity of $10^{38}\,\mathrm{erg\,s^{-1}}$.

There is, of course, a limit on how bright an outburst can be. If we suppose steady spherical accretion of ionised hydrogen onto a compact object, we have in-falling gas under gravitational attraction that is being opposed by an outward radiation pressure of photons. The photons scatter preferentially off the ions' electrons[2], which drag the protons after them as they are attracted by the electrostatic Coulomb force. As long as the gravitational force is greater than the outward radiation pressure, accretion will continue. The point of equilibrium is reached when both become equal:

$$\frac{GM(m_p + m_e)}{r^2} = \frac{L\sigma_{\mathrm{T}}}{4\pi c r^2} \tag{1.5}$$

[2]The scattering cross-section of the proton is $\sim 10^{-8}$ times that of the electron.

On the left we have the gravitational force exerted by a body of mass M on a proton and an electron of masses m_p and m_e, respectively. On the right is the radiation force supplied by a luminosity L, where σ_{T} is the Thomson cross-section of the electrons. Thus, the luminosity at which equilibrium occurs for an accreting neutron star is

$$L_{\mathrm{Edd}} = \frac{4\pi G M m_p c}{\sigma_{\mathrm{T}}} \simeq 1.3 \times 10^{38}\, M_n \ \mathrm{erg\,s^{-1}} \tag{1.6}$$

and is called the Eddington luminosity, or Eddington limit, where M_n is in solar masses. For a standard neutron star of $1.4\, M_\odot$ it turns out to be $\sim 1.8 \times 10^{38}\,\mathrm{erg\,s^{-1}}$, and once this luminosity is reached accretion is expected to stop. In Be/X-ray binaries accretion takes place from a disc, so the Eddington limit will not be exactly the value calculated as accretion will not be spherical, nor necessarily constant. However, it is a useful quantity to have in mind and use a yardstick of sorts to establish just how bright an outburst may be, and how much brighter we might expect it to become. If an outburst is being monitored while it suddenly turns off, then we would know that it had reached its true Eddington limit and knowing the luminosity at which this happened can provide clues as to the nature of the compact object and the accreting material.

The angular momentum of a neutron star is given by

$$\mathcal{L}_n = \frac{2\pi I_n}{P_{\mathrm{s}}} \tag{1.7}$$

where P_{s} is the spin period, and the moment of inertia is given by

$$I_n = \frac{2}{5} M_n R_n^2 \tag{1.8}$$

with M_n and R_n being the mass and radius of the neutron star in standard units.

The torque suffered by a neutron star spinning up or down is given by

$$|\tau| \equiv \left| \frac{d\mathcal{L}_n}{dt} \right| = 2\pi I_n \frac{\dot{P}_s}{P_s^2} \tag{1.9}$$

with $\dot{P}_s$ being the rate of change of the spin period.

For an accreting pulsar undergoing steady spin up/down, the applied torque will depend on the mass accretion rate, $\dot{M}$, and the angular momentum of matter in the accretion disc at the magnetospheric radius, r_m. This torque is given by

$$\tau = \dot{M}\sqrt{GM_n r_m} \tag{1.10}$$

The maximum torque possible will occur when $r_m = r_{co}$, where the corotation radius[3] is given by

$$r_{co} = \left(\frac{GM_n P_s^2}{4\pi^2} \right)^{\frac{1}{3}} \tag{1.11}$$

Substituting this value in Eq. (1.10) will provide the expression for the maximum torque possible:

$$\tau_{\max} = \dot{M} \left[\frac{G^2 M_n^2 P_s}{2\pi} \right]^{\frac{1}{3}} \tag{1.12}$$

Clearly, $|\tau| \leq \tau_{\max}$, so using Eqs. 1.9 and 1.12, and substituting the expression for the moment of inertia from Eq. (1.8), we find the accretion rate will be

$$\dot{M} \geq \frac{2}{5} R_n^2 \dot{P}_s \left[\frac{16\pi^4 M_n}{P_s^7 G^2} \right]^{\frac{1}{3}} \text{ kg s}^{-1} \tag{1.13}$$

[3]The corotation radius is defined as the radius at which matter in the disc is moving at the same speed as the neutron star's surface.

substituting this value in Eq. (1.3) we finally obtain the lower limit on the luminosity that will be produced through accretion:

$$L_{\mathrm{x37}} \geq \frac{2R_{\mathrm{n}}\dot{P}_{\mathrm{s}}}{5 \times 10^{30}} \left[\frac{16\pi^4 G M_n^4}{P_{\mathrm{s}}^7}\right]^{\frac{1}{3}} \tag{1.14}$$

which will be in units of $10^{37}\,\mathrm{erg\,s^{-1}}$ if S.I. units are used. This equation will allow the estimation of the luminosity associated with an outburst if the average spin up/down is measured, and an estimate for the neutron stars mass and radius are made Throughout the present work, whenever this equation is used, the following values are employed as estimates: $R_n = 10\,\mathrm{km}$ and $M_n = 1.4 M_\odot$.

One further value that can be estimated is the magnetic field of the neutron star. Rearranging Eq. (6.24) of Frank et al. (2002), and using the period in place of the frequency, we can place a constraint on its value:

$$B_{12} \leq \left[3.4 \times 10^{-4}\, R_n^{-2}\, M_n^{\frac{-10}{7}}\, L_{\mathrm{x37}}^{\frac{6}{7}}\, \frac{P_{\mathrm{s}}^2}{\dot{P}_{\mathrm{s}}}\right]^{\frac{-7}{2}} \tag{1.15}$$

where the magnetic field will be in units of 10^{12} G if M_n is in $M_\odot$ and R_n in metres.

1.3.7 Evolution of a Be/X-ray binary system

It seems paradoxical to encounter a star at the end of its life (a neutron star) orbiting a star as young as a Be; surely the massive Be star should have died out long ago. The answer to this riddle is that both stars have coevolved and in the past there were episodes of mass transfer from the now-neutron star onto its companion; this "gas transfusion" allowed it to live on after the donor had died in a supernova. Numerical simulations have been successful in reproducing viable Be/X-ray systems; Fig. 1.11 shows what might be the typical scenario, which consists of 6 stages (Charles and Seward 1995):

Stage 1: Two massive stars are formed in a system with a 2.6 binary period.

Stage 2: The larger of the two stars evolves more rapidly and within 12 million years grows enough to fill its Roche-lobe and matter (hydrogen) from its outer layers flows onto the companion.

Stage 3: After $\sim 60\,000$ years the larger star has transferred $\sim 10\,M_\odot$ onto the companion (while at the same time speeding up its rotation), which is now the bigger of the two, and has reached the mass of a B/Be star while its once-massive companion is now a $2.5\,M_\odot$ helium star. Due to conservation of angular momentum the orbit has widened to 20 days.

Stage 4: The helium star continues its rapid evolution and within 3 million years it will again have filled its Roche-lobe and started a second season of mass transfer.

Stage 5: Although probably only $\sim 0.3\,M_\odot$ is exchanged this time, it is enough to leave only the carbon core of the helium star remaining. After ~ 50 years it collapses and goes supernova.

Stage 6: Asymmetries in the supernova explosion will have imparted a kick to the newborn neutron star moving it into an eccentric orbit around its massive Be companion.

1.4 X-ray binaries in the SMC

The Magellanic Clouds are two companion galaxies to the Milky Way, the LMC is ~ 50 kpc away while the SMC is ~ 65 kpc (Udalski 1998). The LMC is $\sim \frac{1}{5}$ the mass of the Milky Way, while the SMC is $\sim \frac{1}{50}$, and is the most irregular. They can be observed only from the Southern skies and their central coordinates are LMC: RA 05 15 00, dec −69 00 00, and SMC: RA 01 00 00, dec −73 00 00. In the present work we concentrate on the SMC.

To the naked eye the SMC appears as a fuzzy, irregular patch (Fig. 1.12). It is more convenient to observe it in neutral hydrogen, H I, which tells us how gas is dis-

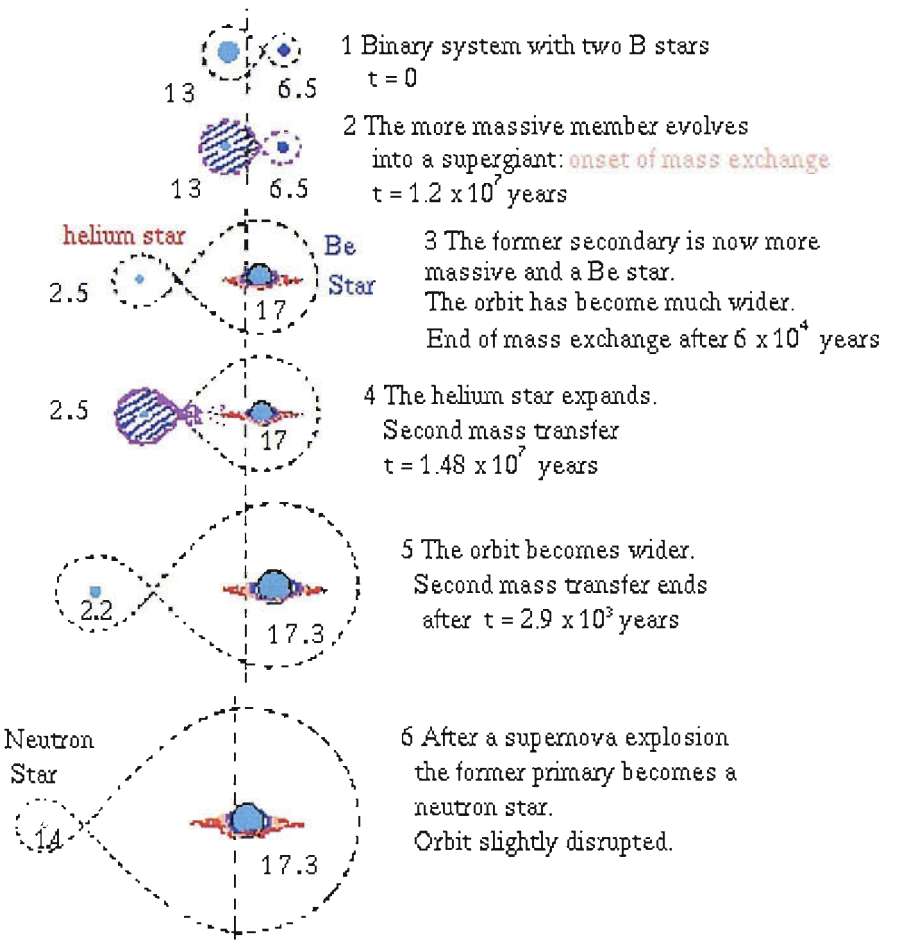

Figure 1.11: Graphical representation of the evolution of a Be/X-ray binary system. Taken from Charles and Seward (1995).

tributed within the galaxy. Fig. 1.13 shows a radio map of the column density of H I towards the SMC, on which have been plotted the X-ray pulsars whose coordinates are known. The two contour lines are at 21.7×10^{20} and 39.0×10^{20} atoms cm^{-2} for reasons that we explain in the following paragraphs.

Are the X-ray binary systems randomly distributed within the SMC? To see whether or not there were preferential sites, a histogram was plotted of the distribution of H I in the SMC. On the same graph we plot another histogram with the distribution of pulsars on the H I map, where the value of $n_{\rm H}$ at the coordinate of each pulsar has been used. Fig. 1.14 shows these distributions. It is clear that the pulsars are not randomly positioned as they do not follow the distribution of gas,

Figure 1.12: The SMC, as seen with the naked eye (© Cristoph Ries).

and over half of them can be found between $\sim 25-50 \times 10^{20}$ atoms cm^{-2}. Furthermore, the SMC curve has a feature in this region, which could be interpreted as either a bump or a dip; in either case, it is at this column density that we find the highest number of pulsars. For this reason we used the values of $n_{\rm H}$ at the beginning of the pulsar histogram peak, and at the highest point of the "feature" to plot the contours on Fig. 1.13.

As a comparison, Fig. 1.15 shows the same histogram for the LMC. It is true that we have included a number of black holes, not only pulsars, but the comparison should stand. We note that the distribution of compact objects follows the distribution of gas, which shows a smooth decline devoid of features.

In view of this apparent preference for a certain range of column densities within the SMC, a proposal was submitted to *Chandra* to carry out 20 observations along the wing, following the contour line of 39.0×10^{20} atoms cm^{-2}. The observations were made in March – April 2006; 2 known pulsars (SXP101 and SXP348) were detected, as were 4 new ones, their positions being marked by red circles in Fig. 1.13. This brings the total number of confirmed X-ray binaries up to 51. The new pulsars were not included in the production of Fig. 1.14, and were not used in the studies

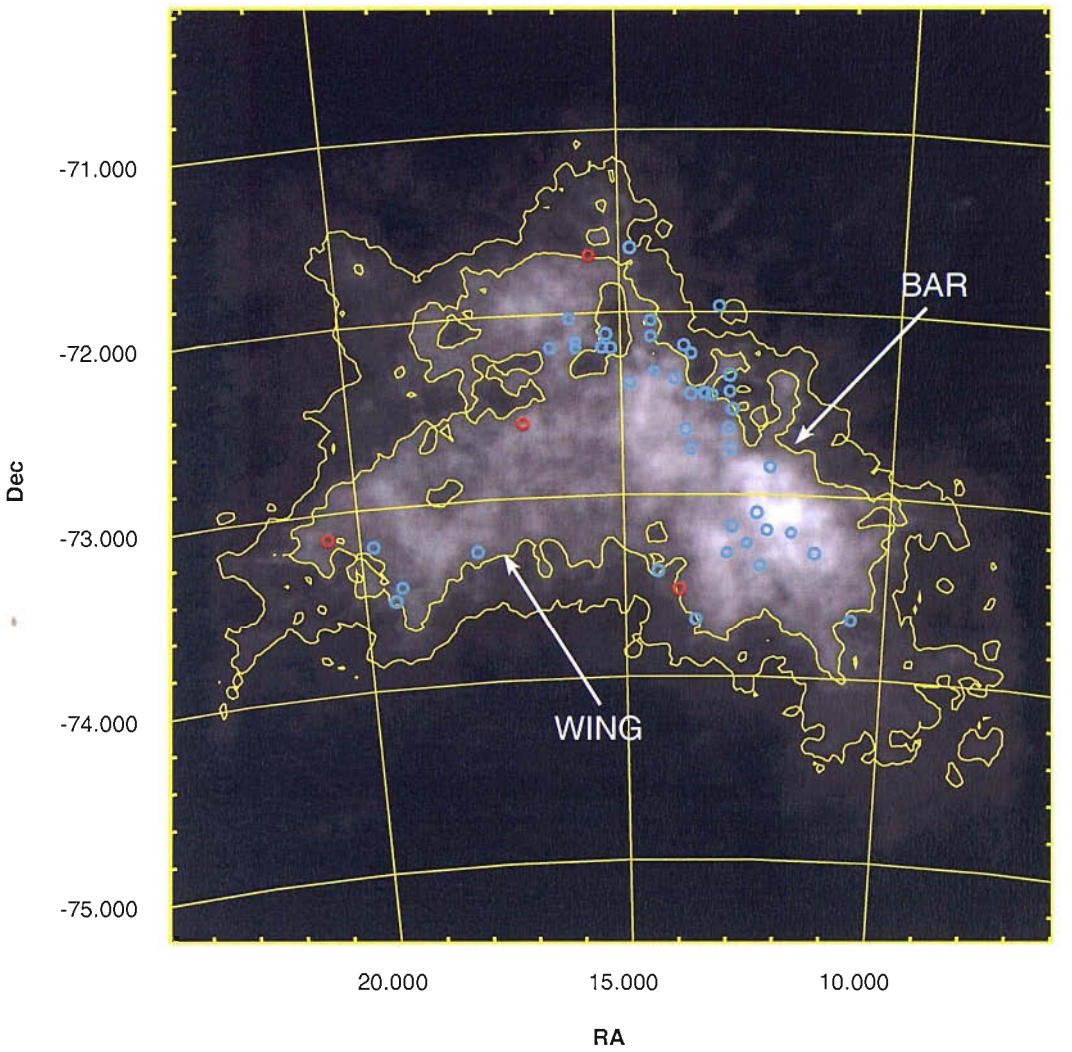

Figure 1.13: Map of the SMC H I distribution with the positions of known pulsars. The 4 newly discovered pulsars are in red. Contour lines are at $n_{\rm H} = 21.7 \times 10^{20}$ and 39.0×10^{20} atoms cm^{-2}. The colour scale of the H I map goes from 0 to 142.8×10^{20} atoms cm^{-2}. (H I data from Stanimirovic et al. (1999).)

described in Chapters 3 and 4 as their discovery occurred during the writing of the present work.

It is not easy to explain the distribution of pulsars without knowing if the feature around 40×10^{20} atoms cm^{-2} is a bump, or if there is a dip around 20–

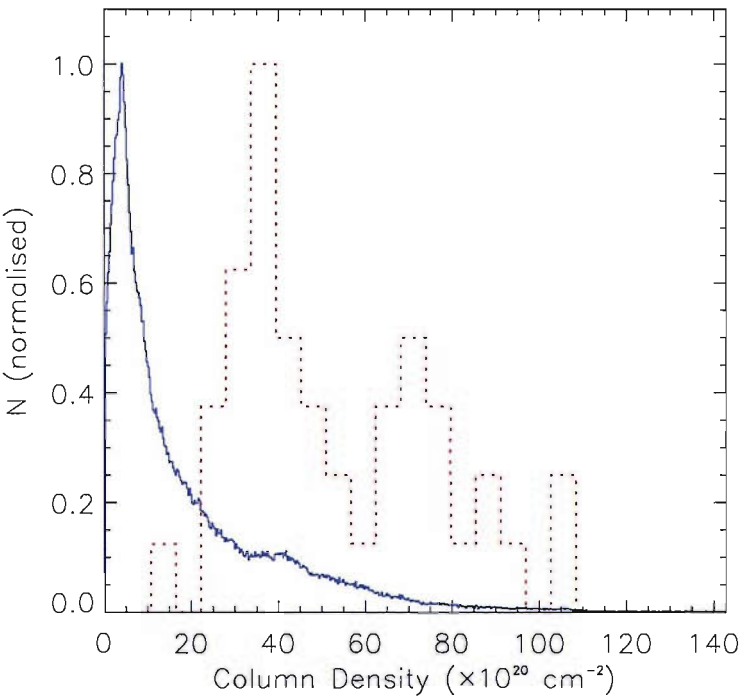

Figure 1.14: Histogram of the SMC H I distribution (continuous blue line) and the corresponding histogram of H I columns at the location of the X-ray pulsars (dotted red line). In both cases, the maximum value for each histogram was assigned $N = 1$ and all other values were scaled to it. 43 pulsars were included in the red histogram. H I data from Stanimirovic et al. (1999).

40×10^{20} atoms cm^{-2}. If it were a dip, then it could be argued that the missing gas had been used up in star formation, so one would expect to find more stars in these regions, and hence more X-ray binaries. Of course, the same explanation could be used if it were a hump; because there is more gas in that region, there are more stars, and more X-ray binaries. In either case, we find no reason for the lack of systems below 20×10^{20} atoms cm^{-2} (except for one, SMC X-1), in clear discrepancy with the LMC distribution.

The SMC has become a veritable goldmine of high mass X-ray binaries in the past decade or so; after the launch of modern satellites (*ROSAT*, *ASCA*, etc.) the number of X-ray binaries discovered increased exponentially. It is important to note that the SMC has a higher number of X-ray systems than would be expected from

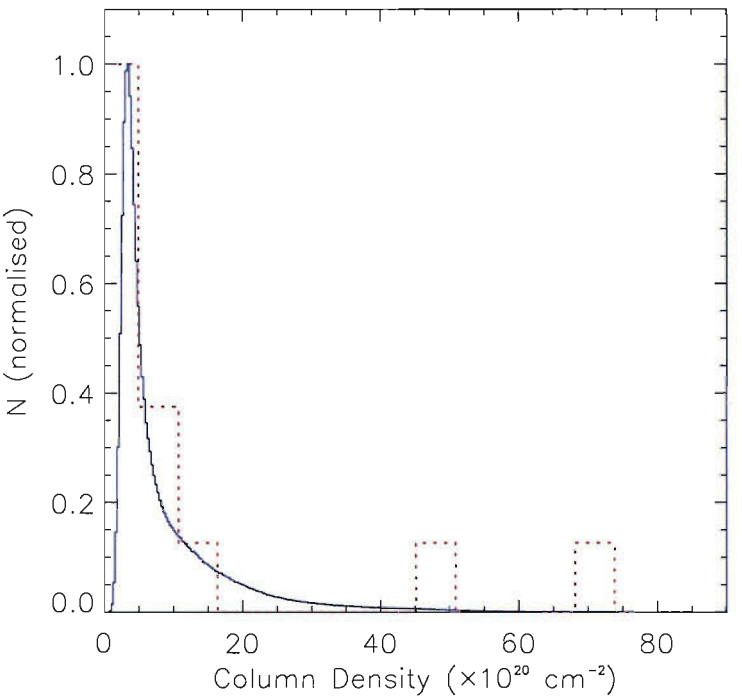

Figure 1.15: Histogram of the LMC H I distribution (continuous blue line) and the corresponding histogram of H I columns at the location of the X-ray pulsars and black holes (dotted red line). In both cases, the maximum value for each histogram was assigned $N = 1$ and all other values were scaled to it. 14 objects were included in the red histogram. H I data from Staveley-Smith et al. (2003).

its mass if we compare it to our own Milky Way, in fact almost 40% of the known systems can be found there. Even taking into account that the ratio Be/(Be + B) is $\sim 2-4$ times larger for the SMC[4], we would still only expect to find $3-5$ Be/X-ray systems. So far there are 50 known. Furthermore, only one of its 51 X-ray systems is not of the Be type (SMC X-1 is a supergiant system). This raises some questions as to how and why the SMC differs from our own, especially considering it is so close. See Coe et al. (2000) for a review of X-ray systems in the Magellanic Clouds, and a possible explanation for this discrepancy in the binary X-ray population compared to the Milky Way. The solution proposed by Yoshizawa and Noguchi (2003) suggests

[4]The Be/(Be + B) ratio found for the interior and exterior of the Milky Way is 0.1 and 0.19 respectively; for the SMC it is 0.39 (Maeder et al. 1999).

that an encounter between the two Magellanic Clouds some 200 Myr ago induced a tidal interaction resulting in a sudden increase in star formation. Although this seems a likely hypothesis, as Be stars are massive stars that tend to be short-lived, the evolutionary process explained in § 1.3.7 takes only ~ 16 Myr to complete, and we would not expect the system to survive for a further 184 Myr. Also, why so many X-ray systems contain Be stars, and not supergiants, remains to be explained. As the number of X-ray systems discovered in the SMC continues to rise, the answer to these questions may become clearer.

Chapter 2

A Study of Be/X-Ray Binaries with *BATSE*

A picture of the Universe in X-rays is indeed unfolding, but it is a picture that changes with every new experiment, month by month.

—Riccardo Giacconi & Herbert Gursky

2.1 *BATSE* — The Burst And Transient Source Experiment

BATSE was a high energy astrophysics experiment in orbit around Earth on-board NASA's Compton Gamma-Ray Observatory (*CGRO*, Fig. 2.1). The primary objective of *BATSE* was to study the phenomenon of gamma-ray bursts, although the detectors also recorded data from pulsars, terrestrial gamma-ray flashes, soft gamma repeaters, black holes, and other exotic astrophysical objects. It was launched in April 1991 and ended its mission in June 2000. *BATSE* responded to, or triggered on, sudden changes in count rates above background levels. It was also capable of detecting less impulsive sources by measuring their modulation using the Earth

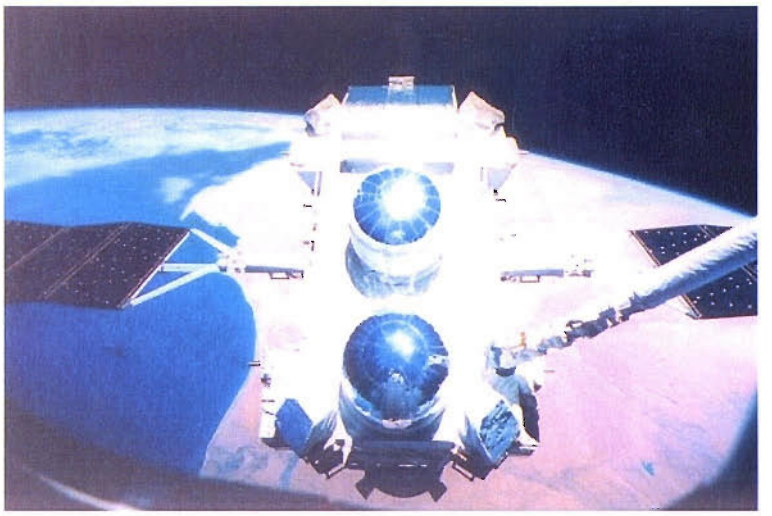

Figure 2.1: A photo of *CGRO*, being deployed by the space shuttle Atlantis. The LADs can be seen on the corners of the spacecraft.

Occultation technique.

The full-sky viewing of *BATSE* enabled the nearly continuous observation of all pulsars brighter than about 15 mCrab. Most of the known accretion-powered X-ray pulsars have periods of $\sim 1 - 1000$ s, so the 1.024 s samples *BATSE* continually returned in the telemetry were used to measure the current state of previously known sources, and search for new ones. By detecting the pulse arrival time (which can usually be done to an accuracy of a few percent of the pulse period), it measured the orbit of the neutron star around the companion, and the rotation period of the neutron star.

2.1.1 The detectors

One of the eight identically configured detector modules of *BATSE* is shown schematically in Fig. 2.2. Each detector module contains two NaI(Tl) scintillation detectors: a Large Area Detector (LAD) optimized for sensitivity and directional response, and a Spectroscopy Detector (SD) optimized for energy coverage and energy resolution. Each LAD has a field of view of 2π sr and the eight planes of the LADS are parallel to the eight faces of a regular octahedron, with the orthogonal primary axes of the

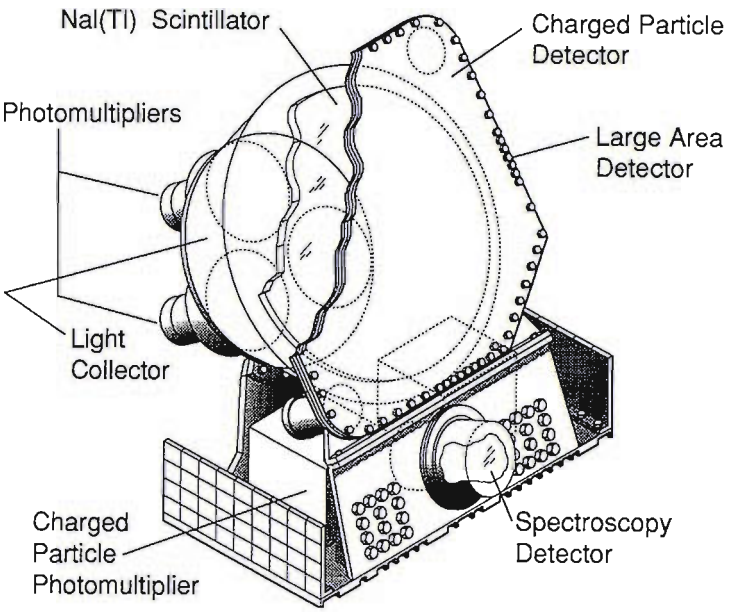

Figure 2.2: Schematic diagram of one of the 8 LADs comprising *BATSE*.

octahedron aligned with the coordinate axes of the Compton spacecraft; this gives *BATSE* a whole-sky field of view. All the data used in the present work came from the LADs.

The LAD detector is a disk of NaI scintillation crystal 20 inches in diameter and 1.27 cm thick, mounted on a 1.91 cm layer of quartz. The large diameter-to-thickness ratio of the scintillation crystal produces a detector response similar to that of a cosine function at low energies where the crystal is opaque to incident radiation. At energies above 300 keV, the angular response is flatter than a cosine. A light collector housing on each detector brings the scintillation light into three 12.7 cm diameter photomultiplier tubes. The signals from the three tubes are summed at the detector. A 0.64 cm plastic scintillation detector in front of the LAD is used as an anticoincidence shield to reduce the background due to charged particles. A thin lead and tin shield inside the light collector housing reduces the amount of background and scattered radiation entering the back side. See Fishman et al. (1989), Paciesas et al. (1989) and The HEASARC *BATSE* webpage (2005) for more details.

Table 2.1:
BATSE Instrument Characteristics

No. of detectors	8 LADs 8 SDs
F.o.V.	Full sky
Sensitive area	$2025\,\mathrm{cm}^2$ per LAD $127\,\mathrm{cm}^2$ per SD
Energy range	$20\,\mathrm{keV} - 1.9\,\mathrm{MeV}$ for LAD $10\,\mathrm{keV} - 100\,\mathrm{MeV}$ for SD
Pulsed source sensitivity	0.05 pulsed Crab ($30 - 250\,\mathrm{keV}$, typical day)

2.1.2 The data

The data as it is initially obtained shows large changes in the detected count rate as the satellite orbits around the earth every ~ 93 minutes. The data is passed through a high-pass filter, which improves sensitivity to pulses between $\sim 2 - 200\,\mathrm{s}$.

Data from combinations of detectors are combined in groups of 2 and 4, as well as used individually, to obtain sensitivity to all locations in the sky. A Fast-Fourier transform is performed on the data, and the power density spectrum produced is searched for peaks that rise above the noise level. Sensitivity can be increased by means of the Earth Occultation Technique (EOT), which takes advantage of the periodic eclipsing of sources by the Earth by measuring their total fluxes twice in each ~ 93 minute orbit, once as they move behind the Earth's limb and then again when they reappear; for full details see Harmon et al. (2002) (or Laycock et al. (2003a) for the EOT applied to high mass X-ray binaries). The data types available from the 8 LADs are the 16-channel continuous or "CONT" data, sampled at 2.048 s intervals, and the 4-channel discriminator or "DISCLA" data sampled every 1.024 s. For the analyses in the present work the DISCLA data was used from which pulsed fluxes and frequencies where extracted (see Bildsten et al. (1997) for a full explanation on the use of DISCLA data for pulsar observations).

For the duration of the mission, data from *BATSE* was inspected every day for

new sources by the team at Marshall Space Flight Center. The periods of known objects (which may not have been observed since their original discovery as much as 20 years ago) were also looked at closely using a different, more sensitive method that can be used when the pulse period is known. An FFT is performed around the frequency of a known pulsar, the frequency with the highest power is tagged together with the amplitude of the pulsed flux, which is calculated from folding the data at the determined period.

2.1.3 Searching for pulsars

To assess the confidence in the detection of a known pulsar, the data was searched through in a narrow frequency range centred on the pulsar's nominal frequency, then DISCLA rates were grouped into $\sim 300\,\mathrm{s}$ intervals. A pulse profile was then estimated using a 6^{th} order Fourier expansion for each of these intervals. The Fourier coefficients μ_k of each interval were varied to find the best fit to a mean profile by χ^2 minimization. The Z_n^2 statistic (Buccheri et al. 1983) can be expressed as

$$Z_n^2 = \sum_{k=1}^{N} \frac{|\mu_{k_{min}}|^2}{\sigma_{\mu_k}^2} \tag{2.1}$$

where $\mu_{k_{min}}$ are the mean Fourier coefficients and σ_{μ_k} their Poisson errors; N can take any value from 1 to 6 (in general $N = 3$ or 6 was used). Unfortunately, *BATSE* noise is generally non-Poissonian (Bildsten et al. 1997), so σ_{μ_k} is multiplied by the reduced χ^2 factor to produce the new statistic Y_n. Monte-Carlo methods are required to convert Y_n into percentile significances in order to establish confidence levels for the detected signal. An advantage to using this method is that any number of harmonics can be excluded from the statistic if there are other sources within the field of view with pulsations at those particular harmonic frequencies. For example, Vela X-1, a bright pulsar with a 283 s pulse period, would often contaminate data in its region of the sky when looking at pulsars with harmonics close to its pulse period, or even one of its harmonics.

2.1.4 Orbital calculations

If an outburst lasts for a significant fraction of a system's binary orbital period, the size and shape of the orbit can be determined by analysing Doppler shifts and pulse arrival delays in the pulsar signal. As an outburst progresses, *BATSE* obtains a continuous history of the daily source intensity and frequency; this detected frequency will be the intrinsic spin frequency of the pulsar plus or minus a shift due to the neutron star's orbit around its companion. The process of calculating the orbit is further complicated by the fact that the neutron star is usually spinning up or down during an outburst, and so it is necessary to dissentangle the orbital from the spin torque effects.

The method used with the *BATSE* data is the piecewise approach explained in detail in Wilson et al. (2003). In essence, it assumes that the torque during an outburst will be approximately constant during small time intervals, such that the intrinsic spin up will be linear during this time. As such, the data available during an outburst will be divided into short segments (3 – 5 data points each) whose intrinsic frequency is described by $\nu_{intr} = \nu_i + \dot{\nu}_i(t - t_i)$, where i is the number of the interval. The frequency we detect will be modulated by the orbit, so that

$$\nu_{det} = \nu_{intr}(1 - \beta) \tag{2.2}$$

where the velocity relative to the observer, $\beta = v/c$, is given by

$$\beta = \frac{2\pi a_{\mathrm{x}} \sin i}{P_{\mathrm{orb}}\, c}\left(\frac{(1-e^2)^{1/2}\cos\omega\cos E - \sin\omega\sin E}{1 - e\cos E}\right) \tag{2.3}$$

where $a_{\mathrm{x}}\sin i$ is the projected semimajor axis of the orbit, P_{orb} is the orbital period, ω is the periapse angle, e is the eccentricity, and E is the eccentric anomaly, given by

$$E - e\sin E = 2\pi\frac{(t - \tau_p)}{P_{\mathrm{orb}}} \tag{2.4}$$

where τ_p is the epoch of periastron passage[1].

In order to compute the orbital parameters of the system, the data in all the segments are fitted to Eq. (2.2) with global values of $P_{\rm orb}$, τ_p, e, ω and $a_{\rm x} \sin i$, but a different ν_{intr} in each segment.

2.2 Studying pulsars from the *BATSE* archive

The raw data taken by *BATSE* over its lifetime is stored at Marshall Space Flight Center and can be extracted and analysed using ever-improving numerical techniques. Bildsten et al. (1997) presented the results of *BATSE*'s first 5 years of monitoring accretion-powered pulsars; this section will take a new look at a number of these pulsars using the improved pulsar searching technique discussed in § 2.1.3 (not available during the data analysis for the aforementioned paper) and also using data from the complete mission ($\sim$ 9 years worth). The coordinates given for the systems are those of Liu et al. (2006).

[1]Eq. (2.4) is known as Kepler's Equation of Elliptical Motion and must be solved numerically.

Table 2.2:

Be/X-ray systems in the Milky Way in present work

Object	P_s (s)	T_P (MJD)	P_{orb} (days)	X_{od}	$\dot{P}$ ($s\,s^{-1}$)	L_x ($erg\,s^{-1}$)	B (G)
4U 0115+634	3.6	49279.268 ± 0.003	$24.317 \pm 6.2 \times 10^{-5}$	0.044	5.8×10^{-11}	2.1×10^{37}	1.3×10^{12}
4U 0728−25	103.2	–	34.5	0.125	5.2×10^{-8}	7.6×10^{36}	4.2×10^{13}
GS 0834−430	12.3	48809.60 ± 0.15	105.8 ± 0.4	0.226	-3.9×10^{-10}	8.2×10^{36}	3.7×10^{12}
GRO J1008−57	93.6	49189.8 ± 0.5	247.8 ± 0.4	0.462	5.6×10^{-9}	1.0×10^{36}	1.4×10^{13}
A 1118−616	405.0	–	–	0.000	3.9×10^{-10}	1.7×10^{35}	3.1×10^{13}
2S 1417−624	17.6	49713.62 ± 0.05	42.12 ± 0.03	0.063	1.8×10^{-9}	1.7×10^{37}	8.0×10^{12}
XTE J1543−568	27.1	51636.71 ± 0.02	75.56 ± 0.25	0.023	8.8×10^{-9}	2.9×10^{37}	1.7×10^{13}
GRO J1750−27	4.5	49931.02 ± 0.01	29.82 ± 0.01	0.009	–	–	–
GS 1843+00	29.5	–	–	0.000	3.7×10^{-8}	1.0×10^{38}	3.6×10^{13}
2S 1845−024	94.8	49611.98 ± 0.18	242.18 ± 0.01	1.000	2.1×10^{-9}	3.9×10^{35}	8.6×10^{12}
GRO J1944+26	15.8	51558.2 ± 0.4	169.2 ± 0.9	0.368	9.5×10^{-10}	1.1×10^{37}	5.8×10^{12}
GRO J1948+32	18.7	–	40.41 ± 0.01	0.012	–	–	–
EXO 2030+375	41.8	50547.22 ± 0.02	46.0214 ± 0.0005	0.764	-9.4×10^{-11}	1.2×10^{35}	1.8×10^{12}
GRO J2058+42	198.0	50411.30	55.03	0.283	7.1×10^{-9}	2.4×10^{35}	1.6×10^{13}

2.2.1 SXP31.0

XTE J0111.2−7317, AX J0111.1−7316
RA 01 11 09.0, dec −73 16 46.0

It was discovered simultaneously by *RXTE* and *BATSE* (Chakrabarty et al. 1998; Wilson and Finger 1998) during the giant outburst seen in Fig. 2.3. SXP31.0 underwent a large spin up during this outburst; at $\dot{P} = 5.3 \times 10^{-8}\,\mathrm{s\,s^{-1}}$, the expected luminosity would be $L_\mathrm{x} = 1.3 \times 10^{38}\,\mathrm{erg\,s^{-1}}$ ($B = 4.3 \times 10^{13}\,\mathrm{G}$), very close to the Eddington limit.

Using the method outlined in 2.1.4 an attempt was made to calculate the orbital parameters of the system. The results can be found in Table 2.3 and are plotted in Fig. 2.4.

Table 2.3:
Orbital parameters for SXP31.0

P_orbital (d)	27.5 ± 0.3
e	0.60 ± 0.08
$a_\mathrm{x} \sin i$ (light-s)	24 ± 10
$\tau_\mathrm{periastron}$ (MJD)	451150.2 ± 0.5

2.2.2 4U 0115+634

RA 01 18 31.9, dec +63 44 24
Counterpart: O9Ve

Discovered in 1978 by *SAS-3* to have 3.61 s pulsations (Cominsky et al. 1978), subsequent observations established its 24.3 d orbital period around a Be companion (Rappaport et al. 1978).

BATSE observed 3 large outbursts (see Fig. 2.5), during which the pulsar was seen to spin up, and then spin down during the periods of quiescence; nonetheless,

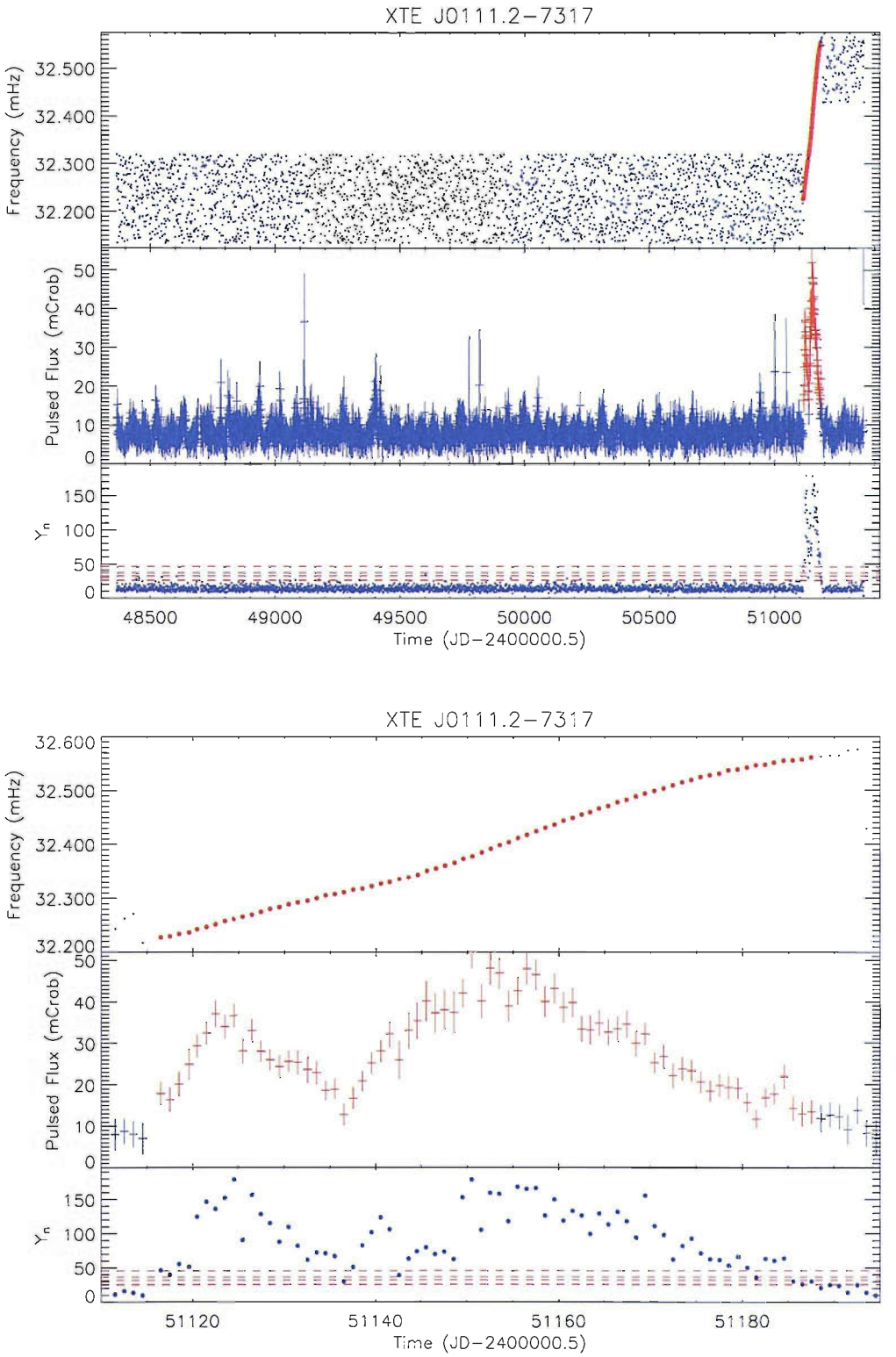

Figure 2.3: SXP31.0 — 1-day averaged frequency and pulsed flux. *Top*: For entire mission, with $Sig_{\min} = 99.9\%$. *Bottom*: Close up of the outburst, with $Sig_{\min} = 90\%$.

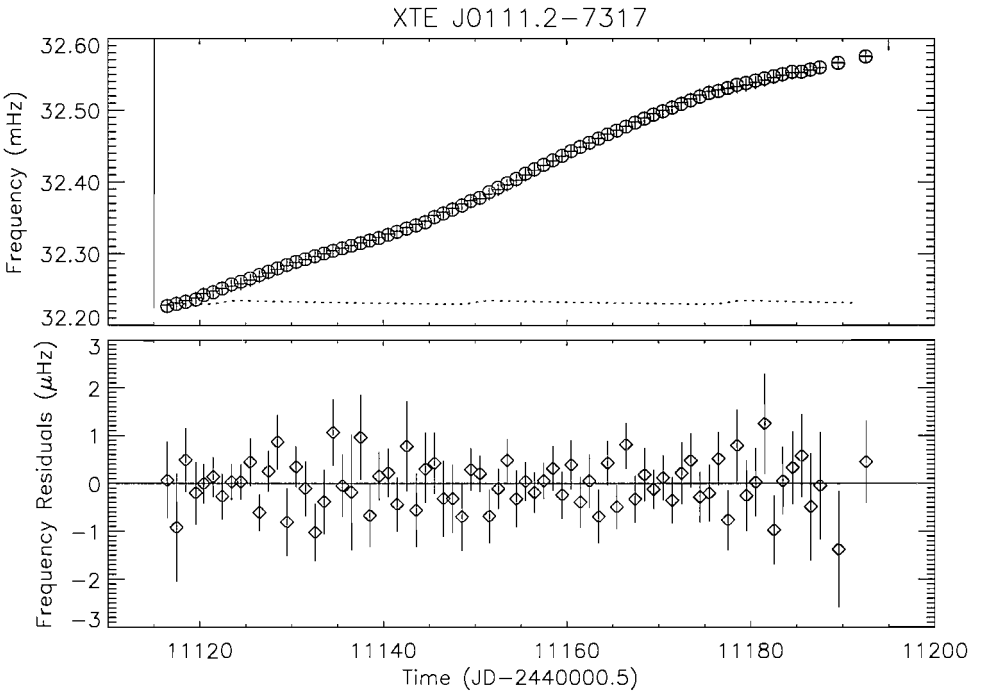

Figure 2.4: Orbital calculation of SXP31.0. *Top*: The crosses are the emitted frequency returned by the model. The dotted line illustrates the magnitude of the orbital effects. The circles are the frequencies, as measured by *BATSE*. *Bottom*: Pulse frequency residuals for the model.

the long term trend is that of spin up. During the first two outbursts (MJD $\sim$49500 and $\sim$50050) the observed spin up was $\dot{P} = 4.0 \times 10^{-11}\,\mathrm{s\,s^{-1}}$ on both occasions, with expected luminosities of $L_\mathrm{x} = 1.5 \times 10^{37}\,\mathrm{erg\,s^{-1}}$ ($B = 1.2 \times 10^{12}\,\mathrm{G}$). The third outburst, the longest and brightest of the 3, displayed a spin up of $\dot{P} = 5.8 \times 10^{-11}\,\mathrm{s\,s^{-1}}$ with $L_\mathrm{x} = 2.1 \times 10^{37}\,\mathrm{erg\,s^{-1}}$ ($B = 1.4 \times 10^{12}\,\mathrm{G}$).

The peaks in the pulsed flux during the outbursts coincide with periastron passage, which was calculated to be given by the ephemeris MJD $49279.2677 \pm 0.0034 + \mathrm{n} \times 24.317037 \pm 0.000062\,\mathrm{d}$. This behaviour is suggestive of an eccentric orbit, which indeed it has, at $e = 0.3402 \pm 0.0002$ (Bildsten et al. 1997).

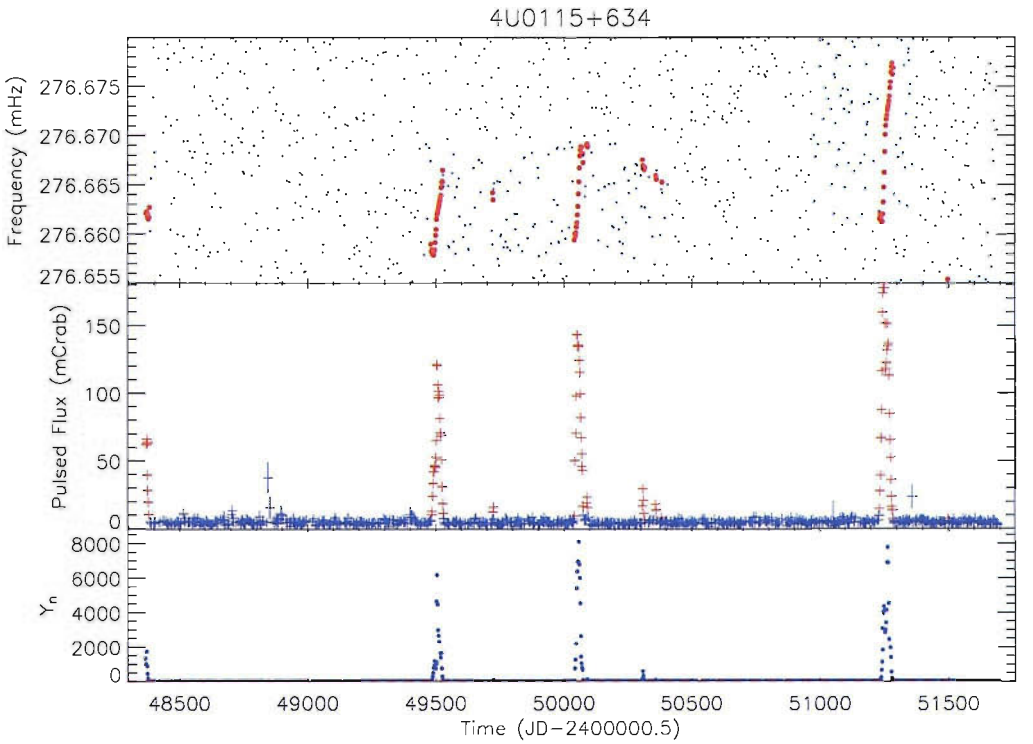

Figure 2.5: 4U 0115+634 — 2-day averaged frequency and pulsed flux for entire mission; $Sig_{\min} = 99.9\%$.

2.2.3 4U 0728−25

3A 0726-260
RA 07 47 23.6, dec −26 06 29
Counterpart: O8–9Ve

This source was observed by a number of space missions (*UHURU*, *ARIEL V* and *EXOSAT*) before pulsations at 34.5 s were eventually detected by *RXTE* (Corbet and Peele 1997). During this observation the orbital period of 103.2 d was also confirmed.

BATSE only detected 4 faint outbursts during MJD ∼49175−49625, the separation between them being approximately 2, 1 and 1 orbital periods. The second outburst, being the brightest, shows a marked spin up with $\dot{P} = 5.2 \times 10^{-8}\,\mathrm{s\,s^{-1}}$, implying $L_x = 7.6 \times 10^{36}\,\mathrm{erg\,s^{-1}}$ ($B = 4.2 \times 10^{13}$ G).

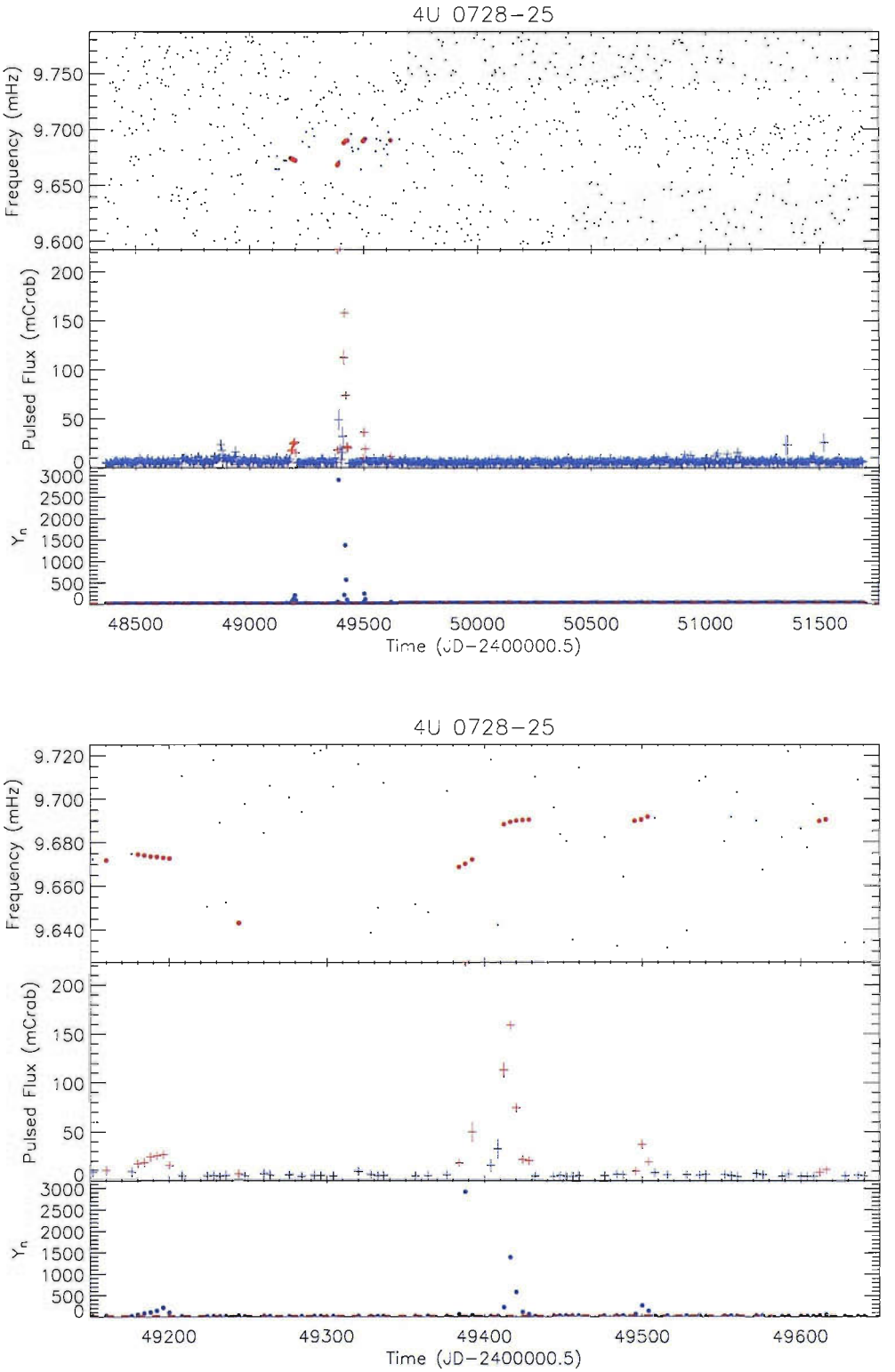

Figure 2.6: 4U 0728−25 — 4-day averaged frequency and pulsed flux. *Top*: For entire mission, with $Sig_{\min} = 99.9\%$. *Bottom*: Closeup of the outbursts, with $Sig_{\min} = 99\%$.

2.2.4 GS 0834−430

RA 08 35 55.4, dec 43 11 11.9
Counterpart: B0–2 III–Ve

Was first detected in 1990 by WATCH, the all-sky monitor on-board *GRANAT*, although it was unresolved from the X-ray burster MX 0836−42 (Lapshov et al. 1992). Observations with *GINGA*detected 12.3 s pulsations (Aoki et al. 1992), but the optical counterpart was not determined until 2000 (Israel et al. 2000). An orbital period of 105.8 ± 0.4 d was calculated from the *BATSE* data by Wilson et al. (1997a), who constrained the value of the orbit's eccentricity to $0.1 \leq e \leq 0.17$.

The average spin up throughout the 7 outbursts (see Fig. 2.7) was $\dot{P} = -3.9 \times 10^{-10}\,\mathrm{s\,s^{-1}}$, implying $L_\mathrm{x} = 8.2 \times 10^{36}\,\mathrm{erg\,s^{-1}}$ ($B = 3.7 \times 10^{12}$ G). This source has shown no activity since then, either in *BATSE* or in the ASM. It should be noted that given its pulse period, and the pulse/orbit period relationship, the expected orbital period would be ~ 40 d. Furthermore, it would be expected that the pulsar spin down to approximate it to the Be region on the Corbet diagram, but instead it is seen to spin up.

2.2.5 GRO J1008−57

RA 10 09 35.2, dec −58 17 35.5
Counterpart: B0e

This source was first detected during a bright outburst in July 1993 by *BATSE* with pulsations at 93.587 ± 0.005 s (Stollberg et al. 1993). This outburst can be seen around MJD 49200 in Fig. 2.8.

After this initial outburst, a number of less significant detections were made, which could correspond to 5 further outbursts. These are spaced ~ 260 d apart, which led to this being proposed as the orbital period of the system (Finger et al. 1994). Shrader et al. (1999) find weak evidence for a ~ 135 d period in the ASM

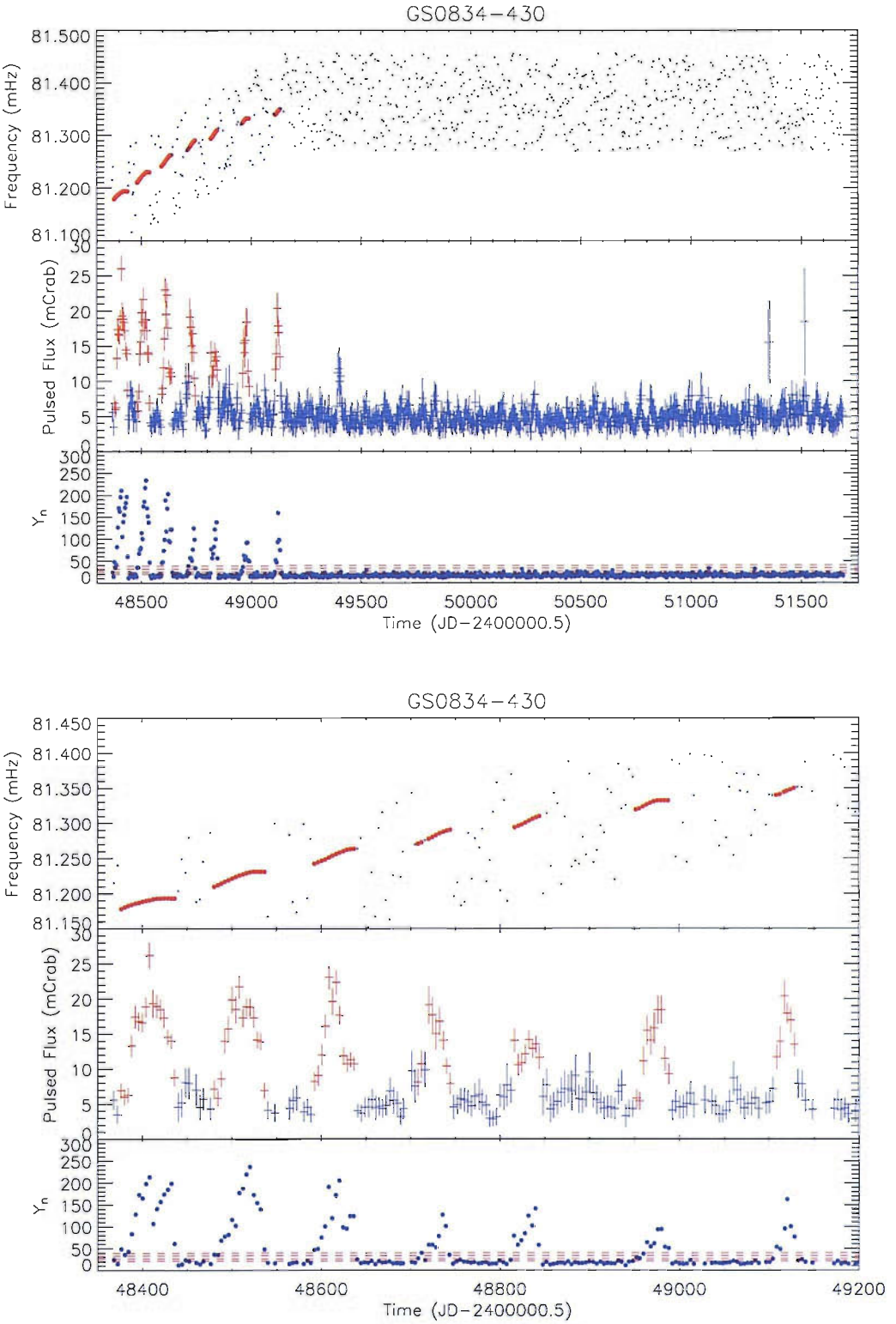

Figure 2.7: GS 0834−430 — 4-day averaged frequency and pulsed flux. *Top*: For entire mission, with $Sig_{\min} = 99.9\%$. *Bottom*: Closeup of the outbursts, with $Sig_{\min} = 99\%$.

data from *RXTE*.

Orbit fitting calculations were carried out using the $Sig_{\min} = 99.9\%$ data points in Fig. 2.8, producing an orbital period of 247.8 d. The results can be seen graphically in Fig. 2.9 and the orbital parameters are in Table 2.4.

Using the frequencies corrected for orbital motion from Fig. 2.9 we derive for the initial outburst a $\dot{P} = 5.6 \times 10^{-9}\,\mathrm{s\,s^{-1}}$, implying $L_\mathrm{x} = 1.0 \times 10^{36}\,\mathrm{erg\,s^{-1}}$ ($B = 1.4 \times 10^{13}$ G). Compare to $L_\mathrm{x} = 4.1 \times 10^{36}\,\mathrm{erg\,s^{-1}}$ and $B = 6.0 - 9.9 \times 10^{13}$ G, obtained by Shrader et al. (1999).

Table 2.4:
Orbital parameters for GRO J1008−57

P_orbital (d)	247.8 ± 0.4
e	0.68 ± 0.02
$a_\mathrm{x} \sin i$ (light-s)	530 ± 60
$\tau_\mathrm{periastron}$ (MJD)	49189.8 ± 0.5

2.2.6 A 1118−616

2E 1118.7-6138
RA 11 20 57.2, dec −61 55 00
Counterpart: O9.5Ve

This source was first reported by Eyles et al. (1975) from *ARIEL V* observations. Ives et al. (1975) monitored the source over 39 days and found X-ray modulation with a period of 6.755 min, which they hypothesised could be the orbital period of a binary system. This period turned out to be the spin period of the neutron star (405 s). The source remained quiet until an outburst was detected by *BATSE* in early 1992 (Coe et al. 1994); this outburst can be seen in Fig. 2.10 beginning around MJD 48620.

The first outburst is too short to attempt an orbital period calculation, and no orbital period has yet been proposed for this system. There are some detections during

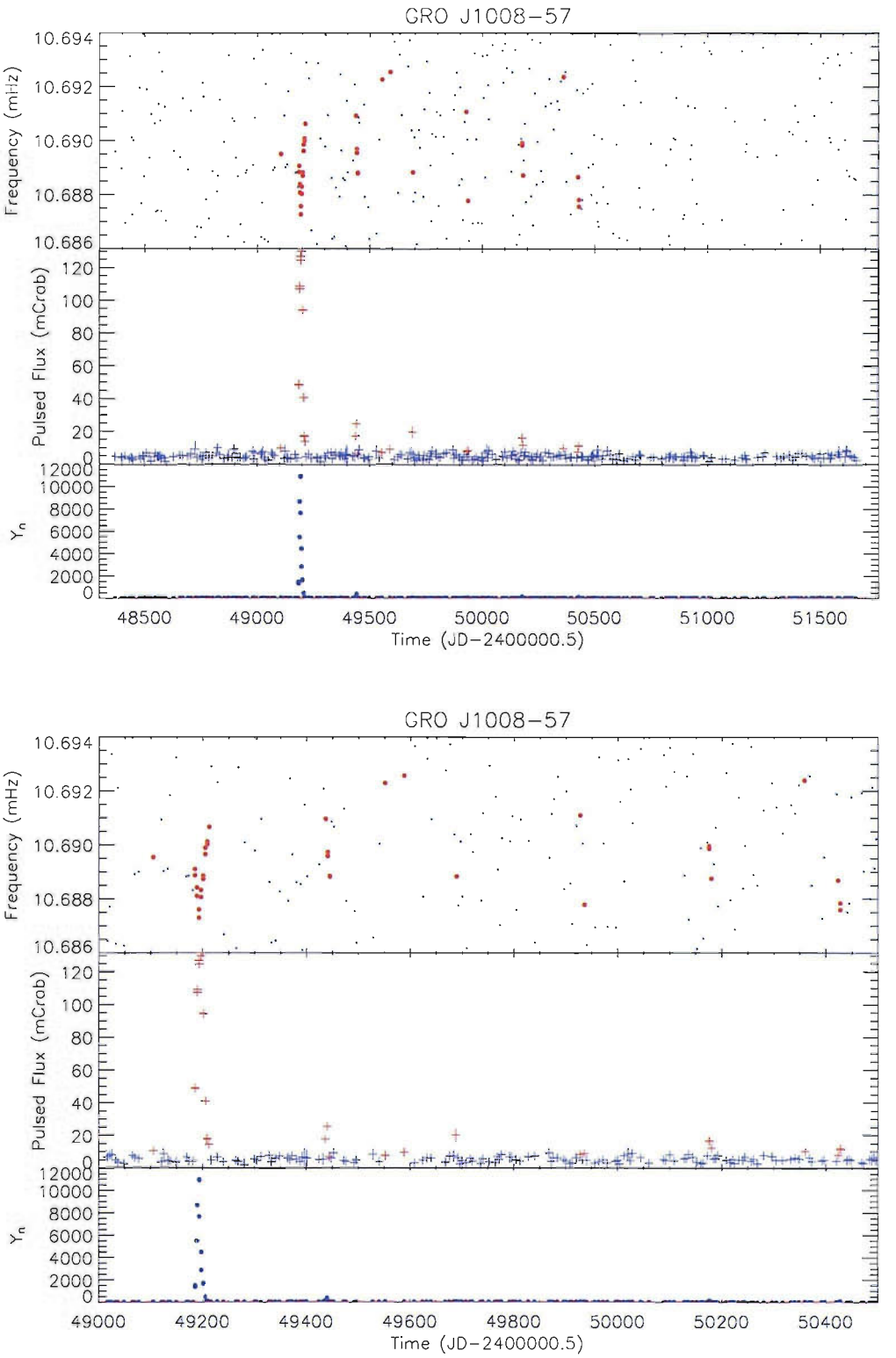

Figure 2.8: GRO J1008−57 — 4-day averaged frequency and pulsed flux. *Top*: For entire mission, with $Sig_{\min} = 99.9\%$. *Bottom*: Closeup of the outbursts, with $Sig_{\min} = 99.9\%$.

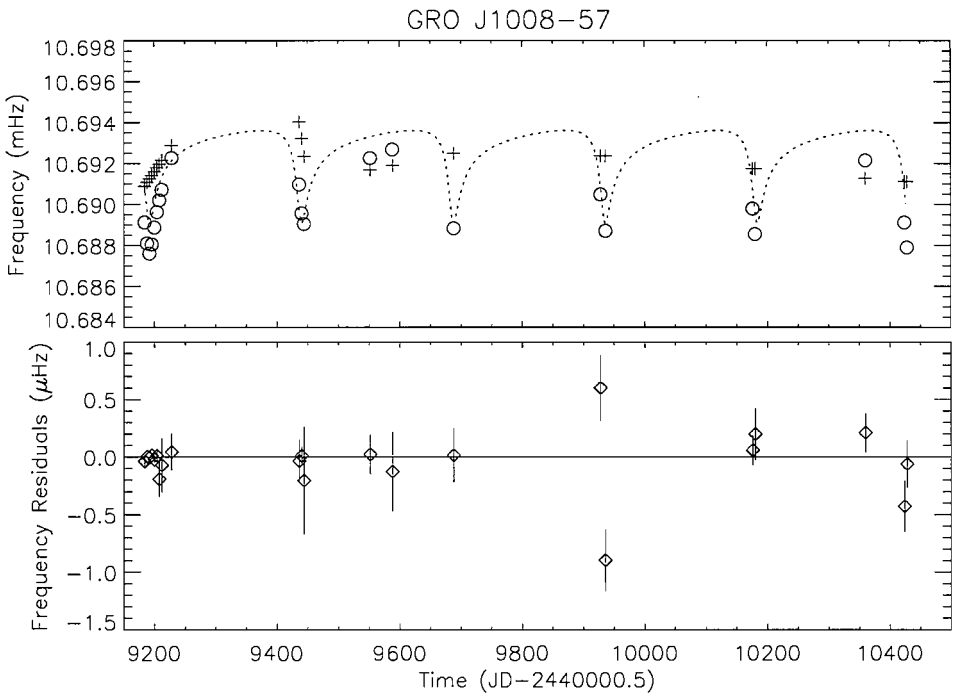

Figure 2.9: Orbital calculation of GRO J1008−57. *Top*: The crosses are the emitted frequency returned by the model. The dotted line illustrates the magnitude of the orbital effects. The circles are the frequencies, as measured by *BATSE*. *Bottom*: Pulse frequency residuals for the model.

MJD 49300 − 50300 that may be due to A 1118−616, but it cannot be unambiguously stated. However, beginning around MJD 51100 the are a series of faint detections that show a clear spin up of the pulsar taking place, which last until MJD ~ 51600. From these detections we derive an average spin up of $\dot{P} = 3.9 \times 10^{-10}\,\mathrm{s\,s^{-1}}$, implying a (not unexpectedly faint) luminosity of $L_{\mathrm{x}} = 1.7 \times 10^{35}\,\mathrm{erg\,s^{-1}}$ ($B = 3.1 \times 10^{13}\,\mathrm{G}$). These outbursts appear to be spaced at $\sim 115\,\mathrm{d}$ intervals, which would be $\sim \frac{1}{2}$ of the expected orbital period from the Corbet diagram.

2.2.7 4U 1145−619

2S 1145−619
RA 11 48 00.0, dec −62 12 25
Counterpart: B0.2IIIe

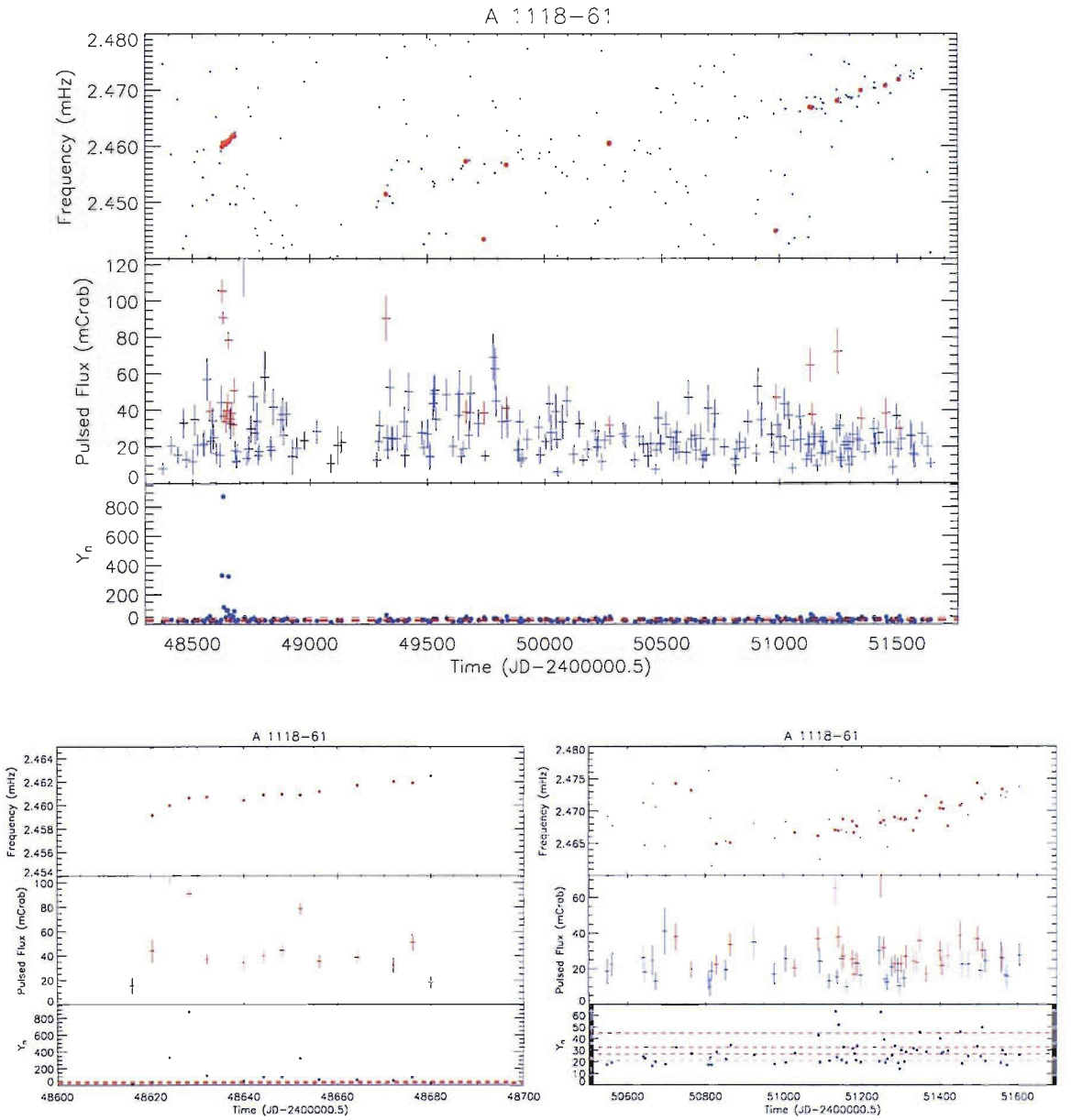

Figure 2.10: A 1118−616 — 4-day averaged frequency and pulsed flux. *Top*: For entire mission, with $Sig_{\min} = 99.9\%$. *Bottom*: Closeup of two series of outbursts, with $Sig_{\min} = 90\%$ for the left, and $Sig_{\min} = 99\%$ for the right.

ARIEL V detected pulsations at 291 and 297 s from the *UHURU* source 4U 1145−619 (White et al. 1978). It was not until observations of this region were carried out with the higher spatial resolution afforded by *EINSTEIN* that these periods were found to belong to two distinct objects, the faster of the two being 4U 1145−619 (Giacconi et al. 1979). Its orbital period was determined from regular outbursts every 187.5 d, and the neutron star was observed to be spinning down during a number of observations carried out with *EXOSAT* during June 1983 − January 1985 (Cook and Warwick 1987).

BATSE detected 11 short, consecutive outbursts of 4U 1145−619 during MJD 48600 − 50600 (see Fig. 2.11), after which it was not detected again. A clear, persistent overall spin down can be observed throughout the series of outbursts, with an average $\dot{P} = 2.4 \times 10^{-9}\,\mathrm{s\,s^{-1}}$, consistent with a low luminosity of $L_x = 3.1 \times 10^{34}\,\mathrm{erg\,s^{-1}}$ ($B = 9.1 \times 10^{12}$ G).

2.2.8 2S 1417−624

4U 1416−62
RA 14 21 12.9, dec −62 41 54
Counterpart: B1Ve

17.6 s pulsations were discovered by *SAS-3* from this X-ray source in 1978 (Kelley et al. 1981). In August 1994 the system underwent a large outburst, followed by a number of shorter, fainter ones, that lasted until December of that year (MJD 49590 − 49700) and were recorded by *BATSE* (see Fig. 2.12). From this series of outbursts Finger et al. (1996) calculated the ephemeris of periastron passage to be MJD $49713.62 \pm 0.05 + \mathrm{n} \times 42.12 \pm 0.03$, with an eccentricity of $e = 0.446 \pm 0.002$. The frequency values in Fig. 2.12 have been orbitally corrected, and as such reflect the intrinsic spin frequency of the pulsar. It is interesting to note that the fainter outbursts during MJD 49720 − 49905 actually peak at apastron, and not periastron as would be expected.

After the above mentioned series of outbursts, one single outburst was recorded

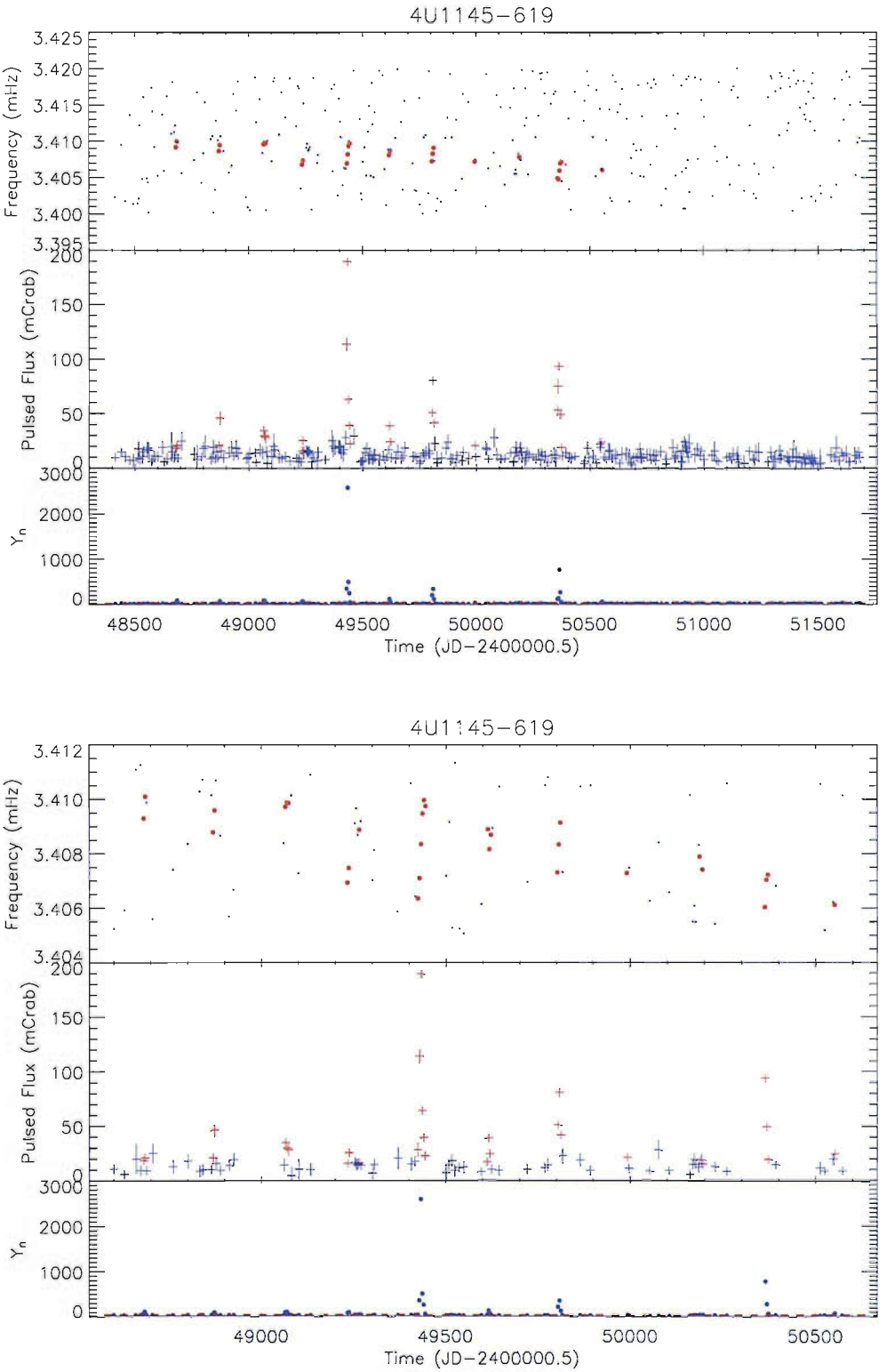

Figure 2.11: 4U 1145−619 — 4-day averaged frequency and pulsed flux. *Top*: For entire mission, with $Sig_{\min} = 99.9\%$. *Bottom*: Closeup of the outbursts, with $Sig_{\min} = 99\%$.

during MJD $\sim$50260 – 50300, peaking shortly after periastron. 2S 1417–624 went undetected until MJD $\sim$51200, when a series of 3 short, faint outbursts preceded a large outburst that lasted $\sim$4 orbits. The faint outbursts once again appear around apastron, while the maximum pulsed flux of the large outburst was detected around periastron. The explanation given by Finger et al. (1996) to explain the initial apastron outbursts was that the material ejected by the Be star at the time of the large outburst (MJD 49590) had travelled beyond the periastron distance but the pulsar was able to accrete from it again at apastron, when it caught up with it. Given the large eccentricity of the orbit this is plausible; however, this would not explain the occurrence of apastron outbursts *preceding* a major outburst.

The pulsar underwent a large spin up during the last large outburst, with a mean $\dot{P} = 1.8 \times 10^{-9}\,\mathrm{s\,s^{-1}}$, which gives an expected luminosity of $L_\mathrm{x} = 1.7 \times 10^{37}\,\mathrm{erg\,s^{-1}}$ ($B = 8.0 \times 10^{12}\,\mathrm{G}$).

2.2.9 XTE J1543–568

RA 15 44 01, dec −56 45 54
Counterpart: —

This source was discovered in early 2000 during a slew of the ASM on-board *RXTE*, subsequent pointed observations detected pulsations at 27.12 ± 0.02 s(Marshall et al. 2000). A look at *BATSE* data found this pulsar too (Finger and Wilson 2000). An orbital solution was found from the pulse period variations using both *BATSE* and *RXTE* data, giving an orbital ephemeris of MJD $51636.71 \pm 0.02 + \mathrm{n} \times 75.56 \pm 0.25$ d, and a very small eccentricity of $e < 0.03$ (in't Zand et al. 2001). This combination of pulse/orbital period makes it a candidate Be/X-ray binary, although the optical counterpart is yet to be found. This will likely be difficult as it is expected to be highly absorbed given the large distance estimated for this system ($d > 10$ kpc) (in't Zand et al. 2001). Fig. 2.13 shows the orbitally-corrected frequencies.

The spin up during the brightest part of the outburst (MJD 51596 – 51688) was

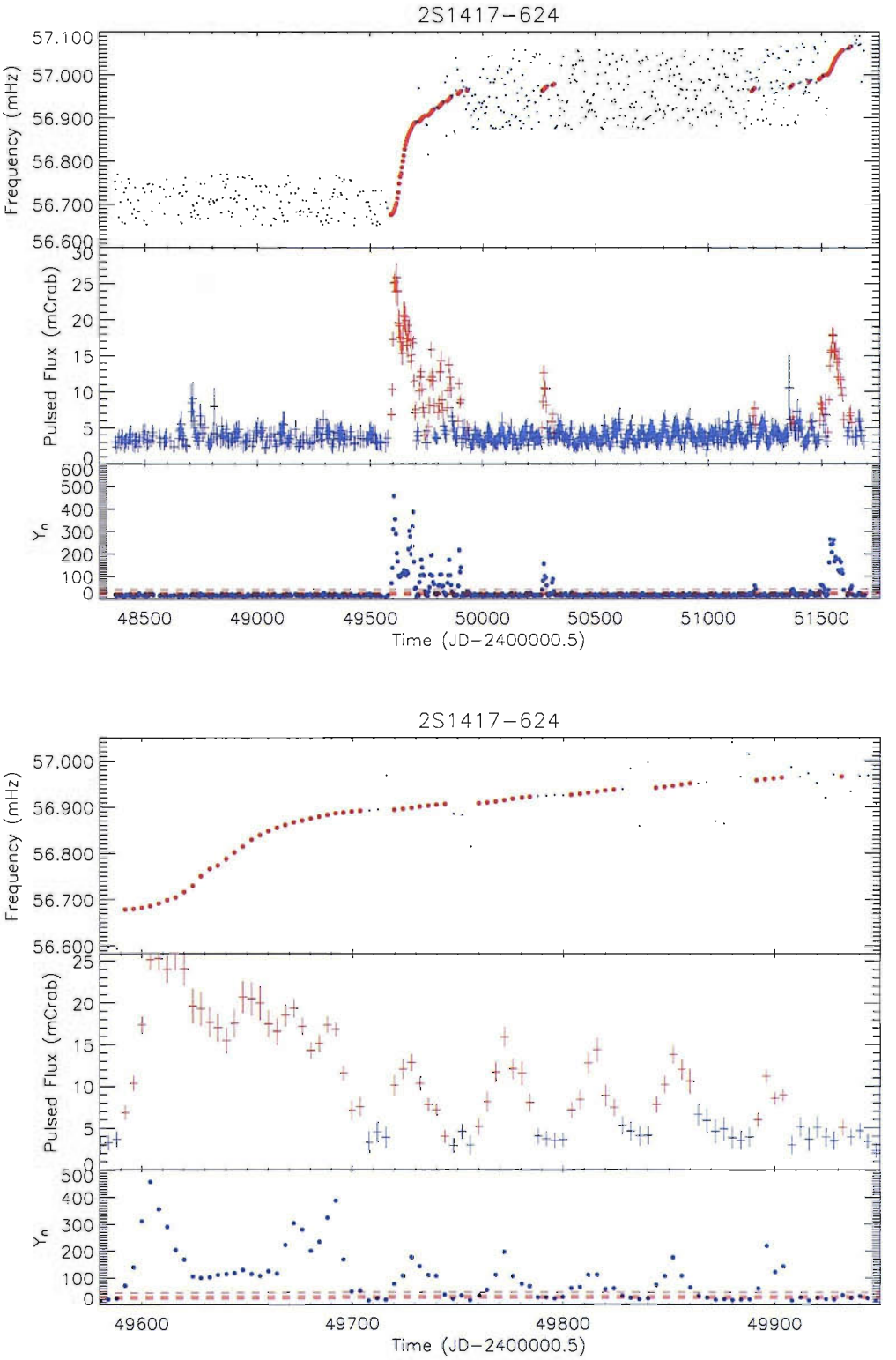

Figure 2.12: 2S 1417−624 — 4-day averaged frequency and pulsed flux. *Top*: For entire mission, with $Sig_{\min} = 99.9\%$. *Bottom*: Closeup of the initial outburst, with $Sig_{\min} = 99.9\%$.

$\dot{P} = 8.8 \times 10^{-9}\,\mathrm{s\,s^{-1}}$, with $L_x = 2.9 \times 10^{37}\,\mathrm{erg\,s^{-1}}$ ($B = 1.7 \times 10^{13}$ G). Given the X-ray flux observed by in't Zand et al. (2001), this luminosity would put XTE J1543−568 at a distance of ~ 22 kpc.

2.2.10 GRO J1750−27

AX J1749.1-2639
RA 17 49 12.7, dec −26 38 36
Counterpart: —

Discovered during the outburst shown in Fig. 2.14, pulsations were detected at 4.45 s, with large spin derivatives during the ~ 60 d period of activity. These period changes were both orbital and intrinsic; fitting an orbital solution to the frequency data returned an ephemeris of MJD $49931.02 \pm 0.01 + \mathrm{n} \times 29.817 \pm 0.009$ d, and $e = 0.360 \pm 0.002$. The estimated luminosity was $L_x = 1.5 \times 10^{38}\,\mathrm{erg\,s^{-1}}$. No optical counterpart has been identified, but given its position on the Corbet diagram it is most probably a Be/X-ray binary system (Scott et al. 1997).

No other detections were made for this source. During the outburst a $\dot{P} = 6.3 \times 10^{-9}\,\mathrm{s\,s^{-1}}$ was measured, giving an expected $L_x = 2.1 \times 10\,\mathrm{erg\,s^{-1}}$

2.2.11 GS 1843+00

GS 1843+009
RA 18 45 36.8, dec 00 51 48.3
Counterpart: B0–2 IV–Ve

This source was discovered by *GINGA* in 1988 during a scan of the Galactic plane (Makino 1988b), later observations discovered pulsations at 29.508 ± 0.002 s (Makino 1988c). *BATSE* detected it in March 1997 (Wilson et al. 1997b). The optical counterpart was identified by Israel et al. (2001).

The March 1997 series of detections are the only ones in the *BATSE* data from

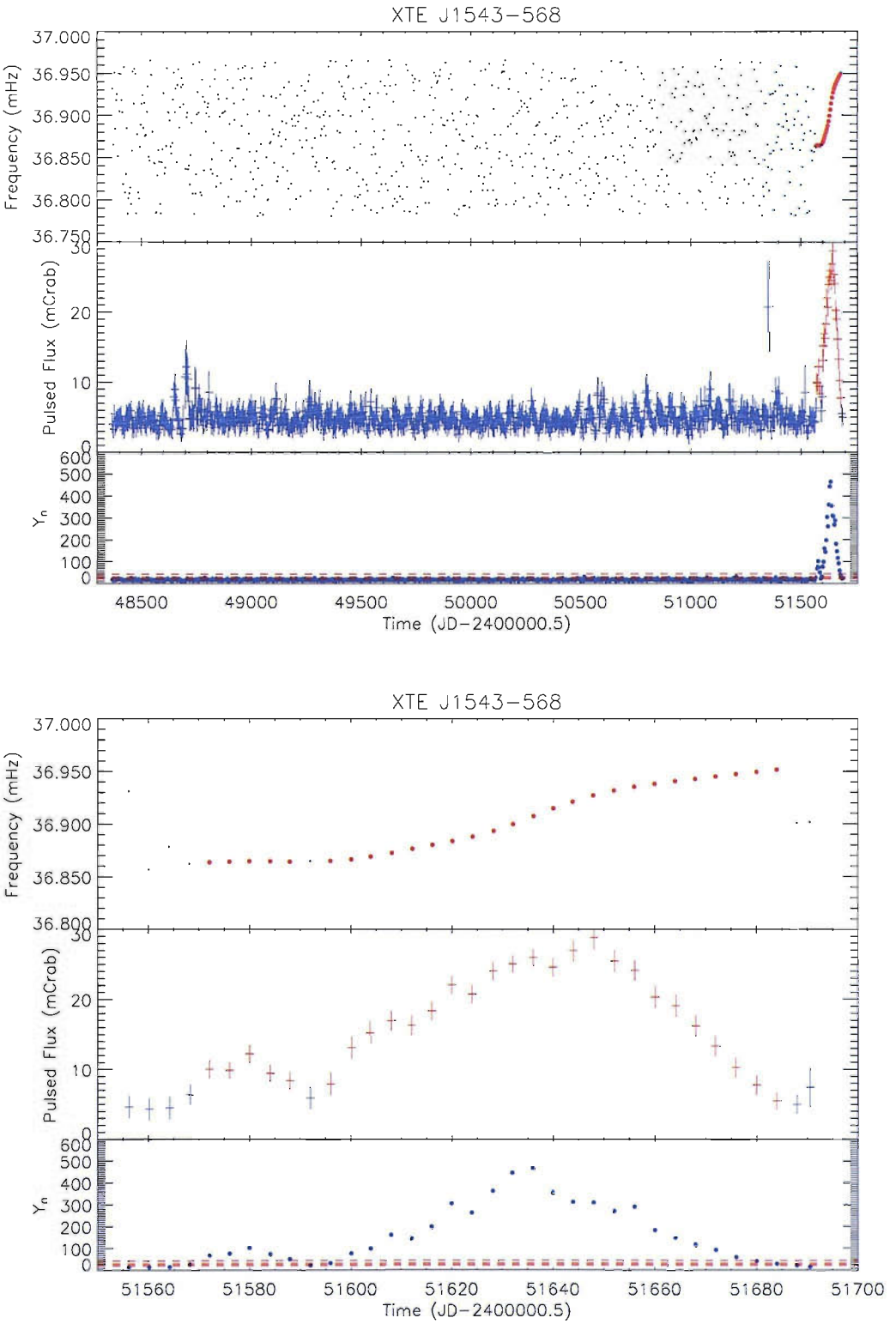

Figure 2.13: XTE J1543−568 — 4-day averaged frequency and pulsed flux. *Top*: For entire mission, with $Sig_{\min} = 99.9\%$. *Bottom*: Closeup of the outburst, with $Sig_{\min} = 99\%$.

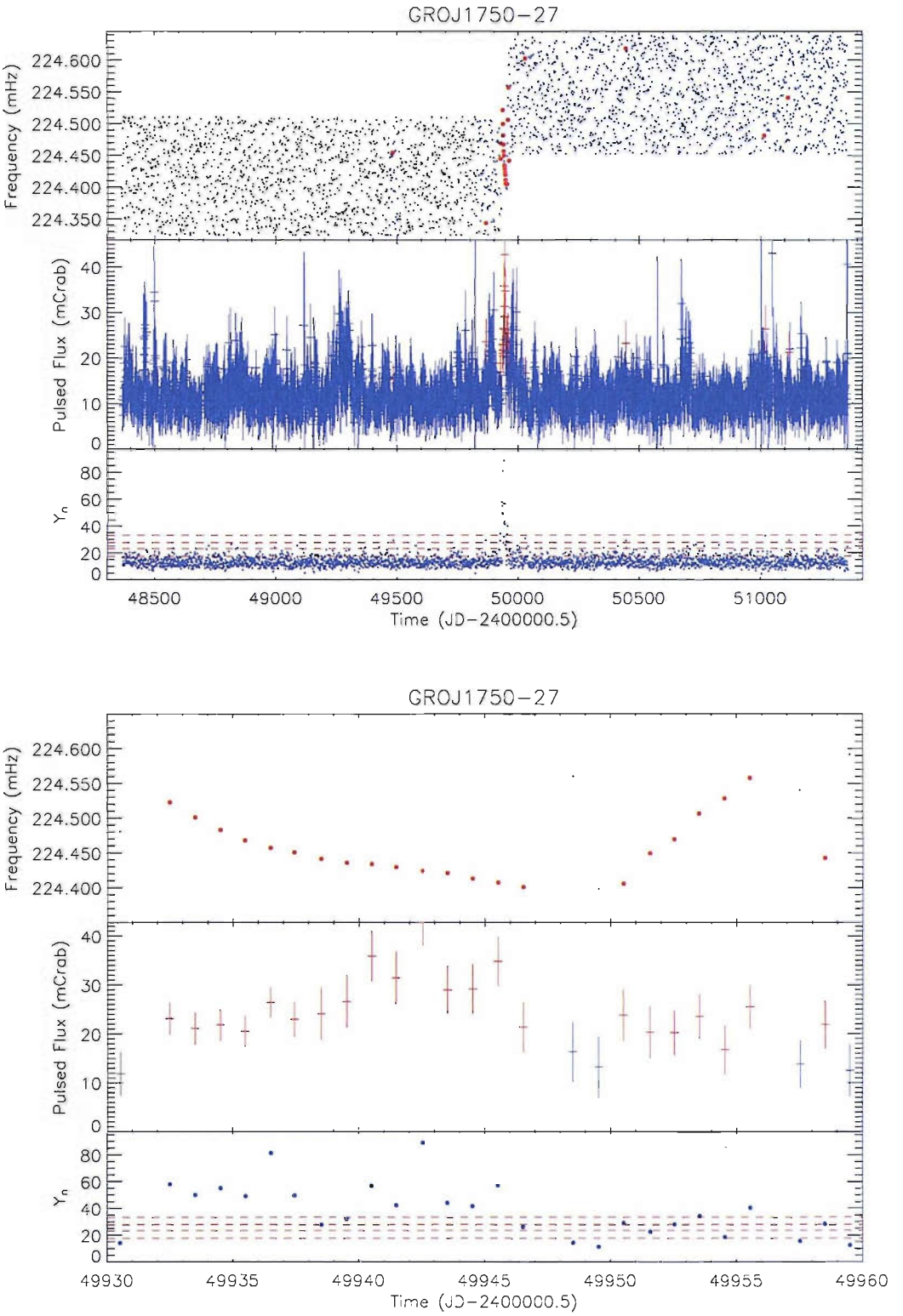

Figure 2.14: GRO J1750−27 — 1-day averaged frequency and pulsed flux. *Top*: For entire mission, with $Sig_{\min} = 99.9\%$. *Bottom*: Closeup of the outburst, with $Sig_{\min} = 90\%$.

this source. There is an almost linear spin up observable during the ~ 17 d outburst with $\dot{P} = 3.7 \times 10^{-8}\,\mathrm{s\,s^{-1}}$ (if we assume all the spin up is intrinsic), corresponding to a luminosity of $L_x = 1.0 \times 10^{38}\,\mathrm{erg\,s^{-1}}$ ($B = 3.6 \times 10^{13}$ G). Given a total (pulsed + unpulsed) flux of $5.1 \pm 0.5 \times 10^{-9}\,\mathrm{erg\,s^{-1}\,cm^2}$ measured by *BATSE* during this outburst (Wilson et al. 1997b), we derive a distance to the source of ~ 12.8 kpc, consistent with the value of $10 < d < 15$ kpc given by Israel et al. (2001).

2.2.12 2S 1845−024

GS 1843−02, GRO J1849−03
RA 18 48 18, dec −02 25 12
Counterpart: —

Discovered by *GINGA* in 1988 with pulsations at 94.8 ± 0.1 s (Makino 1988a). Having displayed recurring Type I outbursts through out *BATSE*'s lifetime (see Fig. 2.16), a thorough study of this system was undertaken in Finger et al. (1999). They derive an ephemeris for periastron passage of MJD $49611.98 \pm 0.18 + \mathrm{n} \times 242.180 \pm 0.012$ d, and find a very eccentric orbit with $e = 0.8792 \pm 0.0054$.

The frequency measurements in Fig. 2.16 have been orbitally corrected and represent the intrinsic spin of the pulsar. It is remarkable that the neutron star has been spinning up in such a consistent fashion during the ~ 9 yr of *BATSE*'s lifetime. The mean spin up is $\dot{P} = 2.1 \times 10^{-9}\,\mathrm{s\,s^{-1}}$, implying $L_x = 3.9 \times 10^{35}\,\mathrm{erg\,s^{-1}}$ ($B = 8.6 \times 10^{12}$ G). This value is about an order of magnitude smaller than the calculated unabsorbed luminosity of $L_x = 6 \times 10^{36}\,\mathrm{erg\,s^{-1}}$ from the MJD ~ 50350 outburst that is given in Finger et al. (1999), assuming a distance of 10 kpc as suggested by Soffitta et al. (1998). Given their reported flux of $5 \times 10^{-10}\,\mathrm{erg\,s^{-1}\,cm^2}$, our luminosity would put this source at a distance of only 2.6 kpc, which is closer than the 5 kpc Galactic arm where it is thought to be located. It should be remembered that the value of $L_x = 3.9 \times 10^{35}\,\mathrm{erg\,s^{-1}}$ is a lower limit and the real value depends on how much matter the system is accreting. More efficient systems will have luminosities that are larger than the minimum we calculate.

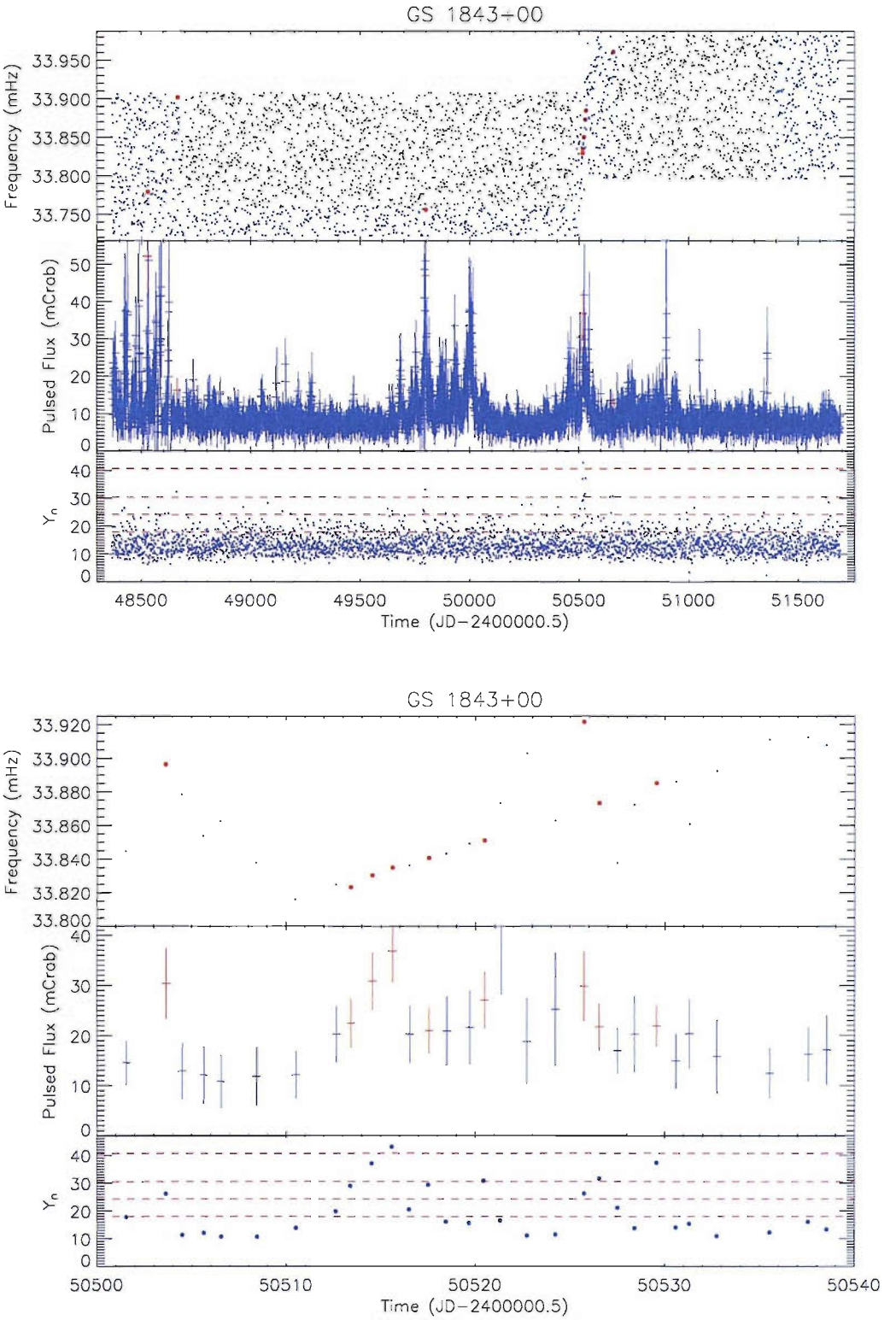

Figure 2.15: GS 1843+00 — 1-day averaged frequency and pulsed flux. *Top*: For entire mission, with $Sig_{\min} = 99.9\%$. *Bottom*: Closeup of the main outburst, with $Sig_{\min} = 99\%$.

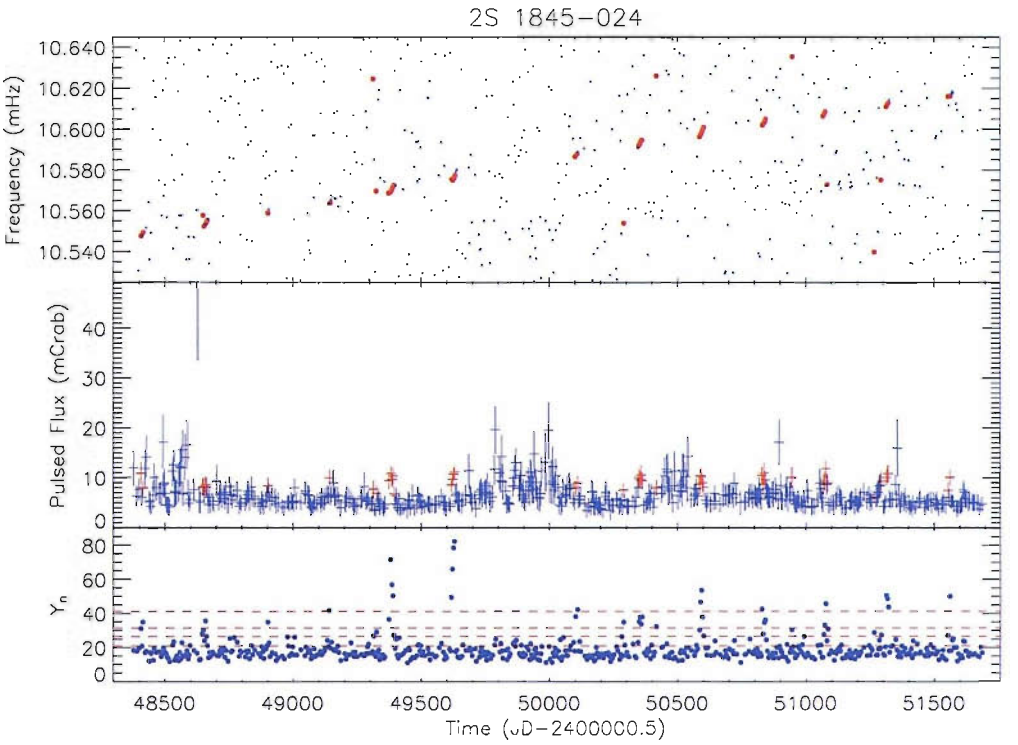

Figure 2.16: 2S 1845−024 — 4-day averaged frequency and pulsed flux for entire mission; $Sig_{\min} = 99\%$.

2.2.13 GRO J1944+26

XTE J1946+274
RA 19 45 39.3, dec 27 21 55.4
Counterpart: B0–1 IV–Ve

This object was discovered simultaneously in September 1998 by *BATSE* (Wilson et al. 1998b) and the *RXTE* ASM (Smith and Takeshima 1998). Pulsations at 15.8 s were detected by *BATSE* and the *RXTE* PCA and the source continued to be monitored during a set of outbursts lasting almost 1100 days. An in-depth study of the source during this time appears in Wilson et al. (2003); they calculate an ephemeris for periastron of MJD $51558.2 \pm 0.4 + \mathrm{n} \times 169.2 \pm 0.9$ d, with $e = 0.33 \pm 0.05$.

This system is similar to GS 0834−430 in that its orbital period is longer (by ~ 4

times) than would be expected given its pulse period, judging from its position in the Corbet diagram; furthermore it is spinning up, making the discrepancy larger. Fig. 2.17 shows the orbitally corrected frequencies; the spin up observed during the series of outbursts following the initial large one (MJD 51160 – 51685) is $\dot{P} = 9.5 \times 10^{-10}\,\mathrm{s\,s^{-1}}$, which would imply $L_\mathrm{x} = 1.1 \times 10^{37}\,\mathrm{erg\,s^{-1}}$, and $B = 5.8 \times 10^{12}\,\mathrm{G}$. This value compares favourably to $B = 3.7 \times 10^{12}\,\mathrm{G}$, which is the magnetic field calculated by Heindl et al. (2001) from a cyclotron resonance scattering feature observed with *RXTE* during an outburst in September–October 1998 (MJD 51040 – 51140), which was not detected by *BATSE*.

2.2.14 GRO J1948+32

KS 1947+300
RA 19 49 30.5, dec +30 12 24
Counterpart: B0Ve

Discovered by *BATSE* in 1995 with pulsations at 18.7 s (Chakrabarty et al. 1995). After this $\sim$40 d outburst it was not detected again by *BATSE*. Later outbursts in 2000–01 were detected by *RXTE* and allowed orbital parameters to be calculated; they find an orbital period of 40.415 ± 0.007 d and a very low eccentricity of $e = 0.034 \pm 0.007$.

2.2.15 EXO 2030+375

RA 20 32 15.2, dec +37 38 15
Counterpart: B0Ve

Discovered by *EXOSAT* in 1985 (Parmar et al. 1989b), this $\sim$41.8 s spin period system has shown regular outbursts throughout its lifetime. Even though *BATSE* missed 7 outbursts during the period of MJD $\sim$50650 – 51000, these were detected by *RXTE*, suggesting that accretion onto the neutron star continued even though the source fell below *BATSE*'s detection threshold. Using *BATSE* data (see Fig. 2.19)

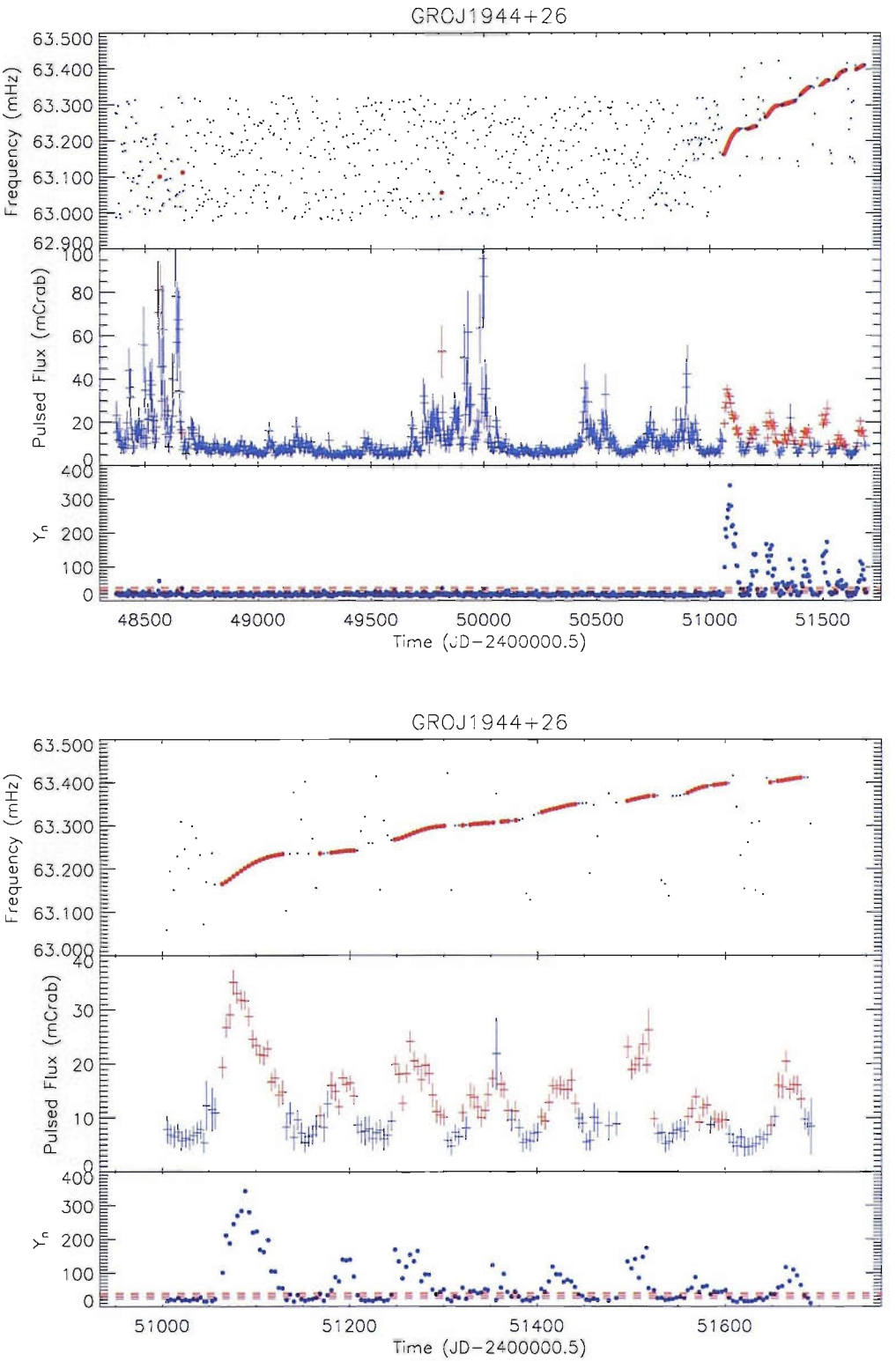

Figure 2.17: GRO J1944+26 — 4-day averaged frequency and pulsed flux. *Top*: For entire mission, with $Sig_{\min} = 99.9\%$. *Bottom*: Closeup of the outbursts, with $Sig_{\min} = 99.9\%$.

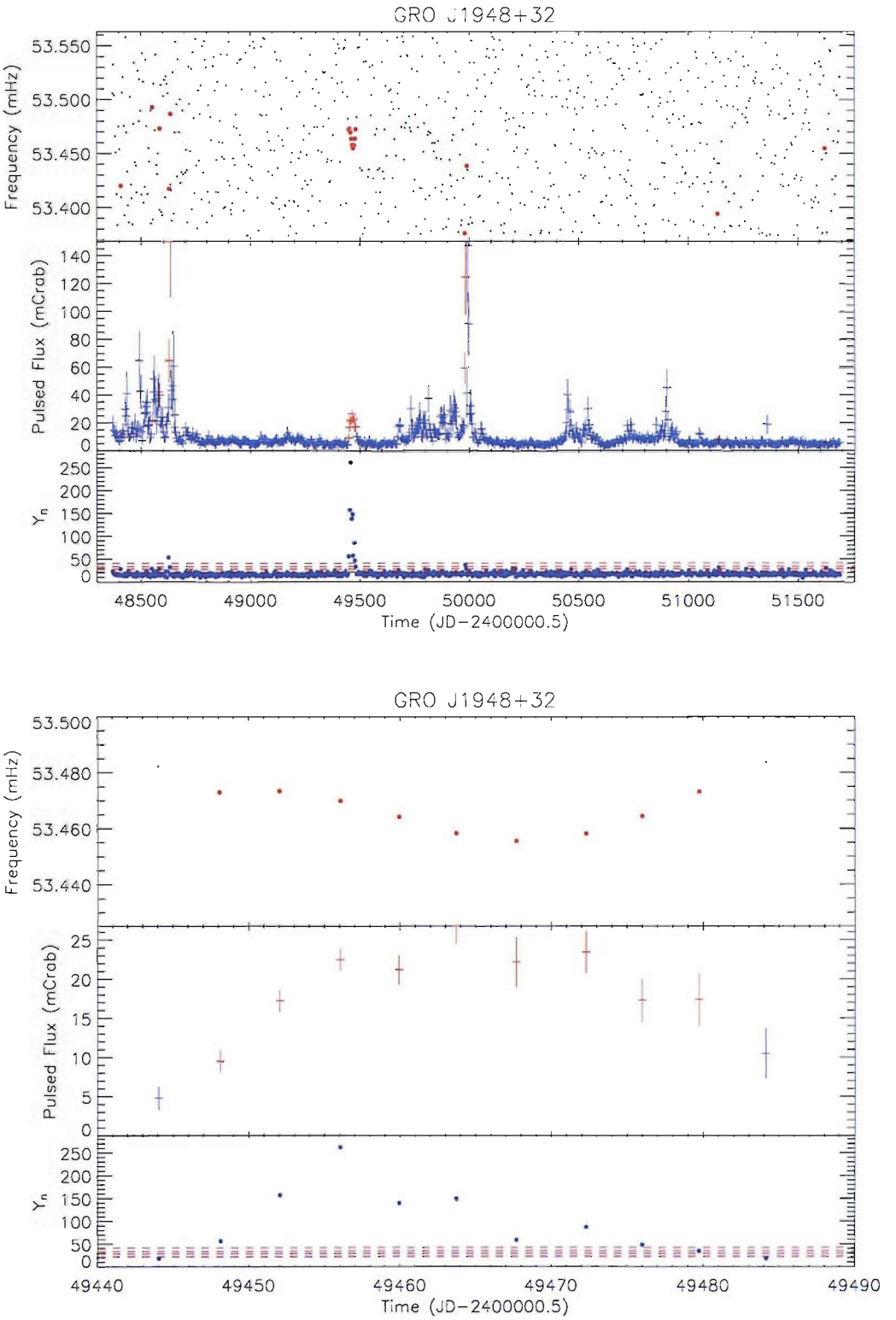

Figure 2.18: GRO J1948+32 — 4-day averaged frequency and pulsed flux. *Top*: For entire mission, with $Sig_{\min} = 99\%$. *Bottom*: Closeup of the main outburst, with $Sig_{\min} = 99\%$.

together with previous *EXOSAT*, and newer *RXTE* data, Wilson et al. (2002) derive an ephemeris for periastron of MJD $50547.22 \pm 0.02 + \mathrm{n} \times 46.0214 \pm 0.0005$ d, with an eccentricity for the orbit of $e = 0.419 \pm 0.002$. The frequency measurements in Fig. 2.19 have been orbitally corrected using this ephemeris, showing a period of spin up before MJD $\sim$49300, with a turnaround to spin down after that date. Hα measurements during this time show a decrease in the density of the Be star's disk, thus reducing the amount of material available for the neutron star to accrete. The X-ray flux levels are correlated with the sign of the spin changes, with higher fluxes being associated with spin up, while spin down occurred at lower fluxes, suggesting that the the angular momentum carried by the accreted material during these fainter outbursts is not enough to offset the intrinsic spin-down torque of the system; the origin of this torque is as yet unclear. After analysing recent *RXTE* data Wilson et al. (2005a) find the X-ray flux increasing during outbursts and predict a transition of the system to spin-up in 2005.

The practically linear spin down of EXO 2030+375 after MJD $\sim$49300 ($\dot{P} = -9.4 \times 10^{-11}\,\mathrm{s\,s^{-1}}$) would require a luminosity of at least $L_\mathrm{x} = 1.2 \times 10^{35}\,\mathrm{erg\,s^{-1}}$ ($B = 1.8 \times 10^{12}$ G), which compares favourably with the value of $L_\mathrm{x} = 9 \times 10^{35}\,\mathrm{erg\,s^{-1}}$ detected by *BATSE*, assuming a distance of 7.1 kpc to the source (Wilson et al. 2002).

2.2.16 GRO J2058+42

CXOU J205847.5+414637
RA 20 58 47.5, dec 41 46 37
Counterpart: O9.5–B0IV–Ve

BATSE discovered pulsations at 198 s from this source in a 46-day outburst in 1995 (see MJD $\sim$50000 in Fig. 2.20) (Wilson et al. 1995). Not until 2005 was the optical counterpart identified (Wilson et al. 2005b). Wilson et al. (1998a) initially proposed a $\sim$110 d orbital period for this system, with outbursts occurring at both periastron and apastron, due to differences in the odd/even outbursts; Fig. 2.20 shows 7 regularly spaced outbursts ($\sim$55 d) which took place after the initial bright one. Later

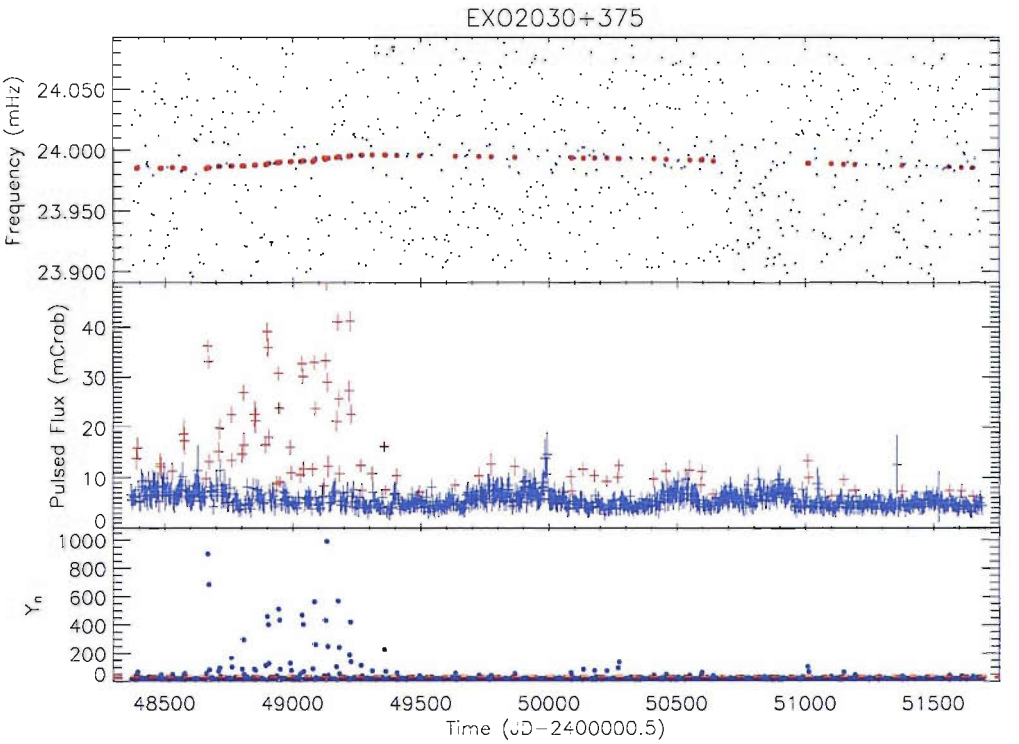

Figure 2.19: EXO 2030+375 — 4-day averaged frequency and pulsed flux for entire mission; $Sig_{\min} = 99.9\%$.

outbursts detected with both *RXTE* and *BATSE* didn't follow this pattern and the orbit was established as $\sim 55\,\mathrm{d}$, with an ephemeris of MJD 50411.3 + n × 55.03 d (Wilson et al. 2000).

The steady, almost linear spin up experienced by this pulsar since MJD ~ 50075 is $\dot{P} = 7.1 \times 10^{-9}\,\mathrm{s\,s^{-1}}$, implying a luminosity of about $L_x = 2.4 \times 10^{35}\,\mathrm{erg\,s^{-1}}$ ($B = 1.6 \times 10^{13}\,\mathrm{G}$), which is a typical value for Type I outbursts exhibited by Be/X-ray binary systems.

2.3 Comments

BATSE proved to be an invaluable source of data for the study of X-ray binaries by allowing for continuous coverage of sources during ~ 9 years. The new data analysis

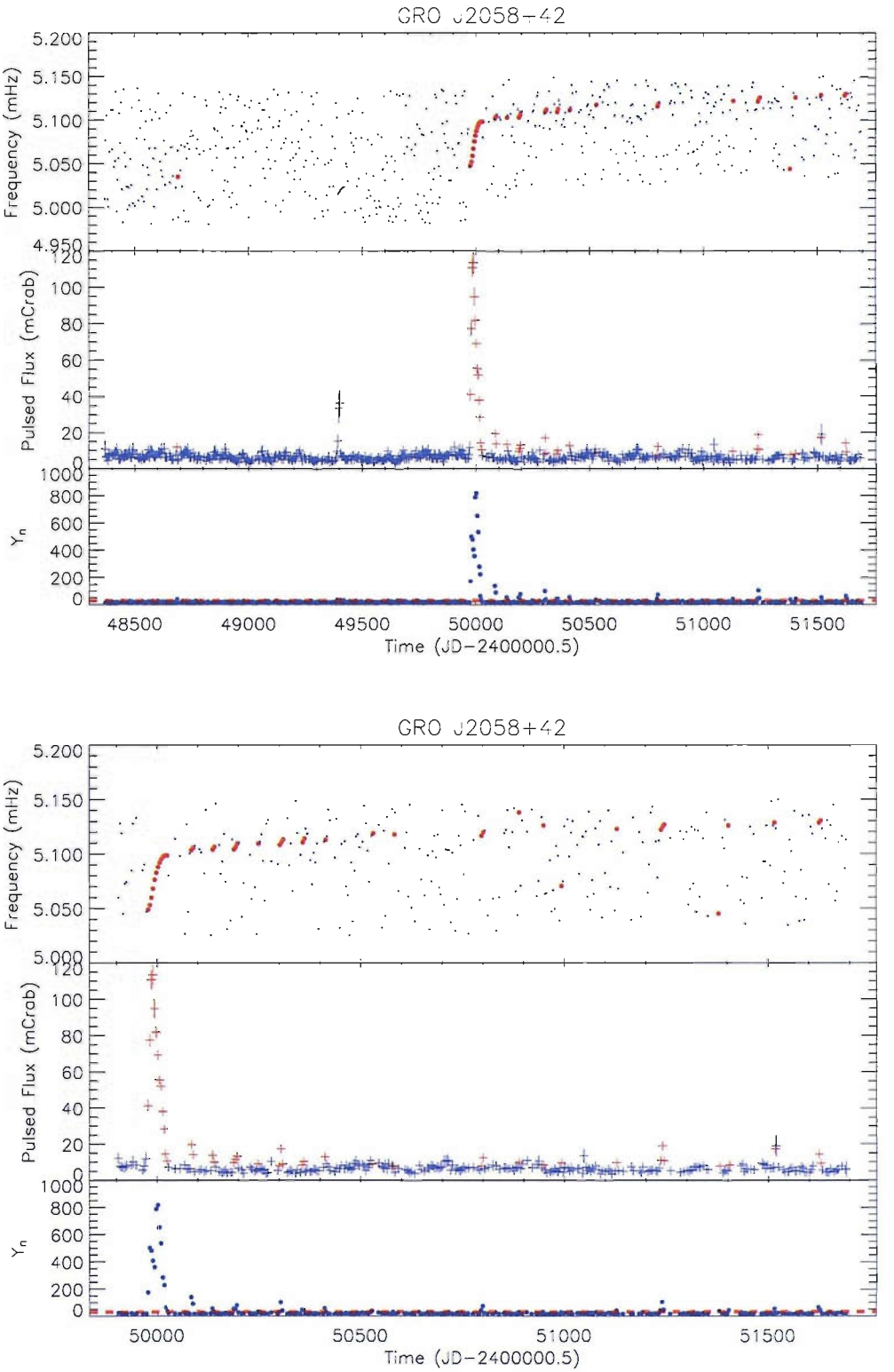

Figure 2.20: GRO J2058+42 — 4-day averaged frequency and pulsed flux. *Top*: For entire mission, with $Sig_{\min} = 99.9\%$. *Bottom*: Closeup of the outbursts, with $Sig_{\min} = 99\%$.

techniques applied to the *BATSE* archive in this chapter have confirmed the light curves presented by Bildsten et al. (1997), although we failed to find any outbursts that might had been missed in previous searches. As such, the improvement has not been large, or maybe we were simply trying to find detections where there were none to be found.

A number of new systems were discovered in bright outbursts after the publication of Bildsten et al. (1997): SXP31.0, XTE J1543−568 and GRO J1944+26. The orbital parameters of two more systems were calculated: SXP31.0 and GRO J1008−57. The orbital period of SXP31.0 is towards the lower end of the Corbet diagram variance, while that of GRO J1008−57 is at the upper end. Furthermore, other studies with *RXTE* ASM data from GRO J1008−57 suggest the orbital period may be $\sim \frac{1}{2}$ of the value we calculated, so a new outburst must be waited for in order to settle the matter. While the orbit calculation technique we used is powerful, it still requires a prolonged outburst lasting more than one orbital cycle in order to be truly effective. Because of this, there are still a number of systems that, although they have shown significant activity, have not had an orbital solution calculated for them; e.g., A 1118−616 or 4U 0728−25 (although an orbital period is known for this last system). In an attempt to find an orbital period for A 1118−616 and GS 1843+00, their pulsed flux light curves were run through a Lomb-Scargle period search, with no success.

Chapter 3

RXTE Data Analysis Techniques

In any case, whenever technical progress opened a new window into the surrounding world, I felt the urge to look through this window, hoping to see something unexpected.

—Bruno Rossi

3.1 *RXTE* – The satellite behind the data

RXTE, the Rossi X-ray Timing Explorer[1], was launched on December 30, 1995 from NASA's Kennedy Space Center. It was initially designed for a required lifetime of two years with a goal of five; at the time of writing, it is still operational. It resides in a low-earth orbit at an altitude of 580 km, with an orbital period of ~ 93 minutes, at an inclination of 23°. Its scientific payload consists of three instruments: The PCA (Proportional Counter Array), a set of large area xenon proportional counters sensitive to 2 – 60 keV photons; HEXTE (High Energy X-ray Timing Experiment),

[1]Named in honour of Professor Bruno B. Rossi, who together with colleagues discovered the first non-solar source of X-rays, Scorpius X-1.

a set of large area sodium iodide scintillators sensitive to 15 – 250 keV; and the ASM (All-Sky Monitor), three wide field-of-view scanning detectors sensitive to 2 – 10 keV. The first two are pointed instruments with collimators giving them a 1° FWHM, while the ASM scans 80% of the sky every orbit. Fig. 3.1 shows a diagram of *RXTE*; for more information and details on the instruments see Bradt et al. (1993) and Jahoda et al. (1996); for an in depth discussion of the PCA instrument see Jahoda et al. (2005).

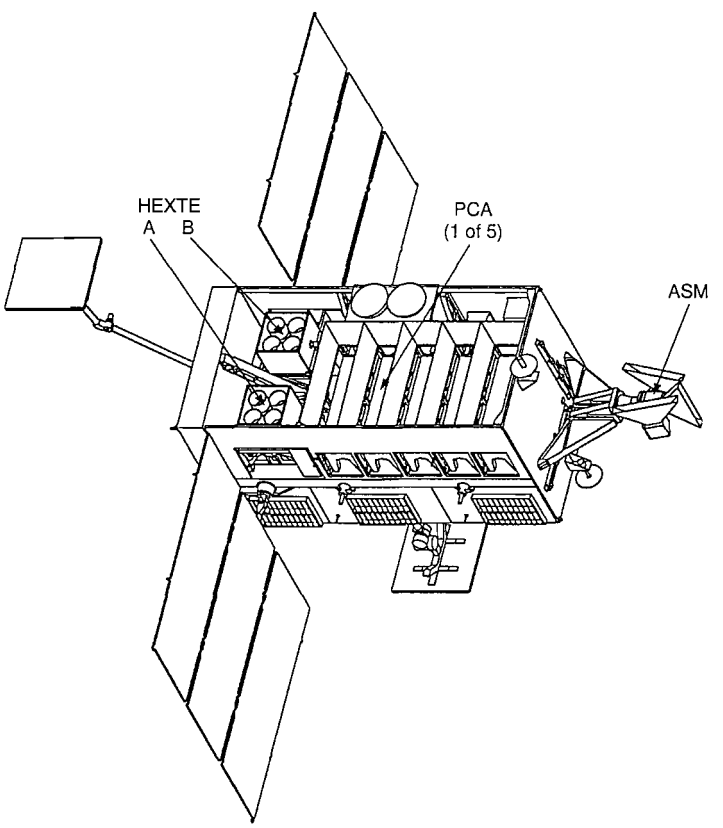

Figure 3.1: Schematic diagram of *RXTE*.

3.1.1 The Proportional Counter Array (PCA)

The PCA (Fig. 3.2(a)) consists of 5 identical proportional counter units (PCUs) placed side by side[2] (see Fig. 3.2(b)). They are filled with a 90/10 mixture of xenon and methane gas at 1.1 atmospheres, and have a top propane layer (which can stop electrons below 2 keV) used as a veto detector for particle background; they are separated from each other by an aluminium-coated mylar window. The xenon volume is divided by wire walls into 3 layers of cells of $\sim 1.3\,\mathrm{cm} \times 1.3\,\mathrm{cm} \times 1\,\mathrm{m}$ (making up the 3 layers of signal anodes); each layer is further divided into 2 halves by connecting alternate cells to either the right or left amplifier chain, thus producing a total of 6 signal chains. The outermost anodes of the 3 layers, plus a complete fourth layer at the bottom, make up the xenon veto. The detector bodies are constructed of aluminium and surrounded by a graded shield consisting of a layer of tin and another of tantalum. On-board callibration is accomplished by using a ^{241}Am source placed at the bottom of the xenon chamber alongside an α-particle detector. One of the decay channels of the source is the simultaneous emission of an α-particle and a 59.6 keV photon; any photon detected coincidently with an α-particle will be flagged as being at 59.6 keV.

Thus, the PCU's design provides 8 "detectors" to be used as discriminators: 6 xenon signal chains, 1 propane veto chain, and the callibration flag. An event will be considered "good" (i.e., an X-ray) when only *one* discriminator is triggered.

The data collected by the PCAs and the ASM are processed on board by the Experiment Data System (EDS). The EDS consists of eight Event Analysers (EA), of which six are dedicated to the PCA and two to the ASM. Each EA contains an Intel 80286 processor and associated memory. The EAs can be programmed independently to process incoming events from the instruments in any of the following modes:

- Transparent mode, using 1, 2, or 3 EAs

[2]For the purpose of this work, we have adopted the convention of numbering the PCUs from 0 to 4.

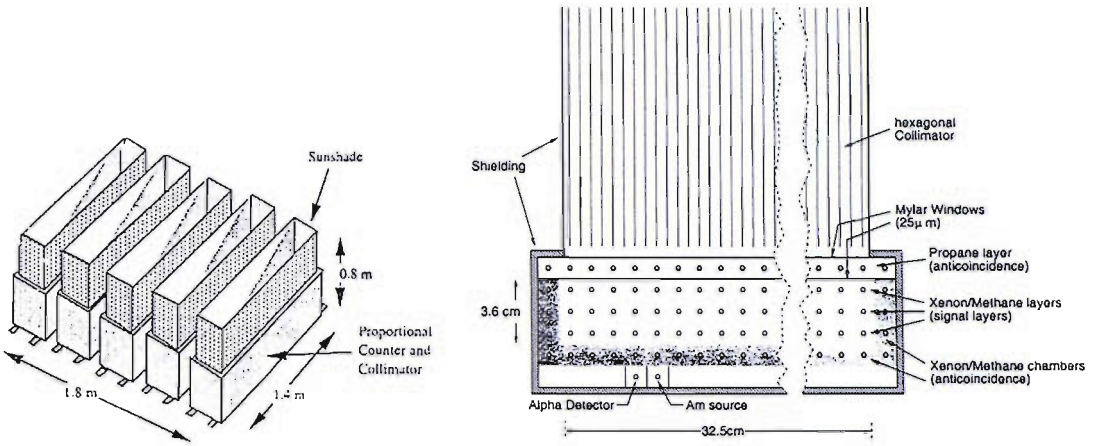

(a) The PCA. (b) Cross section of a PCU.

Figure 3.2: Schematics of the PCA detector on *RXTE*.

Table 3.1:

RXTE's PCA Instrument Characteristics

Energy range	2 – 60 keV
Energy resolution	< 18% at 6 keV
Time resolution	1 μs
Spatial resolution	1° FWHM, 2° FWZI
Detectors	5 proportional counters
Collecting area	6500 cm^2
Sensitivity	0.1 mCrab
Background	2 mCrab

- Event mode, using 1 or 2 EAs
- Binned mode (time and/or energy)
- Burst catcher mode
- Fourier transform mode
- Pulsar fold mode
- Autocorrelation mode
- Arrival time differences histogram mode

Two of the 6 EAs are reserved for standard PCA modes which have remained unchanged throughout the mission and provide data as *standard products*; they are taken in binned mode and have the following characteristics:

Standard 1 provides binned data at 0.125 s, with no energy resolution, accumulated from good xenon events.

Standard 2 provides binned data at 16 s (2 s if the source is bright) accumulated from good xenon events; a 129 channel spectrum is also recorded. Data are taken from each anode of each PCU.

In the present work we use a type of event mode data called GoodXenon, where every photon is tagged with its time, energy and PCU configuration (PCU, layer and anode of detection). This mode makes full use of the PCA's capabilities with a timing resolution of 1 μs and energy resolution of 256 channels. Fig. 3.3 shows the quantum efficiency of the 3 xenon signal layers in PCU2; it is clear that layers 2 and 3 will contribute little to the count rate at lower energies. In view of this, we chose to use only data from layer 1, and restrict the energy range to $3-10$ keV so as to maximise the signal-to-noise.

It should also be noted that on May 12^{th} 2000 PCU0 began losing pressure in the propane layer; within 2 days it had vented the gas into space thus leaving it without a particle veto at the front end. Naturally, the count rate increased in this PCU, and although a new background model was developed for it, it was decided not to use data from PCU0 after this date.

3.1.2 Collimator response of the PCA

The collimator of each PCU is constructed of corrugated sheets of beryllium copper coated with a tin-antimony (95%/5%) solder. The resulting collimator cells are hexagonal with two of the six walls being double thickness. The nominal dimension of the cells is 3.2 mm across, 203.3 mm in length, and 0.069 mm thick. The hexagonal tubes are not perfectly parallel so when modelling the collimator response the *RXTE*

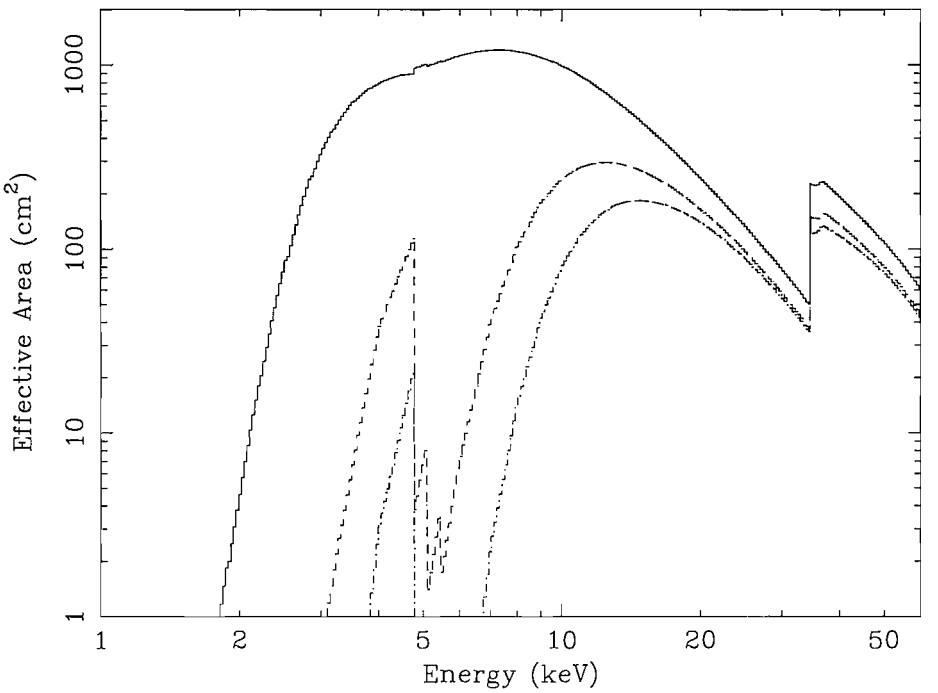

Figure 3.3: Quantum efficiency for layers 1 (solid line), 2 (dashed), and 3 (dot-dash) of PCU2 for January 13 2002. Taken from Jahoda et al. (2005).

team assumes a group of hexagonal tubes each of which has been randomly offset from the vertical by a small angle. This model was fit for each individual PCU to scan data from the Crab nebula, and the results show (see Fig. 3.4) that all the PCUs are off centre to a greater or lesser extent.

Another difference between the PCUs is their throughput. PCU2 has the highest; if the others are scaled to it, the throughput of PCUs 0 – 4 is (in that order) 0.9912, 0.9947, 1.0000, 0.9410 and 0.9277.

Due to the nature of this survey (multiple objects within the field of view at any one time) it was not possible to use the appropriate program from *FTOOLS* to correct the light curves for collimator response. This is only recommended when observing a single source, at a know location in the sky; during observations of the SMC there are a large number of pulsars within the field of view, and their coordinates are not always known. Furthermore, this would require the production of a reduced light curve for each pulsar known to be within the field of view (which could be as many as 20). While this would certainly be the ideal solution, the increase in

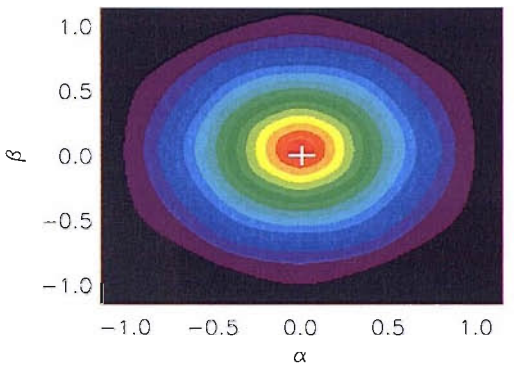

(a) Collimator response of PCU0.

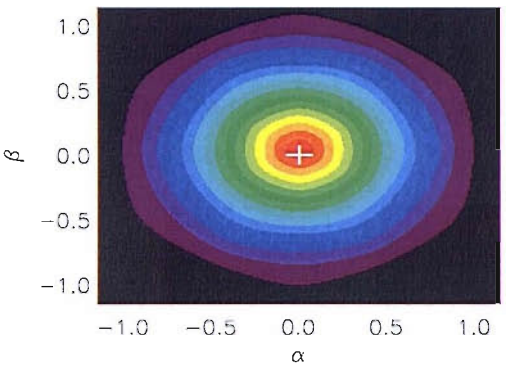

(b) Collimator response of PCU1.

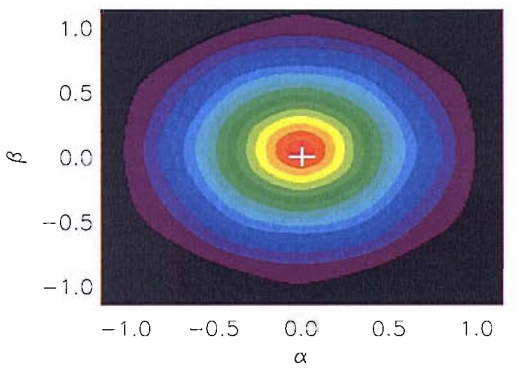

(c) Collimator response of PCU2.

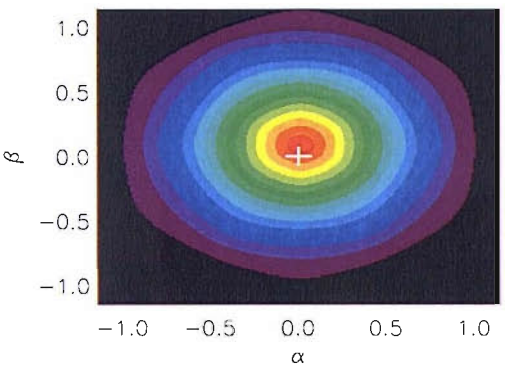

(d) Collimator response of PCU3.

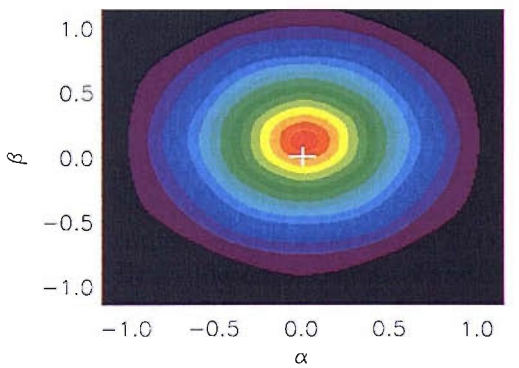

(e) Collimator response of PCU4.

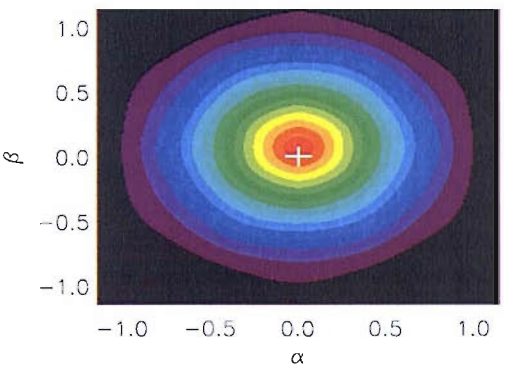

(f) Combined response of the 5 PCUs.

Figure 3.4: a) – e) Individual collimator responses of the PCUs; f) the combined collimator response, effectively the response of the PCA. The crosshair indicates the centre of the FOV, note how each PCU is offset from the centre by a different amount. α and β are in degrees and represent the angles along the width and length of the spacecraft, respectively.

computation time and the extra space required to archive the data make it impractical at the moment. Therefore, in order to account for differences in observed flux from a pulsar when observed at different pointing positions, a collimator correction was applied *a posteriori* to each pulsar's amplitude light curve. A look-up table approach was used, where each pulsar had a collimator response calculated for each of the pointing positions used in the survey (see Table 3.3). A simplified calculation of the collimator response was adopted for ease of use and quickness of computation: Say a pulsar fell 0.25° from the centre of the field of view, then the collimator response along various points 0.25° distant from the centre of the PCU were averaged to give the final collimator correction. The model for the combined collimator response of the PCU, as seen in Fig. 3.4(f), was used for these calculations.

Pulsars with unknown position cannot be collimator corrected, so there is no way for detections to rise significantly above the noise level unless they are very bright. Type I outbursts will only appear bright when the pulsar is close to the centre of the field of view (as with SXP59.0 in Position 1/A), in which case the collimator correction is small anyway. To overcome this limitation pulsars with unknown positions had coordinates "guessed" for them on the basis of where (in which observing positions) they had been detected throughout the mission.

3.2 Pipeline reduction script

The pipeline was written in C-shell script and provided a fully automated way of obtaining clean light curves from the raw data supplied by *RXTE*. The script makes use of many *FTOOLS* programs written by HEASARC and was originally developed by Silas Laycock for use in his thesis (Laycock 2002). Many changes were introduced for the present work in response to problems that arose during the initial use of the original script (e.g., erroneous FITS header information regarding pointing positions, spurious spikes in the flux caused by detectors being switched off, mislabelled Obs. I.D.s leading to good data being thrown out, etc.).

The following are the steps taken during the reduction process:

1. Create a housekeeping FITS file containing pertinent information about the observation, such as pointing coordinates, detector on/off status, time elapsed since SAA passage, etc. This file is named *filter.xfl*.

2. Each individual observation is assigned a pointing position determined from its Obs. I.D., this is done because the pointing position specified in the header of *filter.xfl* is not always correct.

3. Add 2 new columns to *filter.xfl*: TARGET_OFFSET and ON_TARGET. TARGET_OFFSET is the distance (in decimal degrees) that the spacecraft is pointing away from the stipulated pointing position. ON_TARGET is a binary expression that will be 1 when TARGET_OFFSET $\leq 0.0004°$, and 0 otherwise. A new keyword is also added to the FITS header: IN_RANGE, its value will be 0 if the satellite was off-target during the whole observation (and thus, no useful data were collected), and 1 otherwise.

4. The NULL entries in the columns for the electron counts of each detector are converted to the value 0.0. This is required for one of the conditions stated in *gti.cond* (step 8) to work correctly.

5. Three graphs are generated using the housekeeping data (in both a postscript and gif version):

   - (Obs. I.D.)_PCUs_ON: Shows the state (on/off) of each PCU during the observation.
   - (Obs. I.D.)_electrons: Shows the value of the electron flux of each PCU.
   - (Obs. I.D.)_gral_housekeep: Shows the values of the following observation parameters: POINT_RA, POINT_DEC, TARGET_OFFSET, ON_TARGET, NUM_PCU_ON, ELV and TIME_SINCE_SAA.

6. A check is performed to insure that ON_TARGET $\neq 0$ during at least part of the observation; if not, reduction of this Obs. I.D. is aborted and the script jumps to the next one.

7. The date of the observation is obtained to establish the *RXTE* epoch, this is required when choosing which energy channels to reduce as different gains have been used in each of the 4 epochs.

8. Create the file *gti.cond*, which lists the conditions required to consider data good. It is then used to create the good time interval (GTI) file *goodtime.gti*, which lists the times during which data are deemed good.

9. Create the Good Xenon event files.

10. Based on the epoch of the observation, the appropriate energy channels are set such that the energy range of the data extracted is $\sim 3-10\,\mathrm{keV}$.

11. FITS files of Good Xenon (*gx_LR1.lc*) and background (*background.lc*) data are created and binned at 0.01 s, then the background is subtracted from the Good Xenon data to produce the cleaned light curve *gx_LR1_bcor.lc*.

12. The light curve is barycentre corrected to produce *gx_LR1_bcor_fxb.lc*.

13. *gx_LR1_bcor_fxb.lc* is dumped into an ASCII file (*lc.dat*) containing the columns time, flux, flux error.

14. *lc.dat* is now normalised to the number of PCUs that were on at each time interval to create *lcn.dat*, where the time column contains the time in *RXTE* seconds, and the flux is in counts $\mathrm{PCU}^{-1}\,\mathrm{s}^{-1}$.

15. All individual Obs. I.D.s belonging to the same observation, and with the same pointing position, are joined together such that only one light curve is generated for each observation.

16. Two power spectra are generated for each light curve using Lomb-Scargle timing analysis; they span different period spaces (from P_{min} to P_{max}) at different timing resolutions (Δf) and pulsars are later searched for in their corresponding group according to their pulse period. The values used for each group are listed in Table 3.2.

3.2.1 Filtering criteria

Background subtraction is carried out in step 11 using the new background model files (as of 2000) that correct for a slow linear trend in the background rate; as

Table 3.2:
Parameters used for the Lomb-Scargle periodogram

	Group 1	Group 2
$P_{\min}$ (s)	0.5	10
$P_{\max}$ (s)	1000	3000
Δf (Hz)	10^{-5}	5×10^{-7}
Search range (s)	0.5 – 40	40 – 3000

RXTE's orbit degrades the background decreases. The mission-long Faint Model File is available from the HEASARC webpages.

In order to generate the GTIs in step 8, a number of conditions need to be set to filter out the bad data. As mentioned above, there is a housekeeping file registering the status of the satellite and its instruments during each observation; data are recorded every 16 s. The parameters that were used in the filtering process are as follows:

TARGET_OFFSET This distance was required to be less than 0.0004°.

ELV The elevation above the Earth's horizon in degrees; negative values mean the spacecraft is pointing towards the Earth! Although *RXTE* team recommend using data where ELV > 10°, the nature of our research (timing analysis) prompted the use of 5° as the cutoff in order to maximise the length of the observations.

ELECTRON2 The flux of electrons (in electrons s^{-1}) through the propane layer beneath the collimator of PCU2. Although the background models and anti-coincidence detectors take care of most of the particle background, there can be instances of high particle flux when these systems may not be able to properly cope. In these cases it is useful to filter by imposing ELECTRON2 < 0.1 electrons s^{-1}. The choice of PCU2 is due to it being the only detector that remains on all the time (except during SAA passage).

PCU*n*_ON × ELECTRON*n* This condition is applied to PCUs n = 1, 3 and 4. It was added to the prior list after a number of observations were found

to have very short "flares" in the countrate of unknown origin. When bright enough, these flares could corrupt the powerspectrum, or at the very least introduce low-frequency noise. They were discovered to originate when a PCU was turned off during an observation and caused a sharp rise in its electron count, most likely through the back EMF mechanism. By setting the condition PCUn_ON $\times$ ELECTRONn < 0.15 electrons s^{-1} these flares were eliminated with a minimal loss of observing time (no more than 60 s).

3.3 Data analysis

The analysis software was written by the present author and consists of two main programs, PUMA and ORCA. PUMA (PUlsar Monitoring Algorithm) scans through all the power spectra measuring the amplitude of pulsations for all the known pulsars in the SMC; it will also report on bright pulsations at new periods. ORCA (ORbital Calculation Application) reads the pulse amplitude files created by PUMA and constructs a long-term light curve for each pulsar, also looking for periodic signatures indicative of an orbital period. A detailed explanation is provided in the next two sections.

3.3.1 PUMA – PUlsar Monitoring Algorithm

To illustrate the workings of PUMA we will show how it acts upon a sample light curve. Obs. I.D. 20137-03-01 will be used, an observation taken on Nov. 25$^{\text{th}}$, 1997 lasting 2972 s (with a live-time of 2940 s); it was pointing at Position 1c. Fig. 3.5 shows the initial Lomb-Scargle periodogram, where peaks from a number of pulsars clearly stand out. Figs. 3.6 and 3.7 shows the intermediate stages of the cleaning process.

To begin with, PUMA requires a table with the collimator response of every pulsar at each of the pointing positions (see Table 3.3 for the pointing positions), this file will be read in and used for the collimator corrections to be applied by ORCA. The

method used to calculate the collimator response was explained in § 3.1.2.

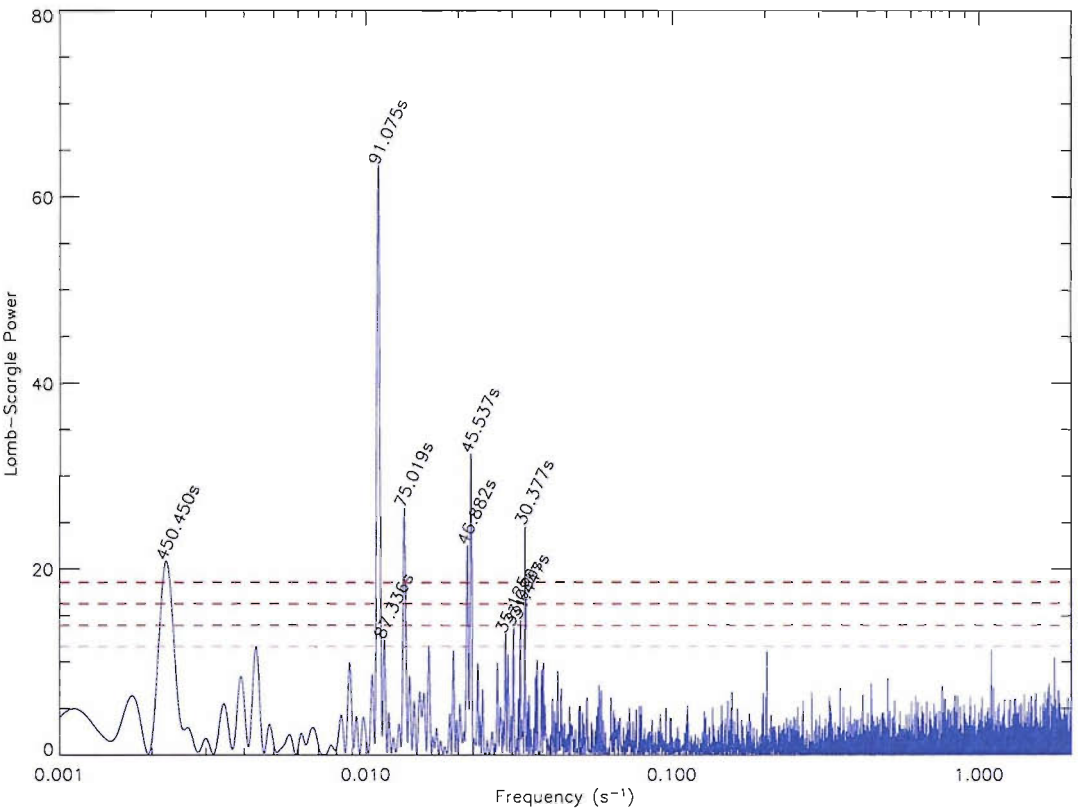

Figure 3.5: Lomb-Scargle periodogram of the Obs. I.D. 20137-03-01 light curve. The dashed, red lines indicate levels of significance; from bottom to top: 90%, 99%, 99.9%, 99.99%.

1. When running the program it is first necessary to specify which pulsars to look for, i.e., Group 1 or 2 (see Table 3.2), and what AOs/Obs. I.D.s to scan.

2. The collimator response file is read in.

3. The light curve, Lomb-Scargle periodogram, filter file and collimator responses of an Obs. I.D. are read in. If the observation is not of the SMC then the program jumps to the next Obs. I.D..

4. Statistical information of the light curve is read from a file (mean counts, variance, standard deviation, duration and number of data points), if it doesn't exist it is calculated and saved to file. The Lomb-Scargle periodogram is read in (Fig. 3.5).

5. The highest peak (above 90% global significance) in the power spectrum is found and, either identified as a known pulsar, or flagged as a UPO (Unknown Pulsating Object).

6. The light curve is folded at this period to produce a pulse profile.

7. Using the pulse profile as a template, the pulsations are then subtracted from the light curve and a Lomb-Scargle periodogram of the cleaned light curve is produced (see top-left power spectrum in Fig. 3.6).

8. This power spectrum is subtracted from the previous one to create a pulsar-specific power spectrum (or P^2S^2), which shows only the contribution of the pulsar to the power spectrum (see top-right power spectrum in Fig. 3.6). This method allows one to see the possible harmonics that may have been lost in the noise or confused with the fundamental of another pulsar. The power of the fundamental and harmonic(s) peaks in the P^2S^2 is measured and a pulse amplitude estimated by adding in quadrature the amplitudes of the individual peaks (see Eq. (3.15)). The significance of the detection is taken to be the local significance of the fundamental peak.

Repeat steps 5 – 8 until there are no peaks left in the power spectrum above 90% significance. Fig. 3.6 shows the intermediate power spectra and P^2S^2s obtained through this process and Fig. 3.8 shows the power spectrum of the fully-cleaned light curve. When this is done, move on to the next step to search for the pulsars that were not detected in the previous steps.

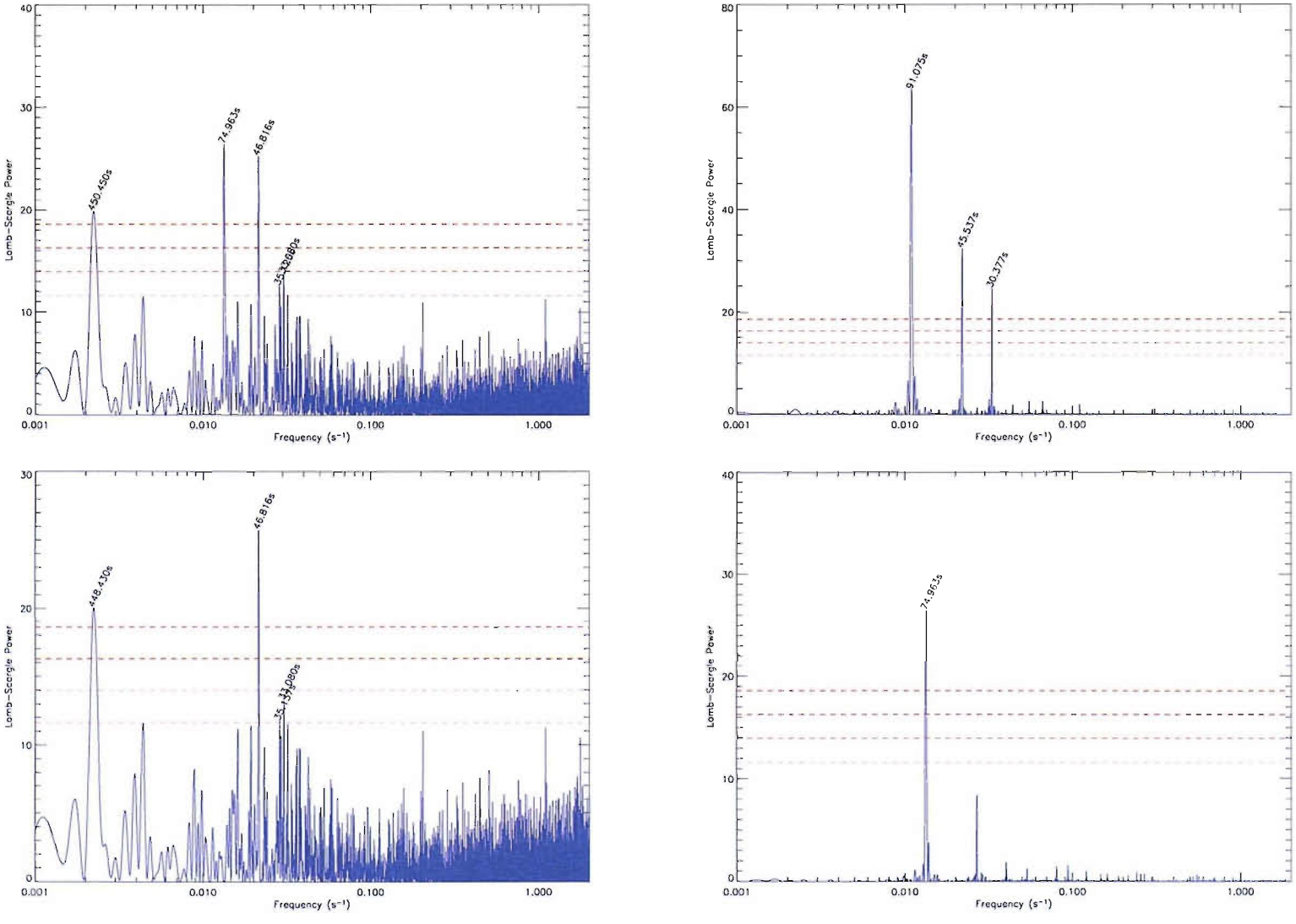

Figure 3.6: The graphs on the left show the power spectrum of the light curves after the brightest pulsar has been subtracted; those on the right show the P^2S^2 of this pulsar, obtained by subtracting one power spectrum from the other. These pulsars are SXP91.1 (*top*), and SXP74.7 (*bottom*).

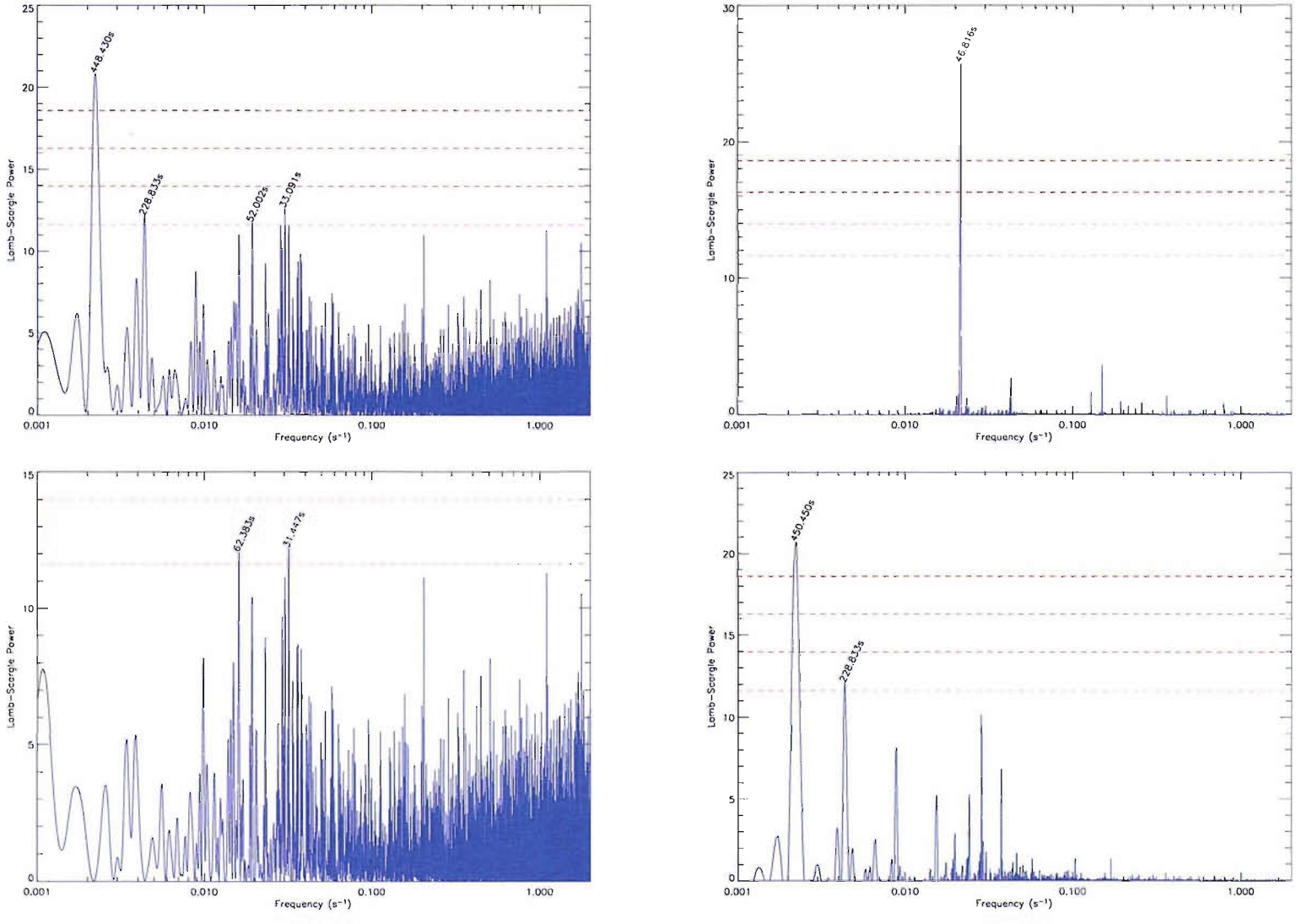

Figure 3.7: Same as Fig. 3.6. The subtracted pulsars are SXP46.6 (*top*), and SXP452 (*bottom*).

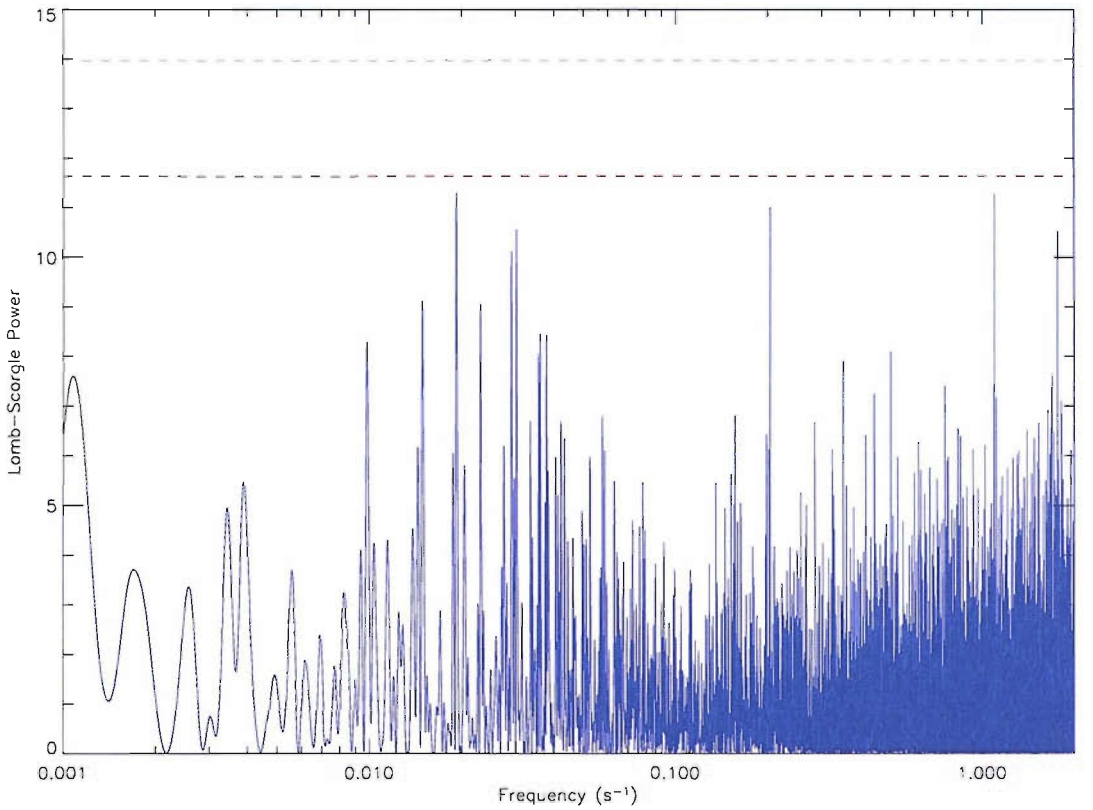

Figure 3.8: Lomb-Scargle periodogram of the Obs. I.D. 20137-03-01 light curve after it has been cleaned of all pulsations with significance $\geq 90\%$.

9. Examine a stretch of the power spectrum centred on the pulsar's nominal frequency and spanning 5% of it on either side. The maximum power within this region is registered; if it is not a peak, then the significance of the detection is set to 0% and the pulsed amplitude is taken as that of the average power within the region. If the maximum is a peak, then the significance of the detection is set to the local significance and the pulsed amplitude calculated from the power of the peak. If the local significance is $\geq 90\%$ then the fully-cleaned light curve is folded to obtain the pulse profile. Note that no harmonics are searched for at this stage, although it may be desireable to incorporate this feature into future versions of PUMA. Repeat this step until all pulsars have been searched for, then move on to next Obs. I.D..

After PUMA has processed all the Obs. I.D.s it will have created a file for each

pulsar with the pertinent data for each observation. The first few lines of such a file, corresponding to SXP91.1, are shown below:

1	2	3	4	5	6	7	8	9	10	11	12
50777.4240	20137-03-01	SMC_X-3	1	91.341	1.90E-09	63.437	100.0000000	100.0000000	0.8308	0.7855	0.2208
50777.4240	20137-03-01	SMC_X-3	2	45.676	4.63E-02	32.386	100.0000000	100.0000000	0.5936	0.7855	0.2031
50777.4240	20137-03-01	SMC_X-3	3	30.442	2.36E-02	24.571	99.9999987	100.0000000	0.5171	0.7855	0.1858
50779.3920	20137-03-02	SMC_X-3	1	91.181	8.63E-10	62.451	100.0000000	100.0000000	0.6471	0.7855	0.1548
50779.3920	20137-03-02	SMC_X-3	2	45.727	1.50E-02	62.635	100.0000000	100.0000000	0.6480	0.7855	0.1399
50779.3920	20137-03-02	SMC_X-3	3	30.485	1.59E-02	10.944	97.7001829	99.9234075	0.2709	0.7855	0.1258
50779.3920	20137-03-02	SMC_X-3	4	22.844	1.17E-02	6.374	10.5438480	90.5867579	0.2067	0.7855	0.1128
50781.2233	20137-03-03	SMC_X-3	1	91.149	1.84E-10	133.770	100.0000000	100.0000000	0.6222	0.7855	0.0832
50781.2233	20137-03-03	SMC_X-3	2	45.592	1.45E-02	6.481	0.1549571	86.7228545	0.1370	0.7855	0.0769
50781.2233	20137-03-03	SMC_X-3	3	30.389	5.33E-03	9.410	70.7877239	98.8652723	0.1650	0.7855	0.0710
50784.1544	20137-03-04	SMC_X-3	1	91.149	1.67E-10	161.211	100.0000000	100.0000000	0.6318	0.7855	0.0849
50784.1544	20137-03-04	SMC_X-3	2	45.583	7.23E-03	25.505	99.9999964	99.9999999	0.2513	0.7855	0.0779
50784.1544	20137-03-04	SMC_X-3	3	30.381	4.79E-03	11.484	95.7201111	99.8555714	0.1686	0.7855	0.0714
50787.3667	20137-03-05	SMC_X-3	1	91.104	1.33E-10	157.361	100.0000000	100.0000000	0.6721	0.7855	0.0893
50790.2935	20137-03-06	SMC_X-3	1	91.108	1.12E-10	133.022	100.0000000	100.0000000	0.5683	0.7855	0.0796
50790.2935	20137-03-06	SMC_X-3	2	45.537	3.91E-03	32.163	100.0000000	100.0000000	0.2795	0.7855	0.0734
50790.2935	20137-03-06	SMC_X-3	3	30.366	3.56E-03	7.655	3.6491712	89.6319138	0.1363	0.7855	0.0678

The columns are:

1. Date of observation in MJD (JD $-$ 2 400 000.5).
2. Obs. I.D.
3. Pointing position; SMC_X-3 corresponds to Position 1c.
4. Harmonic detected; 1 is the fundamental, 2 the first harmonic, etc.
5. Period at which it is detected, in seconds.
6. Error in the period.
7. Lomb-Scargle power of the detection.
8. Global significance of detection.
9. Local significance of detection.
10. Amplitude of the pulsations, in counts $\mathrm{PCU}^{-1}\,\mathrm{s}^{-1}$.
11. Collimator response.
12. Amplitude of the noise in the observation, in counts $\mathrm{PCU}^{-1}\,\mathrm{s}^{-1}$.

3.3.2 ORCA– ORbital Calculation Application

Once all the Obs. I.D.s have been processed by PUMA, ORCAmust be run to read in the individual pulsar files and produce a light curve of the pulsed flux amplitude over the duration of the survey. It then runs these light curves through a Lomb-Scargle analysis to look for possible periodicities. The following chapter will show the results of ORCA's analysis for the SMC pulsars.

1. Read in pulsar information file containing names, coordinates (when known) and pulse periods.
2. For each pulsar in turn, read in the history file produced by PUMA.
3. For each data point subtract the amplitude of the noise[3], then apply the collimator correction to data points above the detection threshold (unless otherwise stated, the threshold used was 99% local significance). Thus we create the finalised pulse amplitude light curve.
4. A Lomb-Scargle periodogram is created from the light curve to look for periodicities likely to be due to orbital modulation.
5. A number of graphs are created from the above information: a light curve (together with a plot of the pulse periods of those observations above the detection threshold, and the local significance of each data point), the Lomb-Scargle periodogram, and the light curve folded at the most significant period in the power spectrum. Examples of these can be found in Chapter 4 and Appendix A.

3.3.3 Folding light curves

If a pulsar is detected in an observation, it is interesting to know what its pulse profile looks like, as it provides information on the type of beam that is being

[3]In a Lomb-Scargle periodogram the noise is defined to have a power of 1. As such, the amplitude corresponding to a power of 1 in each observation was taken to be the amplitude of the noise.

detected (pencil, fan or both). Knowing the typical shape of a pulsar's profile can also help with setting the search criteria for it. If a pulsar of period p displays a single-peak profile, it is likely that the second harmonic will not carry much power and we can set the parameters such that a detection of $\frac{p}{2}$ will not be classified as belonging to said pulsar if this is close to the fundamental period of another pulsar. Conversely, if the pulsar shows a double-peak profile (e.g., SMC X-3), then it is convenient to know that the 1^{st} harmonic might be stronger than the fundamental in the power spectrum and a peak at $\frac{p}{2}$ should be recognised as belonging to the pulsar with pulse period p. Some pulsars even show a triple-peak structure and it is the 2^{nd} harmonic which can be the strongest (e.g., SXP8.80).

de Jager et al. (1988) show that searches for weak periodic signals via light curve folding methods suffer from a bias on the number of bins used to produce the pulse profile. Indeed, if the peak in the pulse is wide, the search will benefit from a small number of bins; conversely, a narrow peak will require a large number of bins to be resolved. Another problem associated with folding a weak signal is the choice of bin placement; a narrow peak that falls in between two adjacent bins might be washed out, while it would have been visible had it been counted in a single bin. The drawback to having narrow bins is that each one will have fewer counts and statistics will be worse, making noise cancellation within each bin harder.

Although we are not folding the light curves to search for pulsars, we can still benefit from improvements in folding technique in order to obtain profiles that are representative of the true shape of the pulses. Based on de Jager's work, Carstairs (1992) suggest a method of folding light curves using a fixed number of bins coupled with different folding start points. For a given pulse shape and signal strength there will be an ideal set of parameters to use when folding. Given the large number of data sets and pulsars we were studying, and that our work with profiles was intended to be of a qualitative rather than quantitative nature, we applied the same parameters to all profiles. This technique was applied both to the pulse and orbital profiles.

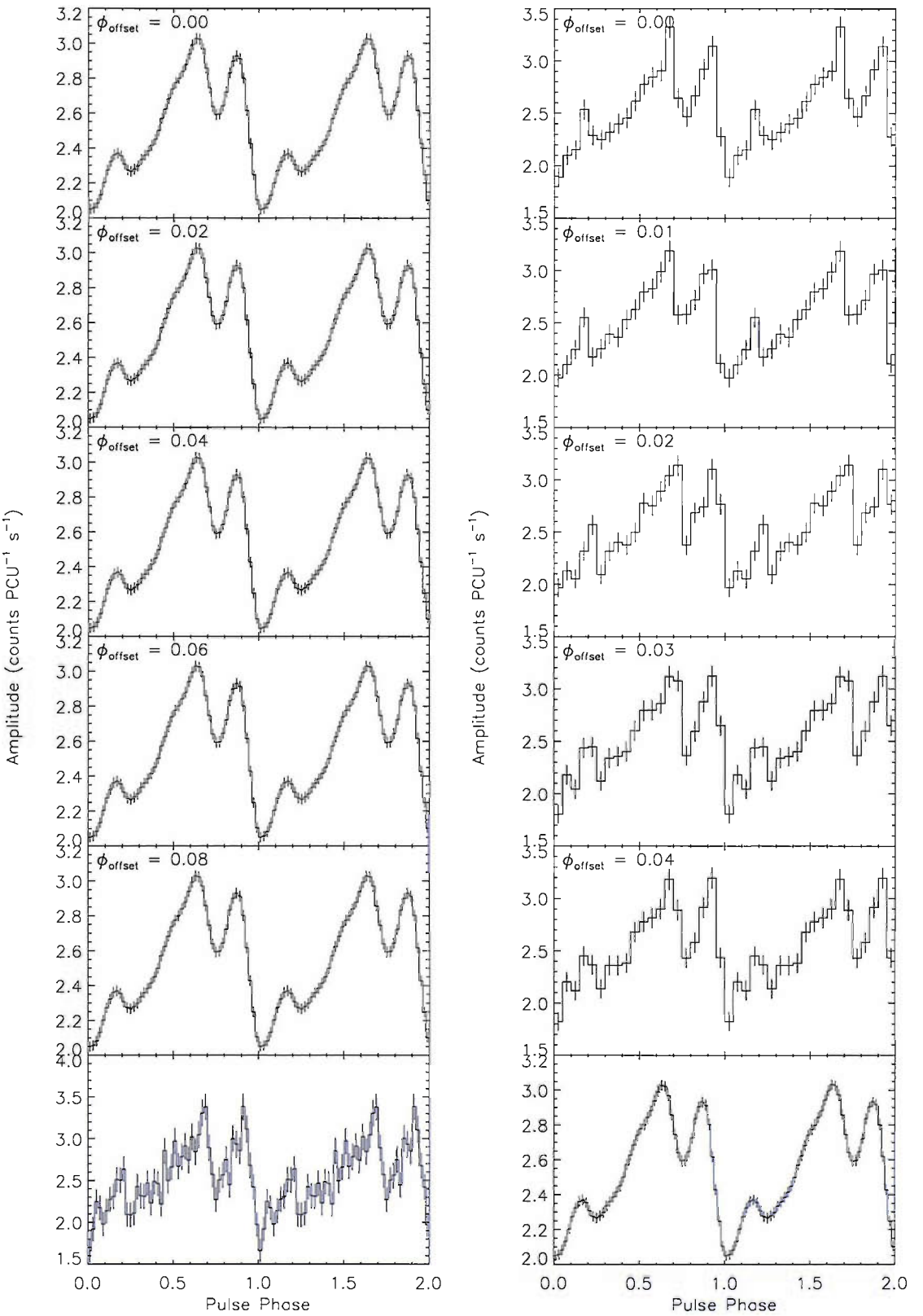

Figure 3.9: Examples of the phase-independent folding method. See text for details.

Our method is as follows: the folded light curve is obtained from m sets of n-binned folded light curves. To begin with, the light curve is folded at the desired period and the time values converted to phase space (ranging from 0 to 1). This "raw" folded light curve is then binned into n bins (of width $1/n$) in the standard way, with each bin starting at phase a/n (with $a = 0, 1, 2, ...n - 1$). This step is repeated again, but this time the bins start at phase $a/n + 1/(n \times m)$. In this way we create m folded light curves from the same data, each consisting of n bins, and only differing in the starting phase of these bins[4]. The general expression for the phase at which each bin begins is $a/n + m/(n \times m)$. Now each folded light curve is further divided into $l = n \times m$ sub-bins, such that in each light curve there will be n groups of m consecutive bins with the same flux value. The final folded light curve will have l bins, each of which is the average of the bins from the m sets of light curves. The error in each bin will be given by the standard error calculated from the m values that were averaged for each l-bin. In the present work we have used $n \times m = 10 \times 5$.

This method, which could be called phase-independent folding (PIF), provides an efficient way of generating folded light curves from poorly sampled data (or, as is our case, data with low S/N) as their shape will not depend on the starting point at which they are folded and, although only every m^{th} bin will be independent, spurious flux values within bins will be evened out while real features should be highlighted. Thus, we obtain the benefits of both wide bins (plenty of counts in each bin for good statistics) and narrow bins (sensitivity to narrow features in the profile).

As an example, Fig. 3.9 shows a number of profiles of SXP8.80 obtained with different methods from the same light curve[5]. The top 5 pairs of profiles have been folded using different starting points, ϕ_{offset}, which is in units of phase. The profiles on the left were obtained via PIF (with 5×10), while those on the right were folded in the standard way using 20 bins. Note how the profiles using the standard method

[4]We define $\phi = 0$ at the time of the first data point in each observation.

[5]The data are from a 5.8 ks (live-time) observation made on MJD 53102, where SXP8.80 was detected above 99.9999999% significance and there were no other bright pulsars present.

differ substantially from one another, simply because they were folded using different starting points. On the other hand, the profiles using the PIF method maintain a consistent shape no matter where the starting fold point is. It should be noted that the light curve used for this example is a best-case scenario as it included a very strong detection of SXP8.80; with a fainter detection the standard folding would have faired evern worse. The two bottom profiles show the light curve folded with 50 bins in the standard way (left) and with PIF (right).

3.3.4 Timing analysis – Lomb-Scargle periodogram

Lomb (1976) studies the statistics of least-squares fits to data in order to find periodic variations. In essence, it amounts to using a linear least-square fit of the data to the model

$$y(t) = A\cos\omega t + B\sin\omega t \tag{3.1}$$

to obtain the data's harmonic content at a frequency ω, where the data, y, are sampled at times, t. These times are expected to be random[6], but in the case of evenly sampled data, the method reduces to a Fourier periodogram obtained via a discrete Fourier transform (DFT), which is defined as

$$FT_y(\omega) = \sum_{j=1}^{N} y(t_j)\, e^{(-i\omega t_j)} \tag{3.2}$$

where N is the number of data points. The periodogram is then conventionally defined as

[6]Scargle (1982) emphasises the use of unevenly sampled data in order to avoid aliases (false peaks) that may arise due to the beating of the sampling frequency with the data window.

$$
\begin{aligned}
P_y(\omega) &= \frac{1}{N} |FT_y(\omega)|^2 \\
&= \frac{1}{N} \left| \sum_{j=1}^{N} y(t_j)\, e^{(-i\omega t_j)} \right|^2 \\
&= \frac{1}{N} \left[\left(\sum_j y_j \cos \omega t_j \right)^2 + \left(\sum_j y_j \sin \omega t_j \right)^2 \right]
\end{aligned}
\tag{3.3}
$$

If there is a sinusoidal signal in the data, of frequency ω_o, the factors *y(t)* and $e^{(-i\omega t_j)}$ will be in phase at $\omega = \omega_o$ and make a large contribution to the sums in Eq. (3.3), while for other values of ω the terms will be randomly positive and negative, and mostly cancel each other out to produce a small sum.

A positive quality of the periodogram is its behaviour with increasing data samples. If our data sample of N points is made up of a real signal sitting on top of noise (or observational errors), it can be described as

$$y(t_j) = y_o \sin(\omega_o t_i + \phi) + R(t_i) \tag{3.4}$$

and it can be shown that the expected value of the power due to the signal (at the signal frequency) is

$$P_y = N\,(y_o/2)^2 \tag{3.5}$$

and that due to observational errors is the variance

$$P_R = \langle R^2 \rangle = \sigma_o^2 \tag{3.6}$$

The signal-to-noise ratio is then given by

$$S/N = \frac{P_y}{P_R} = N\left(\frac{y_o}{2\sigma_o}\right)^2 \tag{3.7}$$

which means the S/N will increase proportionally to the number of data points N (Scargle 1982).

A new periodogram with these same useful properties, but more resistant to uneven sampling, is given by Scargle (1982):

$$P_y(\omega) = \frac{1}{2}\left[\frac{\left[\sum_j y_j \cos\omega\left(t_j-\tau\right)\right]^2}{\sum_j \cos^2\omega\left(t_j-\tau\right)} + \frac{\left[\sum_j y_j \sin\omega\left(t_j-\tau\right)\right]^2}{\sum_j \sin^2\omega\left(t_j-\tau\right)}\right] \tag{3.8}$$

where τ is defined by

$$\tan\left(2\omega\tau\right) = \frac{\sum_j \sin 2\omega t_j}{\sum_j \cos 2\omega t_j} \tag{3.9}$$

This is the Lomb-Scargle periodogram, or power spectrum.

Once a periodogram has been constructed, we are left with the questions: *which of these peaks are real?, and how sure can we be they are real?* Scargle (1982) proposes the normalisation of the periodogram to the variance, σ^2, of the *signal-free* data, where σ is the standard deviation; as such, Gaussian noise will have a power of 1[7]. Furthermore, the probability function *Prob* associated with the periodogram

[7]It is clear that most of the data from observations made by *RXTE* during the survey contain contributions from a number of sources in the field of view, and we shouldn't use their variance in our calculations. However, after analysing a large number of observations, it was found that the average power within the calculated power spectra was essentially 1 (likely due to our low S/N), which justifies our use of the light curve variance (including all pulsar signals) instead of the

will be exponentially distributed[8], and it can be shown that the probability that a periodic signal with power of Z is due to noise is

$$\mathrm{FAP} = 1 - \left(1 - e^{-Z}\right)^{M} \tag{3.10}$$

which is the False Alarm Probability, with M being the number of independent frequencies, which we define as

$$M = 2 \times n_f \times \Delta f \times \tau \tag{3.11}$$

where n_f is the number of scanned frequencies, Δf is the frequency interval used when calculating the periodogram, and τ is the duration of the observation.

A more useful number may be the *significance* of a detection, or how sure we are that it is real; this is simply 1 − FAP, expressed as a percentage. This is the value that will be used in the present work to estimate the importance and believability of a signal, and is given by

$$Sig(\%) = 100 \times \left(1 - e^{-z}\right)^{M} \tag{3.12}$$

In a DFT, the amplitude A of the modulation is related to the power P_{DFT} in the periodogram through

$$A = 2\sqrt{P_{DFT}} \tag{3.13}$$

Due to the differences between Eqs. (3.3) and (3.8), the form of Eq. (3.13) for

variance of the noise, which would have been difficult to obtain.

[8]It will be of the form $Prob = e^{-Z}$, which is the probability of detecting a peak in the periodogram above a certain power, Z.

the Lomb-Scargle case will be

$$A = 2\sqrt{\frac{P_{LS}\,\sigma^2}{N}} \tag{3.14}$$

where N is the number of data points.

If the signal we detect has any harmonics, its total power is divided between the harmonic peaks in the power spectrum. Using only the fundamental to estimate the amplitude of the signal's pulsations could then severely underestimate it if there were considerable power in any of the harmonics (which is often the case). If we know the amplitude of all the harmonics, it can be shown that the total amplitude of the signal will be given by

$$A_{total} = \sqrt{\sum_i A_i^2} \tag{3.15}$$

From the error in the angular frequency detected at a certain power in the Lomb-Scargle periodogram (Horne and Baliunas 1986), we derive the error on the period to be

$$dP = \frac{3}{4}\left(\frac{P^2\,\sigma_n}{\sqrt{N}\,\tau\,A}\right) \tag{3.16}$$

where A is the Lomb-Scargle amplitude defined in Eq. (3.15), and σ_n is the standard deviation of the noise, although we use the standard deviation of the actual data[9].

The Lomb-Scargle periodogram is rather slow when implemented on a computer, requiring of order 10^2N^2 to analyse N data points. A FORTRAN routine using a fast algorithm was translated into the IDL language and used to compute the periodograms. The algorithm follows the prescription of Press and Rybicki (1989),

[9]See footnote on page 89 for an explanation of why this is done.

in which the data is "extirpolated" onto an evenly sampled grid, after which Eq. (3.8) can be solved using FFTs on some of its constituents. We direct the reader to the aforementioned paper for full details. Suffice to say that this method decreases the number of operations to $10^2 N \log N$, while returning essentially the same results as the slow implementation. On our computer, analysis of a 7 ks light curve (7×10^5 data points) took ~ 35 s.

3.4 Survey overview

The initial observations of the SMC with *RXTE* began in 1997. Conducted by James Lochner of NASA's Goddard Space Flight Center, the first observation took place in November of that year when an outburst detected by the ASM was thought to be SMC X-3. It was AO2, and only SMC X-1, 2 and 3 were known. From these initial observations it soon became apparent that there were more X-ray pulsars in the SMC, many more. The observations carried out within the next year brought about the discovery of 5 new systems: SXPs 46.6, 59.0, 74.7, 91.1 and 169; SXP452 also appears in one of the observations, but was not recognised as a new pulsar until further on. Other pulsars were also discovered with *ASCA* and *BeppoSAX*. At present there are 51 known X-ray emitting pulsars in the SMC.

1999 marked the beginning of a coordinated survey of the SMC led by Robin Corbet (also of GSFC) using the PCA. The PCA's 2° field of view provides coverage of a wide area of the SMC, which allows many pulsars to be monitored with just one pointing. A number of different pointing positions have been used throughout the years and are given in Table 3.3 (see also Fig. 3.10); some of the less frequent ones (due to trials and *RXTE* misspointings) never received a name. The most frequently observed is Position 1 (later renamed to A), which has been the main pointing position since AO4, except during AO6 and AO7, when Position 5 was the main target. In total, the collected data spans ~ 420 weeks, a little over 8 years.

The survey has gone through various phases characterised by different observing positions and/or observing modalities. Phases 1 – 4 have already been described in Laycock (2002) and Laycock et al. (2005) but they are outlined here again, together

Table 3.3:
RXTE's SMC survey pointing positions

	RA (°)	Dec (°)
1a	13.03250	-72.428703
1b	12.76669	-72.228897
1c (SMC X-3)	13.72830	-72.444702
1/A	13.47100	-72.445000
2	16.25000	-72.100000
3	18.75000	-73.100000
4	12.68600	-73.267998
5	12.50000	-73.100000
B	16.25000	-72.106003
C	18.75000	-73.416603
D	12.50000	-73.099998
X	16.25000	-72.099999
SMC X-2	13.63890	-73.684502
–	12.44400	-72.759500
–	12.57000	-72.180000
–	12.70000	-72.840000
–	13.04500	-72.337997
–	13.11880	-72.336998
–	13.59000	-72.980000
–	13.82000	-72.480000
–	13.82000	-72.980000
–	15.27000	-72.240000

with the two latest phases not included in previous studies.

Phase 1 AO2 – AO3: These observations used Positions 1a, 1b and 1c and are described in Lochner et al. (1999a, b). Only 30 observations were carried out, their main purpose being to monitor the 5 newly discovered pulsars in those regions.

Phase 2 AO4: Positions 1 – 4 were defined; Position 1 overlaps most of Positions 1a – c and contained the new pulsars, Positions 2 and 4 cover the rest of the bar of the SMC while Position 3 covers the area of the wing containing SMC X-1. A continued survey began at this point in time, with ~ 3 ks observations being

made once a week, mostly of Position 1, with some occasional looks at the other positions.

Phase 3 AO5 – AO6: Only Position 5 was monitored, and was done weekly so as not to create gaps in the data; the majority of the most active systems located in Position 1 also fell within the field of view of Position 5. Time alloted for the project was increased to an average of ~ 5 ks per observation, thus providing better sensitivity to longer period pulsations.

Phase 4 AO7 – AO9: Weekly monitoring returned to Position 1, now renamed Position A, with additional observations of the other positions (B, C and D) being made once a month. These monthly pointings were ~ 15 ks, while the weekly ones were increased to $\sim 6-7$ ks.

Phase 5 AO10: The time available for the monthly observations of alternate positions was invested into increasing the length of the weekly observations of Position A to ~ 10 ks, this being the only monitored position.

Phase 6 AO11: Having mainly monitored the central bar of the SMC, it was decided to move to another location at the northeastern tip of the bar, near position B. This new location, Position X, will be monitored for ~ 10 ks weekly.

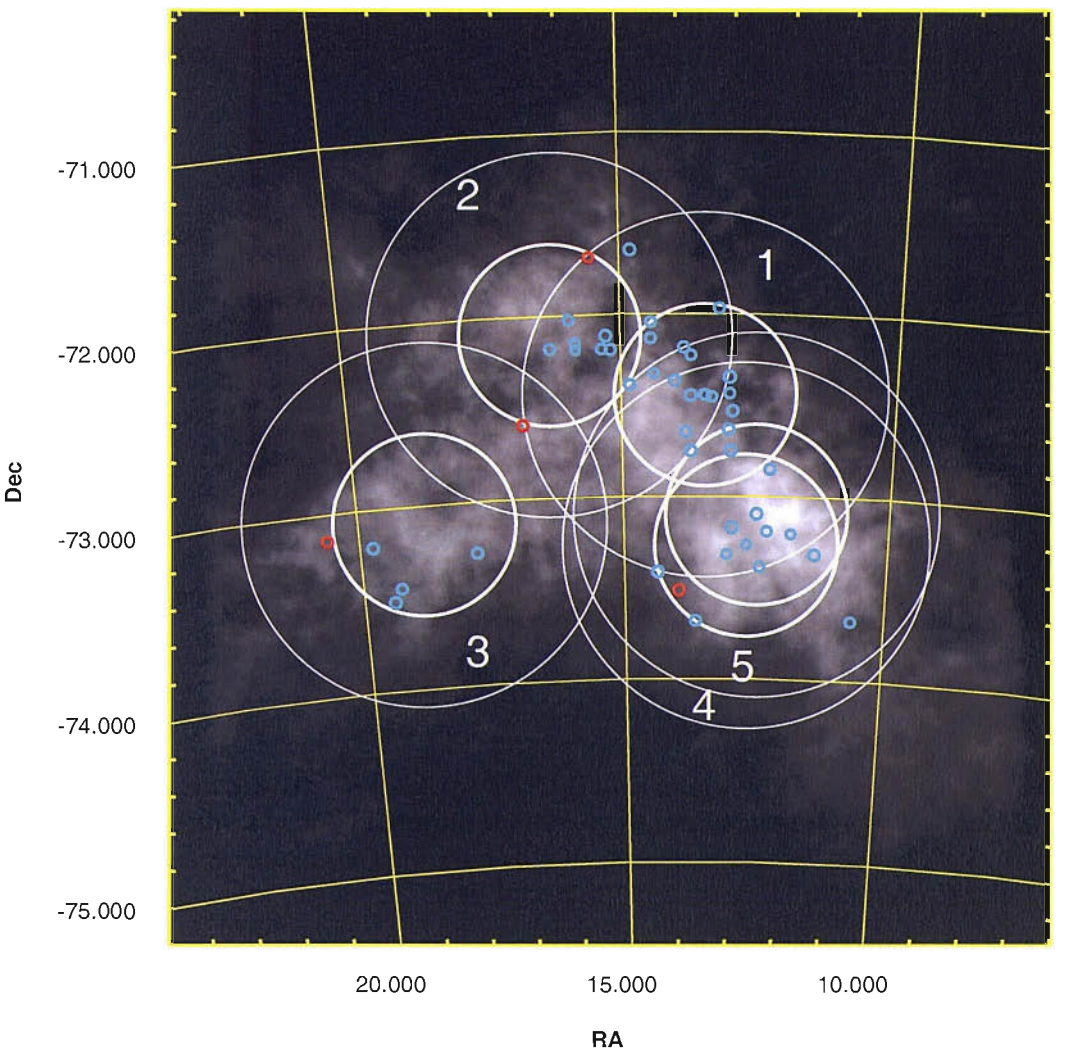

Figure 3.10: Map of the SMC H I distribution with the 5 main pointing positions of *RXTE* during the survey shown as numbered white circles. For each pointing, the inner circle has a diameter of 1°, the outer of 2°. Pulsar positions are marked by small blue and red circles. H I data from Stanimirovic et al. (1999).

Chapter 4

RXTE's Survey of the SMC

One tree falling in a forest makes more noise than one thousand slowly growing.

—Japanese Proverb

There is a theory which states that if ever anyone discovers what the universe is for and why it is here, it will instantly disappear and be replaced by something even more bizarre and inexplicable.
There is another which states that this has already happened.

—The Hitchhiker's Guide to the Galaxy

Data reduction and analysis have been discussed in Chapter 3, the following sections will present the individual light curves obtained for each of the SMC pulsars for which sufficient coverage is available; also presented are the results of orbital calculations for these systems and discussions on pulse profiles and their evolution. The coordinates for those systems with a known optical counterpart were obtained from DSS survey data (McBride 2005, private communication), while the X-ray position, when available, was used for the rest (see Coe et al. (2005) and references therein for further information). Table 4.1 contains all the pertinent information.

Table 4.1

X-ray binary systems in the SMC

Object	P_s (s)	RA	dec	T_P (MJD)	P_{orb} (days)	X_{od}	$\dot{P}$ ($s\,s^{-1}$)	L_x ($erg\,s^{-1}$)	B (G)
SXP0.09	0.087	00 42 35.0	-73 40 30.0	–	–	–	–	–	–
SXP0.72	0.716	01 17 05.2	-73 26 36.0	–	–	–	–	–	–
SXP0.92	0.92	00 45 35.0	-73 19 02.0	52119.9 ± 1.3	42.7 ± 0.1	0.054	–	–	–
SXP2.16	2.165	01 19 00	-73 12 27	–	–	–	–	–	–
SXP2.37	2.374	00 54 34.0	-73 41 03.0	–	–	–	–	–	–
SXP2.76	2.763	00 59 11.7	-71 38 48.0	52272.0 ± 1.0	42.3 ± 0.1	0.098	–	–	–
SXP3.34	3.34	01 05 02.0	-72 11 00.0	52300.8 ± 1.3	26.80 ± 0.04	0.053	–	–	–
SXP4.78	4.782	00 52 06.6	-72 20 44	52228.5 ± 1.5	50.18 ± 0.14	0.102	–	–	–
SXP6.85	6.848	01 03 13	-72 11 32	52196.9 ± 5.7	114.3 ± 0.5	0.500	–	–	–
SXP7.78	7.780	00 52 06	-72 26 06	52250.9 ± 1.4	44.92 ± 0.06	0.484	–	–	–
SXP8.02	8.020	01 00 41.8	-72 11 36	–	–	–	–	–	–
SXP8.80	8.880	00 51 52.0	-72 31 51.7	52279.1 ± 1.4	28.44 ± 0.04	0.118	–	–	–
SXP9.13	9.130	00 49 13.6	-73 11 39	52112.3 ± 1.2	38.40 ± 0.02	0.039	–	–	–
SXP15.3	15.30	00 52 14	-73 19 19	52244.4 ± 2.4	79.6 ± 0.4	0.118	6.74×10^{-9}	8.6×10^{37}	1.5×10^{13}
SXP16.6	16.52	–	–	52271.4 ± 1.7	33.69 ± 0.05	0.134	–	–	–
SXP18.3	18.37	00 53 53	-72 26 42	52274.8 ± 0.5	17.75 ± 0.02	0.032	–	–	–
SXP22.1	22.07	01 17 40.5	-73 30 52.0	–	–	–	–	–	–
SXP31.0	31.01	01 11 09.0	-73 16 46.0	51150.2 ± 0.5	27.5 ± 0.3	0.000	5.3×10^{-8}	1.3×10^{38}	4.3×10^{13}

...Continued on next page

Object	P_s (s)	RA	dec	T_P (MJD)	P_{orb} (days)	X_{od}	$\dot{P}$ ($s\,s^{-1}$)	L_x ($erg\,s^{-1}$)	B (G)
SXP34.1	34.08	00 55 26.9	-72 10 59.9	52258.5 ± 2.7	53.3 ± 0.1	0.267	–	–	–
SXP46.6	46.59	00 53 58.5	-72 26 35.0	52156.6 ± 1.4	137.36 ± 0.35	0.909	7.6×10^{-10}	7.2×10^{35}	5.0×10^{12}
SXP51.0	51.00	–	–	52267.1 ± 1.6	51.76 ± 0.13	0.148	–	–	–
SXP59.0	58.86	00 54 56.6	-72 26 50	52187.5 ± 1.2	122.40 ± 0.42	0.417	5.3×10^{-10}	3.0×10^{36}	1.4×10^{13}
SXP74.7	74.70	00 49 04	-72 50 54	52295.8 ± 1.6	31.94 ± 0.05	0.068	–	–	–
SXP82.4	82.40	00 52 09	-72 38 03	52293.2 ± 1.6	52.63 ± 0.11	0.321	–	–	–
SXP89.0	89.00	–	–	52233.8 ± 6.5	92.8 ± 0.5	0.194	–	–	–
SXP91.1	91.10	00 54 55	-72 13 38	52123.8 ± 3.7	121.95 ± 0.56	0.474	1.8×10^{-8}	3.6×10^{36}	2.5×10^{13}
SXP95.2	95.20	00 52 00	-72 45 00	52240.1 ± 5.9	84.0 ± 0.4	0.147	–	–	–
SXP101	101.40	00 57 26.8	-73 25 02	52111.4 ± 1.2	22.95 ± 0.03	0.155	–	–	–
SXP138	138.00	00 53 23.8	-72 27 15.0	52215.1 ± 6.6	132.6 ± 1.0	0.190	–	–	–
SXP140	140.99	00 56 05.7	-72 22 00.0	52221.5 ± 1.9	61.5 ± 0.2	0.200	–	–	–
SXP144	144.00	–	–	52249.2 ± 3.0	59.49 ± 0.09	0.632	-1.6×10^{-8}	1.1×10^{36}	2.4×10^{13}
SXP152	152.10	00 57 49	-72 07 59	52227.7 ± 3.2	105.7 ± 0.6	0.579	–	–	–
SXP169	167.35	00 52 54.0	-71 58 08.0	52241.1 ± 3.4	68.59 ± 0.14	0.500	2.3×10^{-8}	1.1×10^{36}	2.8×10^{13}
SXP172	172.40	00 51 52	-73 10 35	52219.6 ± 3.4	67.20 ± 0.23	0.641	1.5×10^{-8}	6.9×10^{35}	2.3×10^{13}
SXP202	202.00	00 59 20.8	-72 23 17	52192.0 ± 4.2	140.06 ± 0.92	0.312	–	–	–
SXP264	263.60	00 47 23.7	-73 12 25	52026.6 ± 3.3	109.8 ± 0.8	0.692	–	–	–
SXP280	280.40	00 57 48.2	-72 02 40	52305.4 ± 3.1	103.5 ± 0.6	0.556	–	–	–
SXP293	293.00	00 50 00	-73 06 00	52264.5 ± 5.9	117.65 ± 0.71	0.458	–	–	–
SXP304	304.49	01 01 01.7	-72 07 02	52213.75 ± 3.48	69.59 ± 0.22	0.214	–	–	–

...Continued on next page

Object	P_s (s)	RA	dec	T_P (MJD)	P_{orb} (days)	X_{od}	$\dot{P}$ ($s\,s^{-1}$)	L_x ($erg\,s^{-1}$)	B (G)
SXP323	321.20	00 50 44.8	-73 16 06.0	52245.8 ± 3.6	119.19 ± 0.64	0.545	–	–	–
SXP348	344.75	01 03 13.0	-72 09 18.0	52228.4 ± 3.7	124.2 ± 0.9	0.438	1.7×10^{-7}	1.5×10^{36}	7.7×10^{13}
SXP452	452.01	01 01 19.5	-72 11 22	52129.0 ± 6.0	122.9 ± 1.0	0.444	–	–	–
SXP504	503.50	00 54 55.6	-72 45 10.0	52175.0 ± 13.0	259.7 ± 3.3	1.182	–	–	–
SXP565	564.83	00 57 36.2	-72 19 34.0	52229.7 ± 4.2	84.5 ± 0.4	0.458	–	–	–
SXP701	696.37	00 55 17.9	-72 38 53.0	52248.3 ± 2.4	79.9 ± 0.3	0.000	–	–	–
SXP756	755.50	00 49 42.42	-73 23 15.9	51805.1 ± 11.8	393.7 ± 3.1	1.000	–	–	–
SXP1323	1323.20	01 03 37.5	-72 01 33.2	52765.0 ± 10.0	323 ± 11	0.857	–	–	–

4.1 Light curves and orbital periods

4.1.1 SXP0.92

PSR J0045−7319
RA 00 45 35, dec −73 19 02

History: First discovered as a radio pulsar by Ables et al. (1987) with a period of 0.926499 ± 0.000003 s using the Parkes 64 m radio telescope. Kaspi et al. (1993) observed Doppler shifts in the pulse period which where consistent with a 51 d binary orbit with a companion star having mass $> 4\,M_{\odot}$. Optical observations in that direction detected a B type star with a mass $\sim 10 M_{\odot}$. Further Optical observations of the field revealed a 16^{th} magnitude, $11 M_{\odot}$, B1 main-sequence star, to be the likely companion (Bell 1994).

Survey Results: SXP0.92 received ~ 2 years of uninterrupted coverage during AO5 and AO6, during which time it was only detected once above 99% significance on February 28^{th}, 2002 with $F_{\text{x}_{\text{pul}}} \approx 0.5$ counts $\text{PCU}^{-1}\,\text{s}^{-1}$. If we lower the detection threshold to $Sig_{\text{min}} = 95\%$ we see another detection. This source shows a weak modulation at ~ 43 d; if this is the orbital period, then the ephemeris is MJD $52119.9 \pm 1.3 + \text{n} \times 42.7 \pm 0.1$ d (see Fig. 4.1).

4.1.2 SXP2.16

XTE SMC2165 RA 01 19 00, dec −73 12 27

History: Discovered during the course of this survey by Corbet et al. (2003a) at 2.1652 ± 0.0001 s.

Survey Results: Due to its position near SMC X-1 it has only been within the field of view on 3 occasions. It was detected at a high significance on the 3^{rd} observation, which led to its discovery.

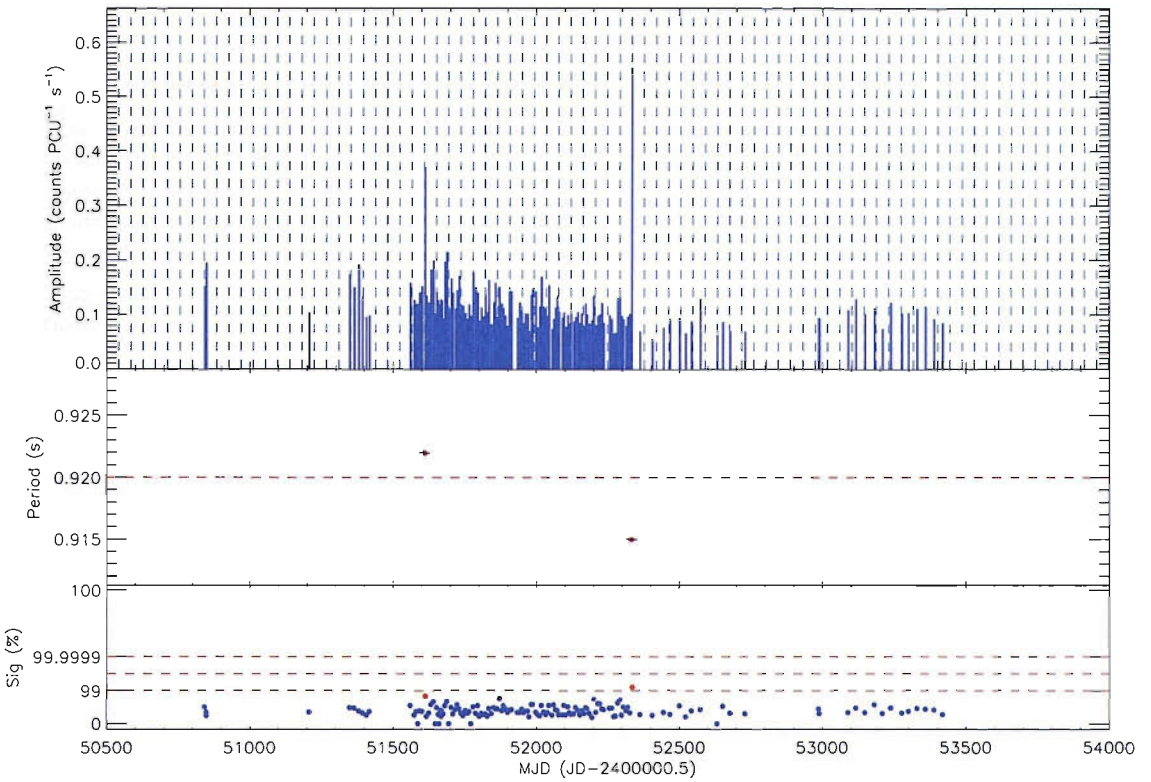

(a) X-ray amplitude light curve.

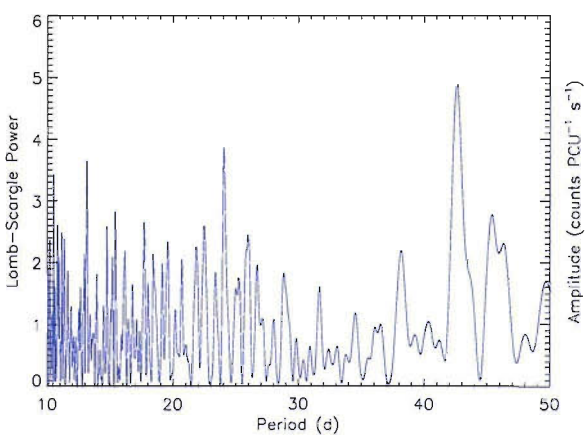

(b) Lomb-Scargle power spectrum.

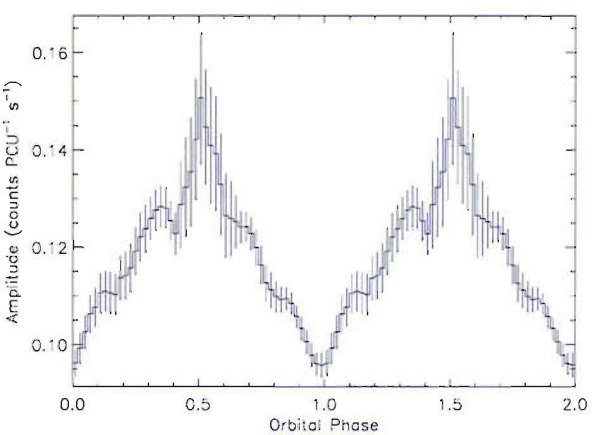

(c) Orbital profile folded at 42.7 d.

Figure 4.1: SXP0.92.

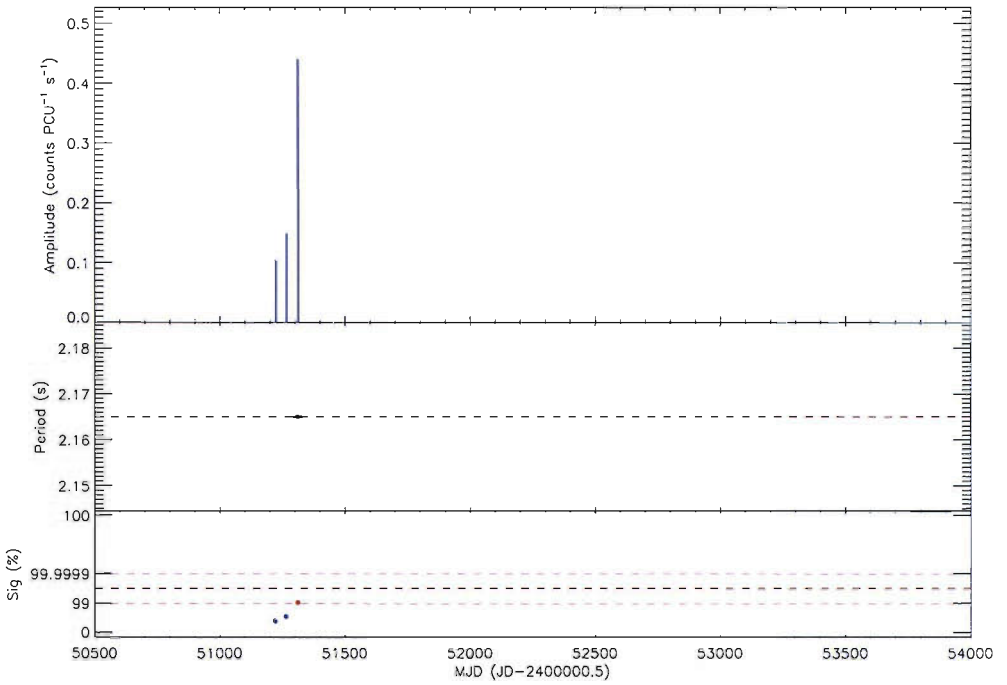

Figure 4.2: X-ray amplitude light curve of SXP2.16.

4.1.3 SXP2.37

SMC X-2
RA 00 54 34, dec −73 41 03

History: SMC X-2 was discovered in *SAS-3* observations of the SMC carried out by (Clark et al. 1978). Further outbursts were also observed by *HEAO 1* and *ROSAT*, but no pulsations were detected until it was observed in the present survey by *RXTE* during a long outburst lasting from January through to May, 2000 (Corbet et al. 2001; Laycock 2002).

Survey Results: After the aforementioned outburst, SMC X-2 was only detected on 3 further occasions, but at a much lower significance, with $F_{x_{pul}} < 1$ counts PCU^{-1} s^{-1}. When lowering the detection threshold to 90% significance 4 other possible detections appear. Lomb-Scargle analysis of this light curve, from the end of the major outburst onwards, reveals a weak period at $\sim$21.5 d. The ephemeris of this period would be MJD 52536.0 $\pm$ 0.7 + n $\times$ 21.54 $\pm$ 0.03 d, and it is worth noting that during the giant outburst the luminosity peaked on, or very near to, dates predicted by

this ephemeris[1]. If this is indeed the orbital period, the folded light curve suggests SMC X-2 could be a partially-eclipsing system.

4.1.4 SXP2.76

RX J0059.2−7138
RA 00 59 11.7, dec −71 38 48

History: First reported by Hughes (1994) from a *ROSAT* observation showing 2.7632 s pulsations that varied greatly with energy. In the low-energy band of the *ROSAT* PSPC (0.07 − 0.4 keV) the source appears almost unpulsed while in the high-energy band (1.0 − 2.4 keV) the flux is $\sim 50\%$ pulsed. Its companion was confirmed as a 14^{th} magnitude Be star by Southwell and Charles (1996).

Survey Results: This source is near the edge of the field of view of Position 1/A so we would expect to detect only the brighter outbursts. If the detection threshold is set to $Sig_{\min} = 99\%$ only 3 detections, belonging to 2 outbursts, are seen. Lowering the threshold to $Sig_{\min} = 95\%$ brings out three further outbursts, which are consistent with an ephemeris of MJD $52272 \pm 1 + \text{n} \times 42.3 \pm 0.1$ d. Sensitivity to this source will be increased during AO11 as SXP2.76 lies only $\sim 0.5°$ away from the centre of Position X.

[1]It should be mentioned that there is a peak in the power spectrum at 42.92 ± 0.17 d, which would make our proposed 21.53 d period the harmonic. Given the weakness of both peaks it is not clear if this is the case or not. We must await further outbursts to settle the matter.

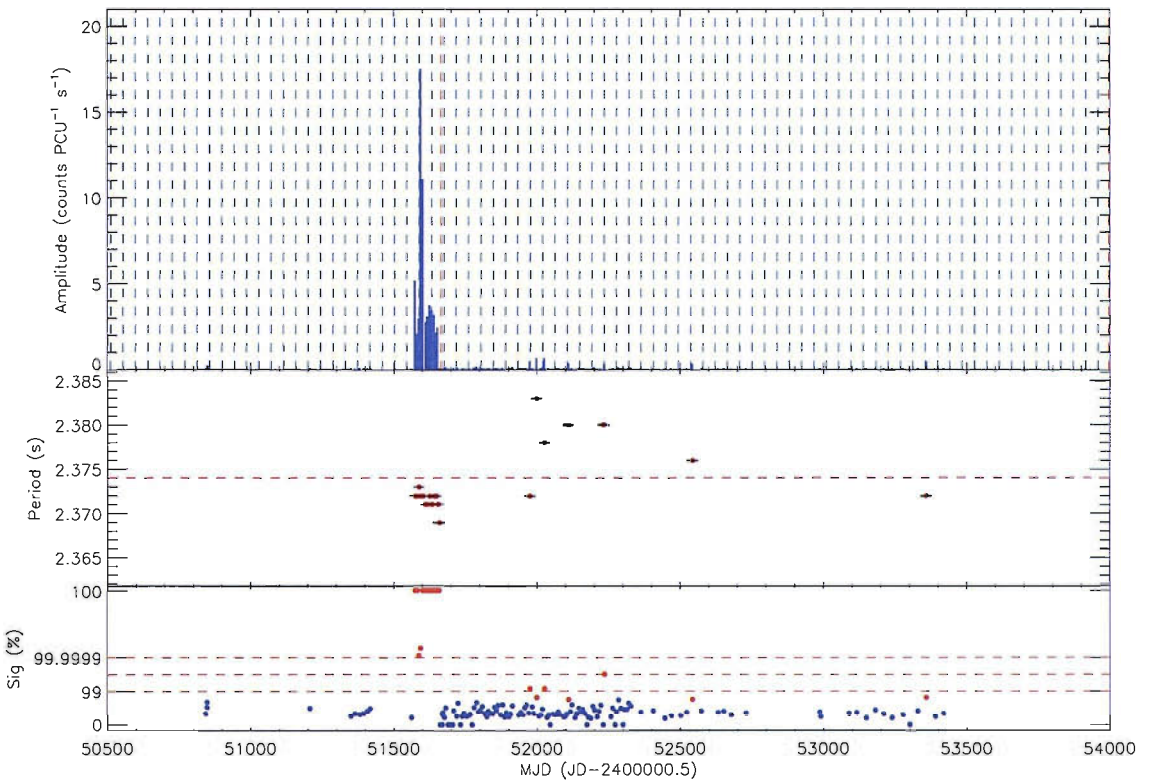

(a) X-ray amplitude light curve. Lomb-Scargle analysis was carried out on the data between the vertical, dashed, red lines. For clarity, only every other ephemeris line has been plotted.

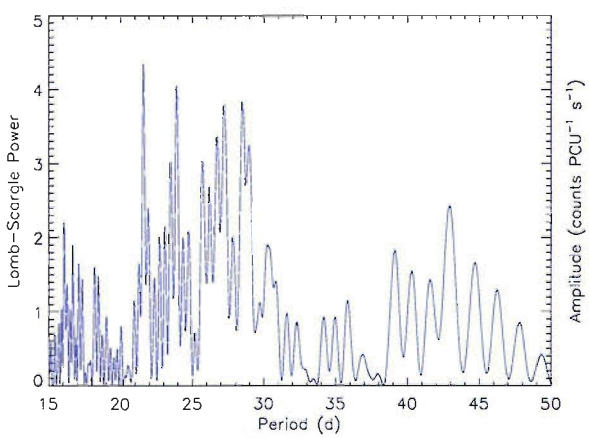

(b) Lomb-Scargle power spectrum.

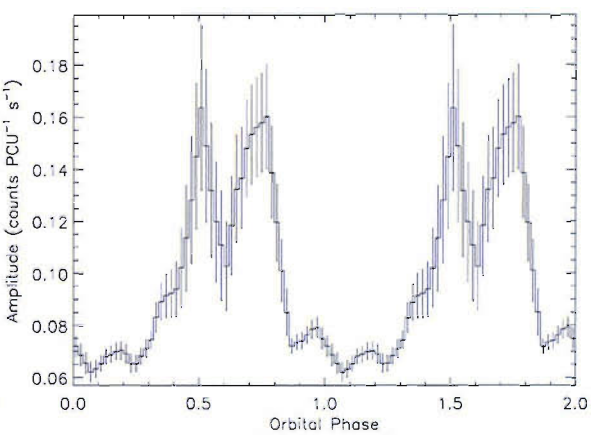

(c) Orbital profile folded at 21.54 d.

Figure 4.3: SXP2.37.

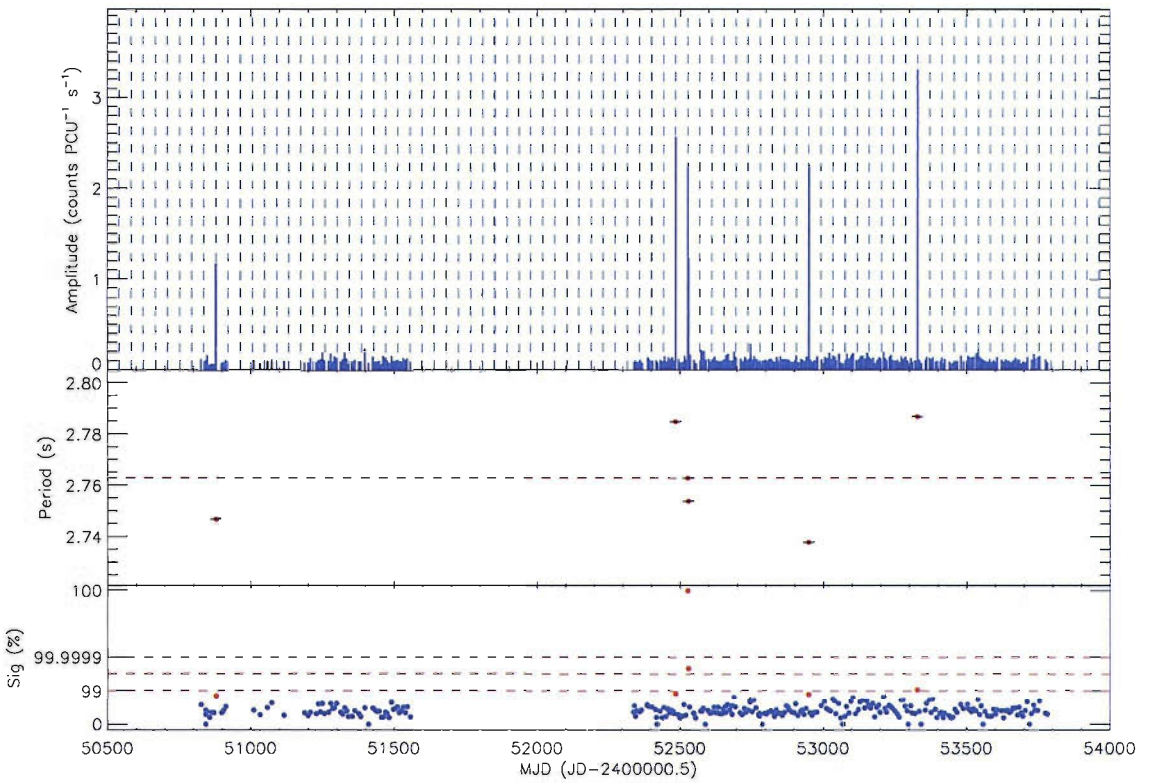

(a) X-ray amplitude light curve.

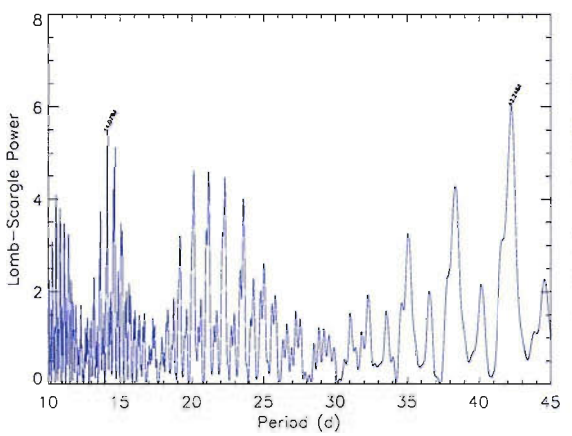

(b) Lomb-Scargle power spectrum.

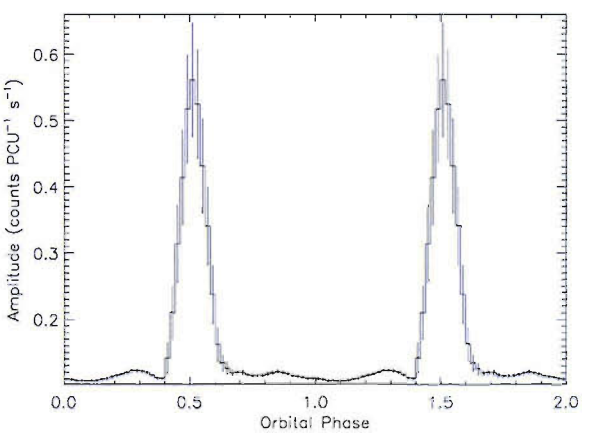

(c) Orbital profile folded at 42.3 d.

Figure 4.4: SXP2.76.

4.1.5 SXP3.34

AX J0105−722, RX J0105.3−7210
RA 01 05 02, dec −72 11 00

History: Was reported as an *ASCA* source with 3.34300 ± 0.00003 spulsations by Yokogawa and Koyama (1998c). Its optical counterpart is proposed to be [MA93] 1506 (Coe et al. 2005), who also find an 11.09 d modulation in MACHO data. Although this could be the orbital period of the system (as it falls within the expected range on the Corbet diagram), Schmidtke and Cowley (2005a) report the find of a strong 1.099 d period in MACHO data and that the 11.09 d value is an alias of this main period. They attribute the modulation to non-radial pulsation in the Be star.

Survey Results: There have been no significant detections of this pulsar during this survey, although it should be noted that it was outside the field of view during AO5 and AO6 (March 2000 − February 2002). Using a lower threshold of $Sig_{\mathrm{min}} = 90\%$ brings out four possible detections which are consistent with a ~ 27 d period. SXP3.34 is also near the edge of Position 1/A, but close to the centre of Position X. *RXTE* will be more sensitive to this source during AO11 which might provide some unambiguous detections of this pulsar. If the aforementioned period is due to orbital motion, the ephemeris is MJD $52300.8 \pm 1.3 + \mathrm{n} \times 26.80 \pm 0.04$ d.

4.1.6 SXP4.78

XTE J0052−723
RA 00 52 06.6, dec −72 20 44

History: Was discovered by the present survey in late December 2000 and reported in Laycock et al. (2003b), where [MA93] 537 was proposed as the optical counterpart. Another possible counterpart is suggested in Coe et al. (2005) as the star AzV129 is found to have a 23.9 ± 0.1 d period in both MACHO colours, which would agree with the expected orbital period inferred from the Corbet diagram.

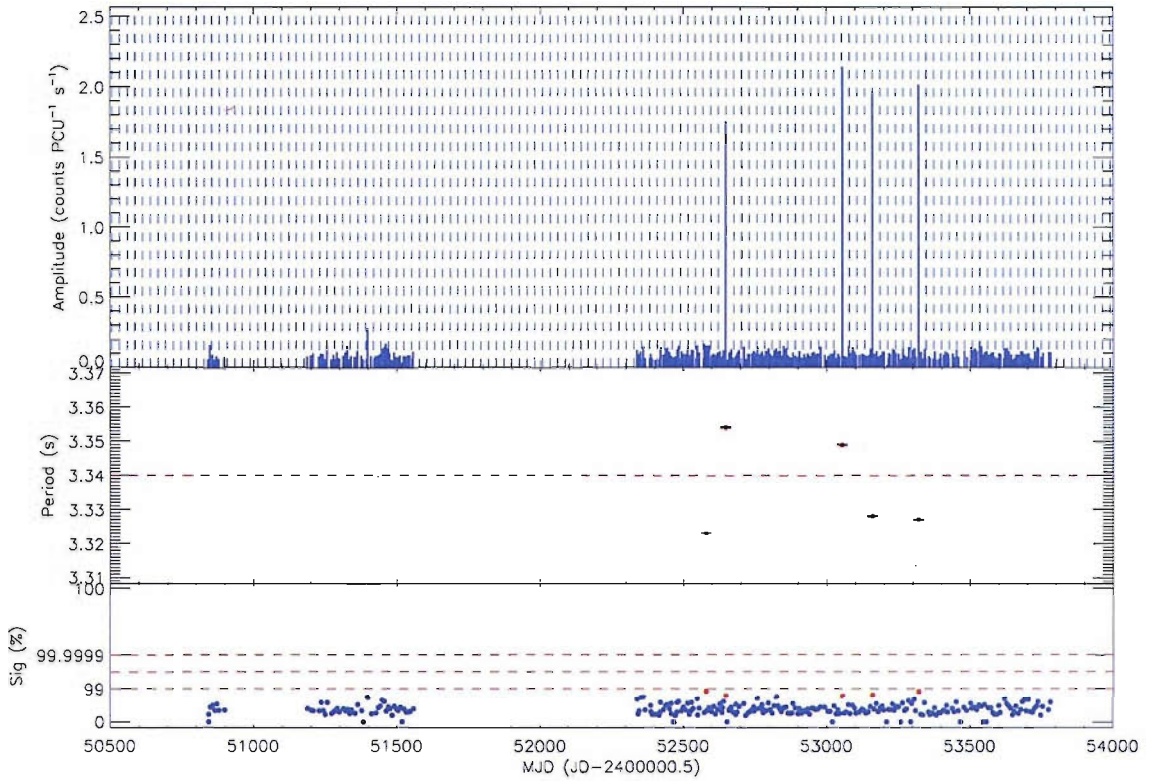

(a) X-ray amplitude light curve.

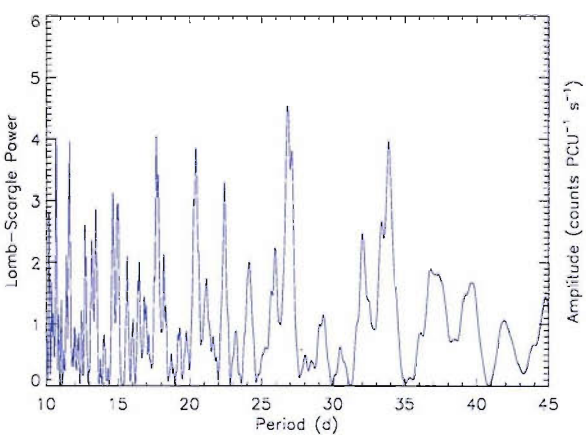

(b) Lomb-Scargle power spectrum.

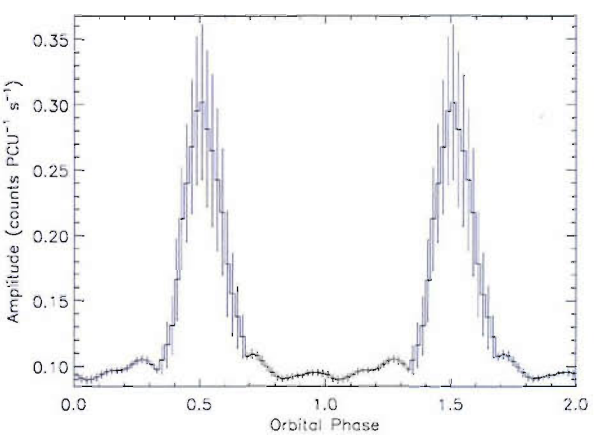

(c) Orbital profile folded at 26.80 d.

Figure 4.5: SXP3.34.

Survey Results: SXP4.78 was detected on one occasion after its initial outburst in March 2003 at a much weaker $F_{x_{pul}} \simeq 0.8\,\mathrm{counts\,PCU^{-1}\,s^{-1}}$. It then underwent a relatively bright (peaking at $\sim 1.2\,\mathrm{counts\,PCU^{-1}\,s^{-1}}$) outburst in late 2005 that lasted ~ 8 weeks. Despite the long outburst, no orbital modulation is apparent in the spin period data, which could imply that either we are viewing the system at small inclination angle and the accretion torques during the outburst were negligible, or that we are viewing the system at some intermediate angle and the accretion torques are counteracting the Doppler effect. Lomb-Scargle analysis of the flux outside of the 2 main outbursts, with $Sig_{\mathrm{min}} = 95\%$, finds a weak period at ~ 50 days that nonetheless fits the inter-outburst detections very well with an ephemeris of MJD $52228.5 \pm 1.5 + \mathrm{n} \times 50.18 \pm 0.14\,\mathrm{d}$ (see Fig. 4.6).

A 1 ks observation with *Chandra* was carried out on March 3rd 2006 in an attempt to establish the pulsar's coordinates. Unfortunately, the outburst had ended and no source was detected within the *RXTE* error box provided by Laycock et al. (2003b).

4.1.7 SXP6.85

XTE J0103−728
RA 01 01, dec −72.43

History: First detected in April 2003 with a pulse period of $6.8482 \pm 0.0007\,\mathrm{s}$ (Corbet et al. 2003e).

Survey Results: It has been detected on 3 other occasions at varying fluxes ($F_{x_{pul}} \approx 0.8 - 1.8\,\mathrm{counts\,PCU^{-1}\,s^{-1}}$), but high above the noise level. Lomb-Scargle analysis returns a clear period of $113.9 \pm 0.6\,\mathrm{d}$; this is the minimum time lapse between any two outbursts and probably drives the result. If the detection threshold is brought down to 95% significance, a number of further outbursts appear, which are mostly consistent with the $\sim 114\,\mathrm{d}$ ephemerides. Given its pulse period, from the Corbet diagram one would expect an orbital period of $\sim 114/3 = 38\,\mathrm{d}$. The current ephemeris is MJD $52196.9 \pm 5.7 + \mathrm{n} \times 114.3 \pm 0.5\,\mathrm{d}$ (see Fig. 4.7).

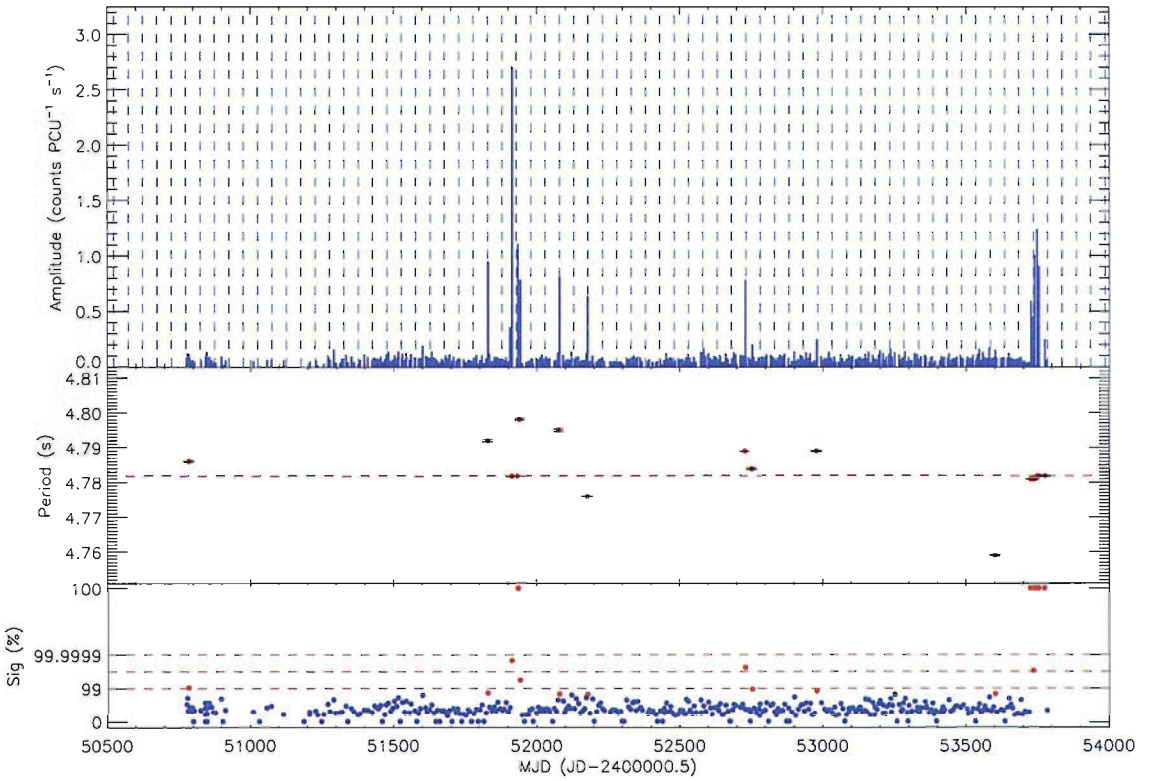

(a) X-ray amplitude light curve.

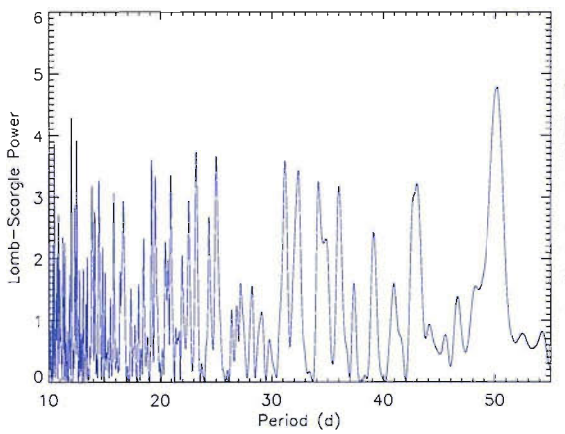

(b) Lomb-Scargle power spectrum.

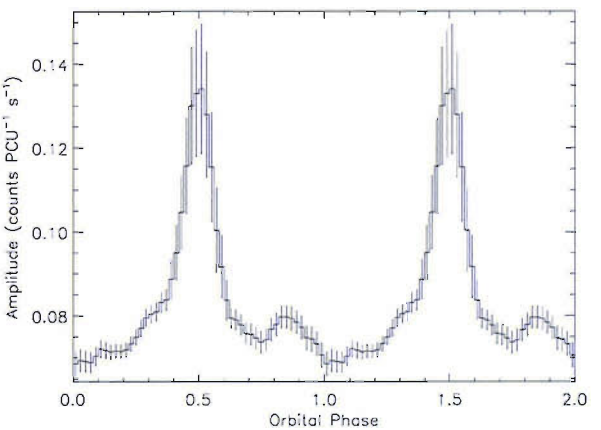

(c) Orbital profile folded at 50.18 d.

Figure 4.6: SXP4.78. Only the data outside the two large outbursts were used in the folded profile of c).

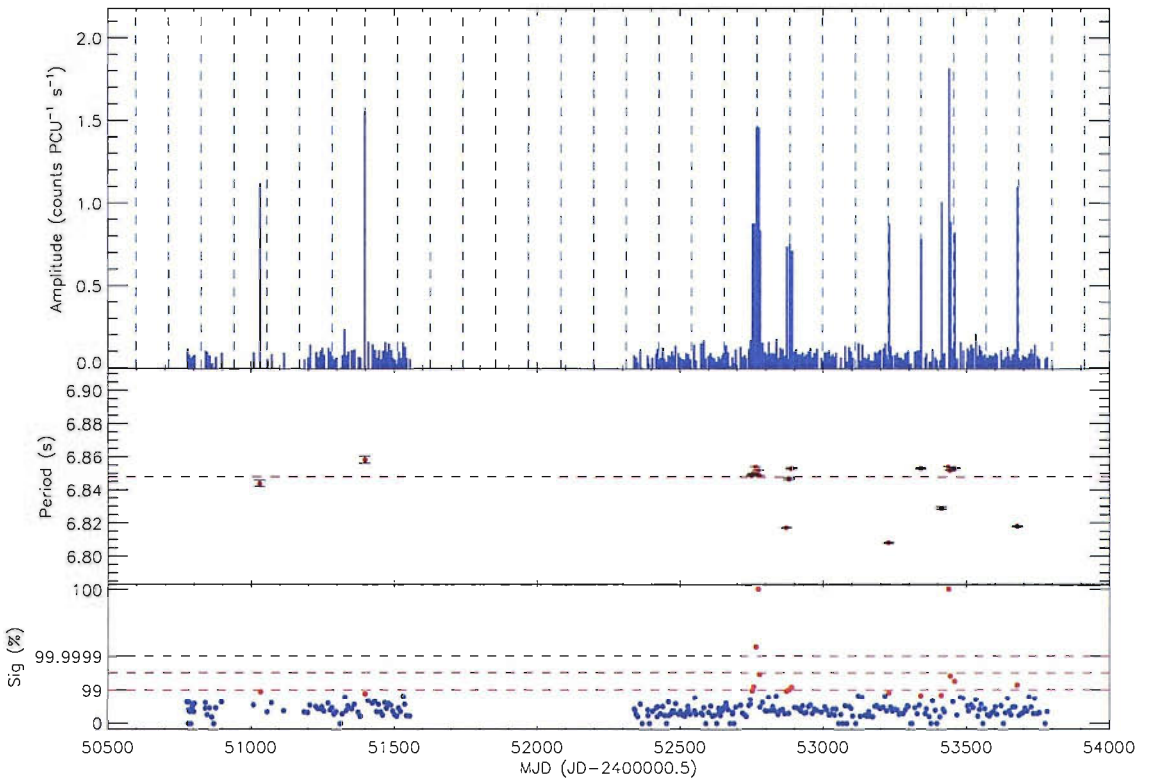

(a) X-ray amplitude light curve.

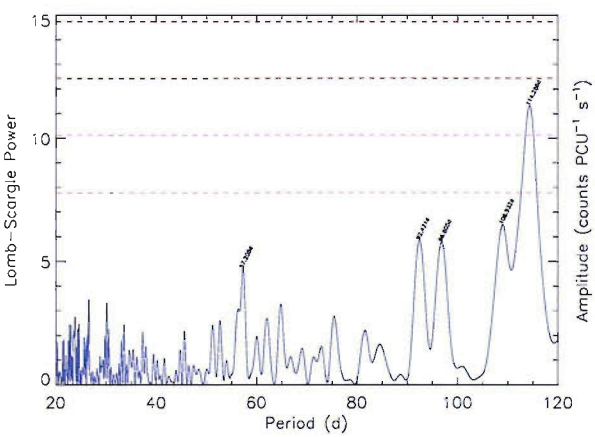

(b) Lomb-Scargle power spectrum.

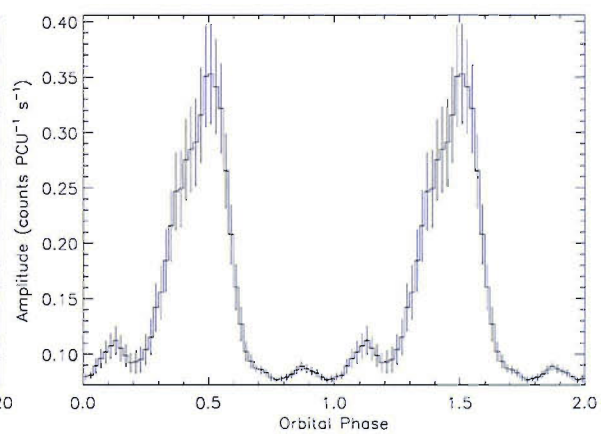

(c) Orbital profile folded at 114.3 d.

Figure 4.7: SXP6.85.

4.1.8 SXP7.78

SMC X-3
RA 00 52 06, dec −72 26 06

History: Originally detected by Clark et al. (1978), it was not identified with the previously detected *RXTE* 7.78 s source until 2004 (Edge et al. 2004a). Corbet et al. (2003b, 2004b) proposed an orbital period from a series of recurrent XX-ray outbursts (in the present survey) of 45.1 ± 0.4 d. An optical modulation in the MACHO red data of 44.6 ± 0.2 d is reported by Coe et al. (2005), while Edge (2005) finds a strong 44.8 ± 0.2 d modulation in the OGLE counterpart, present even when there was no significant X-ray activity.

Survey Results: SMC X-3 would be the archetypal Type Ib source. It has displayed in the past 10 years 3 distinct periods of outbursts ($F_{\mathrm{x_{pul}}} \approx 0.3$ counts PCU^{-1} s^{-1}), lasting $\sim 200-400$ d. Timing analysis of the complete light curve reveals a clear period at 44.92; the ephemeris we derive is MJD $52250.9 \pm 1.4 + \mathrm{n} \times 44.92 \pm 0.06$ d. The folded light curve may show evidence of detections at apastron. During the longer of the outburst seasons (circa MJD 52500) the pulsar appears to show some spin up, about $\dot{P} = 3.7 \times 10^{-10}$ s s^{-1}, implying $L_{\mathrm{x}} = 2.3 \times 10^{37}$ erg s^{-1} ($B = 3.6 \times 10^{12}$ G). However, it is interesting to note that the long term behaviour seems to be that of spin down.

4.1.9 SXP8.02

CXOU J010042.8−721132
RA 01 00 41.8, dec −72 11 36

History: Proposed as the first anomalous X-ray pulsar (AXP) in the SMC by Lamb et al. (2002a), they found the source to have displayed little variability in the past 20 years. It is characterised by a very soft spectrum and low luminosity ($\sim 1.5 \times 10^{35}$ erg s^{-1}). If it is an AXP then we would not expect to find any orbital modulation in its emission.

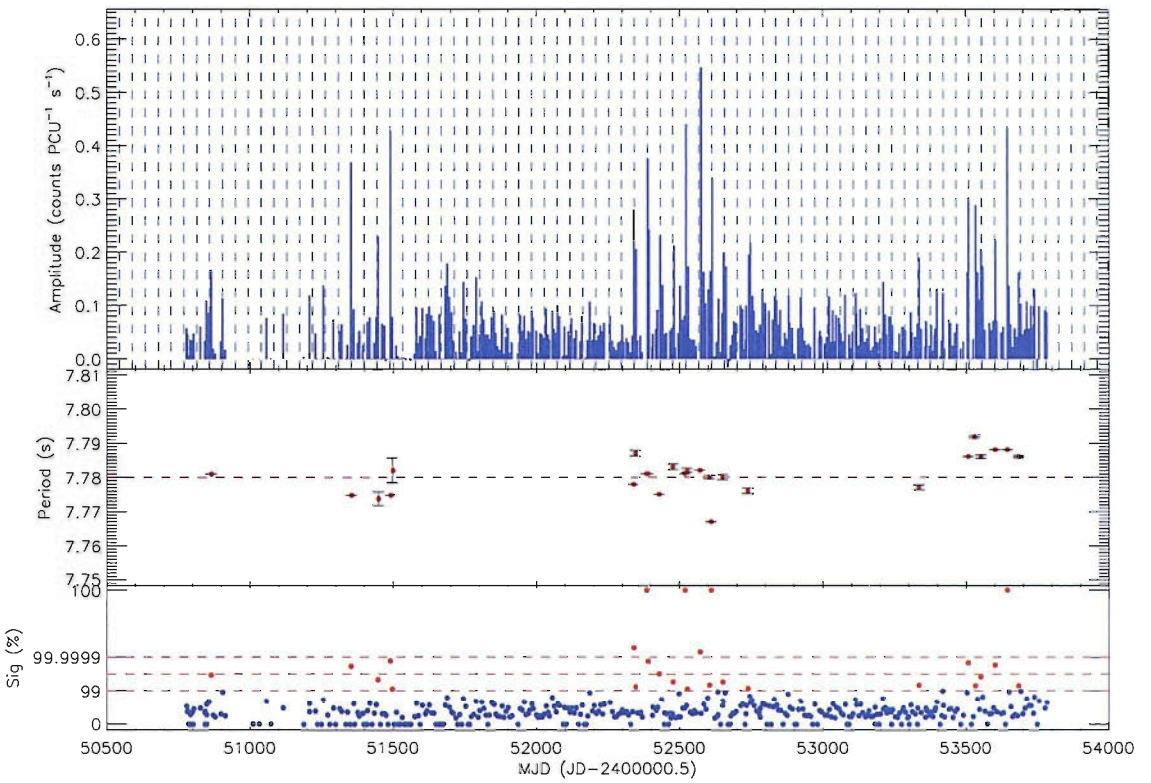

(a) X-ray amplitude light curve.

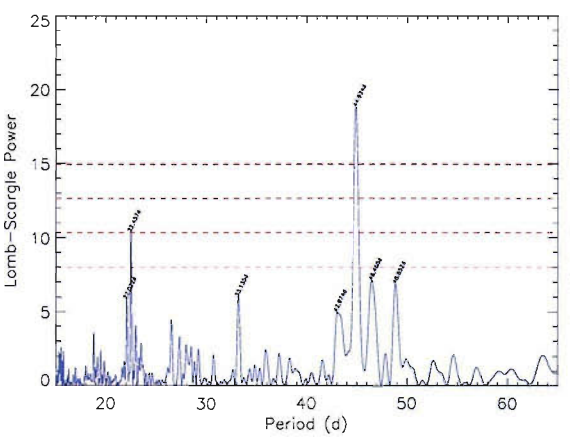

(b) Lomb-Scargle power spectrum.

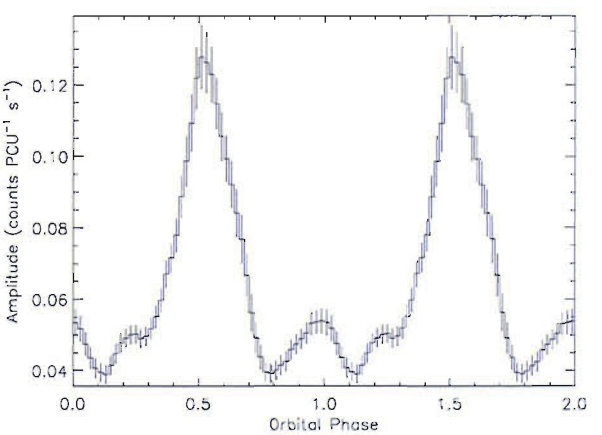

(c) Orbital profile folded at 44.92 d.

Figure 4.8: SXP7.78.

Survey Results: During AO5 and AO6 it was outside the field of view of our observations. Coverage from AO7 onwards has been good and timing analysis of these dates shows a possible periodicity at ~ 23.2 d, which is likely driven by the only two clear detections of SXP8.02, which were separated by that time range. If SXP8.02 is truly an anomalous pulsar, it should show no periodicity in its X-ray emission (see Fig. 4.9).

4.1.10 SXP8.80

RX J0051.8−7231, 1E0050.1−7247, 1WGA J0051.8−7231
RA 00 51 52.0, dec −72 31 51.7

History: Israel et al. (1997) detected this source several times between 1979 and 1993. A number of optical counterparts have been proposed, we believe [MA93] 506 to be the correct one (Haberl and Pietsch 2004). From a number of outbursts during July 2003 − May 2004 Corbet et al. (2004a) derived an orbital ephemeris of MJD $52850 \pm 2 + \mathrm{n} \times 28.0 \pm 0.3$ d.

Survey Results: Two Type II outbursts together with the aforementioned series of Type I outbursts have been detected. A period of ~ 28 d is found using Lomb-Scargle analysis on the data not containing the Type II outbursts, consistent with the value from Corbet et al. (2004a) derived via O-C calculations. The new ephemeris from the survey data is MJD $52279.1 \pm 1.4 + \mathrm{n} \times 28.44 \pm 0.04$ d. As can be seen in Fig. 4.10(a), the two Type II outbursts began roughly at periastron, lasted about 1 orbit, and peaked at apastron. This could be explained by a number of scenarios: a) The neutron star forms an accretion disc at periastron, which it digests throughout the orbit; b) an accretion disc is formed at periastron which is accreted onto the neutron star along the orbit at the same time as wind accretion is taking place taking place; c) the Be star ejects matter forcefully enough that it moves outwards as an annulus and the neutron star is able to capture material along its orbit as it moves away from the Be star, but capture decreases as soon as it passes apastron.

None of these scenarios completely explain the behaviour of the X-ray emission

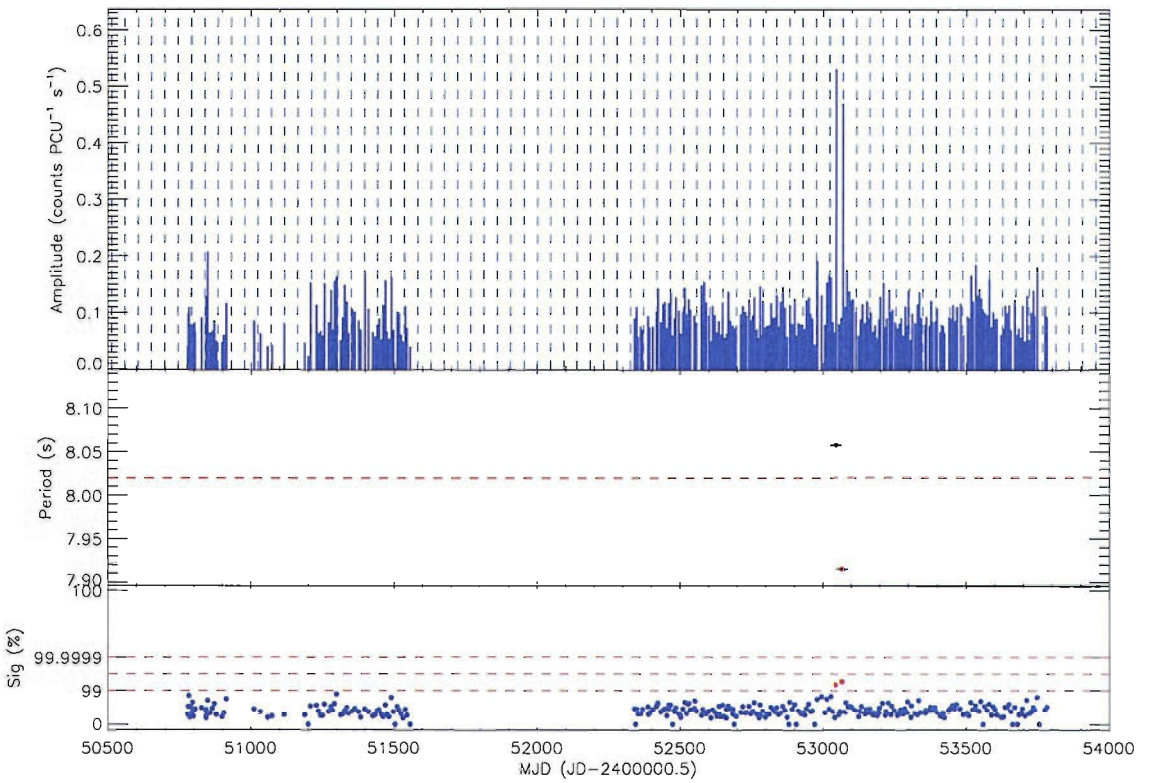

(a) X-ray amplitude light curve. The ephemeris used in a) is MJD 52277.77 ± 0.70 + $n \times 23.24 \pm 0.03$ d.

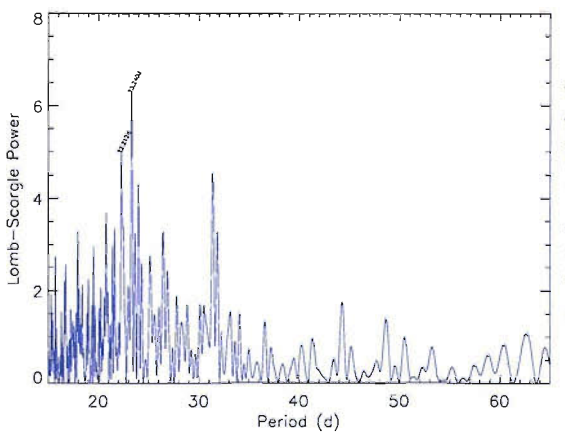

(b) Lomb-Scargle power spectrum.

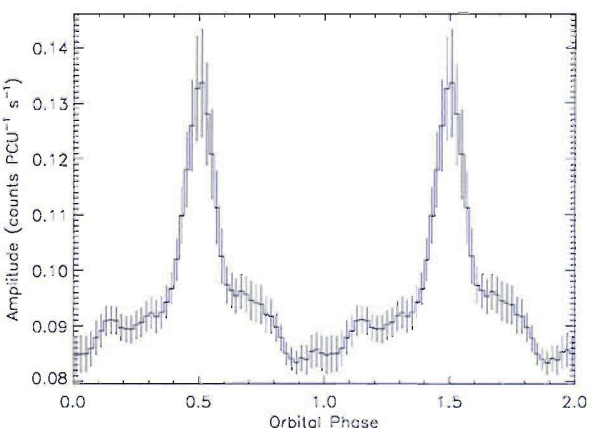

(c) Light curve folded at 23.2 d.

Figure 4.9: SXP8.02.

during the Type II outbursts. If a) is correct, then why would accretion become greatest at apastron on both occasions. Scenario c) suffers a similar drawback as it would require the annulus to move at similar speeds on both outbursts in order for the outburst to peak precisely at apastron. Scenario b) would require a very dense wind in order for its accretion to be comparable to disc accretion.

Perhaps the answer is purely geometrical, it may be that the Be star is partially eclipsing the neutron star during periastron; this could explain the feature at orbital phase 0.3 (see Fig. 4.10(c)), that is then followed by a sharp rise. Simultaneous observations of this system in the X-ray and the optical during an outburst would help clarify this enigma.

4.1.11 SXP9.13

AX J0049−732, RX J0049.2−7311
RA 00 49 13.6, dec −73 11 39

History: Discovered during an *ASCA* observation in November 1997, pulsations were detected at 9.1321 ± 0.0004 s (Imanishi et al. 1998). There has been much debate as to which is the correct optical counterpart to this source, Schmidtke et al. (2004); Filipović et al. (2000) identify it with the *ROSAT* source RX J0049.5−7310 but Coe et al. (2005) conclude that it is a Hα source coincident with RX J0049.2−7311. Timing analysis of the OGLE data shows a peak at 40.17 d and its probable harmonic at 20.08 d (Edge 2005). It should be noted that Schmidtke et al. (2004) find a 91.5 d or possibly an $\sim$187 d period for RX J0049.5−7310, both of which are too long if we are to place unlimited faith in the Corbet diagram.

Survey Results: Although coverage of this source has been very complete, it has only been detected in outburst 3 times since MJD $\sim$53550. Lomb-Scargle analysis of data prior to this date shows two peaks of similar, yet low, significance at 38.1 d and 19.2 d (a harmonic?). These would be consistent with the optical period derived by Edge (2005) so we have used $2 \times 19.2 = 38.4$ d as the orbital period, with an ephemeris of MJD $52112.3 \pm 1.2 + n \times 38.40 \pm 0.02$ d. The folded

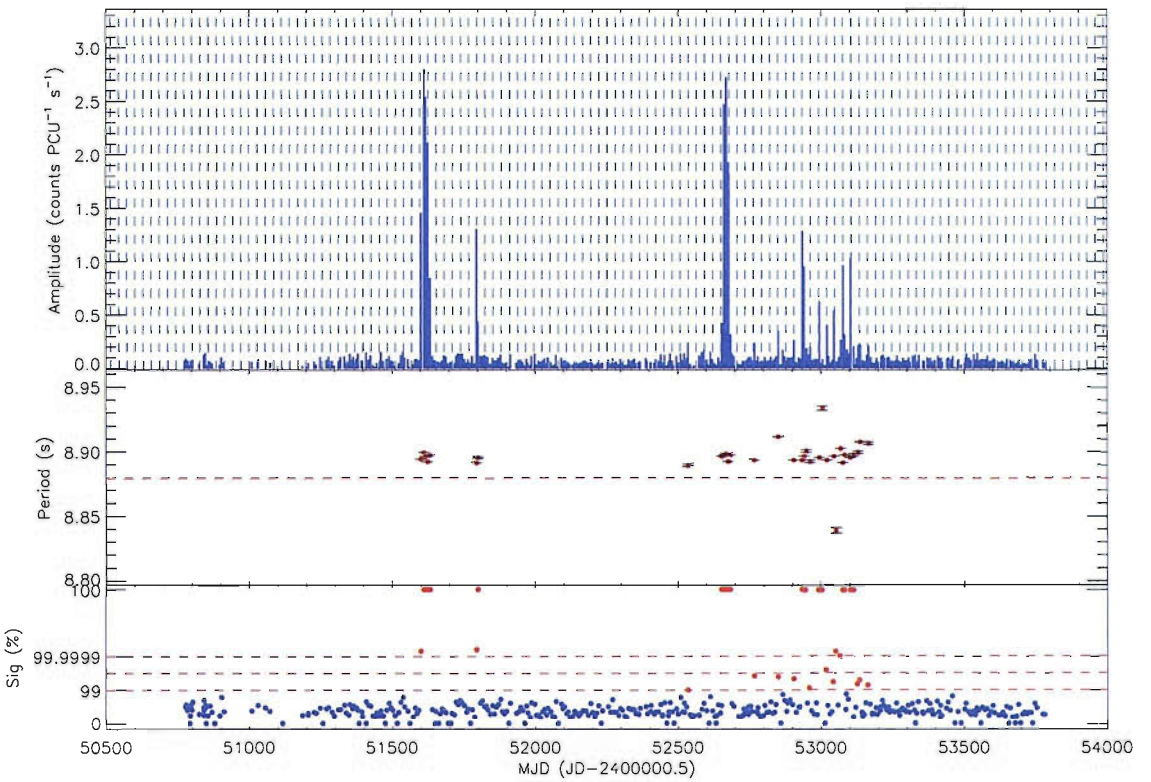

(a) X-ray amplitude light curve.

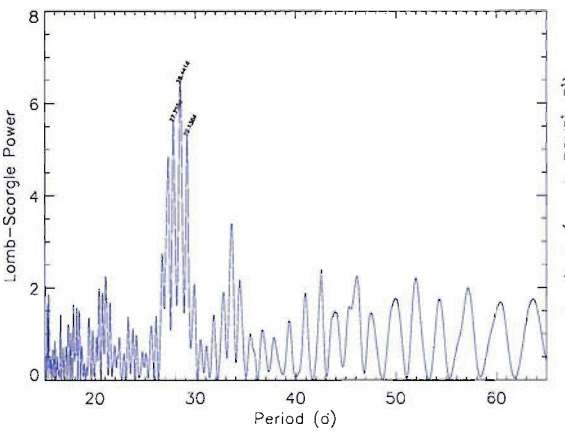

(b) Lomb-Scargle power spectrum.

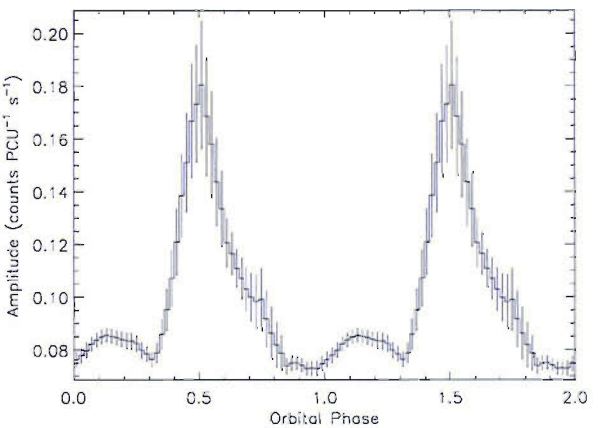

(c) Orbital profile folded at 28.44 d.

Figure 4.10: SXP8.80. Only the data outside the two large outbursts were used in the folded profile of c).

light curve (Fig. 4.11(c)) shows a sharp, symmetrical peak around periastron with an asymmetrical, hump-like feature ~ 0.45 of a phase behind. The clear detections after MJD ~ 53550 occur roughly around periastron.

4.1.12 SXP15.3

RX J0052.1−7319
RA 00 52 14, dec −73 19 19

History: Lamb et al. (1999) found 15.3 s pulsations in *ROSAT* and *BATSE* data from 1996. They estimate the luminosity to be $\sim 10^{37}\,\mathrm{erg\,s^{-1}}$ with a pulse fraction of $\sim 27\%$. Edge (2005) finds an ephemeris of MJD $50376.1 + \mathrm{n} \times 75.1 \pm 0.5$ d describes the modulation in the MACHO and OGLE light curves. It should be noted that this ephemeris is likely driven by the large 1996 X-ray outburst which is clearly visible in the OGLE data; this Type II outburst peaked around MJD 50375.

Survey Results: There was a very minor detection of SXP15.3 in February 2000 (MJD 51592.2), and a more significant one in August 2003 (MJD 52882.6) at $F_{\mathrm{x_{pul}}} \simeq 1.6\,\mathrm{counts\,PCU^{-1}\,s^{-1}}$. Two more bright detections separated by 13 days occurred in March 2005; then, on July 12$^{\mathrm{th}}$ a very bright outburst began, lasting until October 17$^{\mathrm{th}}$ (almost 100 days long). During this time the pulsed flux oscillated between ~ 2.0 and $\sim 5.6\,\mathrm{counts\,PCU^{-1}\,s^{-1}}$. A clear spin up is detected up until September 15$^{\mathrm{th}}$, when the period started increasing. The maximum period change was $\Delta P = 3.3 \times 10^{-2}$ over the course of 56.68 d, giving a $\dot{P} = 6.74 \times 10^{-9}\,\mathrm{s\,s^{-1}}$. We derive the expected luminosity from such a level of spin up (if it were all intrinsic with no orbital contribution) to be $L_{\mathrm{x}} = 8.6 \times 10^{37}\,\mathrm{erg\,s^{-1}}$ ($B = 1.5 \times 10^{13}$ G).

It is likely this outburst lasted for more than one orbital cycle (expected to be $\sim 30-50$ d from the Corbet diagram) so some orbital modulation might be visible in the period data. An attempt was made to fit these data to an orbital model with constant global spin up, and also with a piece-wise approach where the spin up varies throughout the outburst (see § 2.1.4 for an explanation of this method) but no orbital solution was found. Lomb-Scargle analysis of the data outside of

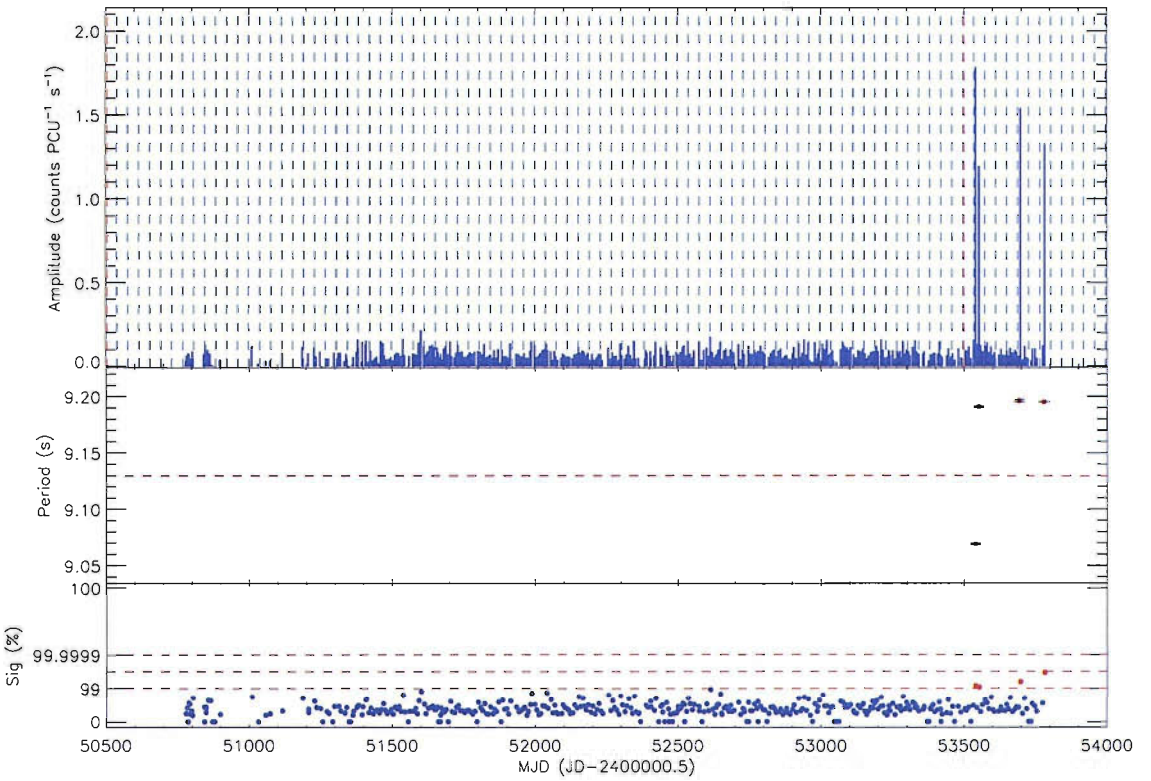

(a) X-ray amplitude light curve.

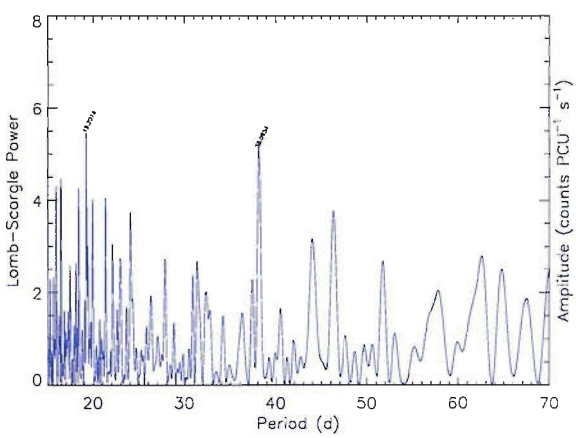

(b) Lomb-Scargle power spectrum.

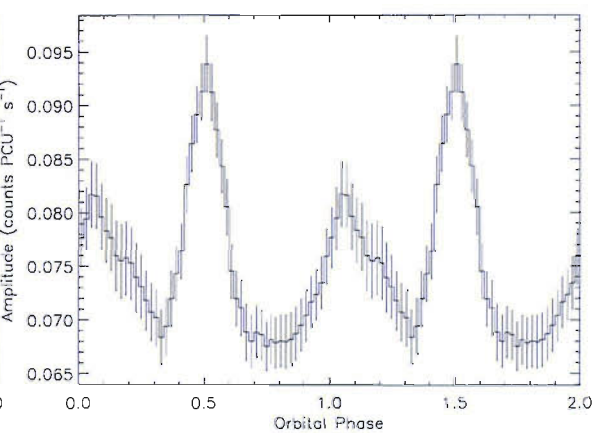

(c) Orbital profile folded at 38.40 d.

Figure 4.11: SXP9.13.

the outburst finds a weak period at $\sim$79 d, which is similar to the optical period of 75.1 d. The ephemeris is MJD $52244.4 \pm 2.4 + n \times 79.6 \pm 0.4$ d, and it should be noted that the long Type II outburst peaks around MJD 53596.8, a calculated date of periastron passage.

4.1.13 SXP16.6

XTE J0050−731
No position available

History: Discovered with a deep 121 ks observation taken for this survey in September 2000, Lamb et al. (2002b) report the find and tentatively identify it with RX J0051.8−7310, which had been observed previously by both *ROSAT* and *ASCA*. This identification is proved erroneous in Yokogawa et al. (2002), and so SXP16.6 remains unidentified, although it is often referred to as RX J0051.8−7310.

Survey Results: There have been no strong outbursts of SXP16.6, with most detections barely rising above 99% local significance, although their amplitude is high above the background. Lomb-Scargle analysis finds a strong modulation at 33.7 d, which we propose as the orbital period of the system. The ephemeris is MJD $52271.4 \pm 1.7 + n \times 33.69 \pm 0.05$ d.

4.1.14 SXP18.3

XTE J0055−727
RA 00 53 53, dec −72 26 42

History: Reported by Corbet et al. (2003d) from observations of this survey's data belonging to November/December 2003. Its position was established from scans with *RXTE*'s PCA. No optical counterpart has yet been identified. A number of further outbursts between May – October 2004 provide an ephemeris of MJD $53145.7 \pm 1.3 + n \times 34.6 \pm 0.4$ d from O-C orbital calculations (Corbet et al. 2004d).

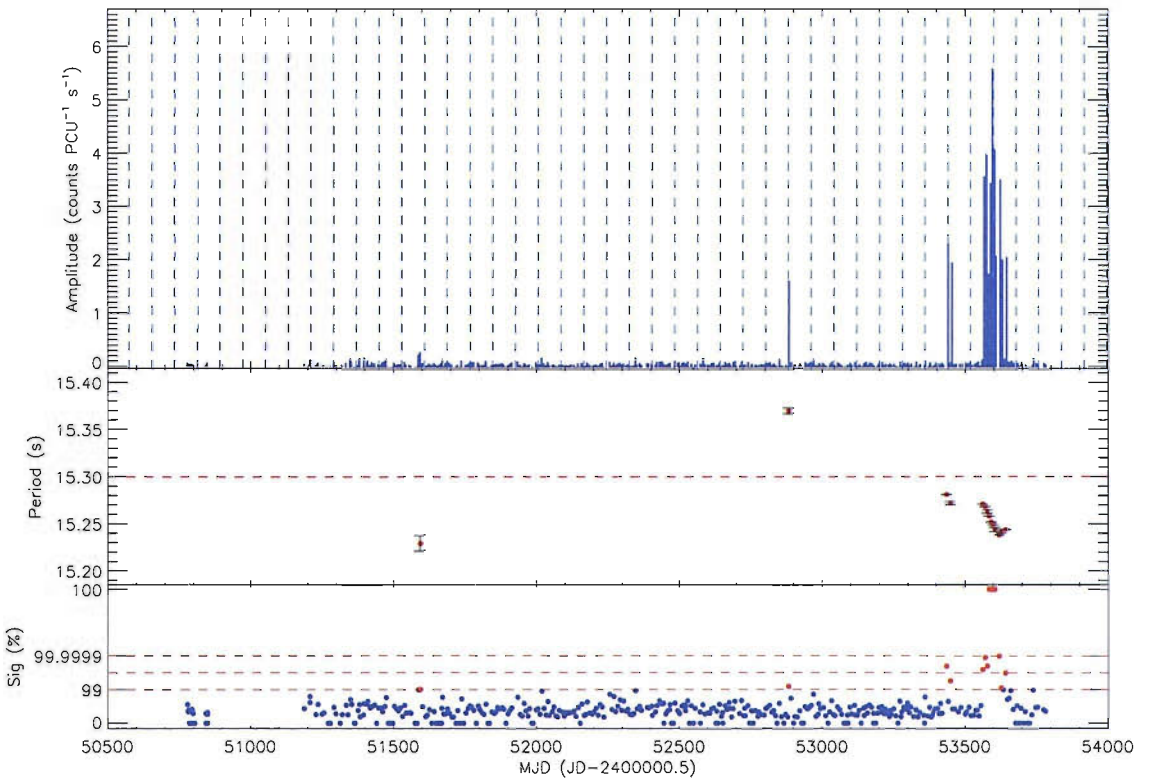

(a) X-ray amplitude light curve.

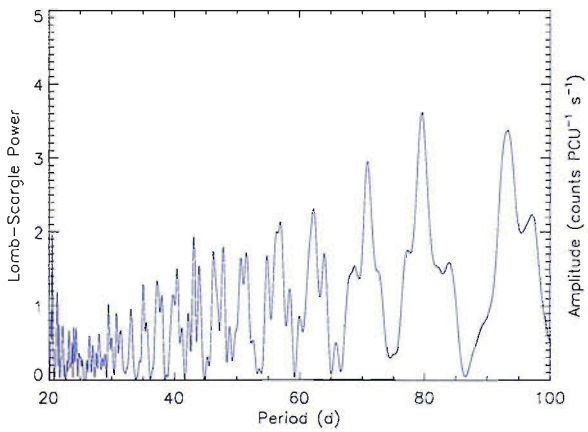

(b) Lomb-Scargle power spectrum.

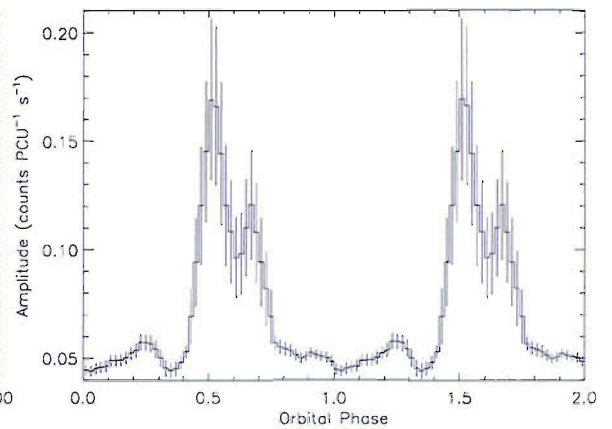

(c) Orbital profile folded at 79.6 d.

Figure 4.12: SXP15.3. Only the data outside the large outburst were used to compute the Lomb-Scargle periodogram in b) and in the folded profile in c).

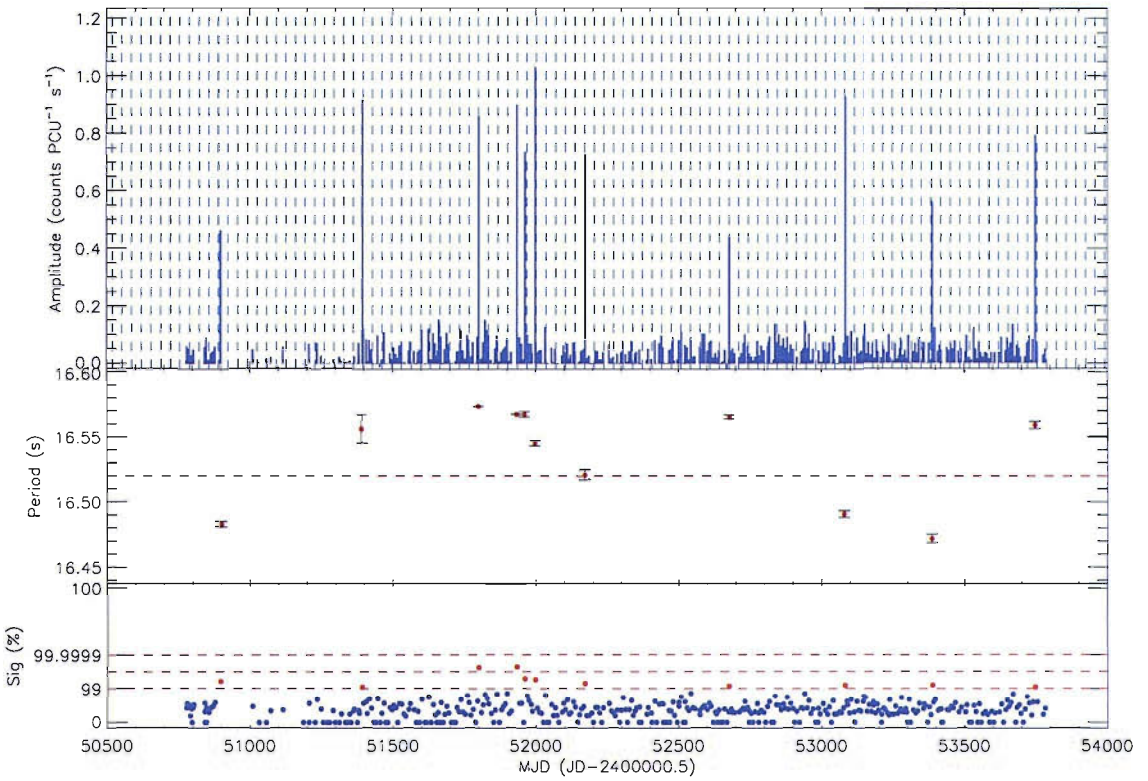

(a) X-ray amplitude light curve.

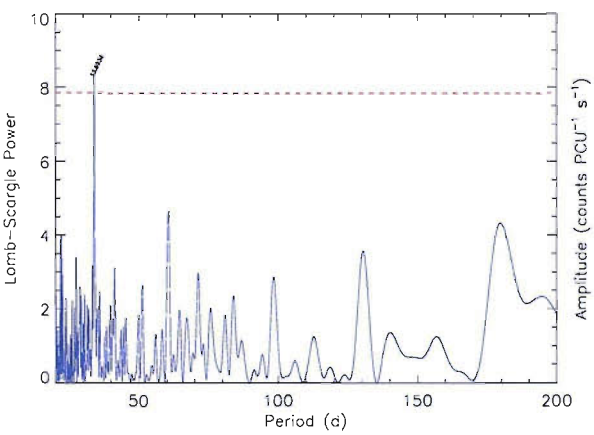

(b) Lomb-Scargle power spectrum.

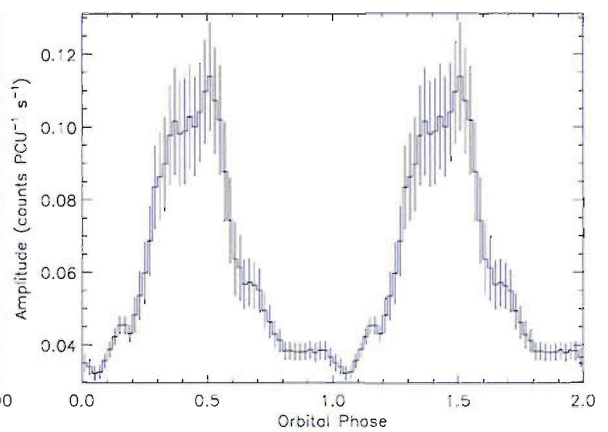

(c) Orbital profile folded at 33.69 d.

Figure 4.13: SXP16.6.

Survey Results: No significant activity is detected before the initial outburst and Lomb-Scargle analysis of all the data finds a period of ~ 17.7 d, slightly more than double the O-C period. reducing the detection threshold to $Sig_{\rm min} = 97\%$ increases the significance of this period and brings up an earlier outburst at MJD 51600.2. The dates of some of the outbursts make them incompatible with a ~ 35 d orbital period. The exact ephemeris we derive is MJD $52274.8 \pm 0.5 + {\rm n} \times 17.75 \pm 0.02$ d.

4.1.15 SXP22.1

RX J0117.6−7330
RA 01 17 40.5, dec −73 30 52.0

History: Discovered with *ROSAT* as an X-ray nova in September 1992 (Clark et al. 1996), its companion was identified as a 14.2 magnitude OB by Charles et al. (1996). It was observed with *ROSAT* again in October, but no pulsations were detected (Clark et al. 1997) The companion's classification as a Be (B1-2) star was confirmed by Coe et al. (1998). 22 s pulsations were finally detected in *ROSAT* and *BATSE* data by Macomb et al. (1999).

Survey Results: There are only 3 observations of this pulsar's region and it was not significantly detected in any of them (see Fig. 4.15).

4.1.16 SXP31.0

XTE J0111.2−7317, AX J0111.1−7316
RA 01 11 09.0, dec −73 16 46.0

History: Was simultaneously discovered by *RXTE* and *BATSE* (Chakrabarty et al. 1998; Wilson and Finger 1998) during a giant outburst (see Chapter 2).

Survey Results: Being in the same field as SXP22.1, it was only observed 3 times, the first during the end of the aforementioned giant outburst. The two detections are ~ 43 days apart and a spin up of 0.4 s is measured, which implies a luminosity

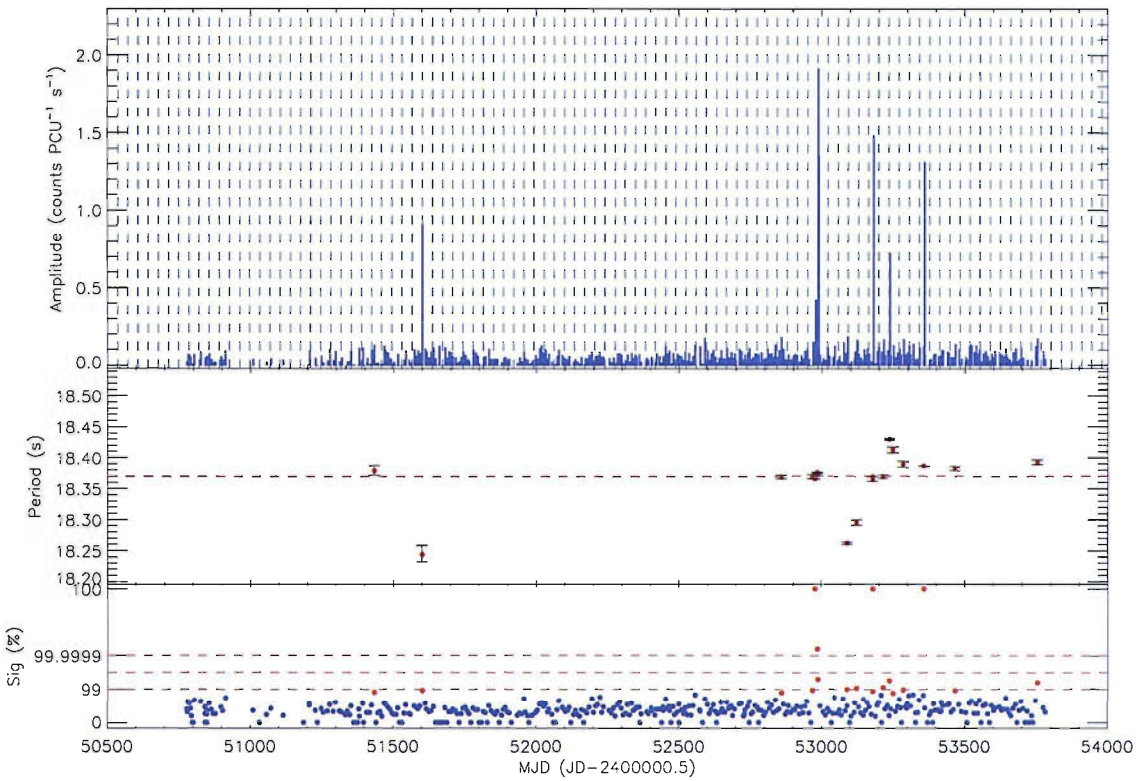

(a) X-ray amplitude light curve. For clarity, only every other ephemeris line has been plotted.

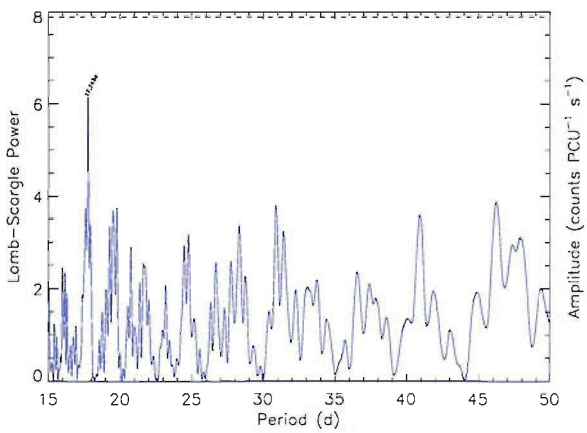

(b) Lomb-Scargle power spectrum.

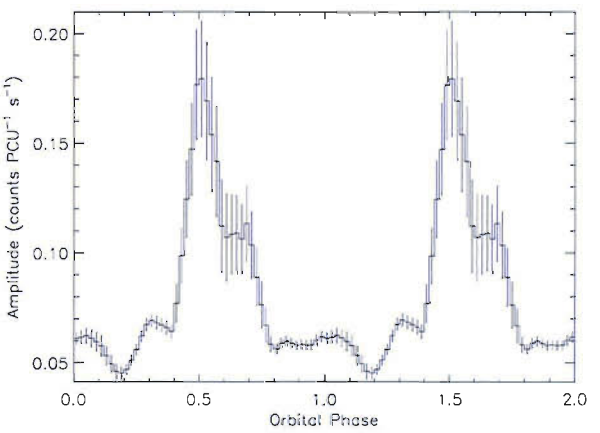

(c) Orbital profile folded at 17.75 d.

Figure 4.14: SXP18.3.

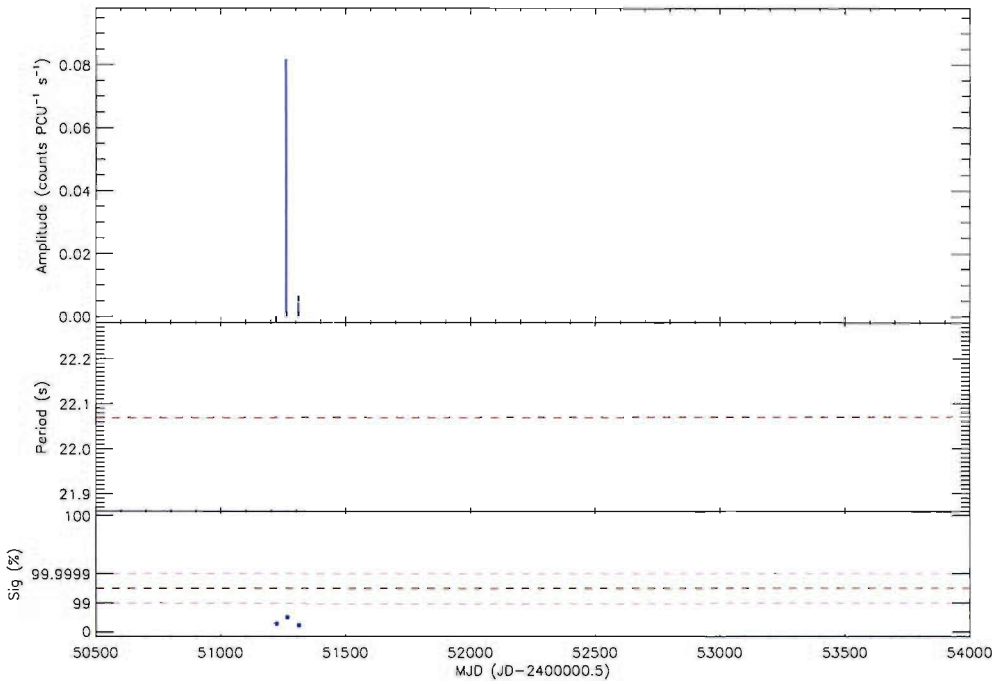

Figure 4.15: X-ray amplitude light curve of SXP22.1.

of $L_x = 2.7 \times 10^{38}\,\mathrm{erg\,s^{-1}}$. As Laycock et al. (2005), in an in depth spectral analysis of these observations, derive a value of $L_x = 4.6 \times 10^{37}\,\mathrm{erg\,s^{-1}}$, we can assume we are seeing Doppler shifted periods due to orbital motion. No further information can be derived from these observations.

The orbital period in Table 4.1 for this system was obtained from the analysis of *BATSE* data carried out in § 2.2.1.

4.1.17 SXP34.1

RX J0055.4−7210
RA 00 55 26.9, dec −72 10 59.9

History: Discovered in archival Chandra data at 34.08 ± 0.03 s and lying 0.6 arcsec from a known *ROSAT* source (Edge et al. 2004d, c).

Survey Results: Only two significant detections above 99% local significance are

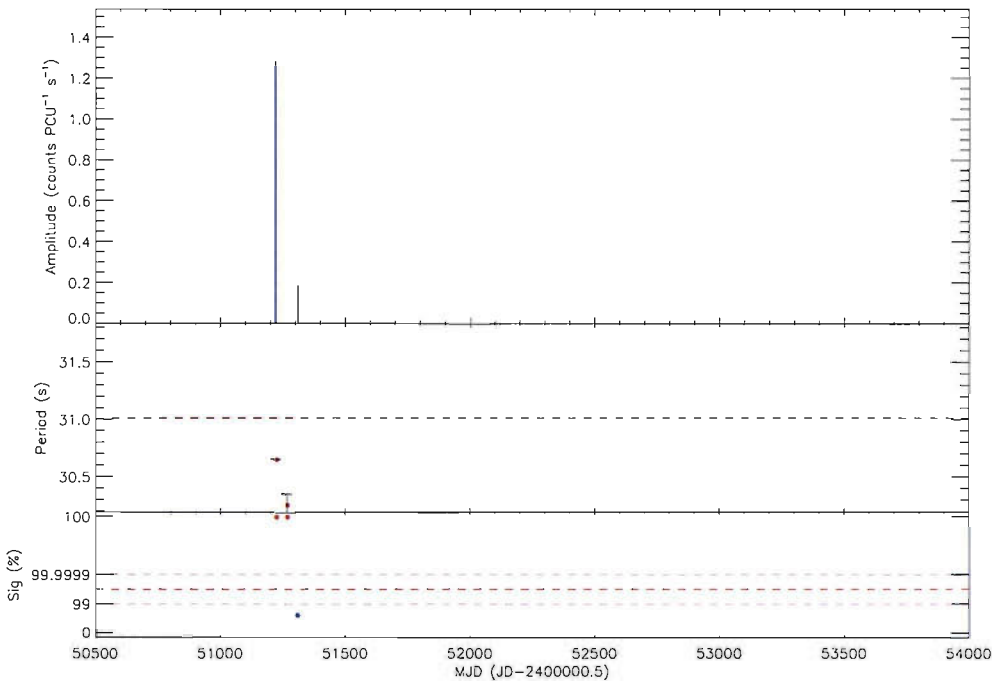

Figure 4.16: X-ray amplitude light curve of SXP31.0.

present. If the threshold is lowered to 90% we gain 10 further detections. Timing analysis on this light curve finds 2 weak periods at 48.7 d and 53.3 d, the latter being slightly stronger. Both lie on the expected region of the Corbet diagram, but without any clear, bright detections it is difficult to establish the real orbital period. Therefore, we present graphs for both of them in Figs. 4.17 and 4.18, their respective ephemerides being MJD $52238.7 \pm 2.4 + n \times 48.7 \pm 0.1$ d and MJD $52258.5 \pm 2.7 + n \times 53.3 \pm 0.1$ d.

4.1.18 SXP46.6

XTE J0053−724, 1WGA 0053.8−7226
RA 00 53 58.5, dec −72 26 35

History: Discovered in the first observation in this survey with a period of 46.63 ± 0.4 s while it was undergoing a long outburst (Corbet et al. 1998). The optical counterpart is still not clear. Laycock et al. (2005) derive a period of 139 ± 6 d from 6 X-ray outbursts in the earlier part of this survey.

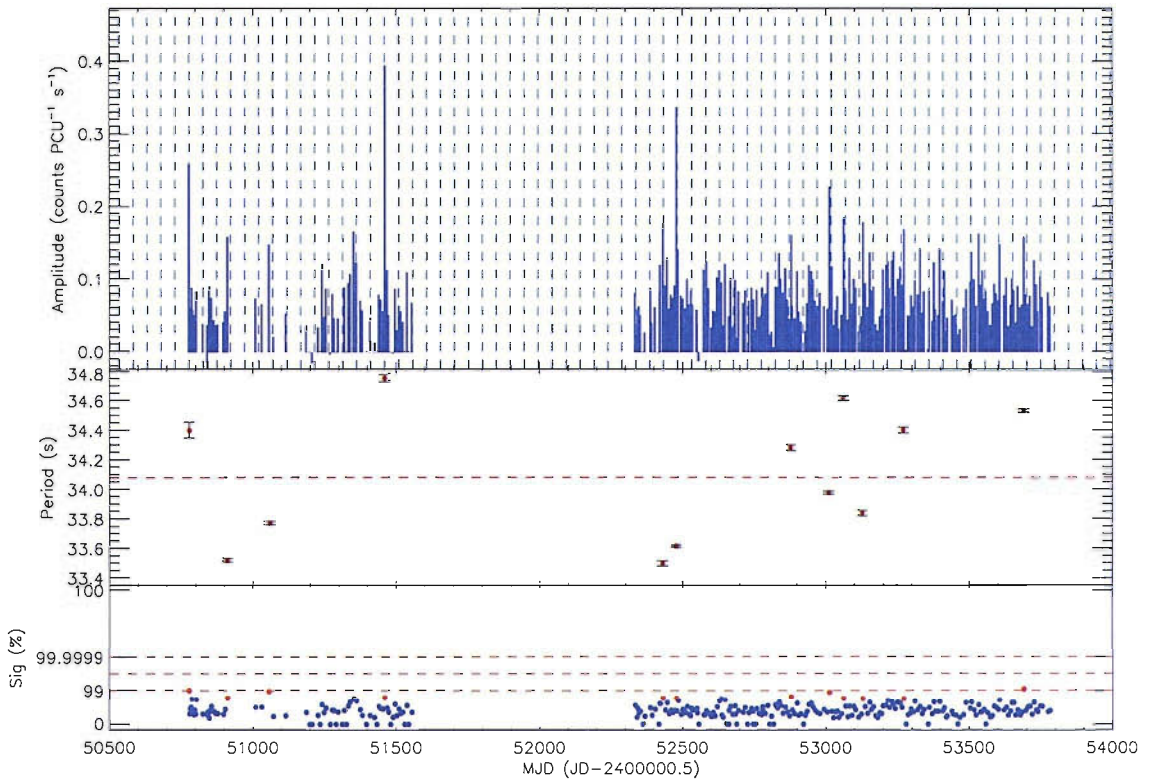

(a) X-ray amplitude light curve showing the possible 48.8 d orbital period.

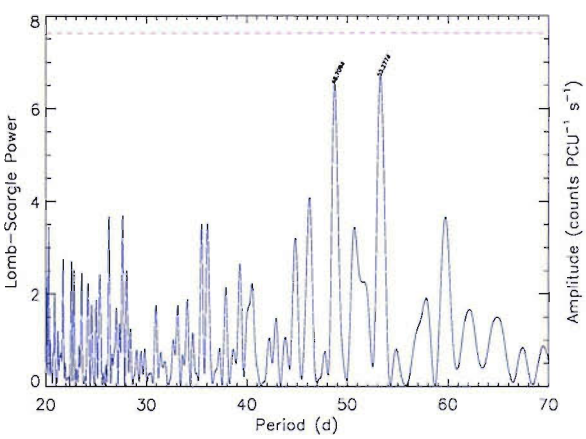

(b) Lomb-Scargle power spectrum.

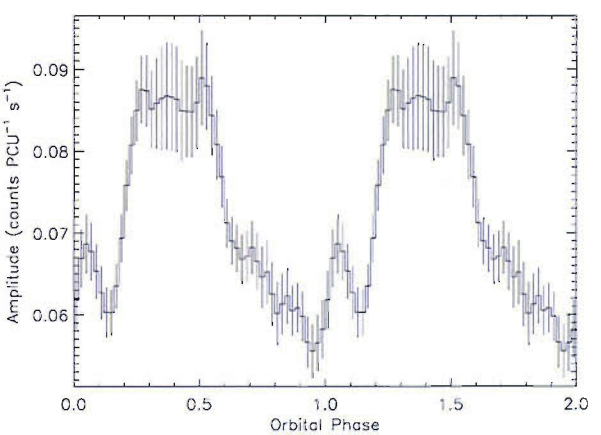

(c) Orbital profile folded at 48.8 d.

Figure 4.17: SXP34.1, possible orbital period = 48.8 d.

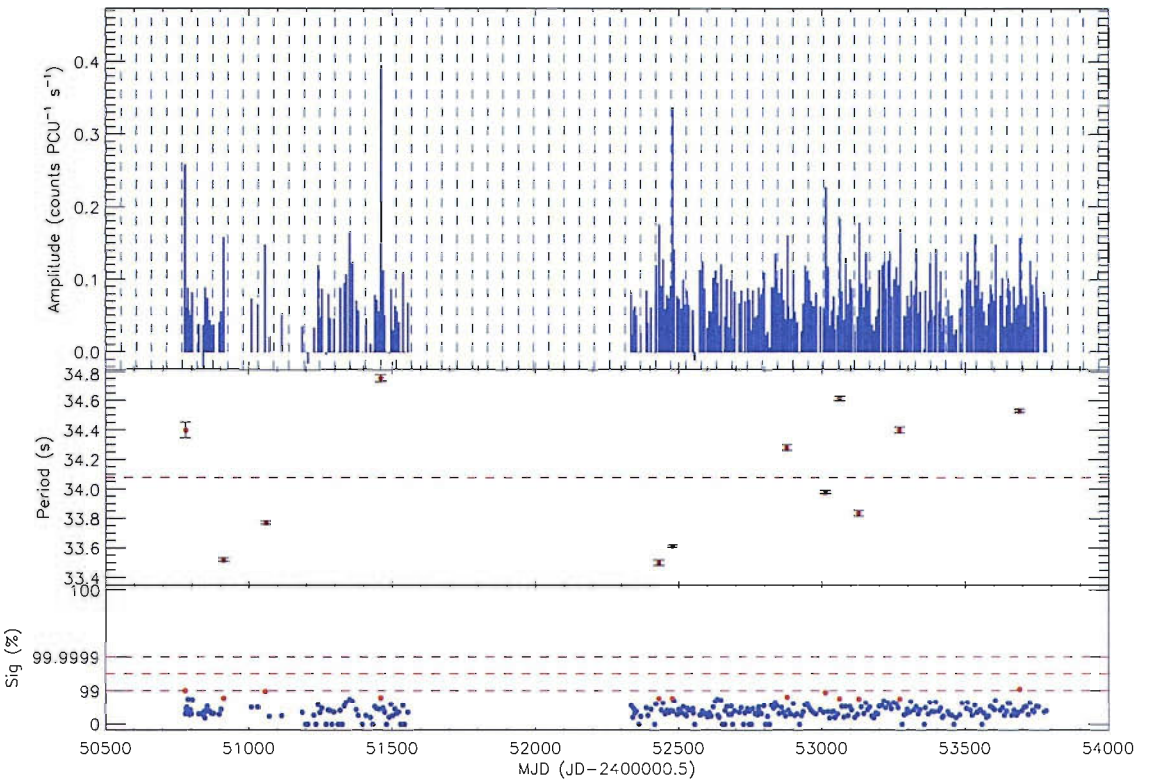

(a) X-ray amplitude light curve showing the possible 53.3 d orbital period.

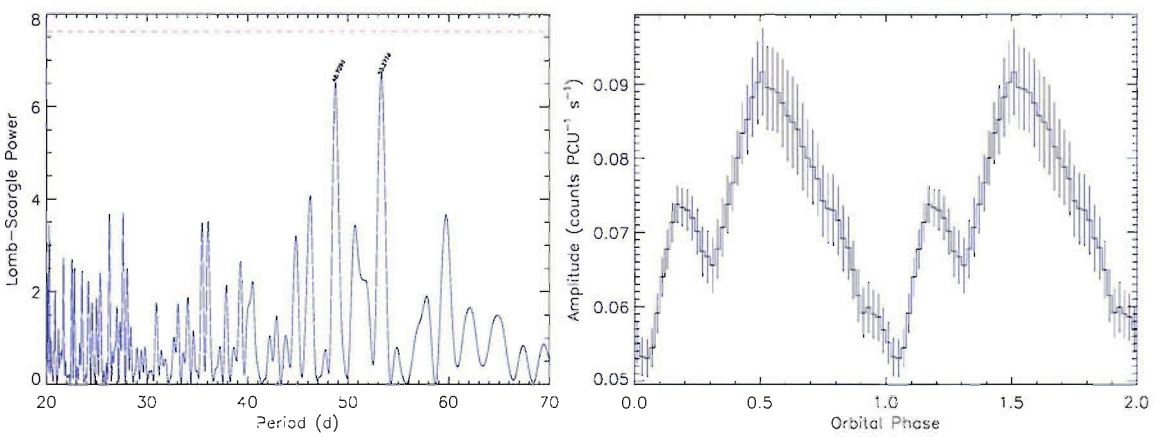

(b) Lomb-Scargle power spectrum.

(c) Orbital profile folded at 53.3 d.

Figure 4.18: SXP34.1, possible orbital period = 53.3 d.

Survey Results: The source was thought to be incactive after January 2002. In the meantime a new SMC pulsar with a 46.4 s period was announced (Corbet et al. 2002). Lomb-Scargle analysis of both pulsars revealed the same orbital periods and very similar ephemeris, suggesting they are the same pulsar which has been slowly spinning up (Galache et al. 2005). The estimated luminosity required for a spin up of $\dot{P} = 1.05 \times 10^{-9}\,\mathrm{s\,s^{-1}}$ during MJD 50800−51900 is $L_\mathrm{x} = 9.9 \times 10^{35}\,\mathrm{erg\,s^{-1}}$ ($B = 6.0 \times 10^{12}$ G), and for a $\dot{P} = 4.68 \times 10^{-10}\,\mathrm{s\,s^{-1}}$ during MJD, $L_\mathrm{x} = 4.4 \times 10^{35}\,\mathrm{erg\,s^{-1}}$ ($B = 4.0 \times 10^{12}$ G). The ephemeris of the outbursts is now best described by MJD $52156.6 \pm 1.4 + \mathrm{n} \times 137.36 \pm 0.35$ d (as reported in Galache et al. (2005)).

4.1.19 SXP51.0

SMC 51
No position available

History: Was erroneously proposed as a new 25.5 s pulsar in Lamb et al. (2002b) from the deep 121 ks observation. Laycock (2002) identifies the 25.5 s peaks in the power spectrum as harmonics of SXP51.0's true pulse period. No position is available; it lies within Position 4, and most likely in the overlap between Positions 1/A and 4.

Survey Results: Lomb-Scargle analysis of the light curve shows a peak at ∼51.8, which would agree with the expected orbital period from the Corbet diagram. As the most significant detections appear at these ephemerides, it is proposed as the orbital period of the system. The ephemeris is MJD $52267.1 \pm 1.6 + \mathrm{n} \times 51.76 \pm 0.13$ d.

4.1.20 SXP59.0

XTE J0055−724, RX J0054.9−7226, 1WGA J0054.9−7226
RA 00 54 56.6, dec −72 26 50

History: Discovered in *RXTE* observations of the vicinity of SMC X-3 (Marshall

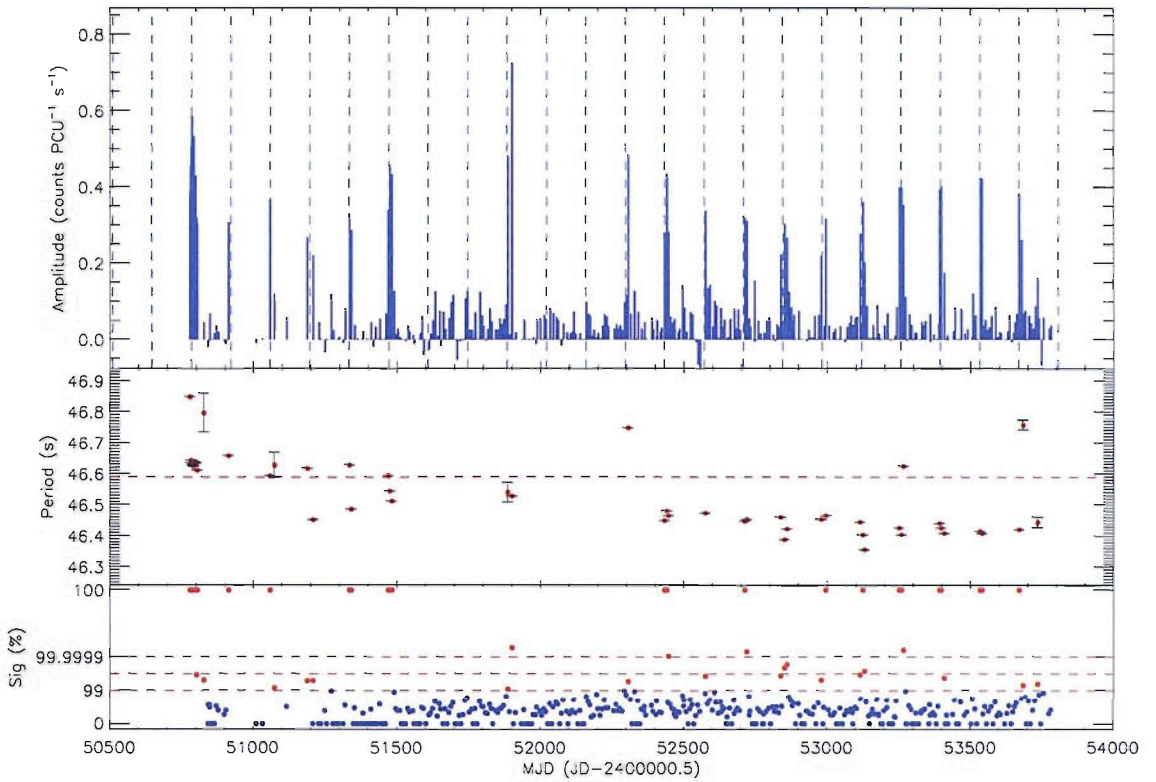

(a) X-ray amplitude light curve.

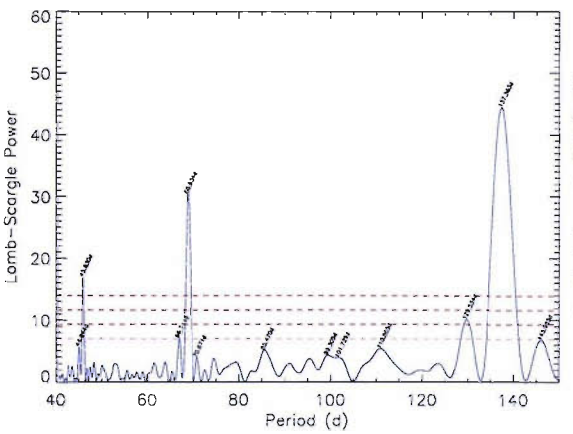

(b) Lomb-Scargle power spectrum.

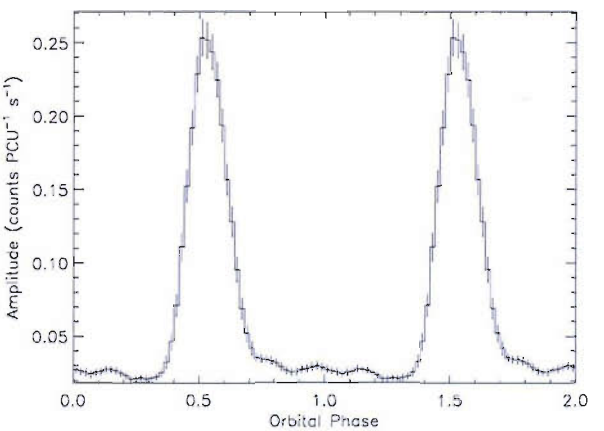

(c) Orbital profile folded at 137.35 d.

Figure 4.19: SXP46.6.

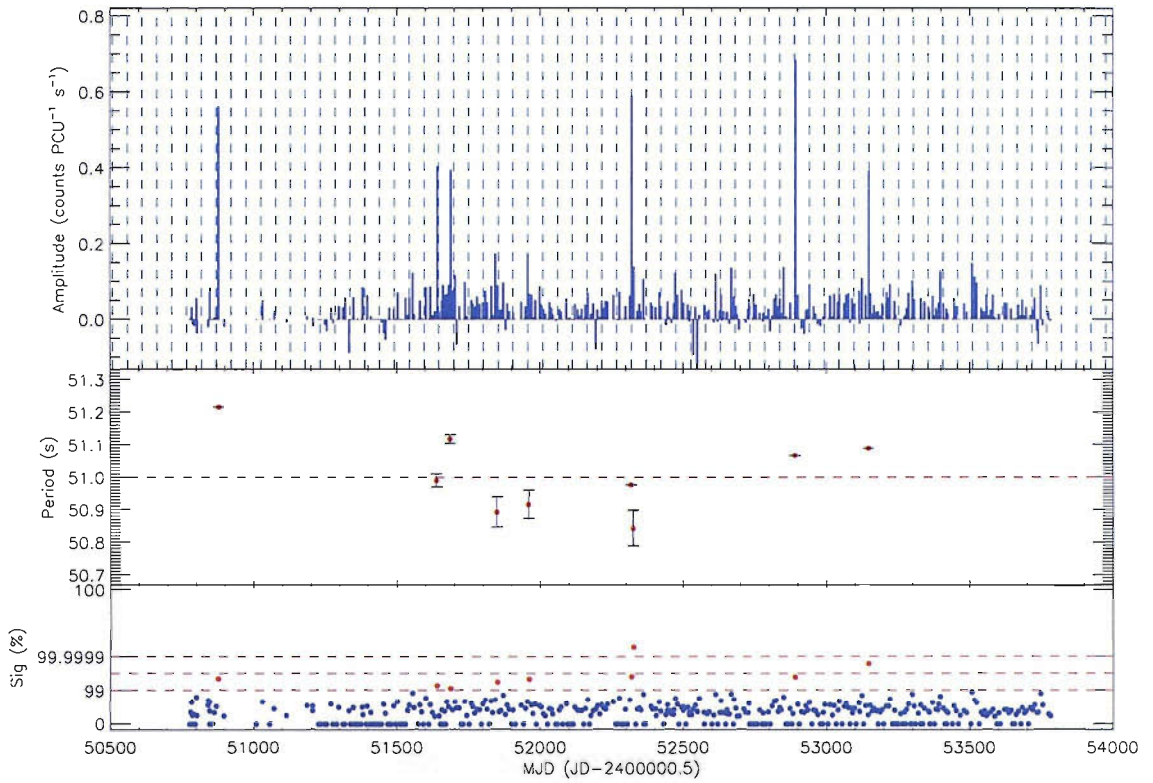

(a) X-ray amplitude light curve.

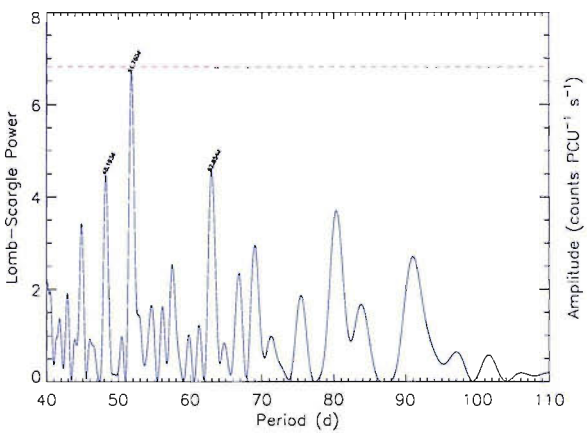

(b) Lomb-Scargle power spectrum.

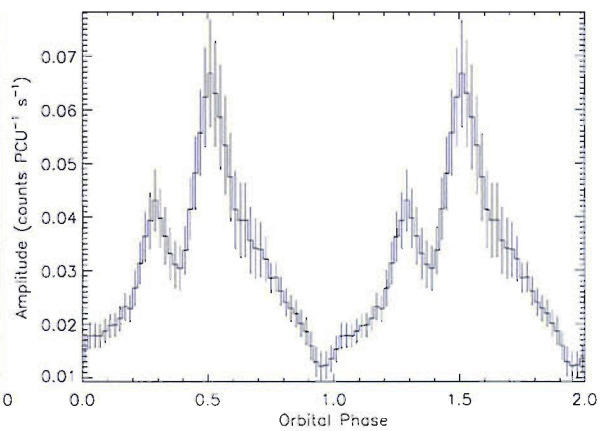

(c) Orbital profile folded at 51.76 d.

Figure 4.20: SXP51.0.

et al. 1998), it showed 4 bright, very similar, outbursts during January 1998 – September 1999 from which Laycock et al. (2005) derived an orbital period of 123 ± 1 d. The optical counterpart was established by Stevens et al. (1999); timing analysis of OGLE and MACHO data found periodicities in the 120 – 130 srange, which were considered inconclusive (Coe et al. 2005).

Survey Results: SXP59.0 remained undetected since September 1999 until a bright outburst in mid 2002 began a series of 5 outbursts. From the whole data range we extract an ephemeris of MJD $52187.5 \pm 1.2 + \mathrm{n} \times 122.40 \pm 0.42$ d.

During the 1998 – 99 outbursts a spin up was detected of $\dot{P} = 4.7 \times 10^{-9}\,\mathrm{s\,s^{-1}}$ and again throughout the 5 outbursts of 2002 – 2003, with a value of $\dot{P} = 5.9 \times 10^{-9}\,\mathrm{s\,s^{-1}}$. The luminosities associated with these spin ups are, respectively, $L_\mathrm{x} = 2.6 \times 10^{36}\,\mathrm{erg\,s^{-1}}$ ($B = 1.3 \times 10^{13}$ G) and $L_\mathrm{x} = 3.3 \times 10^{36}\,\mathrm{erg\,s^{-1}}$ ($B = 1.4 \times 10^{13}$ G). In both groups of outbursts the initial and final periods were very similar, which would imply that SXP59.0 must have spun down during the $\sim$1100 days it was undetected[2]. The average spin down was $\dot{P} = -4.2 \times 10^{-9}\,\mathrm{s\,s^{-1}}$, which should have been associated with a luminosity of $L_\mathrm{x} = 2.9 \times 10^{36}\,\mathrm{erg\,s^{-1}}$. Although SXP59.0 was further away from the centre of the field of view during AO5 – AO6 (MJD 51600 – 52300), it should have been picked up as a number of the detections during the second outburst season were made when *RXTE* was pointing at Position D (essentially the same coordinates as Position 5). In view of this, the spin down mechanism for SXP59.0 must be something other than reverse accretion torque.

[2]This coincidence of end periods for the outbursts may indicate that the equilibrium period of SXP59.0 is $\sim$58.75 s. Using Eq. (6.26) in Frank et al. (2002), we derive the magnetic field of the pulsar: $\sim 4.9 \times 10^{10}$ G, which is 2 orders of magnitude lower than the values derived from the spin up during outbursts.

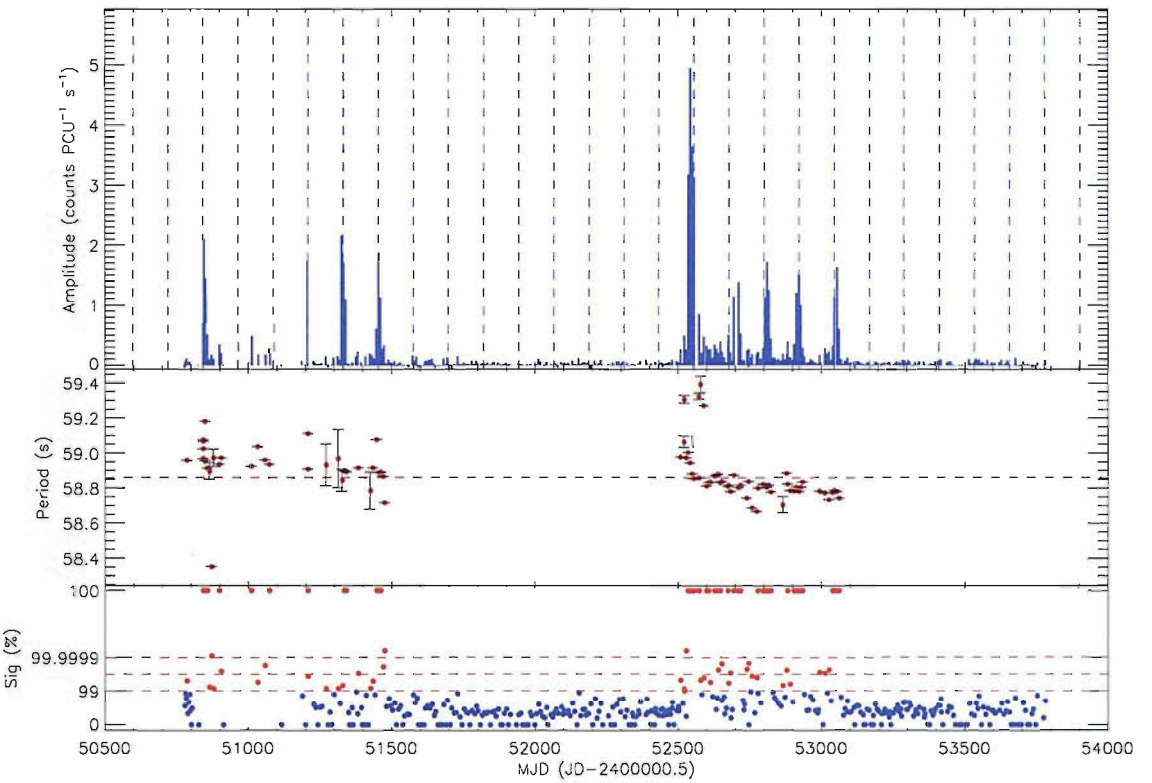

(a) X-ray amplitude light curve.

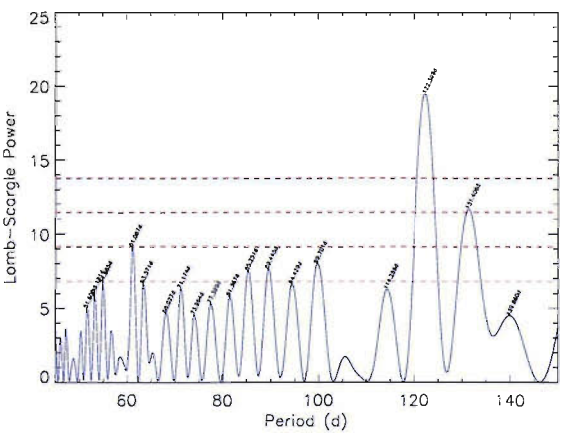

(b) Lomb-Scargle power spectrum.

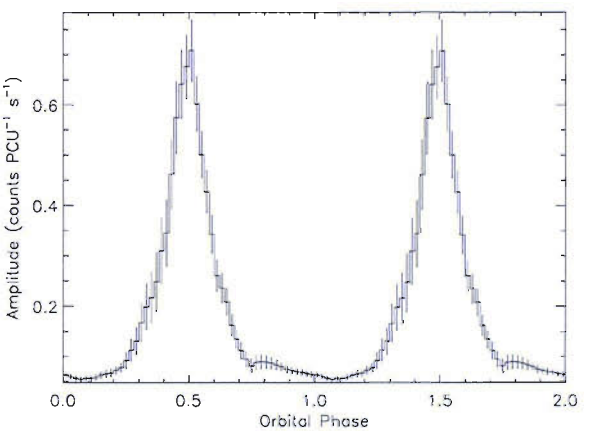

(c) Orbital profile folded at 122.40 d.

Figure 4.21: SXP59.0.

4.1.21 SXP74.7

RX J0049.1−7250, AX J0049−729
RA 00 49 04, dec −72 50 54

History: Discovered in the first observation of this survey with a period of 74.8 ± 0.4 s (Corbet et al. 1998). Kahabka and Pietsch (1998) identified it with the *ROSAT* source RX J0049.1−7250 and Stevens et al. (1999) found a single Be star within the *ROSAT* error radius which they proposed as the optical counterpart. Only 3 X-ray outbursts where observed in the early stages of this survey, from which Laycock et al. (2005) derived a possible orbital period of 642 ± 59 d, based on the separation between the outbursts. Schmidtke and Cowley (2005b); Edge (2005) find a 33.4 d periodicity in OGLE data.

Survey Results: Three further outbursts were observed ~ 2 yr after the previous ones. They are weak and separated by ~ 40 days. The only other detection came after another ~ 2 yr hiatus. Lomb-Scargle analysis of the data excluding the bright, long outbursts circa MJD 50785 and 52080 finds a strong period of ~ 32 d, which is close to the reported optical period. The derived ephemeris is MJD $52295.8 \pm 1.6 + n \times 31.94 \pm 0.05$ d.

4.1.22 SXP82.4

XTE J0052−725
RA 00 52 09, dec −72 38 03

History: First observed by *RXTE* in this survey (Corbet et al. 2002), its position was determined from archival *Chandra* data (Edge et al. 2004b). Edge (2005) reports a 52.8 period in OGLE data of the optical counterpart.

Survey Results: This source has shown activity throughout the survey, although an orbital period has proved elusive. The Lomb-Scargle periodogram shows a very significant peak at ~ 362 d (with a number of harmonics). The third strongest

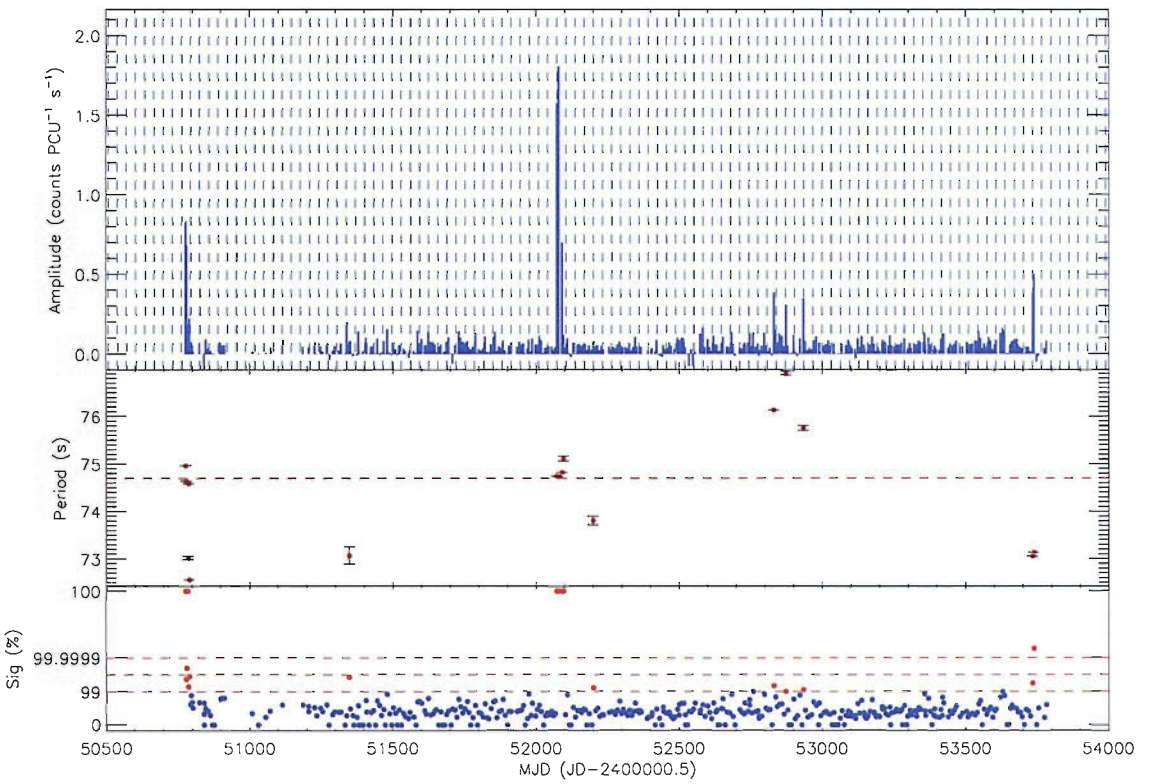

(a) X-ray amplitude light curve.

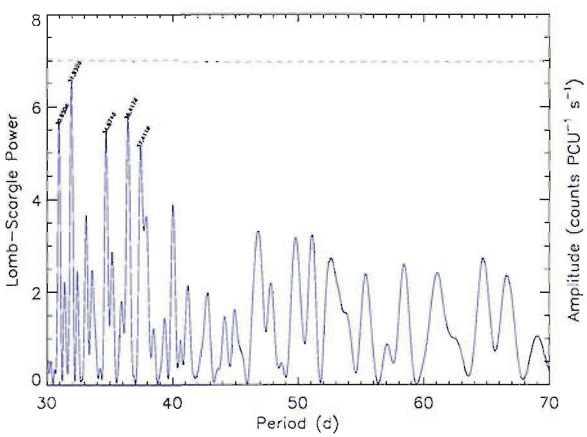

(b) Lomb-Scargle power spectrum.

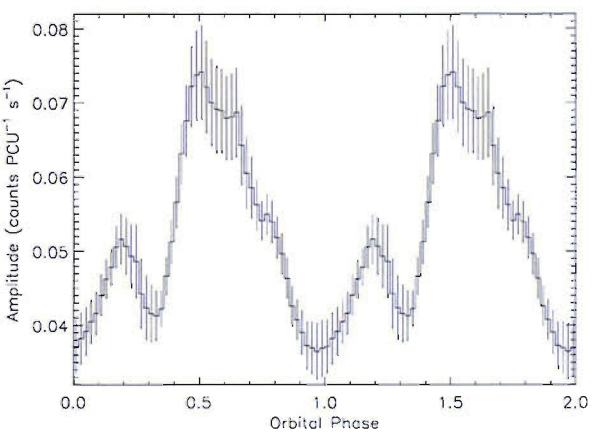

(c) Orbital profile folded at 31.94 d.

Figure 4.22: SXP74.7. Only the data outside the large outbursts circa MJD 50785 and 52080 were used to compute the Lomb-Scargle periodogram in b) and in the folded profile in c).

period is 52.6 d (we note that $52.6 \simeq 362/7$), which becomes even stronger when using $Sig_{\rm min} = 95\%$, as a number of low-luminosity detections are added to the brighter ones. The brightest detections are clearly $\sim$364 d apart, which would skew the Lomb-Scargle results, but in view of the measured optical period and that a 52.6 d X-ray period fits the less luminous detections as well as the brighter ones, we believe 52.6 d to be the orbital period of this system and suggest the possible existence of a supra orbital period of $\sim$1 yr. The orbital ephemeris we derive is MJD $52293.2 \pm 1.6 + {\rm n} \times 52.63 \pm 0.11$ d. Taking out the larger MJD $\sim$52450 outburst does not significantly affect the results; it is simply a bright Type I outburst.

4.1.23 SXP89.0

XTE SMC pulsar
No position available

History: Reported by Corbet et al. (2004b) from observations in March 2002, although it is not clear whether this is SXP91.1 after spinning up.

Survey Results: The first outburst is a single detection in February 2000 2 years before the official discovery[3], 4 others occurred 2 years later in a short space of time (within $\sim$260 days). They follow a high-low-high-low brightness pattern, with very similar high/low countrates. The separation between them is $\sim$88 d which should be close to the orbital period. We took out the two bright outbursts circa MJD 52340 and 52510 from the data to analyse it; the resulting periodogram shows two peaks of similar, yet low, significance and we present the results from both in Figs. 4.24 and 4.25. The ephemerides are, respectively, MJD $52233.8 \pm 6.5 + {\rm n} \times 92.8 \pm 0.5$ d and MJD $52239.4 \pm 0.9 + {\rm n} \times 87.3 \pm 0.5$ d. Given these ephemerides, it seems likely that SXP89.0 is not SXP91.1.

Judging by the folded light curves and the fit of the ephemerides to the X-ray

[3]This detection may in fact be SXP91.1 towards the end of its initial series of outbursts, although technically it should have been just outside of the field of view at the time this detection took place.

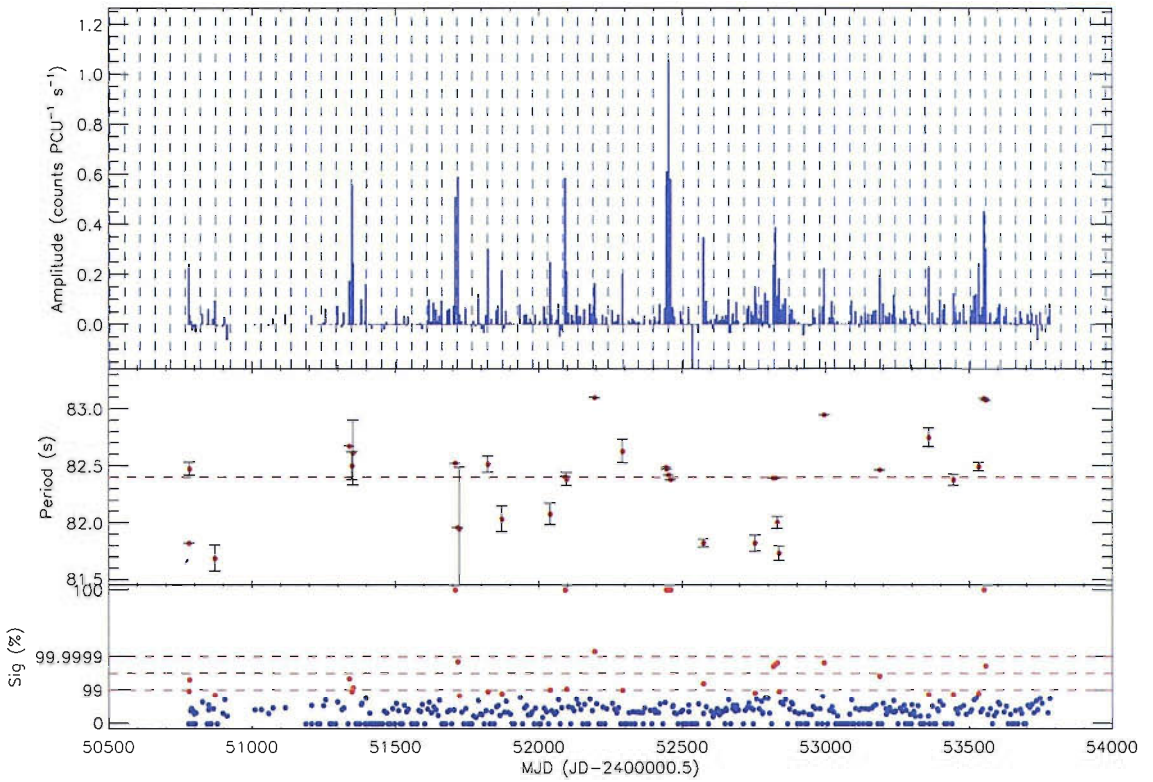

(a) X-ray amplitude light curve.

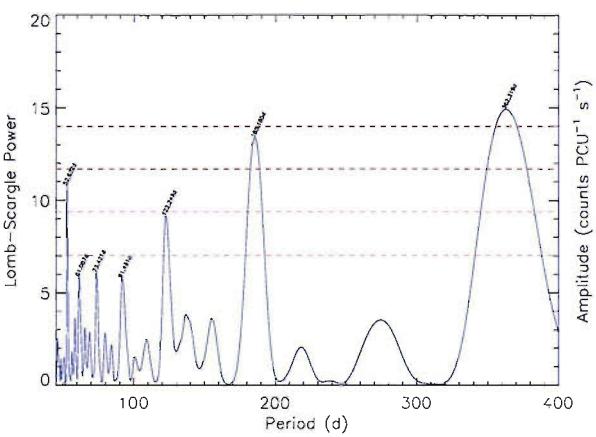

(b) Lomb-Scargle power spectrum.

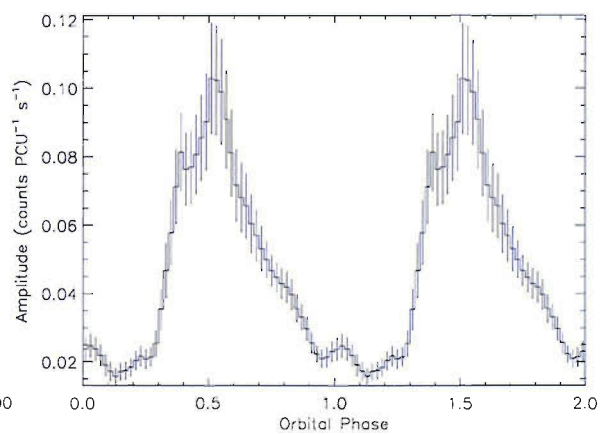

(c) Orbital profile folded at 52.63 d.

Figure 4.23: SXP82.4.

data, we believe the correct orbital period is 92.8 d; if this is the case, then the orbital profile appears to show significant emission at apastron.

4.1.24 SXP91.1

AX J0051−722, RX J0051.3−7216
RA 00 54 55, dec −72 13 38

History: Discovered in the first observation in this survey with a period of 92 ± 1.5 s (Marshall et al. 1997), further analysis improved this measurement to 91.12 ± 0.05 s (Corbet et al. 1998). An orbital period of 115 ± 5 d was derived by Laycock et al. (2005) from early survey data (before MJD 52200).

Survey Results: Only two further outburst have been detected after MJD 52200, both at a very low luminosity compared to the initial outbursts. The Lomb-Scargle periodogram of the whole light shows complicated structure, but the highest peak (with significance $> 99\%$) gives an orbital period of ~ 122 d, consistent with earlier estimates, although it should be noted that the ephemerides don't coincide with the two last outbursts. Timing analysis of the light curve post MJD 52300 shows no clear periods. The ephemeris we derive is MJD $52123.8 \pm 3.7 + \mathrm{n} \times 121.95 \pm 0.56$ d. Using the periods from detections with $Sig_{\mathrm{min}} = 99.99\%$ we find an average spin up during the outbursts of $\dot{P} = 1.8 \times 10^{-8}\,\mathrm{s\,s^{-1}}$, with a luminosity of $L_{\mathrm{x}} = 3.6 \times 10^{36}\,\mathrm{erg\,s^{-1}}$ ($B = 2.5 \times 10^{13}$ G).

4.1.25 SXP95.2

SMC 95
RA 00 52 00, dec −72 45 00

History: Was discovered in March 1999 in data from this survey (Laycock et al. 2002); the position was obtained with PCA scans over the source and has a large uncertainty. The X-ray orbital period suggested is 283 ± 8 d (Laycock et al. 2005).

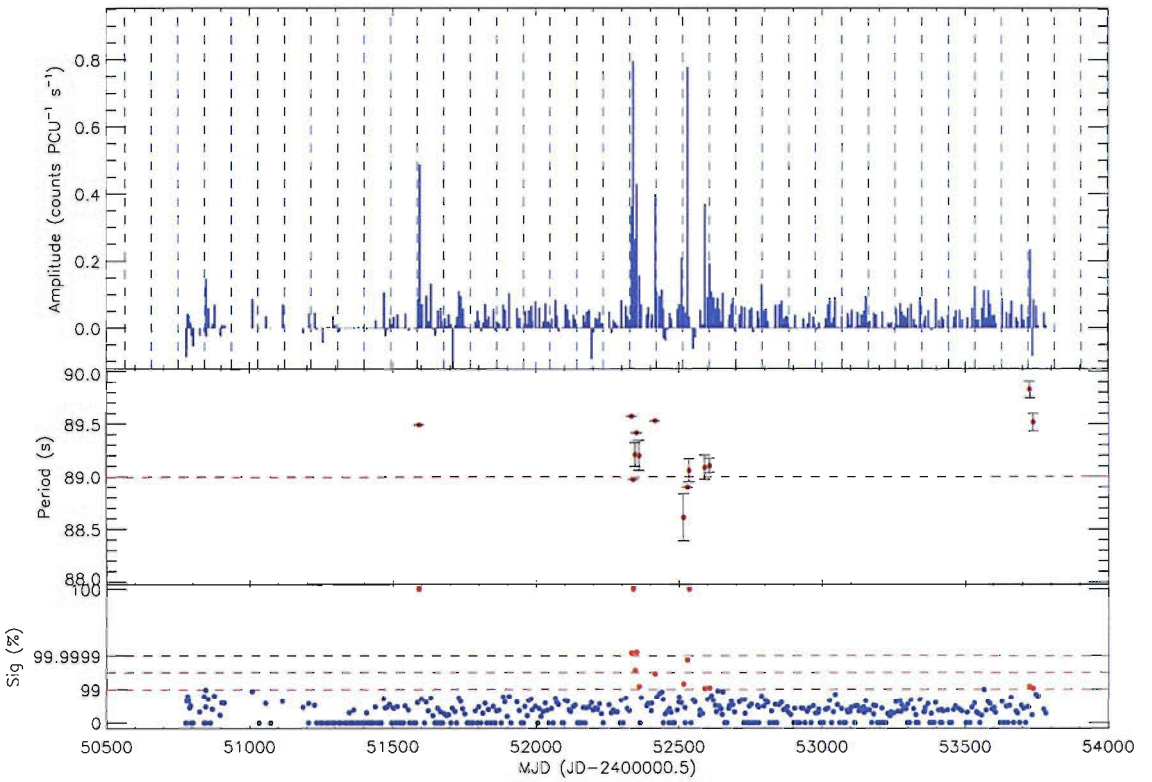

(a) X-ray amplitude light curve showing the possible 92.8 d orbital period.

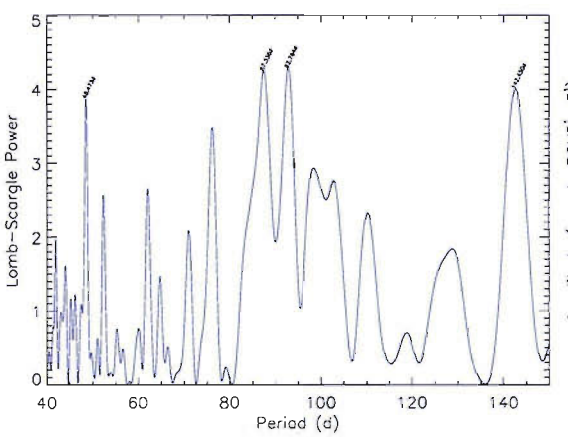

(b) Lomb-Scargle power spectrum.

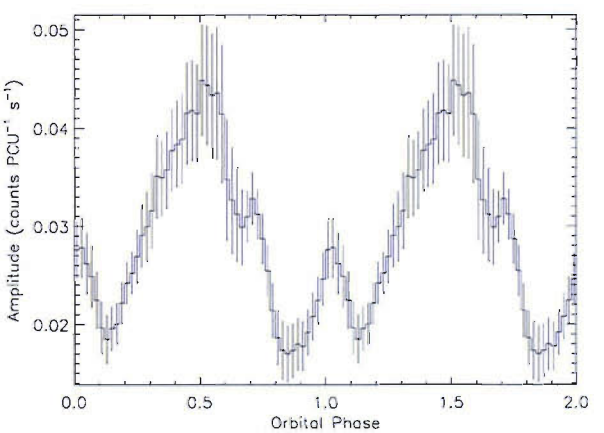

(c) Orbital profile folded at 92.8 d.

Figure 4.24: SXP89.0, possible orbital period = 92.8 d.

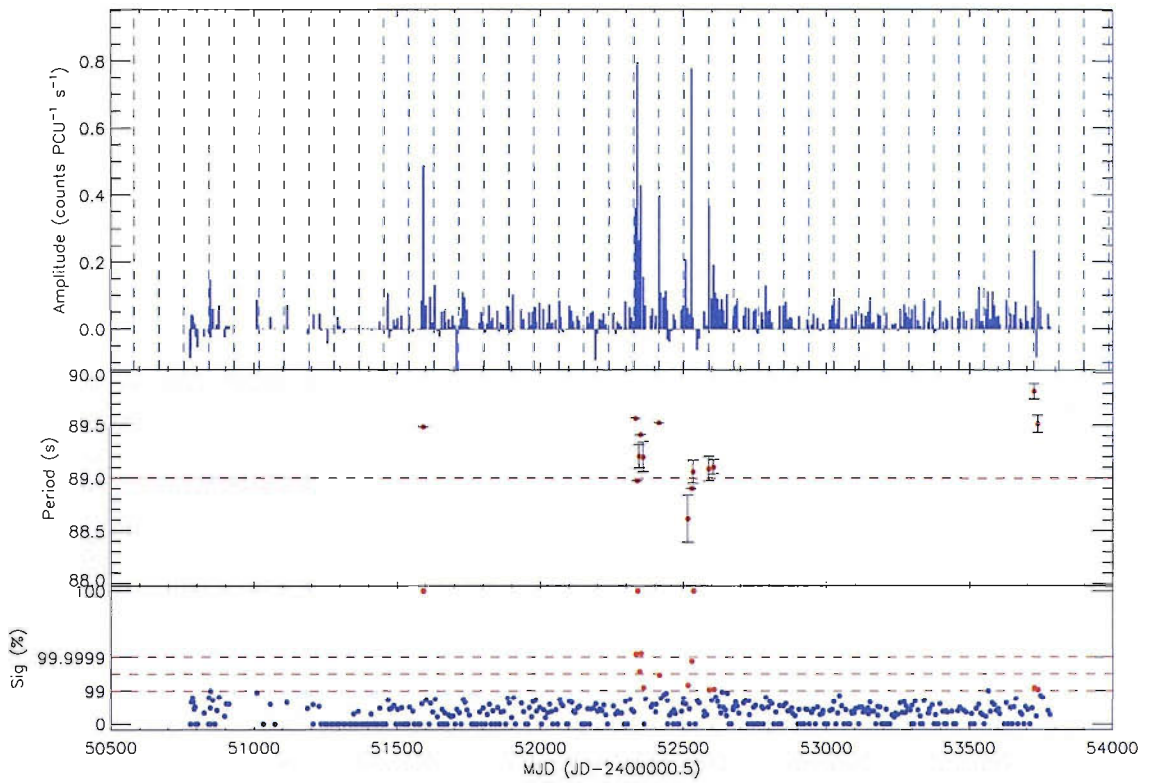

(a) X-ray amplitude light curve showing the possible 87.3 d orbital period.

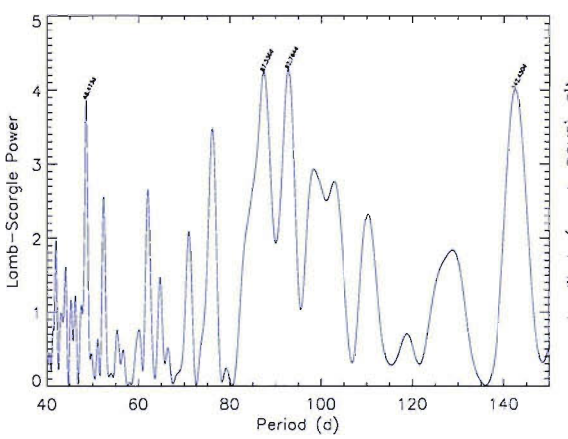

(b) Lomb-Scargle power spectrum.

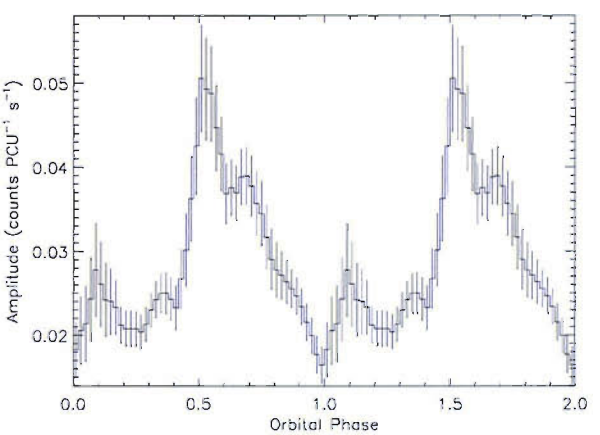

(c) Orbital profile folded at 87.3 d.

Figure 4.25: SXP89.0, possible orbital period = 87.3 d.

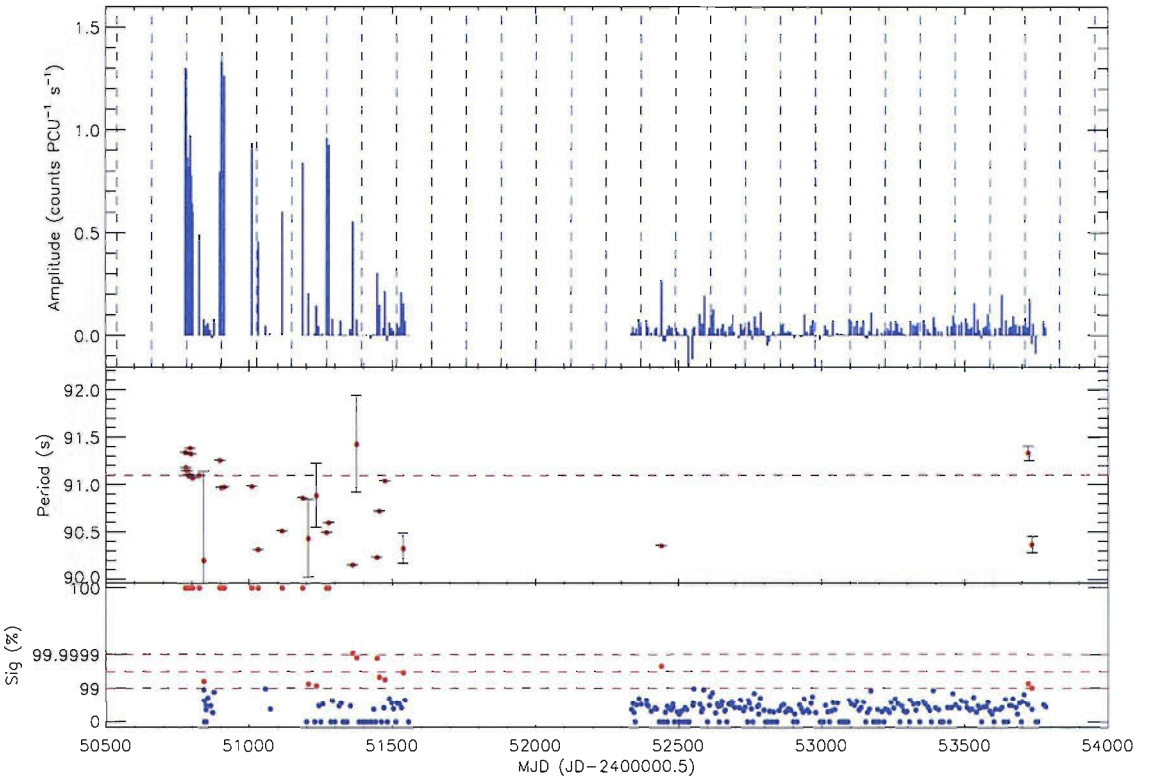

(a) X-ray amplitude light curve.

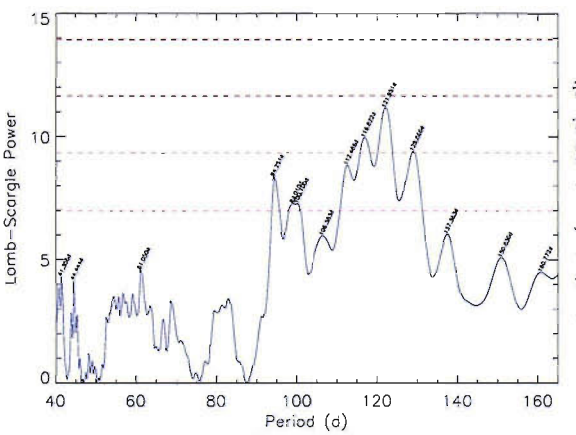

(b) Lomb-Scargle power spectrum.

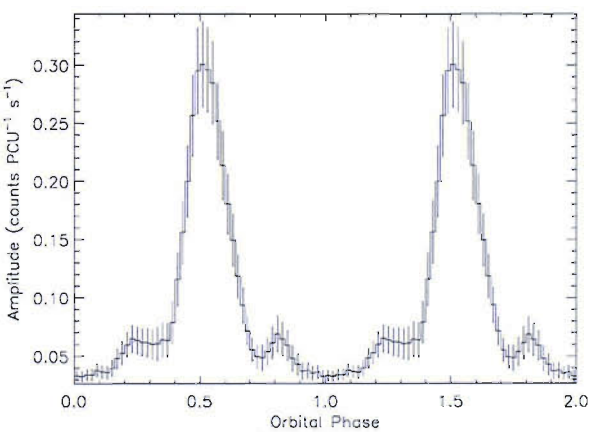

(c) Orbital profile folded at 121.95 d.

Figure 4.26: SXP91.1.

Stevens et al. (1999) identified the optical counterpart; Schmidtke et al. (2004) find an 88.25 d period in their analysis of MACHO data for this star.

Survey Results: Only 3 other marginal detections are available in the data. Lomb-Scargle analysis does not return any clear period, but there is a peak at ~ 148 d (which is twice the separation between the 2 major outbursts) which also fits two of the other minor detections. This value is in agreement with the pulse/orbital period relationship, and its ephemeris is MJD $52133.4 \pm 4.4 + \mathrm{n} \times 147.7 \pm 1.3$ d (see Fig. 4.28(a)). If the two bright outbursts are taken out of the data, we then find a period of 84 d, which is closer to the optical period and may be the correct orbital period of the system; its ephemeris is MJD $52240.1 \pm 5.9 + \mathrm{n} \times 84.0 \pm 0.4$ d (see Fig. 4.27(a)). It should be noted that both ephemerides agree with the last two significant detections, but neither with the MJD 52040 detection, which makes deciding which is the correct one difficult. More detections are required in order to settle the matter.

4.1.26 SXP101

RX J0057.3−7325, AX J0057.4−7325
RA 00 57 26.8, dec −73 25 02

History: Discovered in an *ASCA* observation at a period of 101.45 ± 0.07 s (Yokogawa et al. 2000b), and identified also as a *ROSAT* source. An tentative optical counterpart is suggested in Edge and Coe (2003), but no definitive companion has yet been found. Searches in OGLE data of 24 objects within the *ASCA* error circle revealed no periodicities (Edge 2005).

Survey Results: This pulsar lies in the SE edge of the wing and was in the field of view of Positions 4 and 5, so coverage is only continuous through AO5 and AO6. During this time 3 outbursts of low brightness were observed, with maybe 4 other data points just under the significance threshold being source detections. At 99% significance threshold a weak period of 22.90 ± 0.03 d is detected. Lowering the threshold to 95% brings out 5 further outbursts, which do not change the period.

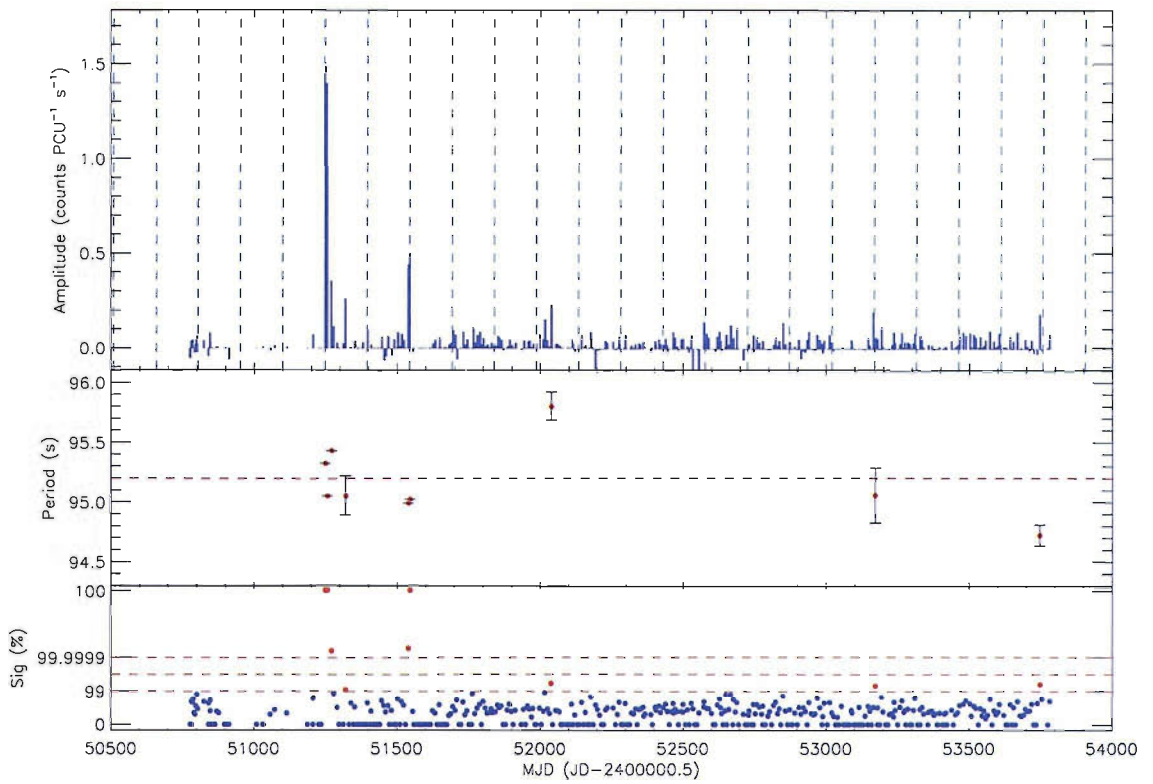

(a) X-ray amplitude light curve showing the possible 147.7 d orbital period.

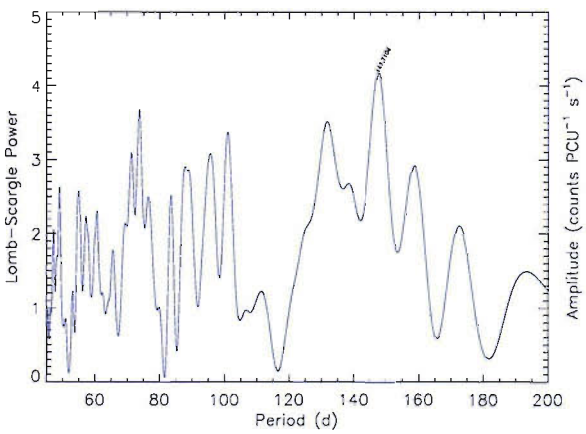

(b) Lomb-Scargle power spectrum.

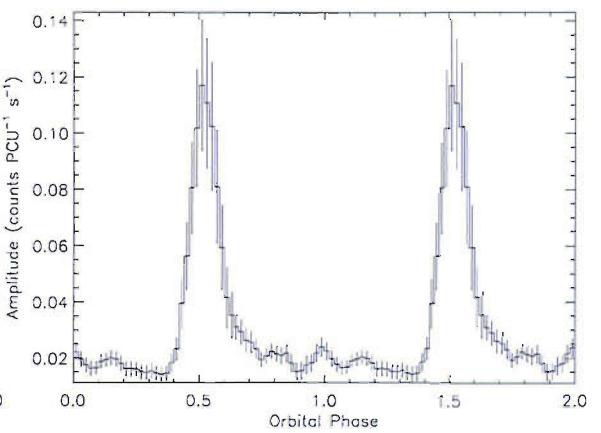

(c) Orbital profile folded at 147.7 d.

Figure 4.27: SXP95.2, possible orbital period = 147.7 d.

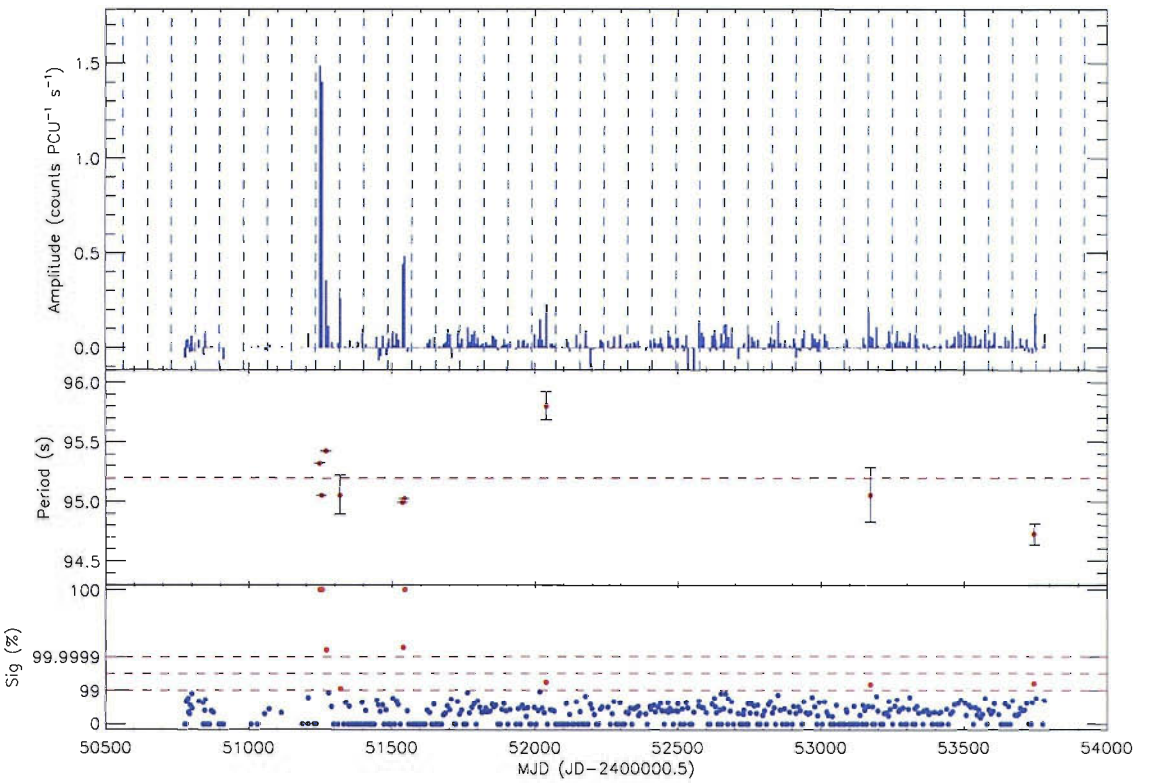

(a) X-ray amplitude light curve showing the possible 84.0 d orbital period.

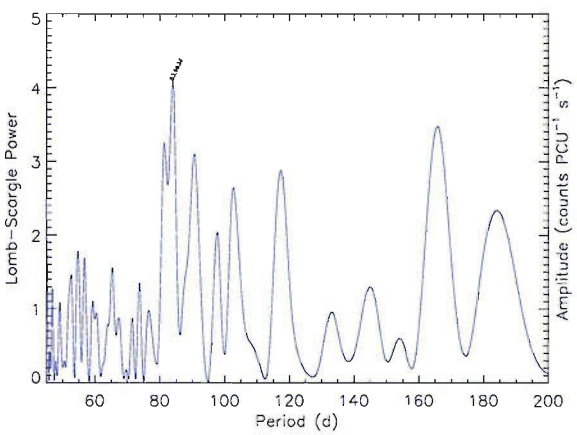

(b) Lomb-Scargle power spectrum.

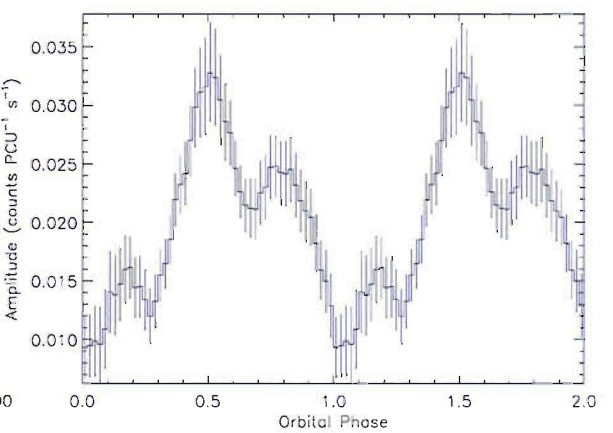

(c) Orbital profile folded at 84.0 d.

Figure 4.28: SXP95.2, possible orbital period = 84.0 d.

We are reticent to claim this as the orbital period, as the expected value would be ~ 100 d, but the folded light curve shows a clear, wide peak, with a small hump at apastron. Longer coverage would be required to establish whether or not this is truly the orbital period; its ephemeris is MJD $52111.4 \pm 1.2 + \mathrm{n} \times 22.95 \pm 0.03$ d.

4.1.27 SXP138

CXOU J005323.8−722715
RA 00 53 23.8, dec −72 27 15.0

History: Discovered in archival *Chandra* data (Edge et al. 2004b), the optical counterpart is [MA93] 667 (Edge 2005). The MACHO light curves for the companion star reveal peaks at ~ 125.1 d intervals (stronger in the red band).

Survey Results: X-ray data from this survey show two strong detections ~ 125 d apart. Lowering the detection threshold to 95% significance does not bring out any further detections, most likely because SXP138 is located very close to the centre of Position 1/A, which leads to a small collimator correction (the two bright detections took place when *RXTE* was observing Position 5, for which there is a larger collimator correction for SXP138). In order for these two detections not to sway the Lomb-Scargle analysis, they were removed from the data. We find two possible periods in the power spectrum at ~ 133 and ~ 123 d; we present both results in Figs. 4.30 and 4.31. The ephemerides are, respectively, MJD $52215.1 \pm 6.6 + \mathrm{n} \times 132.6 \pm 1.0$ d, MJD $52226.0 \pm 3.7 + \mathrm{n} \times 122.6 \pm 0.9$ d. The 122.6 d ephemeris seems to coincide with the two bright detections, which leads us to believe this is the likely orbital period of the system; it is also the closest to the reported optical period. If 122.6 d is the orbital period, then the folded light curve in Fig. 4.31(c) could be showing an eclipse of the neutron star by its Be companion.

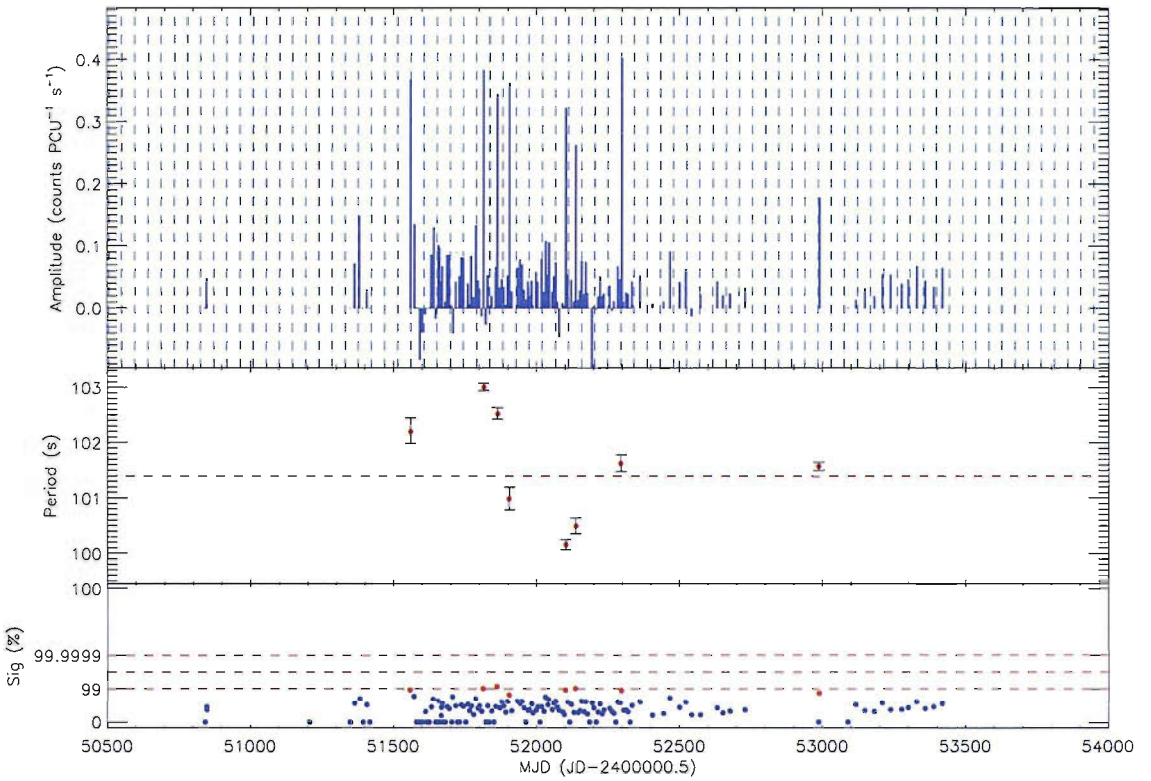

(a) X-ray amplitude light curve. For clarity, only every other ephemeris line has been plotted.

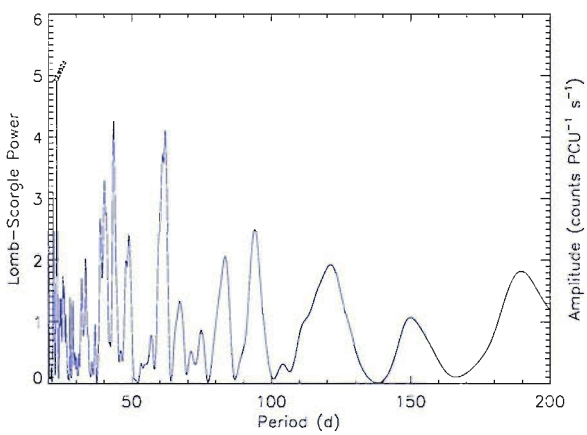

(b) Lomb-Scargle power spectrum.

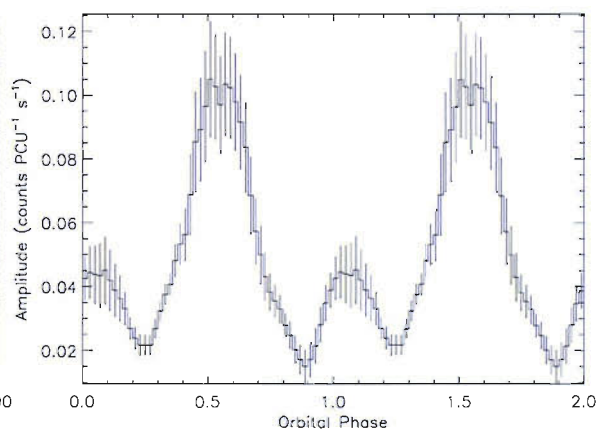

(c) Orbital profile folded at 22.95 d.

Figure 4.29: SXP101.

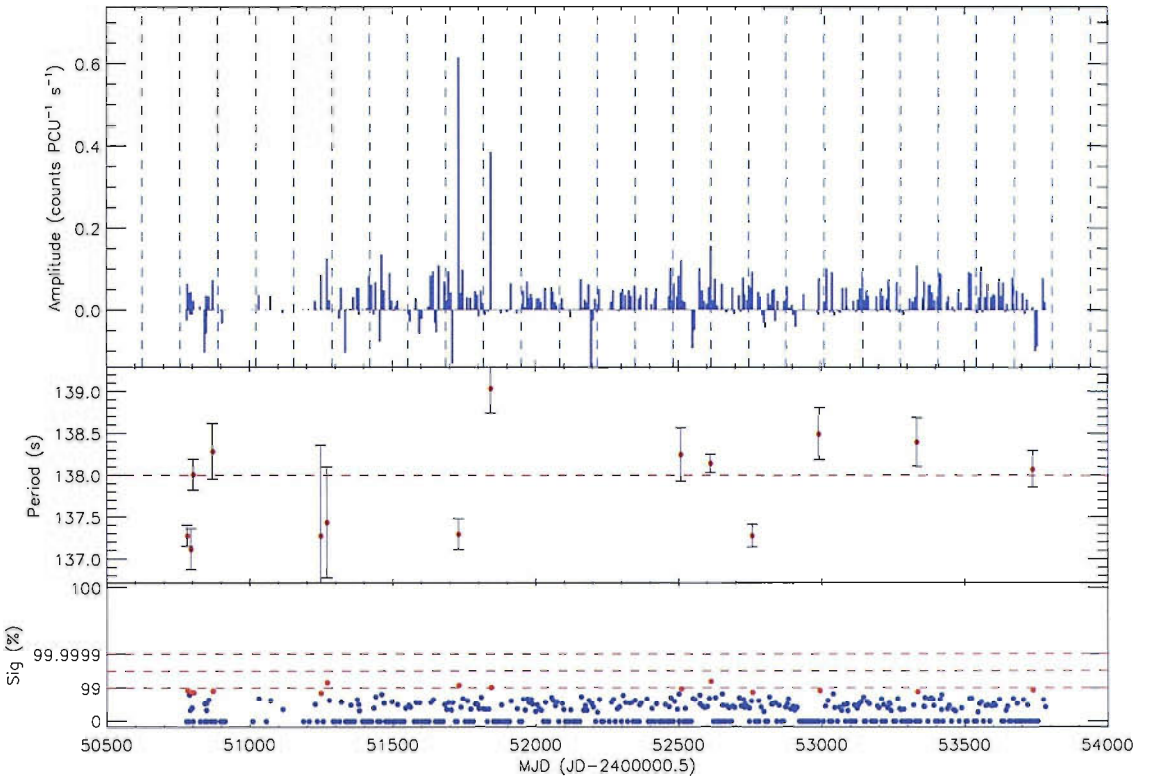

(a) X-ray amplitude light curve showing the possible 132.6 d orbital period.

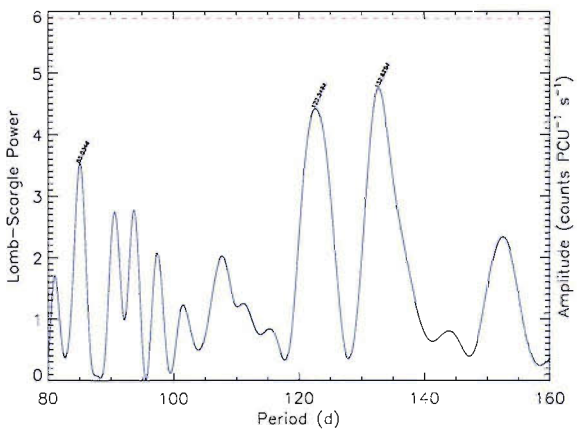

(b) Lomb-Scargle power spectrum.

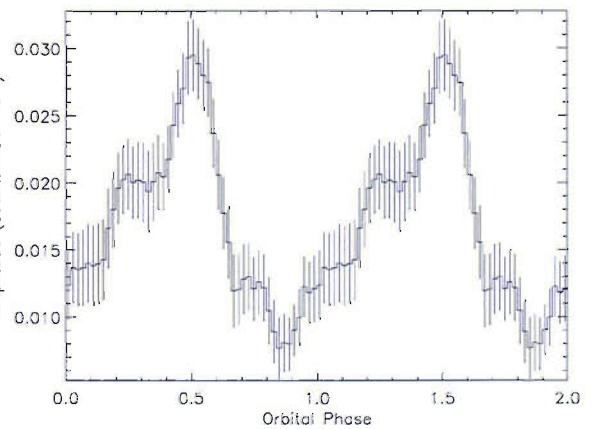

(c) Orbital profile folded at 132.6 d.

Figure 4.30: SXP138, possible orbital period = 132.6 d.

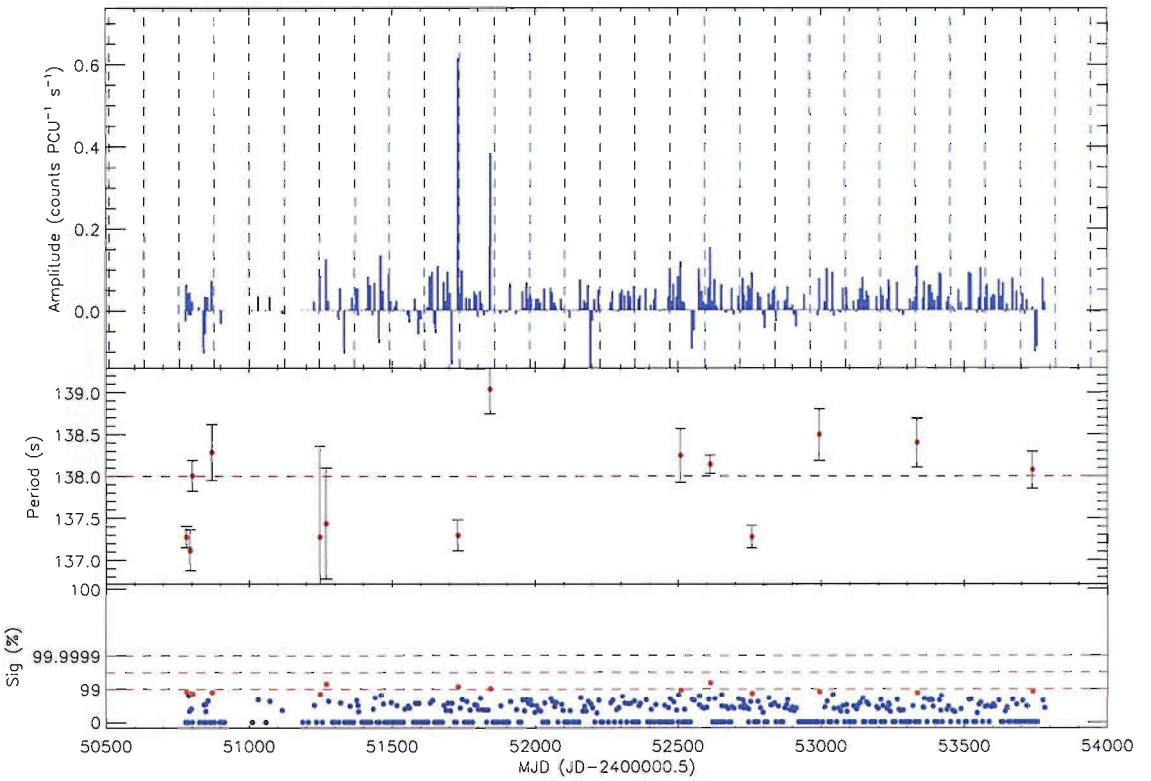

(a) X-ray amplitude light curve showing the possible 122.6 d orbital period.

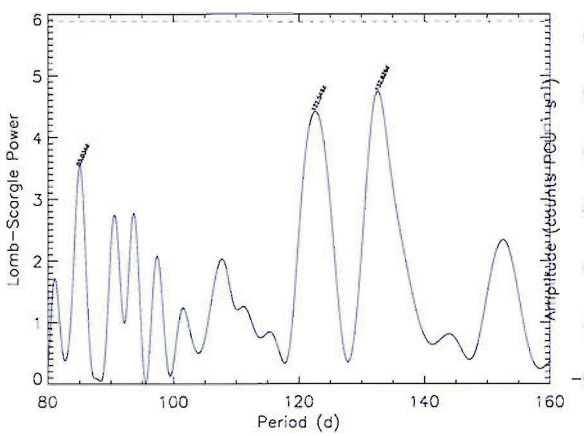

(b) Lomb-Scargle power spectrum.

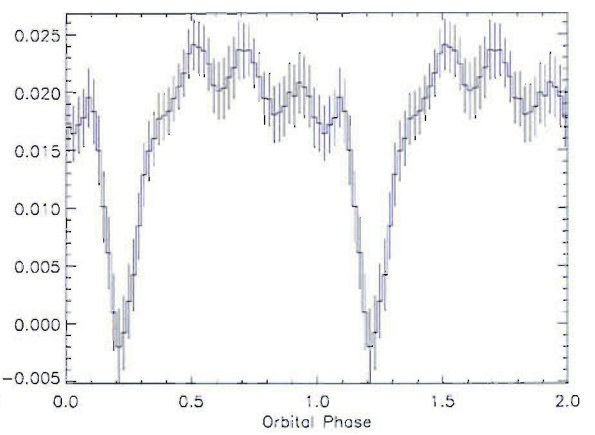

(c) Orbital profile folded at 122.6 d.

Figure 4.31: SXP138, possible orbital period = 122.6 d.

4.1.28 SXP140

XMMU J005605.2−722200, 2E0054.4−7237
RA 00 56 05.7, dec −72 22 00

History: Discovered in *XMM* observations by Sasaki et al. (2003). The optical counterpart is believed to be [MA93] 904 (Haberl and Pietsch 2004); no optical periods have been reported.

Survey Results: None of the detections has been longer than 1 week, with only 2 of them showing significant brightness. As there are a number of data points with a significance just below 99%, we used $Sig_{\rm min} = 98\%$ to bring them out. The strongest period we find is $\sim$61 d (Fig. 4.32), although this would be $\sim \frac{1}{2}$ the expected Corbet period. For this reason, we also present the data using twice the period (Fig. 4.33). The respective ephemerides are MJD $52221.5 \pm 1.9 + {\rm n} \times 61.5 \pm 0.2$ d and MJD $52214.1 \pm 6.2 + {\rm n} \times 123.00 \pm 0.4$ d.

4.1.29 SXP144

XTE SMC pulsar
No position available

History: Detected in observations from this survey in April 2003 by Corbet et al. (2003e), who later reported an ephemeris of MJD $52779.2 \pm 2.9 + {\rm n} \times 61.2 \pm 1.6$ d (Corbet et al. 2003c).

Survey Results: Although there are a few minor detections before the initial discovery, April 2003 saw the beginning of a regular pattern of outbursts which have continued until the present day. The neutron star has displayed an extremely linear and constant spin *down* during this time, with an average $\dot{P} = 1.6 \times 10^{-8}\,{\rm s\,s^{-1}}$; from this we would expect $L_{\rm x} = 1.1 \times 10^{36}\,{\rm erg\,s^{-1}}$ ($B = 2.4 \times 10^{13}$ G). The new outburst ephemeris we derive is MJD $52249.2 \pm 3.0 + {\rm n} \times 59.49 \pm 0.09$ d which is slightly lower than we would have expected, especially since it is spinning down, moving it even

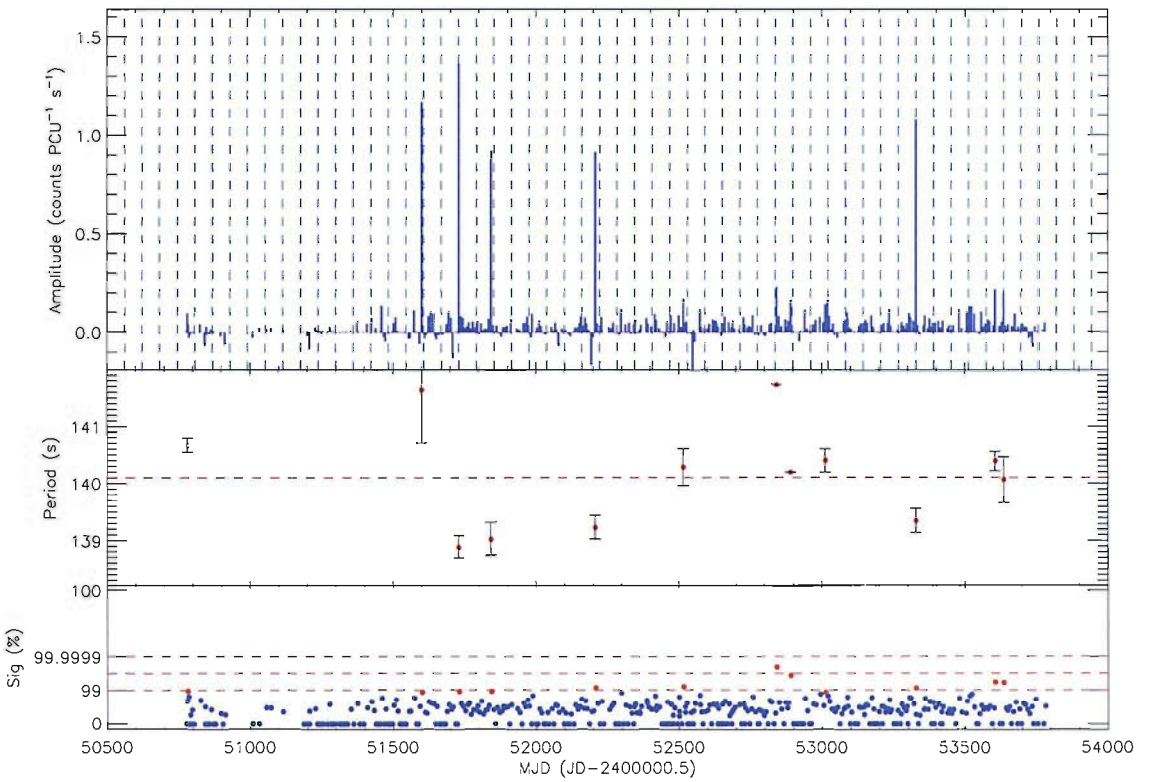

(a) X-ray amplitude light curve showing the possible 61.5 d orbital period.

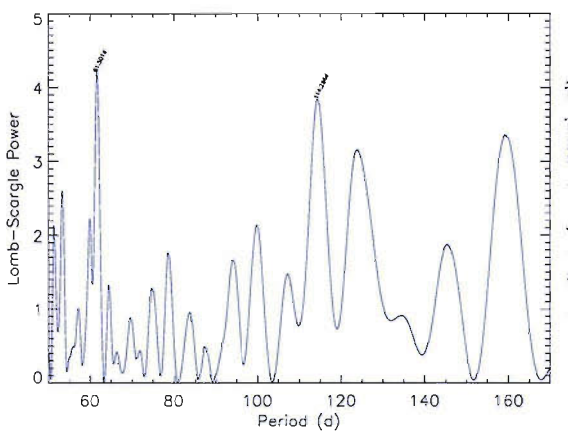

(b) Lomb-Scargle power spectrum.

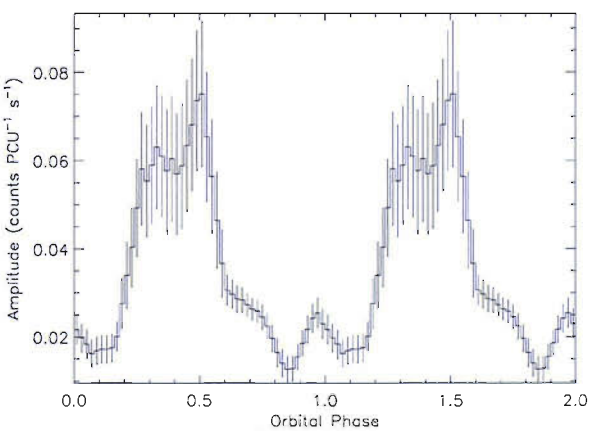

(c) Orbital profile folded at 61.5 d.

Figure 4.32: SXP140, possible orbital period = 61.5 d.

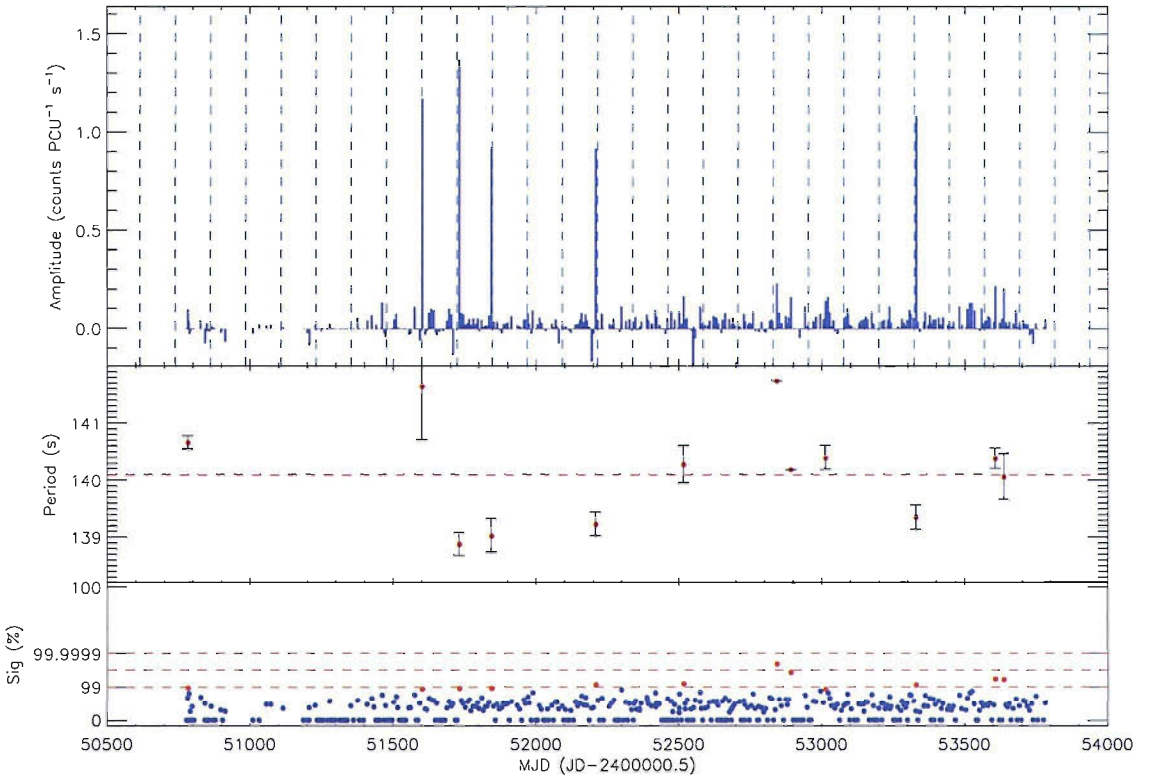

(a) X-ray amplitude light curve showing the possible 123.0 d orbital period.

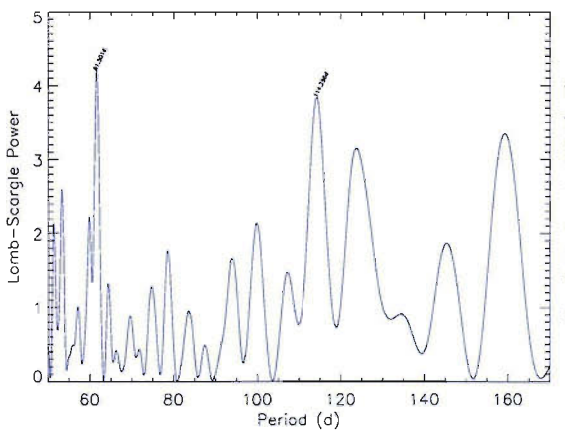

(b) Lomb-Scargle power spectrum.

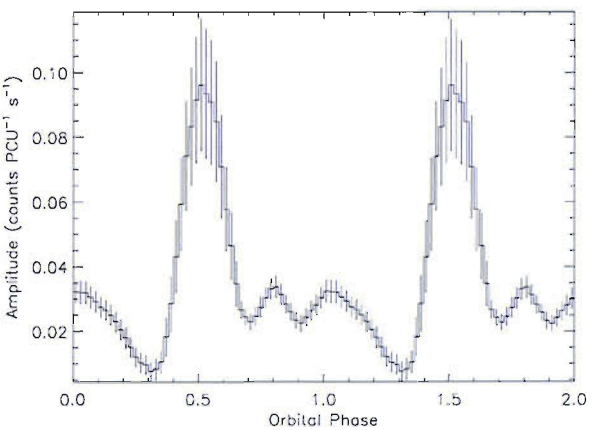

(c) Orbital profile folded at 123.0 d.

Figure 4.33: SXP140, possible orbital period = 123.0 d.

further away from the Be group on the Corbet diagram. This could make sense if we were observing two outbursts per orbit but there is nothing in the light curve or orbital profile that would indicate this is the case. In fact, Fig. 4.34(c) seems to show evidence of small apastron outbursts.

4.1.30 SXP152

CXOU J005750.3−720756
RA 00 57 49, dec −72 07 59

History: Haberl and Sasaki (2000) suggested this object as a Be binary pulsar based on a Hα-emitting object in the [MA93] catalogue, although *ROSAT* observations of this source had not detected any pulsations. These were found in a long *Chandra* observation by Macomb et al. (2003) at a period of 152.098 ± 0.016 s (they report a very high pulse fraction of $64 \pm 3\%$ and a $L_{\rm x} = 2.6 \times 10^{35}\,{\rm erg\,s^{-1}}$), and in an *XMM* observation by Sasaki et al. (2003) at 152.34 ± 0.05 s.

Survey Results: The periodogram of the light curve shows an interesting structure, with no defined period. The lack of periodic outbursts, despite its clear X-ray activity, may point towards a low eccentricity system. This would facilitate accretion onto the neutron star at points other than at periastron (as is expected in a high eccentricity system). Analysis of the optical light curve of the companion star may clarify its situation. The ephemeris we find for the strongest period in the power spectrum is MJD $52227.7 \pm 3.2 + {\rm n} \times 105.7 \pm 0.6$ d.

4.1.31 SXP169

XTE J0054−720, AX J0052.9−7158, RX J0052.9−7158
RA 00 52 54.0, dec −71 58 08.0

History: First detected by *RXTE* in December 1998 at a period of 169.30 s (Lochner et al. 1998). Laycock et al. (2005) suggest a possible orbital period of 200 ± 40 d.

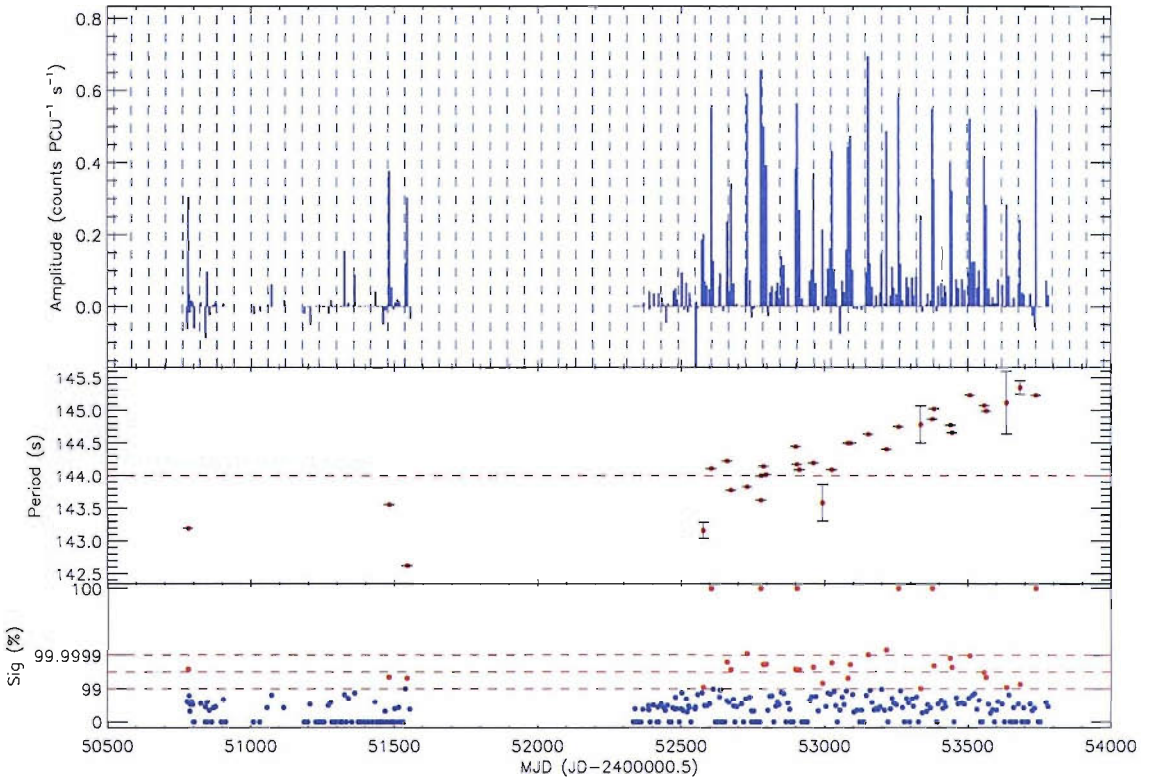

(a) X-ray amplitude light curve.

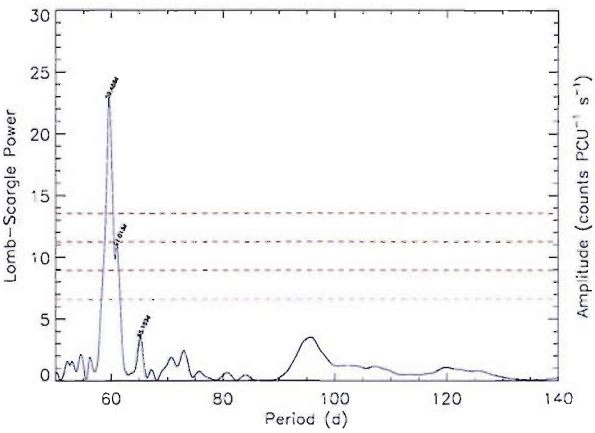

(b) Lomb-Scargle power spectrum.

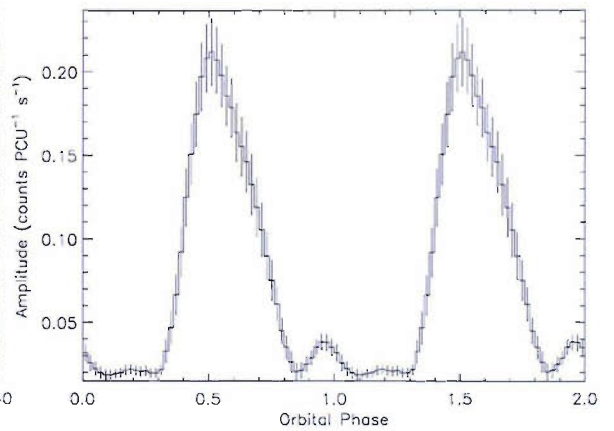

(c) Orbital profile folded at 59.49 d.

Figure 4.34: SXP144.

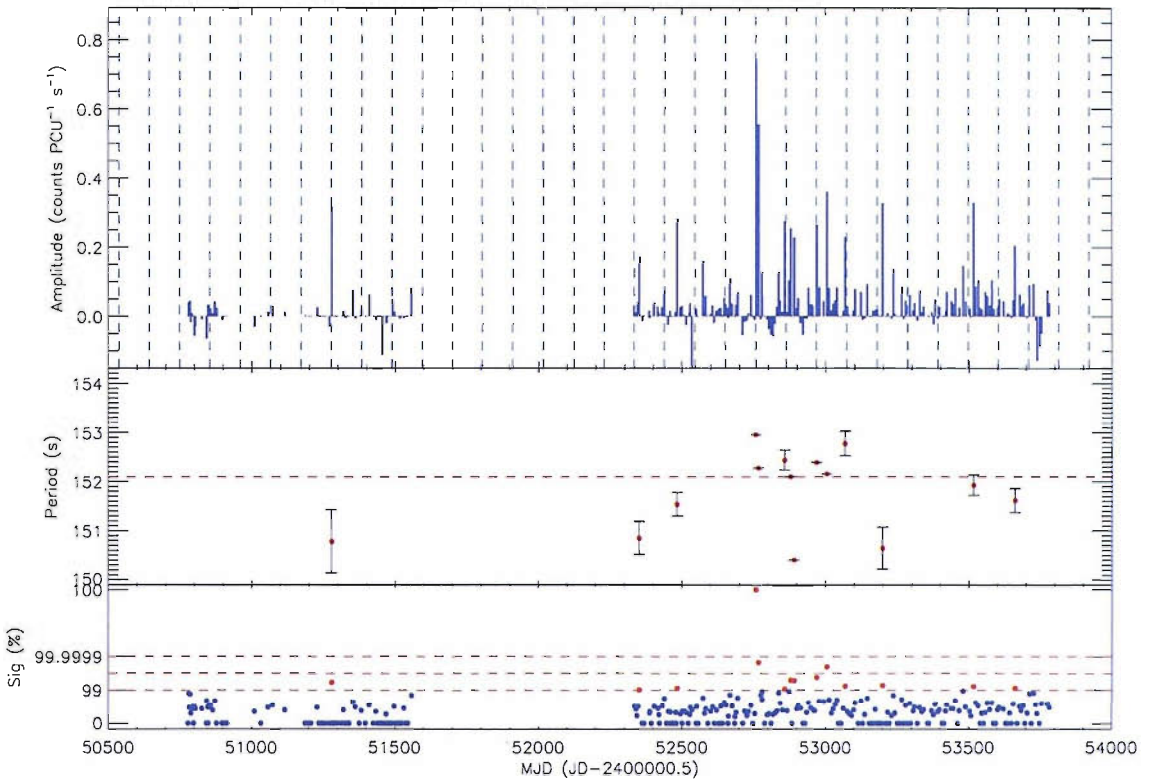

(a) X-ray amplitude light curve.

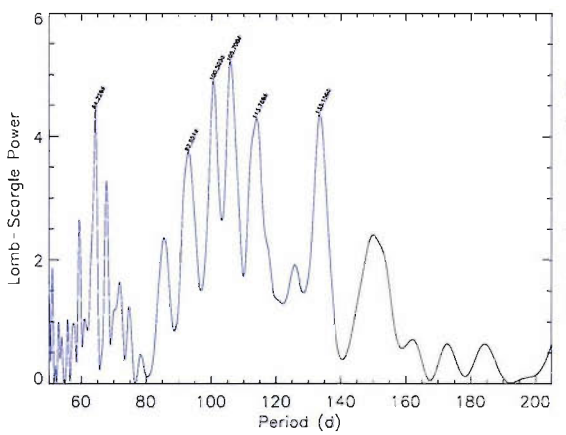

(b) Lomb-Scargle power spectrum.

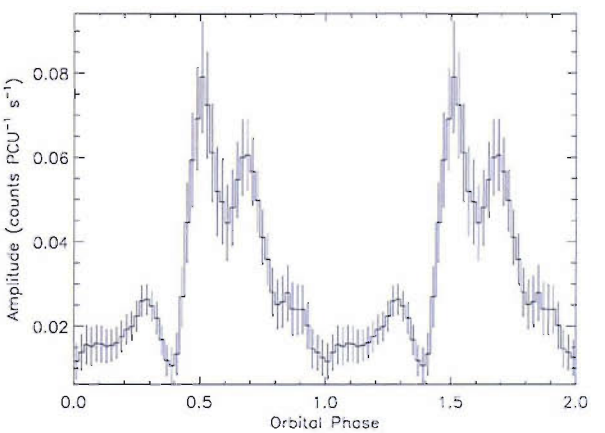

(c) Orbital profile folded at 105.7 d.

Figure 4.35: SXP152.

Galache et al. (2005) reported an orbital period of 68.6 ± 0.2.

Survey Results: Corbet et al. (2004b) announced a new SMC pulsar at 164.7 s, with an unknown position. After comparing the long term light curves and the ephemerides from timing analysis it became apparent that SXP165 and SXP169 were the same source. A consolidated light curve is presented here, where the spin up of SXP169 can be seen. Similar to SXP59.0, there appear to be two groups of outbursts that begin and end at similar periods (although the end, if there ever was one, of the first group cannot be seen for lack of coverage, and the second group seems to experience a reversal of spin torque towards the end). For the first group we estimate $\dot{P} = 2.5 \times 10^{-8}\,\mathrm{s\,s^{-1}}$, implying $L_\mathrm{x} = 1.2 \times 10^{-36}\,\mathrm{erg\,s^{-1}}$ ($B = 3.0 \times 10^{13}$ G); for the second, $\dot{P} = 2.0 \times 10^{-8}\,\mathrm{s\,s^{-1}}$, implying $L_\mathrm{x} = 9.6 \times 10^{35}\,\mathrm{erg\,s^{-1}}$ ($B = 2.6 \times 10^{13}$ G). Lomb-Scargle analysis provides a clear period, and the outbursts are described by the ephemeris MJD $52241.1 \pm 3.4 + \mathrm{n} \times 68.59 \pm 0.14$ d. This is yet another pulsar that has $\frac{1}{2}$ the expected orbital period.

4.1.32 SXP172

AX J0051.6−7311, RX J0051.9−7311
RA 00 51 52, dec −73 10 35

History: Found in an *ASCA* observation (Torii et al. 2000), it was identified with the *ROSAT* source RX J0051.9−7311, which has a Be optical counterpart (Cowley et al. 1997). Laycock et al. (2005) suggest a possible orbital period of ~ 67 d based on the X-ray activity up until MJD 52350.

Survey Results: SXP172 underwent a phase of intense, semi-regular, activity during MJD 51600 − 52400. In order to clean up the light curve during these times we increased the detection threshold to $Sig_\mathrm{min} = 99.9999\%$ (Fig. 4.37(a)) obtaining an ephemeris of MJD $52227.2 \pm 2.0 + \mathrm{n} \times 66.9 \pm 0.2$ d. The spin up observed during these outbursts, $\dot{P} = 1.5 \times 10^{-8}\,\mathrm{s\,s^{-1}}$, would imply $L_\mathrm{x} = 6.9 \times 10^{35}\,\mathrm{erg\,s^{-1}}$ ($B = 2.3 \times 10^{13}$ G).

Next we did the opposite and brought down the detection threshold to Sig_min

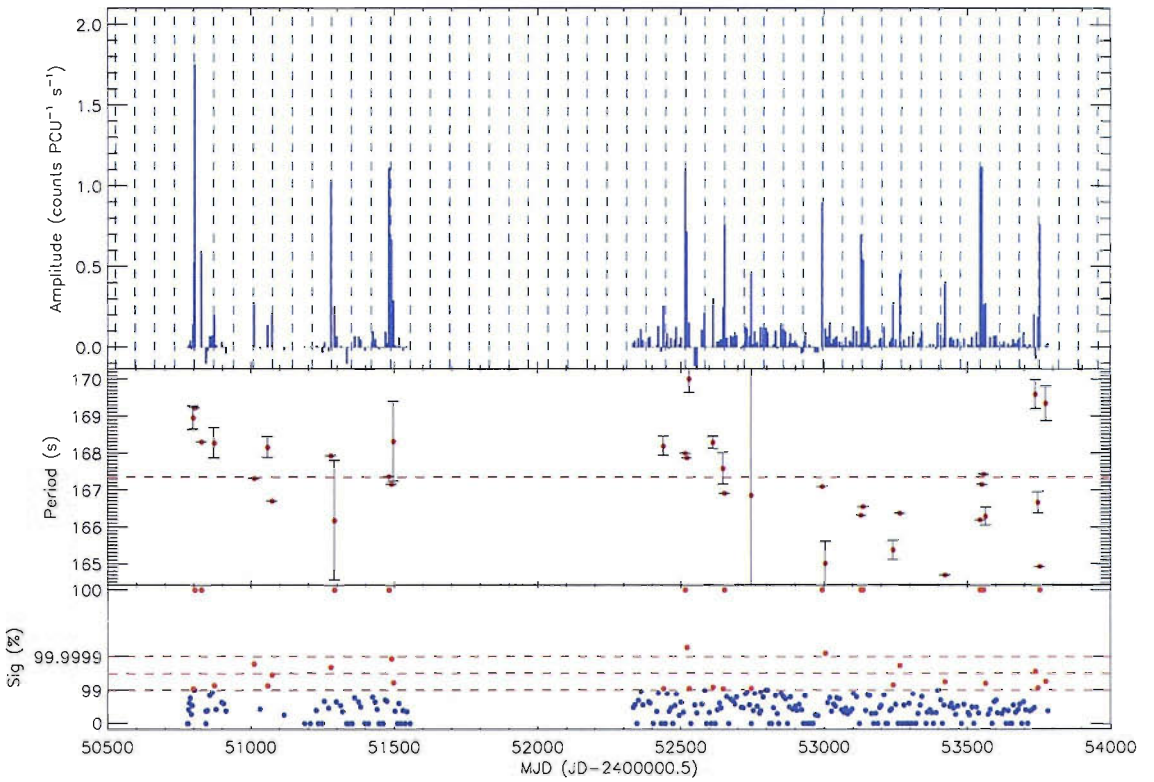

(a) X-ray amplitude light curve.

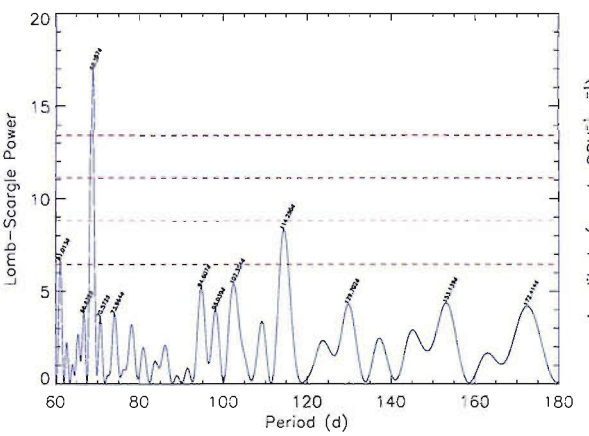

(b) Lomb-Scargle power spectrum.

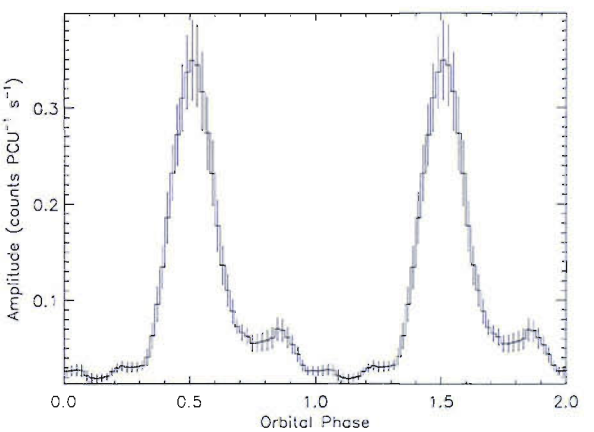

(c) Orbital profile folded at 68.59 d.

Figure 4.36: SXP169.

= 98%. The outburst ephemeris we obtain is similar (although the orbital period is now more significant) and is MJD $52219.6 \pm 3.4 + n \times 67.20 \pm 0.23$ d (Fig. 4.38). We believe this is the orbital ephemeris of the system.

4.1.33 SXP202

XMMU J005920.8−722316
RA 00 59 20.8, dec −72 23 16

History: Detected in a number of archival *XMM* observations and reported in Majid et al. (2004); the authors found an early B type star at the X-ray coordinates and classified it as a HMXB.

Survey Results: This source has shown little activity throughout the survey except for one very bright detection in January 2006. Lomb-Scargle analysis of the data excluding this bright detection finds an ephemeris of MJD $52192.0 \pm 4.2 + n \times 140.06 \pm 0.92$ d, which agrees with the faint beginning of the latest outburst (see Fig. 4.39.

4.1.34 SXP264

XMMU J004723.7−731226, RX J0047.3−7312, AX J0047.3−7312
RA 00 47 23.7, dec −73 12 25

History: First found by Ueno et al. (2004) in *XMM* observations, it was initially reported by Yokogawa et al. (2003) from *ASCA* observations. It had originally been proposed as a Be/X-ray binary candidate by Haberl and Sasaki (2000) based on its optical variability. Edge et al. (2005a) identified the companion as the emission line star [MA93] 172 and found an optical period of 48.8 ± 0.6 d, which they propose as the orbital period of the system. Further analysis of the OGLE light curve returns the ephemeris MJD $50592 \pm 2 + n \times 49.2 \pm 0.2$ d (Edge 2005).

Survey Results: Due to its location this pulsar was only observed consistently

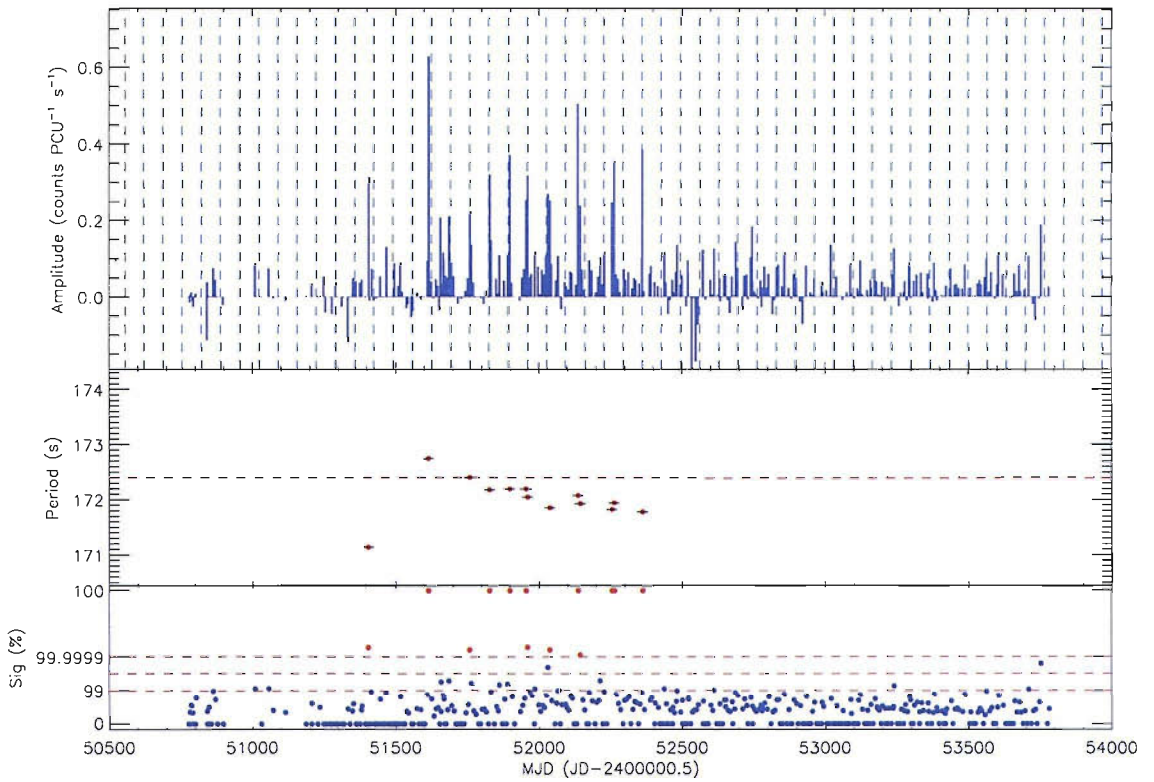

(a) X-ray amplitude light curve showing the possible 66.9 d orbital period.

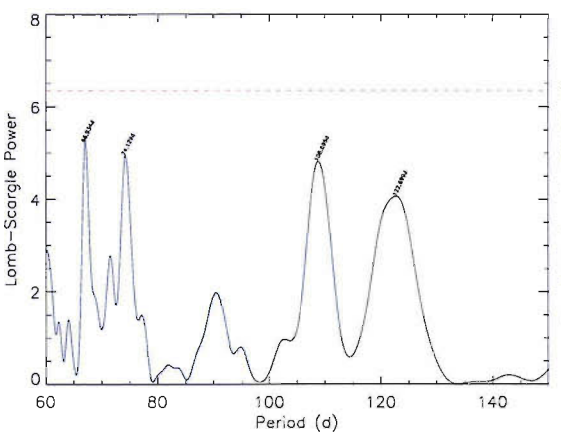

(b) Lomb-Scargle power spectrum.

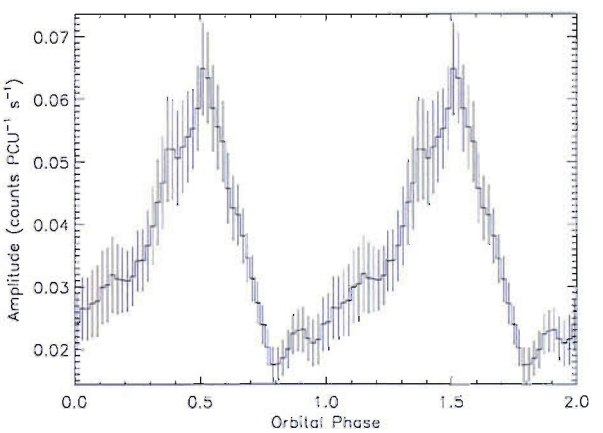

(c) Orbital profile folded at 66.9 d.

Figure 4.37: SXP172, possible orbital period = 66.9 d.

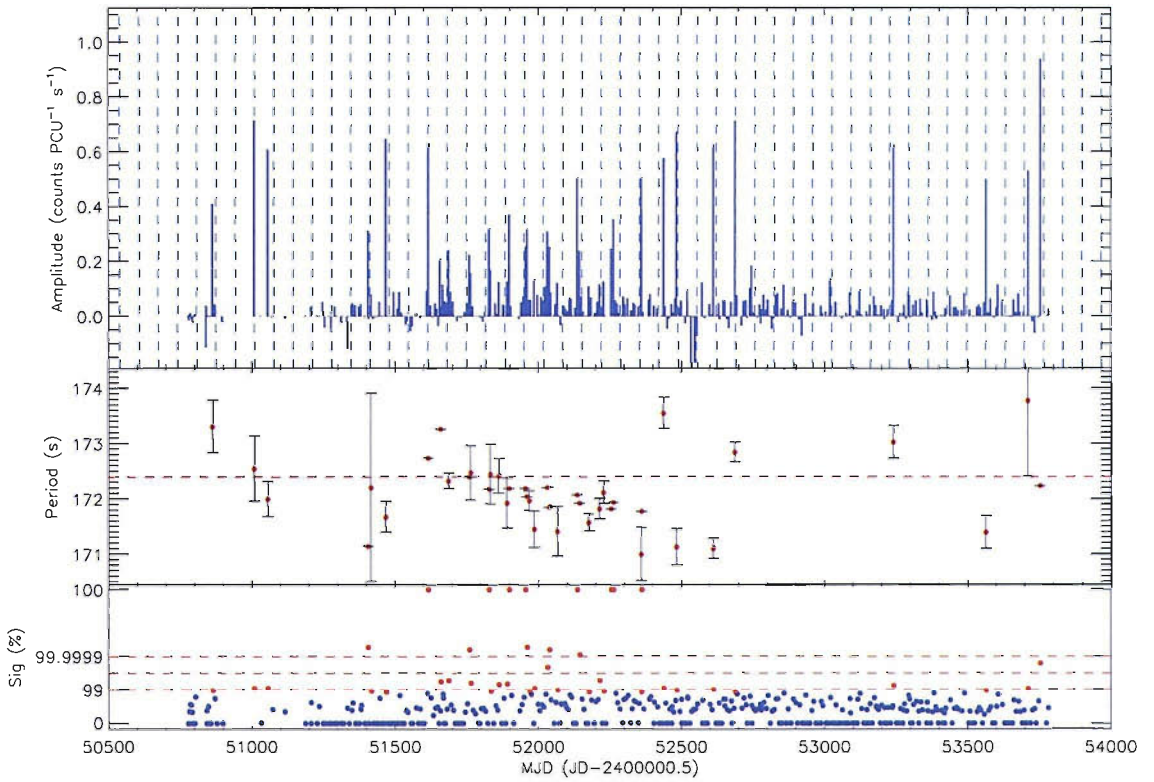

(a) X-ray amplitude light curve showing the possible 67.20 d orbital period.

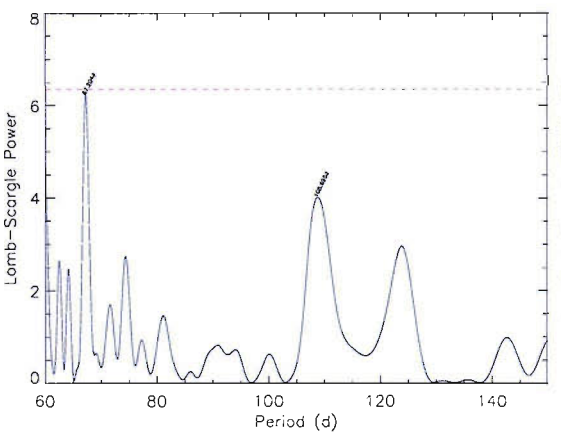

(b) Lomb-Scargle power spectrum.

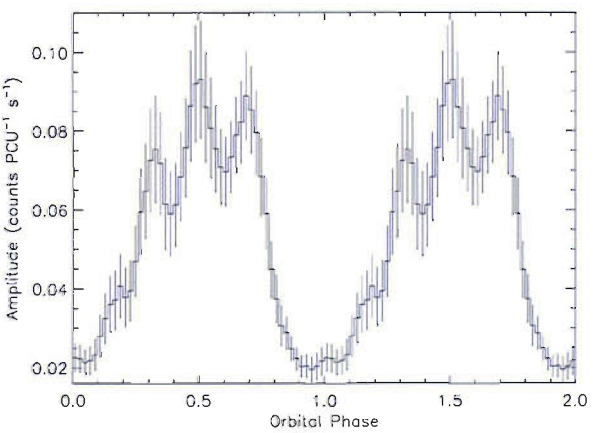

(c) Orbital profile folded at 67.20 d.

Figure 4.38: SXP172, possible orbital period = 67.20 d.

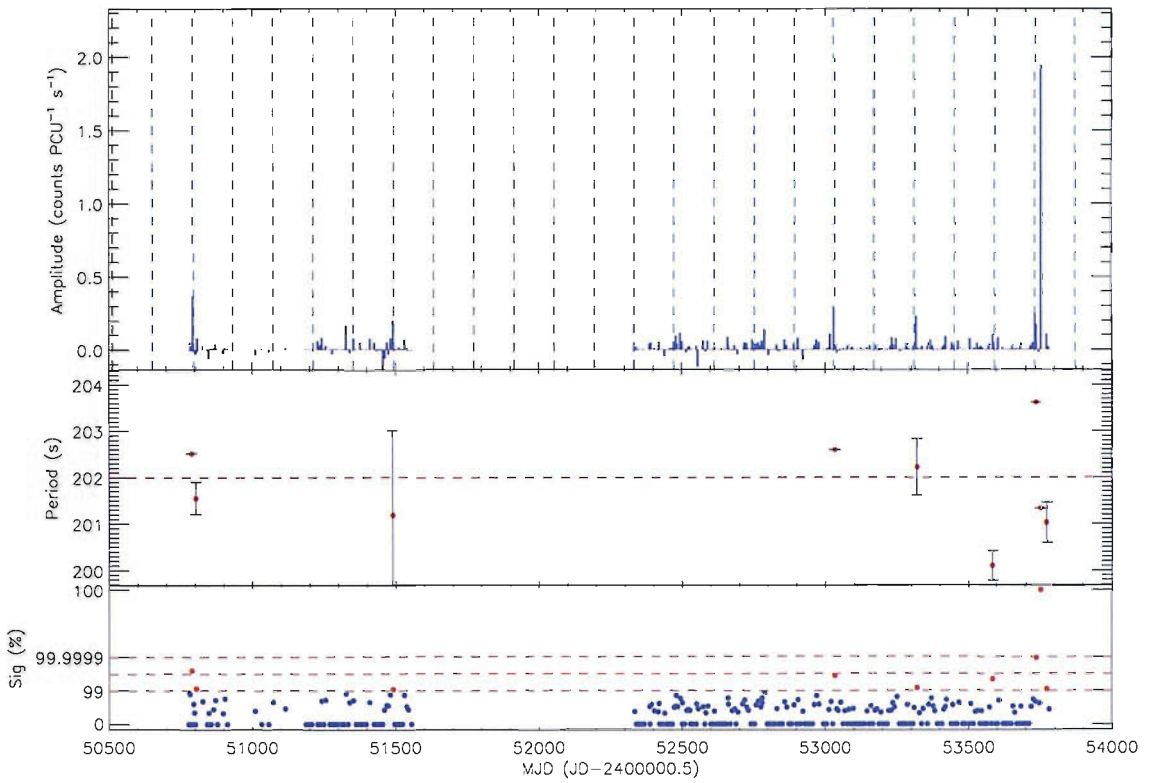

(a) X-ray amplitude light curve.

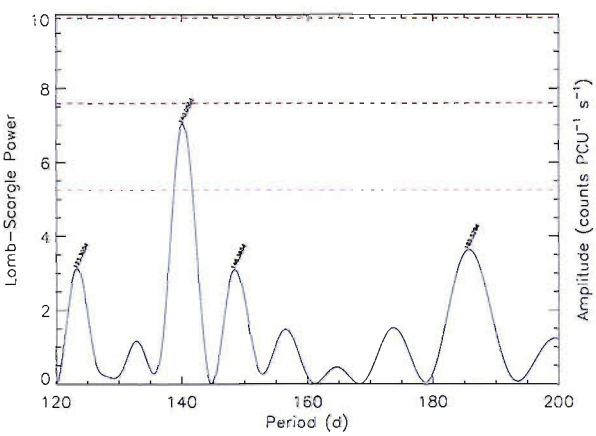

(b) Lomb-Scargle power spectrum.

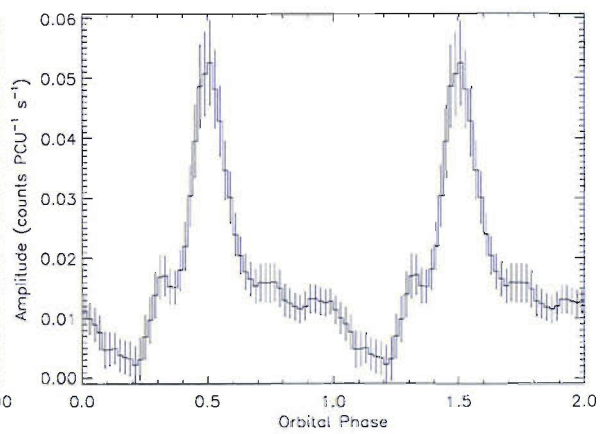

(c) Orbital profile folded at 140.06 d.

Figure 4.39: SXP202.

during AO5 and AO6. No major outbursts were observed and the main periodicity found in the X-ray is ~ 110 d (ephemeris MJD $52026.6 \pm 3.3 + n \times 109.8 \pm 0.8$ d); the power spectrum shows no significant peaks at the optical period, although a weak period is present at 51.8 d (ephemeris MJD $52052.0 \pm 2.6 + n \times 51.8 \pm 0.2$ d). The evidence for an orbital modulation in the X-rays is therefore inconclusive, but we present the data for both these periods in Figs. 4.40 and 4.41.

4.1.35 SXP280

RX J0057.8−7202, AX J0058−72.0
RA 00 57 48.2, dec −72 02 40

History: Discovered in March 1998 in an *ASCA* observation by Yokogawa and Koyama (1998a) at a period of 280.4 ± 0.3 s. Schmidtke et al. (2004) find a clear 59.72 d period in MACHO and OGLE data of RX J0057.8−7202, but they claim this binary shows no pulses, so it may be a source confusion.

Survey Results: There are only 5 clear detections of this source throughout the survey, and the power spectrum shows no significant periods. There are a number of data points just below 99% significance, so $Sig_{\rm min} = 95\%$ was also used. In this case, 5 more detections appear and a period of ~ 104 d seems to fit most of the outbursts. The ephemeris for this period is MJD $52305.4 \pm 3.1 + n \times 103.5 \pm 0.6$ d. There is no peak around 59.72 d.

4.1.36 SXP293

XTE J0051−727
RA 00 50 00, dec −73 06 00

History: Reported by Corbet et al. (2004c) from observations during this survey of the outburst at MJD 53097.

Survey Results: There are no high-significance detections in this survey, and the

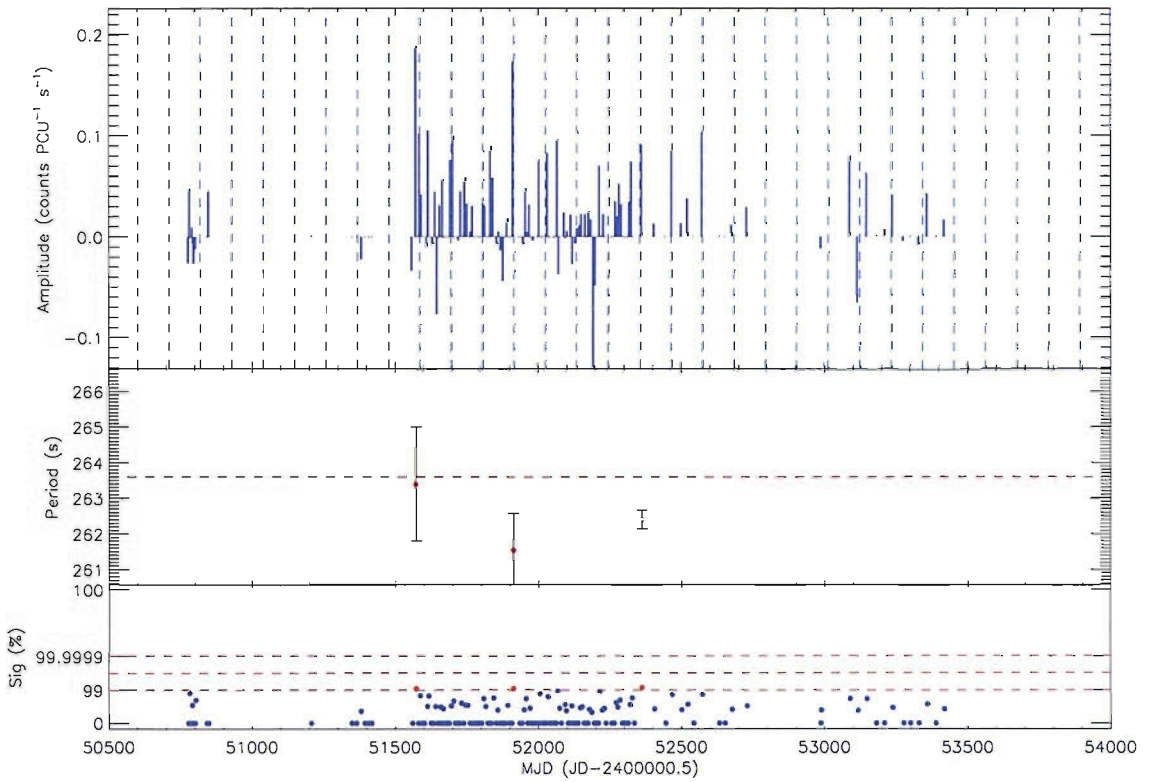

(a) X-ray amplitude light curve showing the possible 109.8 d orbital period.

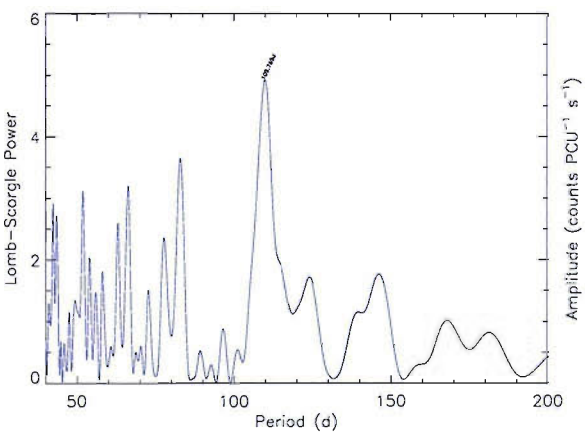

(b) Lomb-Scargle power spectrum.

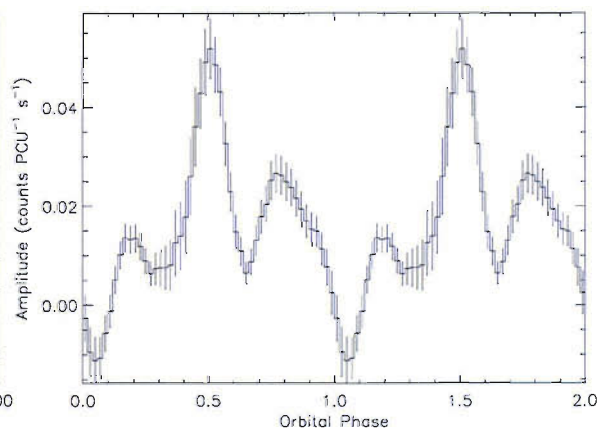

(c) Orbital profile folded at 109.8 d.

Figure 4.40: SXP264, possible orbital period = 109.8 d.

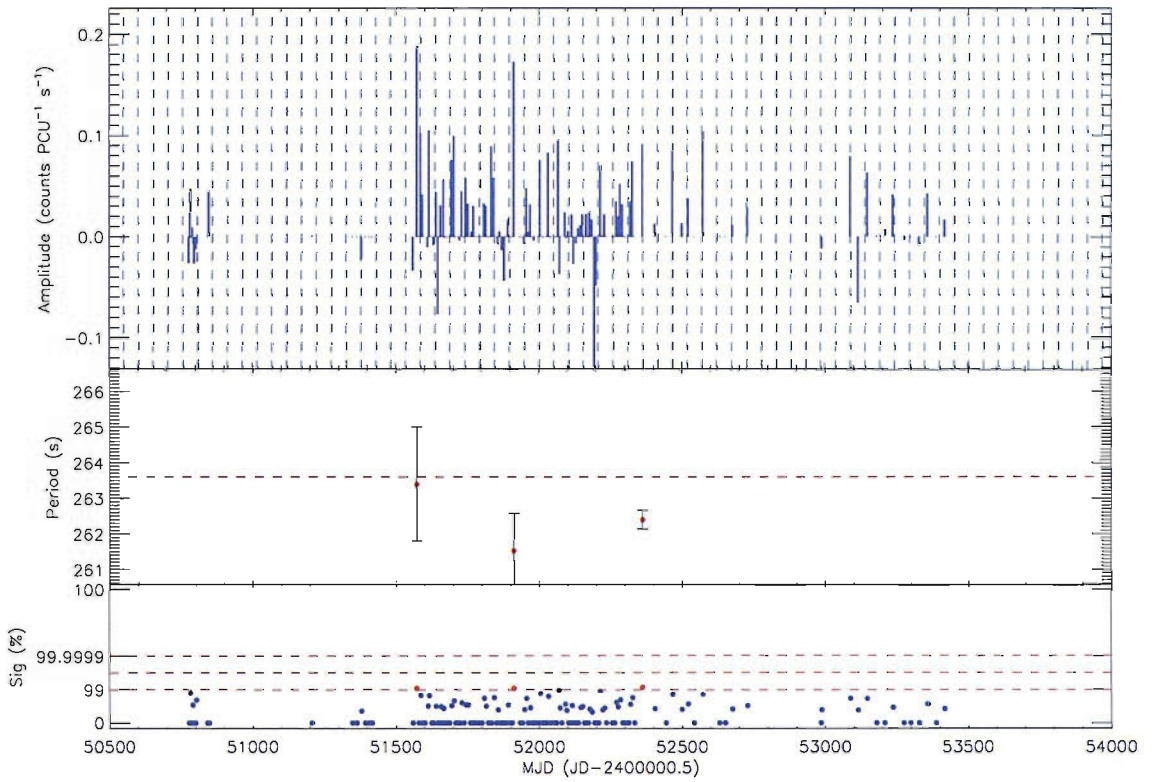

(a) X-ray amplitude light curve showing the possible 51.8 d orbital period.

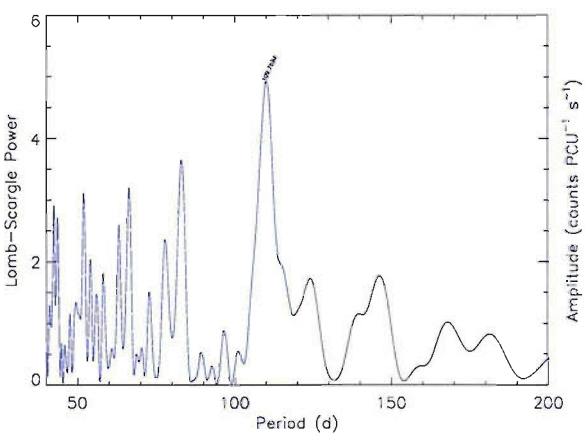

(b) Lomb-Scargle power spectrum.

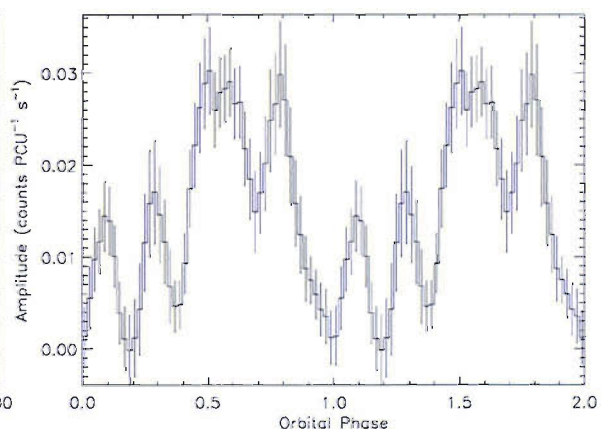

(c) Orbital profile folded at 51.8 d.

Figure 4.41: SXP264, possible orbital period = 51.8 d.

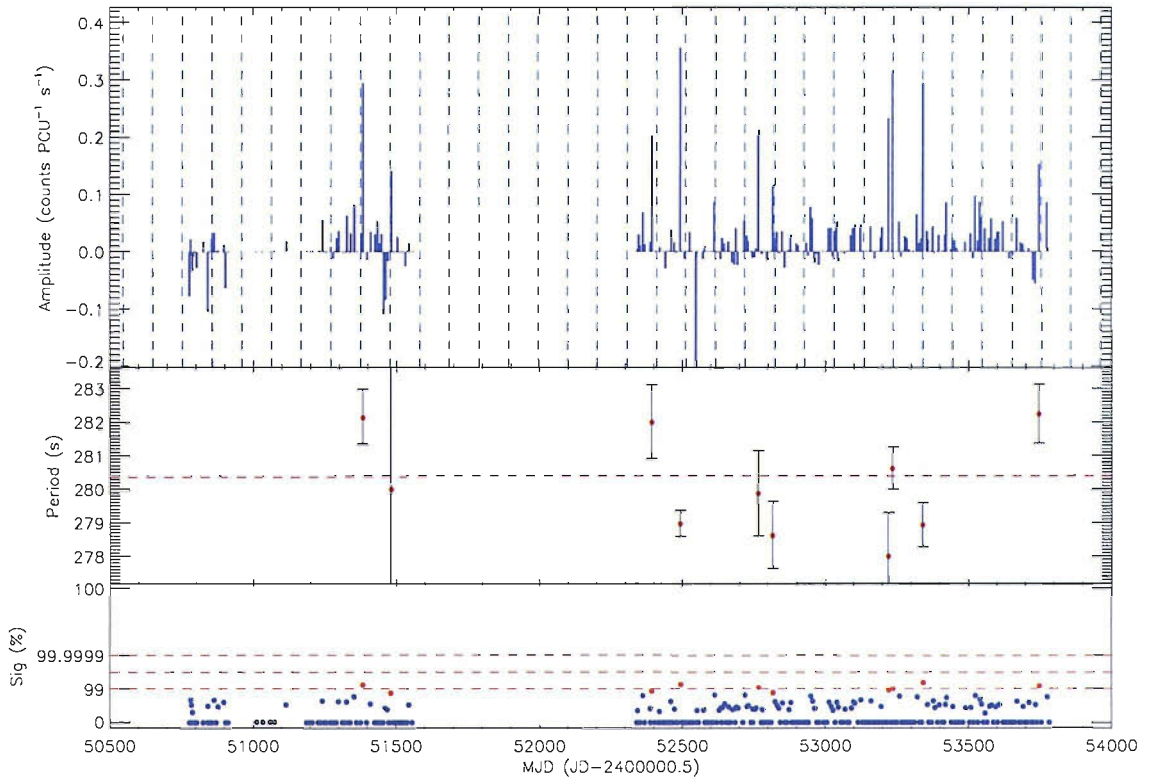

(a) X-ray amplitude light curve.

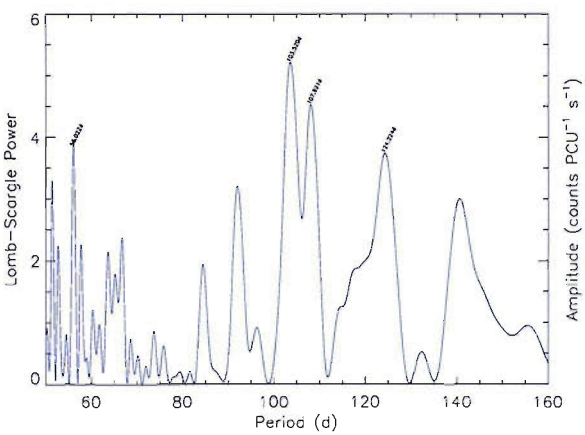

(b) Lomb-Scargle power spectrum.

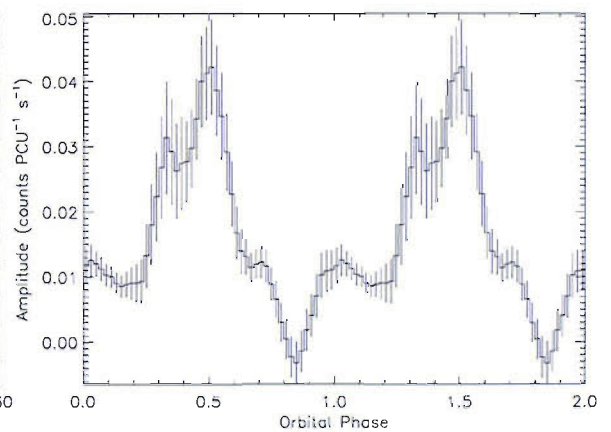

(c) Orbital profile folded at 103.5 d.

Figure 4.42: SXP280.

power spectrum returned no clear periods. A different approach was tried for this system by applying the collimator response to all the data; Fig. 4.43(c) shows the resulting power spectrum. From the strongest period we obtain an ephemeris of MJD $52264.5 \pm 5.9 + \mathrm{n} \times 117.65 \pm 0.71$ d.

4.1.37 SXP304

RX J0101.0−7206, CXOU J010102.7−720658
RA 01 01 01.7, dec −72 07 02

History: Discovered in *Chandra* observations at 304.49 ± 0.13 s, the optical counterpart is identified as the emission line star [MA93] 1240 (Macomb et al. 2003). The authors measured an unusually high pulse fraction of $90 \pm 8\%$ at a luminosity of $L_{\mathrm{x}} = 1.1 \times 10^{34}\,\mathrm{erg\,s^{-1}}$.

Survey Results: This source was out of the field of view during AO5 and AO6, so it has only been adequately covered from AO7 onwards. A number of Type Ib outbursts took place during MJD 52600 − 53000, and it was not detected again until recently, in MJD 53747, when it began a 2 − 3 week outburst, the longest and brightest observed so far in this survey. Lomb-Scargle analysis of the data before this outburst finds a period of 69.6 d; although this value is smaller than would be expected from the spin/orbital period relationship, we believe it represents the orbital period of the system. The ephemeris is MJD $52213.75 \pm 3.48 + \mathrm{n} \times 69.59 \pm 0.22$ d. Note that the bright outburst at MJD 53747 coincides with periastron passage.

4.1.38 SXP323

RX J0050.7−7316, AX J0051−733
RA 00 50 44.8, dec −73 16 06.0

History: Pulsations at 323.2 ± 0.4 s were detected in November 1997 (Yokogawa and Koyama 1998a) at coordinates of the *ROSAT* source RX J0050.7−7316. Cowley

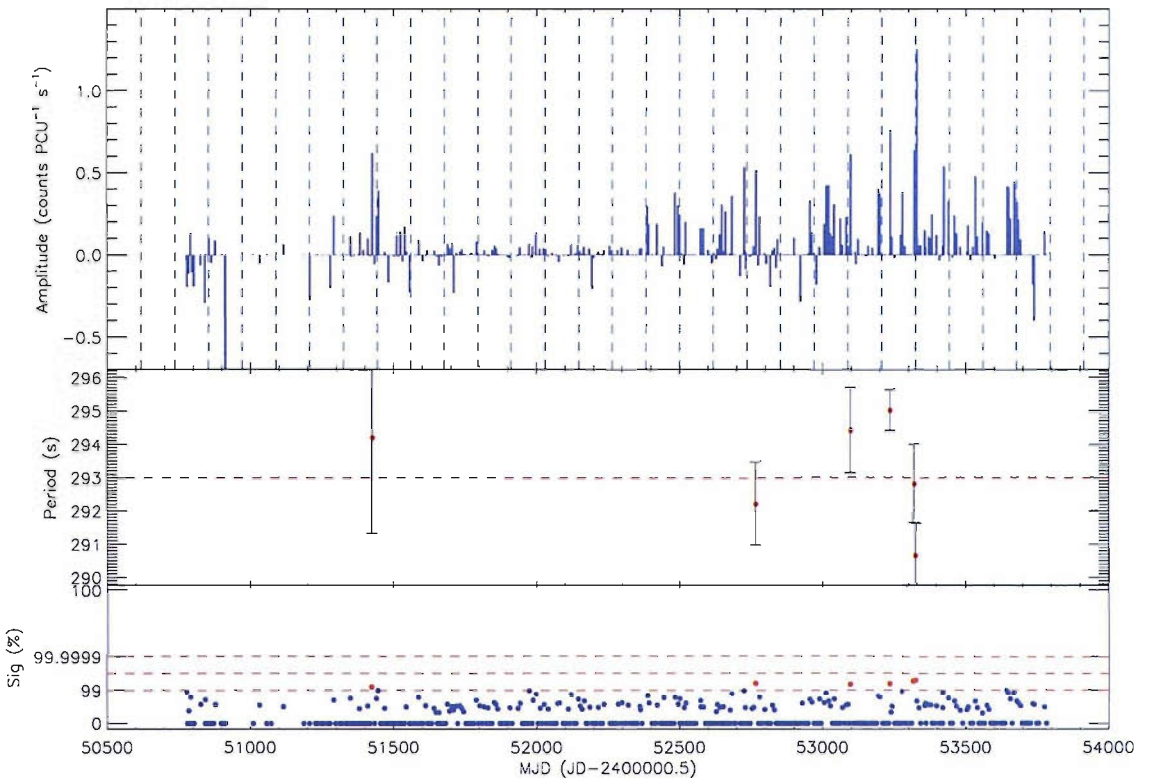

(a) X-ray amplitude light curve.

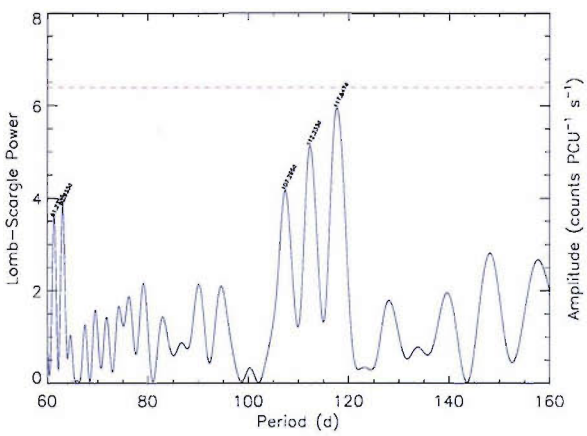

(b) Lomb-Scargle power spectrum.

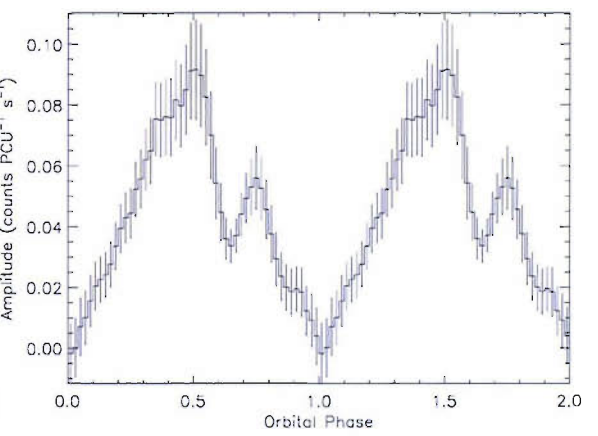

(c) Orbital profile folded at 117.65 d.

Figure 4.43: SXP293.

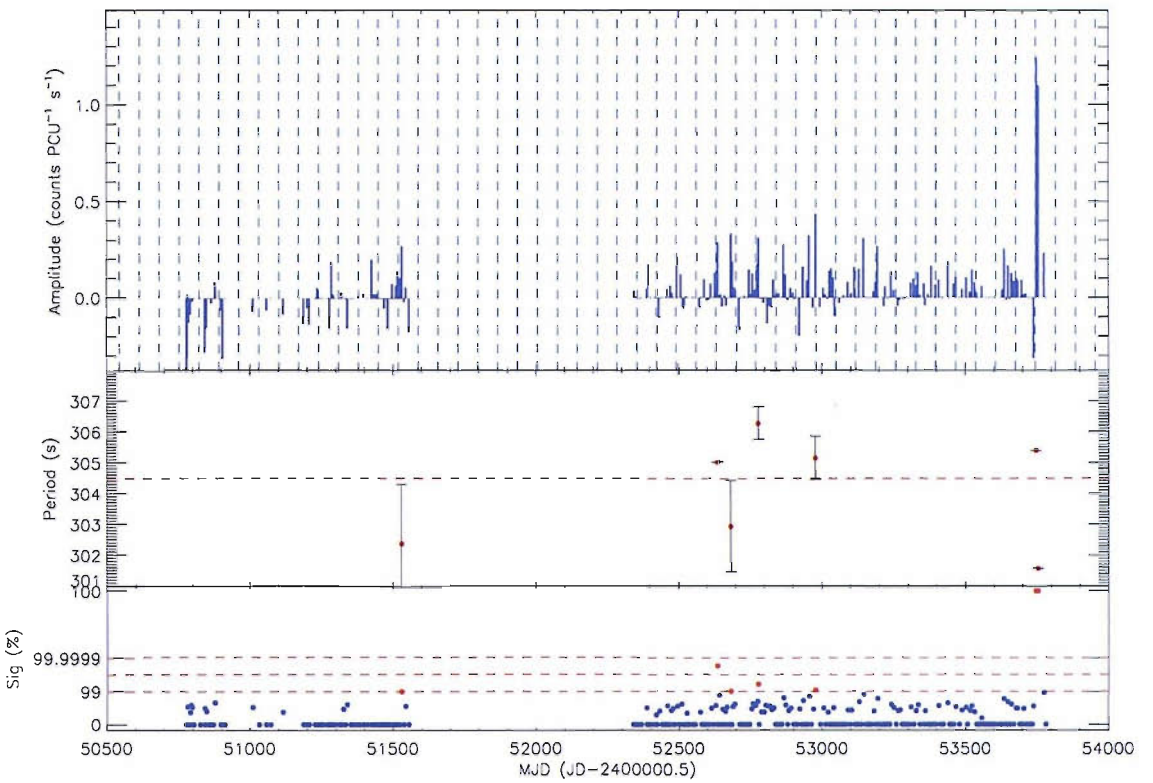

(a) X-ray amplitude light curve.

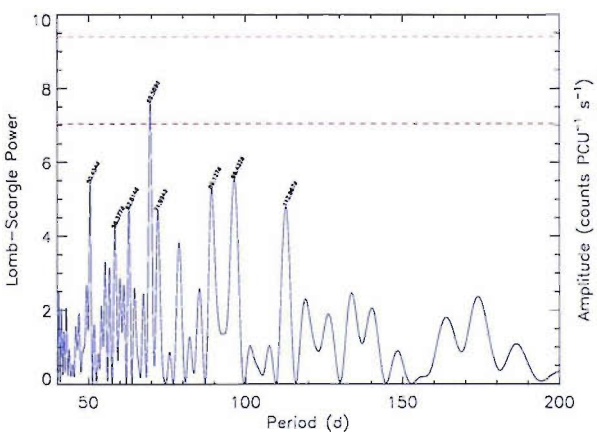

(b) Lomb-Scargle power spectrum.

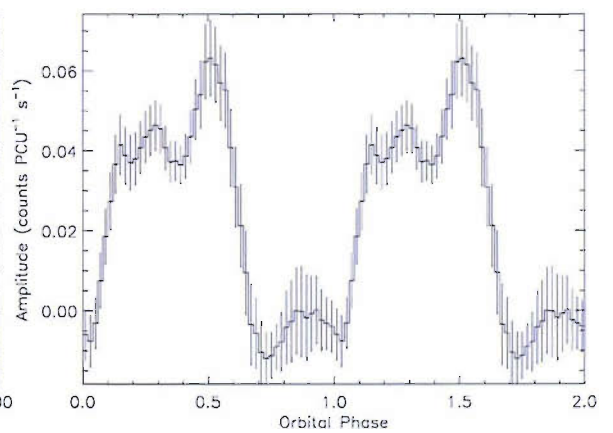

(c) Orbital profile folded at 69.59 d.

Figure 4.44: SXP304.

et al. (1997) identify the optical counterpart as a Be star. This system has been found to exhibit optical and IR variability at periods of ~ 0.7 and 1.4 d (Coe et al. 2002) and 1.695 d (Coe et al. 2005). These periods are too short to be the orbital period of the system and are most likely pulsations in the Be star. Laycock et al. (2005) suggest an orbital period of 109 ± 18 d from X-ray data earlier in this survey.

Survey Results: This pulsar showed quite regular and bright activity during this survey. Using $Sig_{\rm min} = 97\%$, a clear orbital period of 119.2 d is found through timing analysis, which is consistent with that previously reported by Laycock et al. (2005) from a subset of this survey data. The ephemeris is MJD $52245.8 \pm 3.6 + {\rm n} \times 119.19 \pm 0.64$ d.

4.1.39 SXP348

RX J0102−722, SAX J0103.2 −7209, AX J0103.2−7209
RA 01 03 13.0, dec −72 09 18.0

History: Pulsations at 345.2 ± 0.1 s were detected in *BeppoSAX* observations in July 1998 (Israel et al. 1998). Subsequently, pulsations at 348.9 ± 0.1 s were found in archival *ASCA* data from May 1996 implying a $\dot{P} = -5.39 \times 10^{-8}\,{\rm s\,s^{-1}}$ (Yokogawa and Koyama 1998b). The *ROSAT* source lies in a supernova remnant with a Be companion; no optical variability has been found in it (Edge 2005).

Survey Results: This source has been detected by a number of different instruments, but always at low luminosities ($\sim 10^{36}\,{\rm erg\,s^{-1}}$), so it is not surprising that there are not many detections in the survey. Furthermore, it has also been detected at a wider range of periods than other pulsars (from 340 to 348 s), which makes it more difficult to pick out in the periodograms from weekly observations. For this reason we used $Sig_{\rm min} = 98\%$ to bring out some data points just below 99% significance. We also chose to exclude the bright outbursts at MJD 52387 and the longer outburst around MJD 53738 from the timing analysis. The ephemeris we find is MJD $52228.4 \pm 3.7 + {\rm n} \times 124.2 \pm 0.9$ d, which places these two outburst shortly after periastron (see Fig. 4.46(a)).

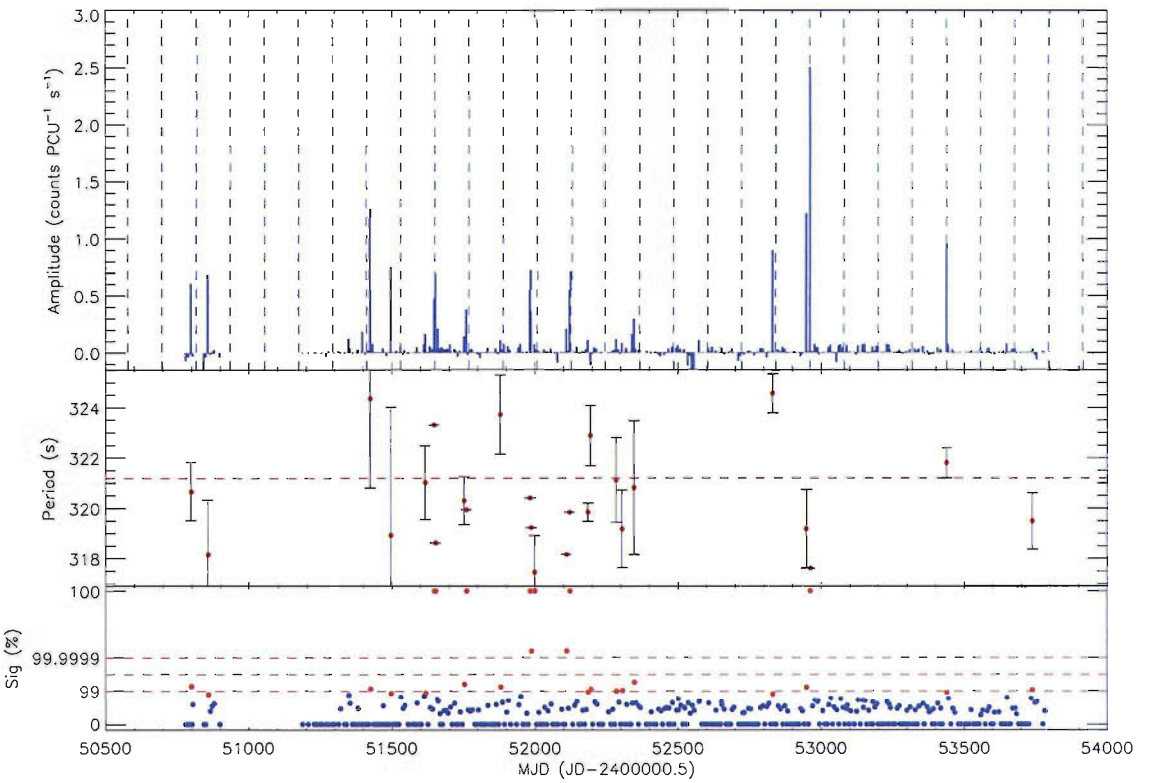

(a) X-ray amplitude light curve.

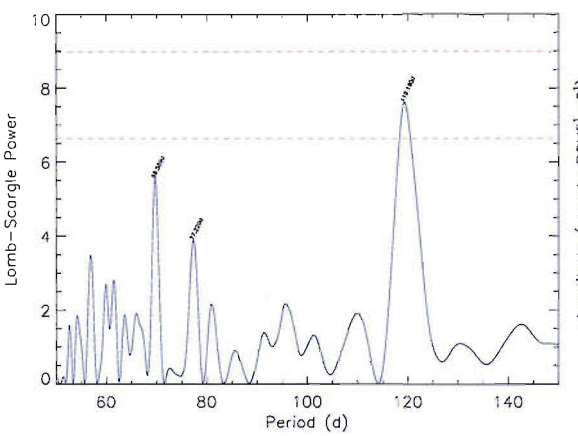

(b) Lomb-Scargle power spectrum.

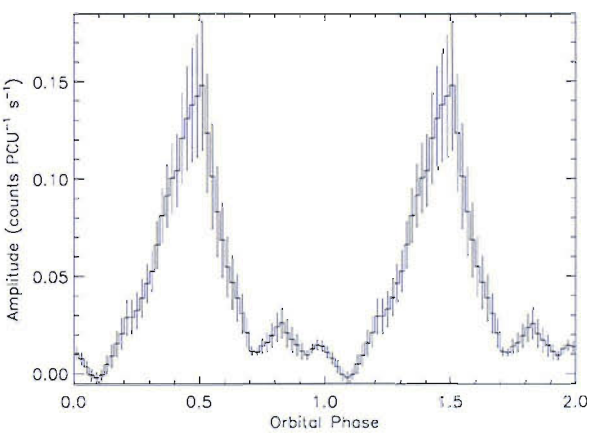

(c) Orbital profile folded at 119.19 d.

Figure 4.45: SXP323.

If the 4 outbursts between MJD 52600−53000 are used to estimate the luminosity of SXP348, we find a $\dot{P} = 1.7 \times 10^{-7}\,\mathrm{s\,s^{-1}}$ and $L_\mathrm{x} = 1.5 \times 10^{36}\,\mathrm{erg\,s^{-1}}$ ($B = 7.7 \times 10^{13}$ G), which are values within the expected range for Be/X-ray binaries and give us confidence that these are actual detections of SXP348.

4.1.40 SXP452

RX J0101.3−7211
RA 01 01 19.5, dec −72 11 22

History: Was initially proposed as an X-ray binary by Haberl et al. (2000). Pulsations were detected in *XMM* observations during 2001 at 455 ± 2 s and in 1993 *ROSAT* data at 450−452 s, implying a $\dot{P} = 2.3 \times 10^{-8}\,\mathrm{s\,s^{-1}}$; the optical counterpart was identified as a Be star Sasaki et al. (2001). Schmidtke et al. (2004) propose an orbital period of 74.7 d for this system based on its optical variability.

Survey Results: Applying $Sig_\mathrm{min} = 96\%$ we find a number of outbursts that are well described by the ephemeris MJD $52129 \pm 6 + \mathrm{n} \times 122.9 \pm 1.0$ d, even though this period is not very significant in the power spectrum. There is no evidence for the reported 74.7 d optical period. It should be noted that this source was present in the very first observation of this survey (its brightest detection so far) but was not recognised as a new pulsar at the time.

4.1.41 SXP504

RX J0054.9−7245, AX J0054.87244, CXOU J005455.6−724510
RA 00 54 55.6, dec −72 45 10

History: Discovered in archival Chandra data with 503.5 ± 6.7 s pulsations (Edge et al. 2004d, c). Also reported by Haberl et al. (2004) from an *XMM* observation at 499.2 ± 0.7 s and $L_\mathrm{x} = 4.3 \times 10^{35}\,\mathrm{erg\,s^{-1}}$. An orbital period of 268.0 ± 1.4 d was determined from optical (OGLE) data, and corroborated by preliminary X-ray data

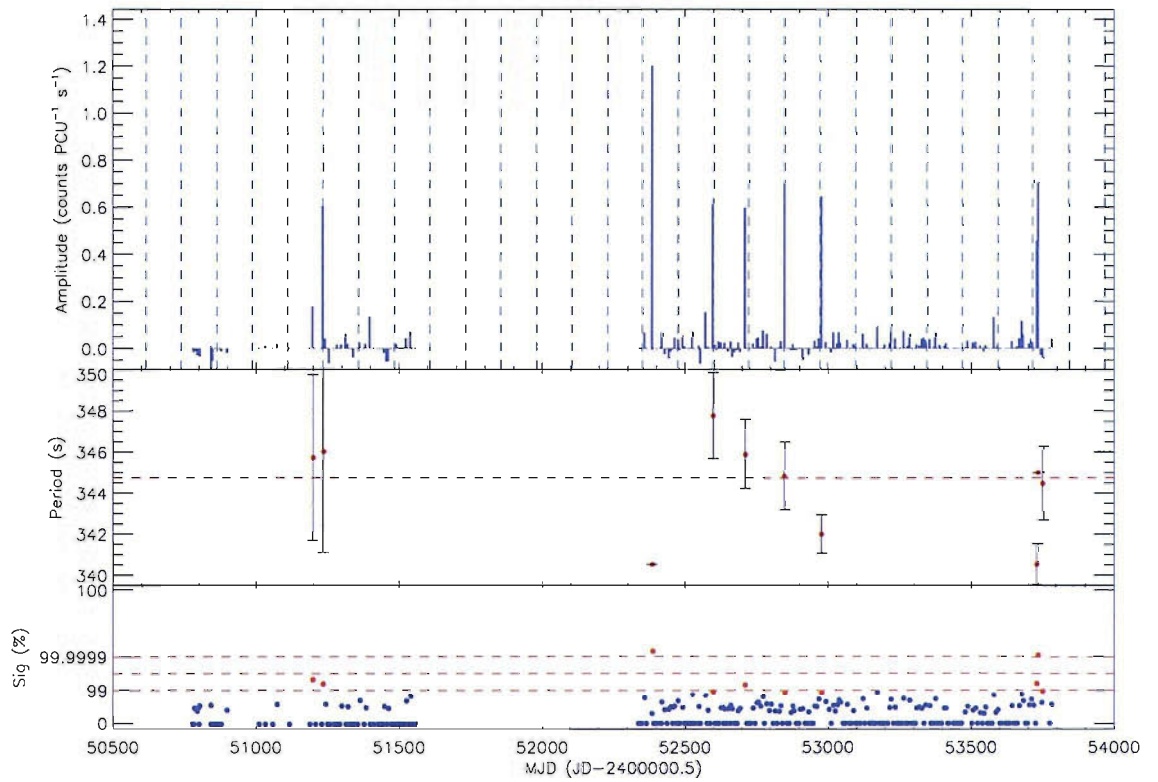

(a) X-ray amplitude light curve.

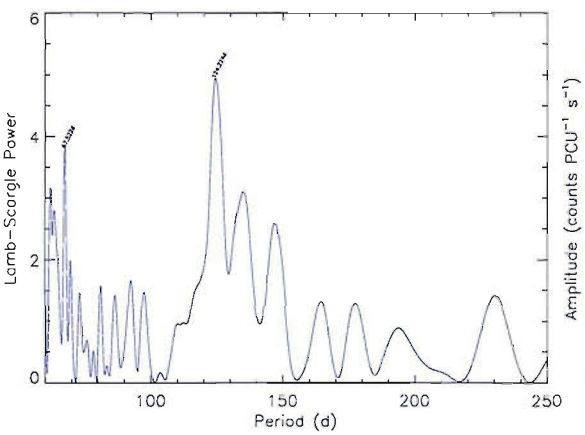

(b) Lomb-Scargle power spectrum.

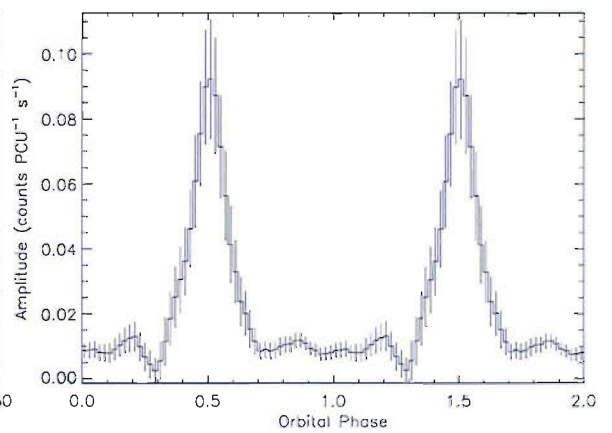

(c) Orbital profile folded at 124.2 d.

Figure 4.46: SXP348.

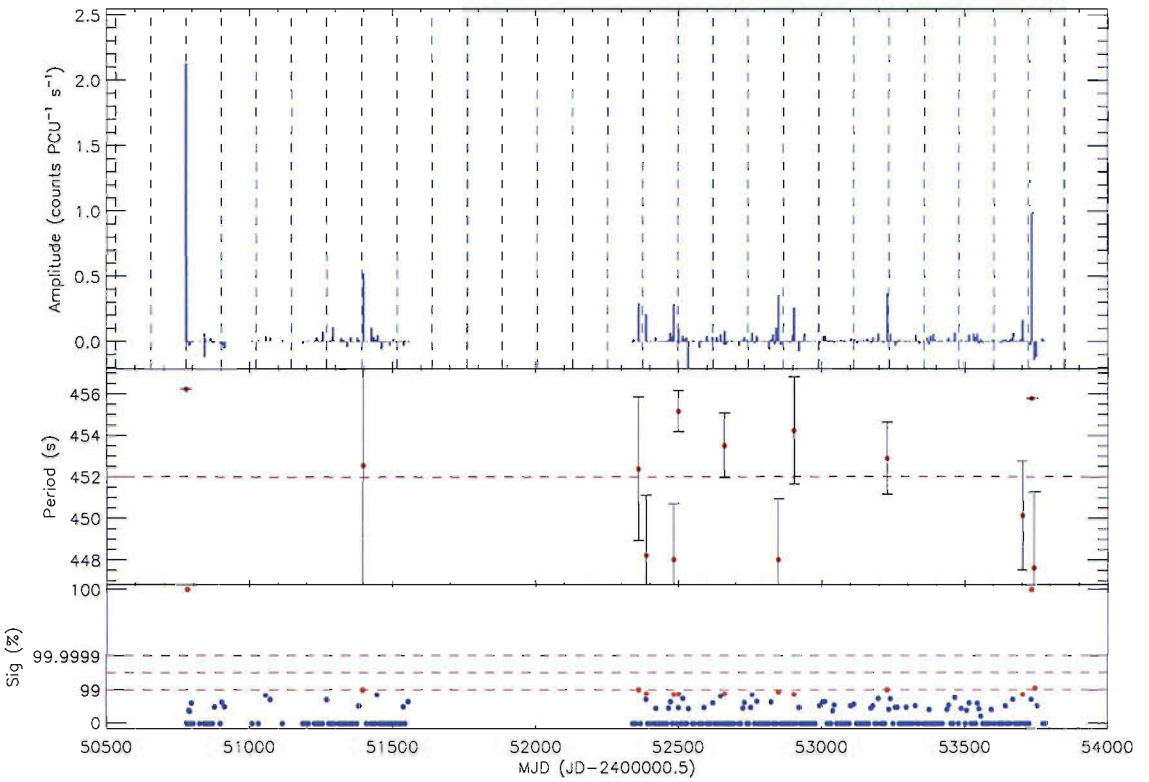

(a) X-ray amplitude light curve.

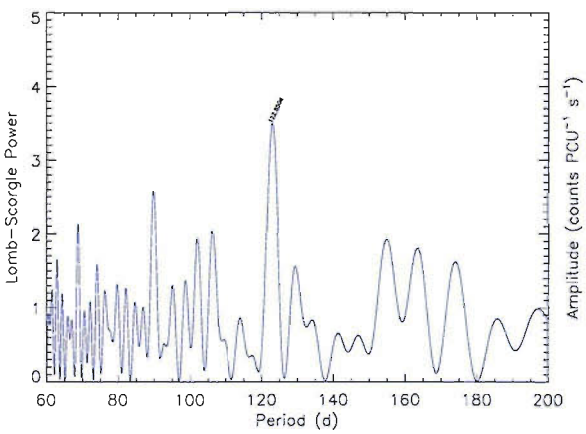

(b) Lomb-Scargle power spectrum.

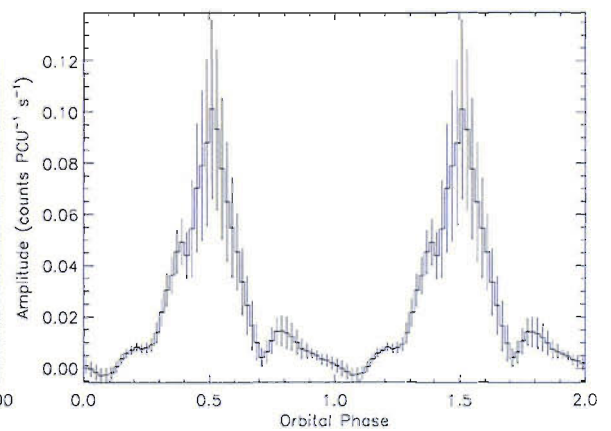

(c) Orbital profile folded at 122.9 d.

Figure 4.47: SXP452.

from the present survey (Edge et al. 2005b). The optical ephemeris was later refined to MJD $50556 \pm 3 + \mathrm{n} \times 268.0 \pm 0.6$ d (Edge et al. 2005c; Edge 2005).

Survey Results: Lomb-Scargle analysis of the entire survey (with or without the bright outbursts circa MJD 52440 and 52980) returns a slightly different orbital period from the one previously reported: ~ 260 d. The ephemeris we find is MJD $52175 \pm 13 + \mathrm{n} \times 259.7 \pm 3.3$ d. This source displays a lot of activity in between periastron passages, which might be indicative of a low eccentricity orbit and makes timing analysis more difficult.

4.1.42 SXP565

CXOU J005736.2−721934
RA 00 57 36.2, dec −72 19 34

History: Discovered in *Chandra* observations at 564.81 ± 0.41 s with a pulse fraction of $48 \pm 5\%$ ($L_{\mathrm{x}} = 5.6 \times 10^{34}\,\mathrm{erg\,s^{-1}}$), the optical counterpart is idenified as the emission line star [MA93] 1020 (Macomb et al. 2003). An optical period of 95.3 d has been reported for this system (Schmidtke et al. 2004), but this period is not seen in OGLE data (Edge 2005).

Survey Results: This source shows a lot of activity, but no clear outbursts. The power spectrum has two main peaks of similar significance at 84.5 and 286.5 d. The folded profile at 84.5 d shows a broad curve with a fast rise, followed by a slow, almost-linear decay. The folded profile at 286.5 d shows a less-convincing, more triangular curve with features. It should be noted, however, that $286.5/3 \simeq 95.2$, which is the value of the optical period. It might be possible for the Be disc to vary with a beat period of 3:1 with respect to the 285.7 d orbital period. A one-arm oscillation in the disc could be responsible for the optical variability. No periodicity in the 286 d range has been found in the optical data (Cowely & Schmidtke 2006, private communication). This source requires further study (and more data!) to firmly establish an orbital period from the X-ray data. The ephemerides of the ~ 85 and ~ 287 d periods are MJD $52229.7 \pm 4.2 + \mathrm{n} \times 84.5 \pm 0.4$ d and MJD $52084 \pm 14 +$

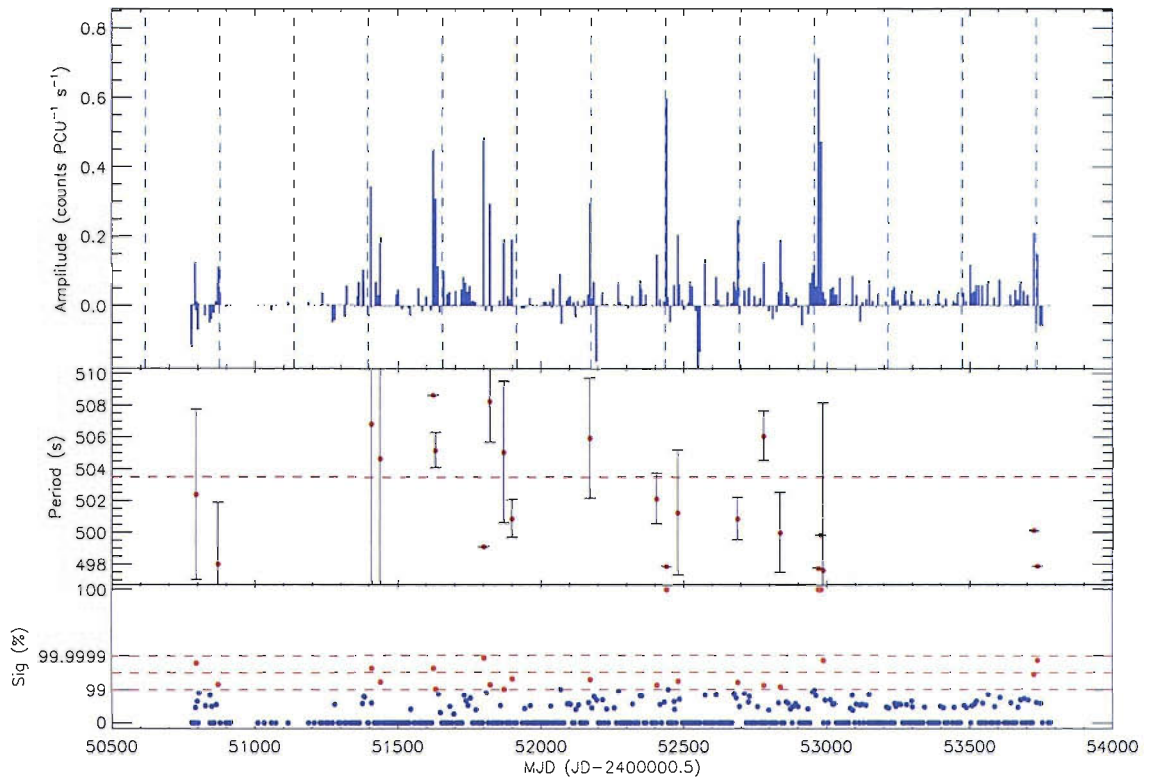

(a) X-ray amplitude light curve.

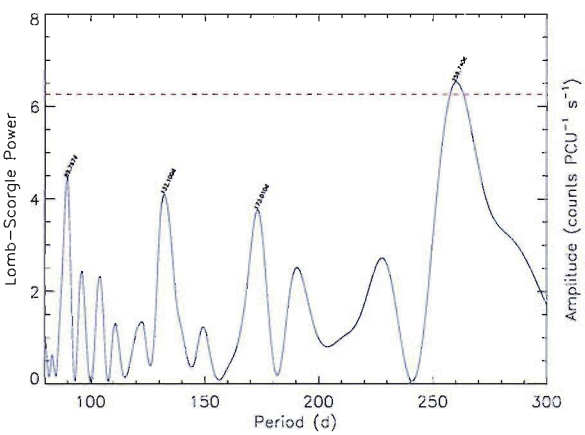

(b) Lomb-Scargle power spectrum.

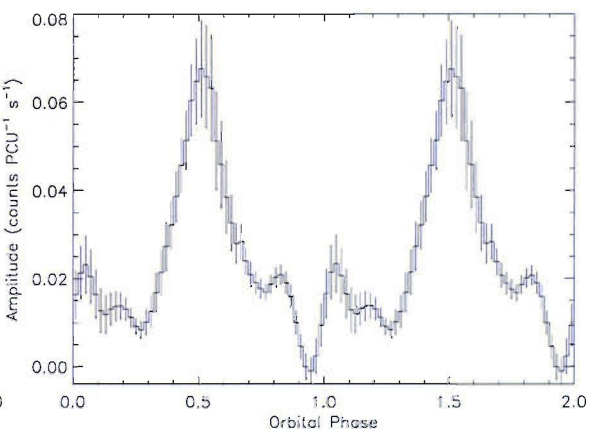

(c) Orbital profile folded at 259.7 d.

Figure 4.48: SXP504.

$n \times 286.5 \pm 4.2$ d, respectively. The expected orbital period based on the spin/orbit relationship would be $\sim 130-260$ d, so the periods found lie just outside the extremes of this range.

4.1.43 SXP701

RX J0055.2−7238, XMMU J005517.9−723853
RA 00 55 17.9, dec −72 38 53

History: First observed during an *XMM* TOO observation at 701.6 ± 1.4 s and located within the error circle of a *ROSAT* object (Haberl et al. 2004). Fabrycky (2005) finds optical periods of 6.832 and 15.587 h, which are attributed to stellar pulsations. No orbital period has been proposed.

Survey Results: Similar to SXP565, it displays much X-ray variability with no bright outbursts. The periodogram shows 4 peaks at 79.9, 98.8, 134.2 and 211.0 d. The profiles are unconvincing, except for the 79.9 d period, which looks similar to SXP565's profile at 84.5 d. In an attempt to highlight the brightest detections, the collimator correction was applied only to data points whose *global* significance was greater than 90%; there are only two such detections. The power spectrum now shows the 79.9 d period at a higher power, with a signifcance of $\sim 94\%$. We are hesitant to claim this as the orbital period due to its shortness, but it would seem there is real X-ray variability on this timescale. The ephemeris of this period is MJD $52248.3 \pm 2.4 + n \times 79.9 \pm 0.3$ d; the ephemeris of the 211 d period is MJD $52144.5 \pm 10.6 + n \times 211.0 \pm 2.3$ d.

4.1.44 SXP756

RX J0049.6−7323, AX J0049.4−7323
RA 00 49 42.42, dec −73 23 15.9

History: Pulsations at 755.5 ± 0.6 s were detected in a very long (~ 177 ks) *ASCA*

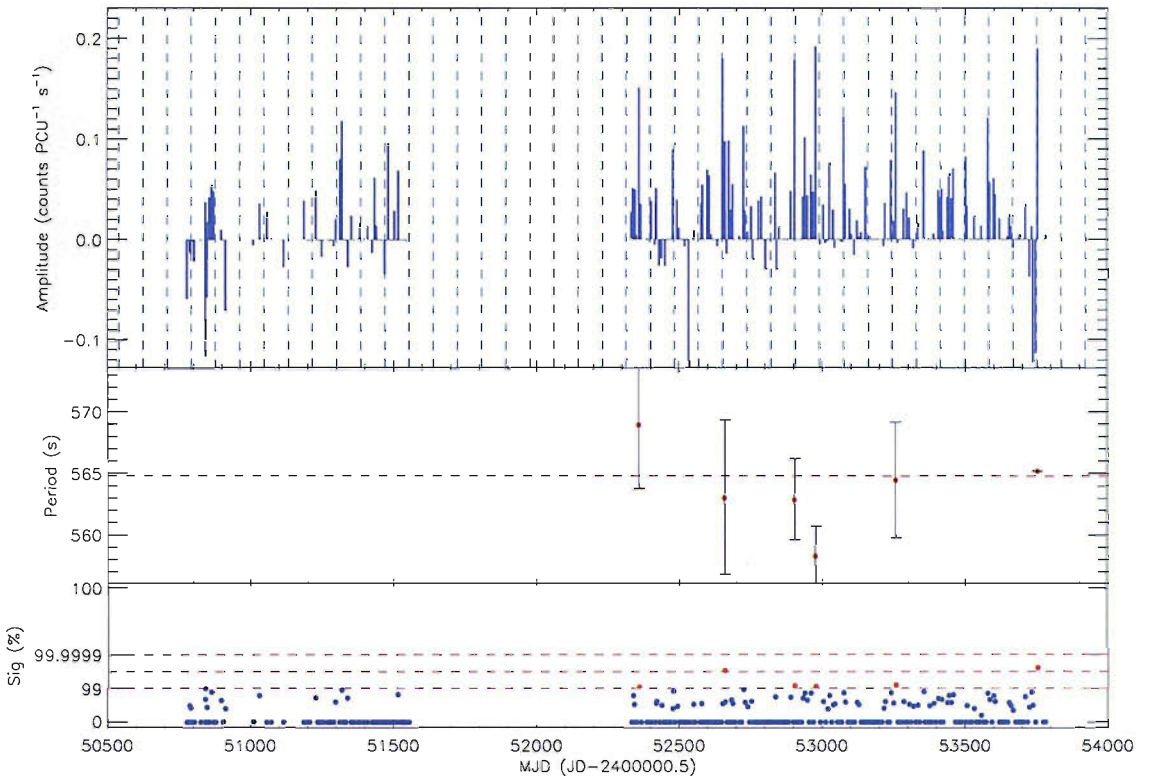

(a) X-ray amplitude light curve showing the possible 84.5 d orbital period.

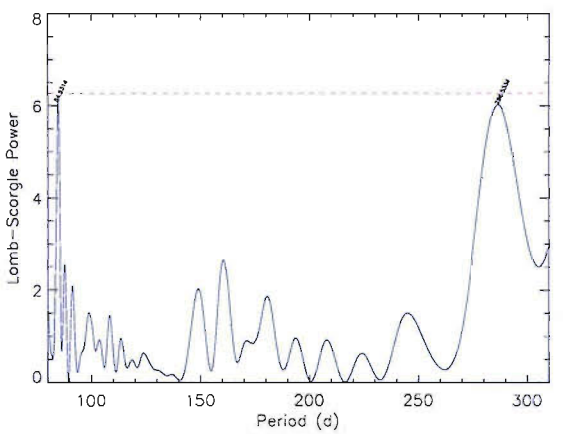

(b) Lomb-Scargle power spectrum.

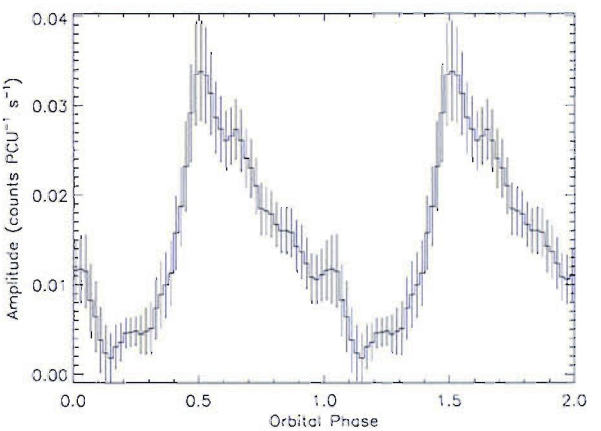

(c) Orbital profile folded at 84.5 d.

Figure 4.49: SXP565 possible orbital period = 84.5 d.

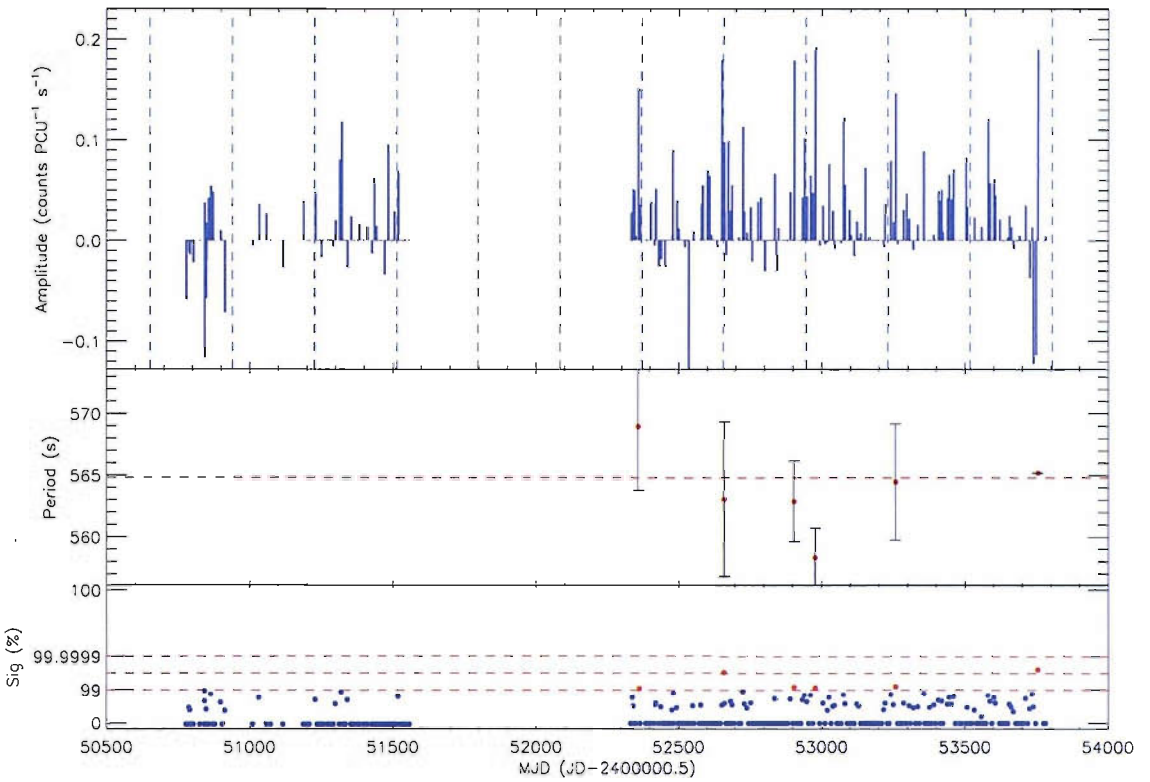

(a) X-ray amplitude light curve showing the possible 286.5 d orbital period.

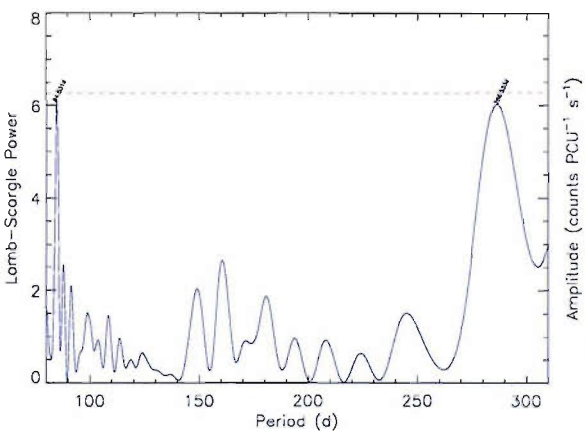

(b) Lomb-Scargle power spectrum.

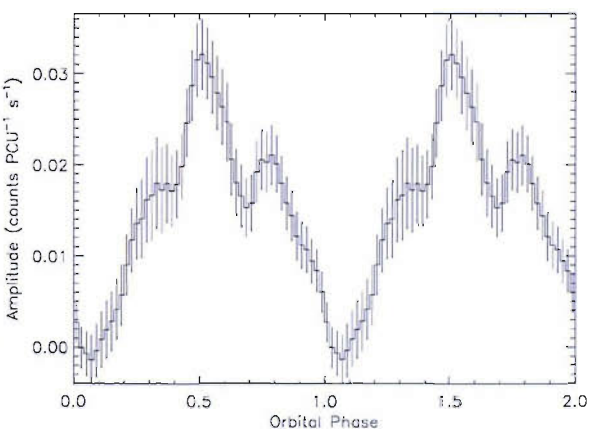

(c) Orbital profile folded at 286.5 d.

Figure 4.50: SXP565 possible orbital period = 286.5 d.

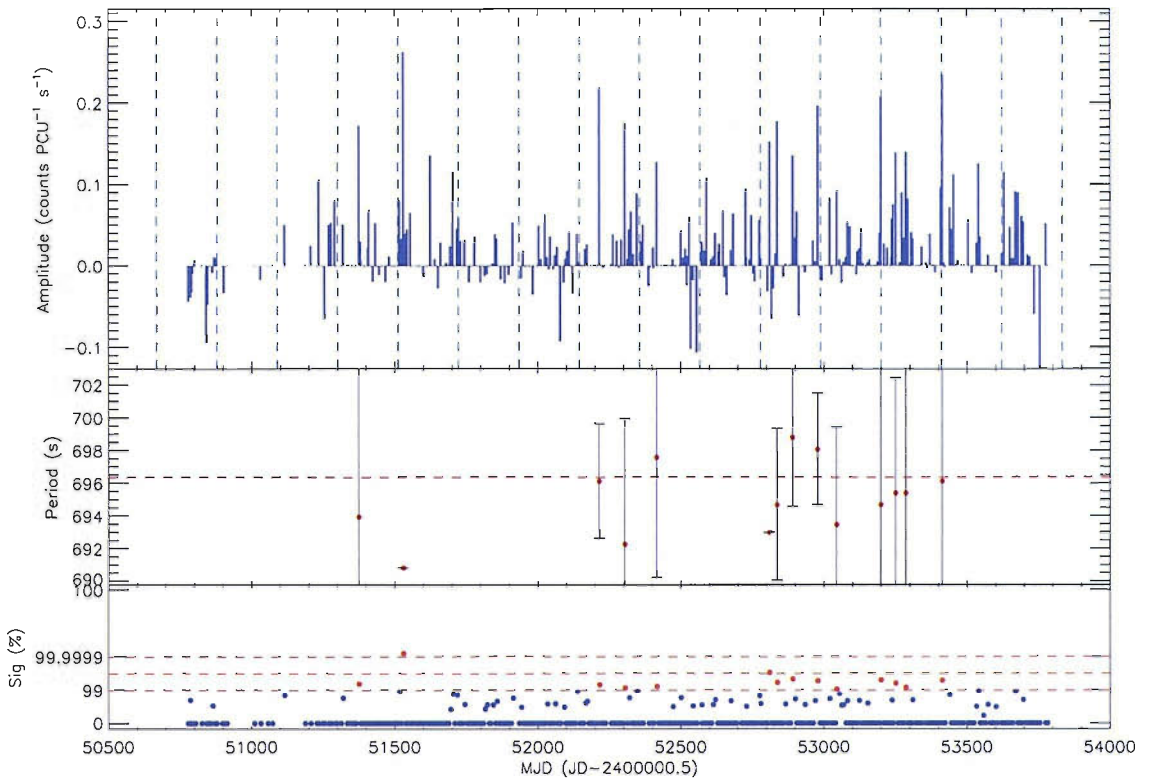

(a) X-ray amplitude light curve.

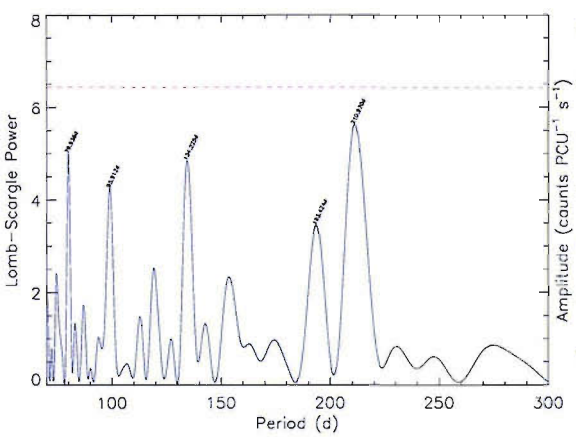

(b) Lomb-Scargle power spectrum.

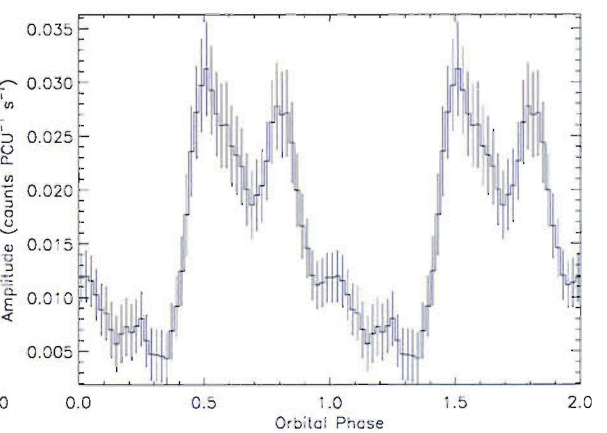

(c) Orbital profile folded at 211.0 d.

Figure 4.51: SXP701.

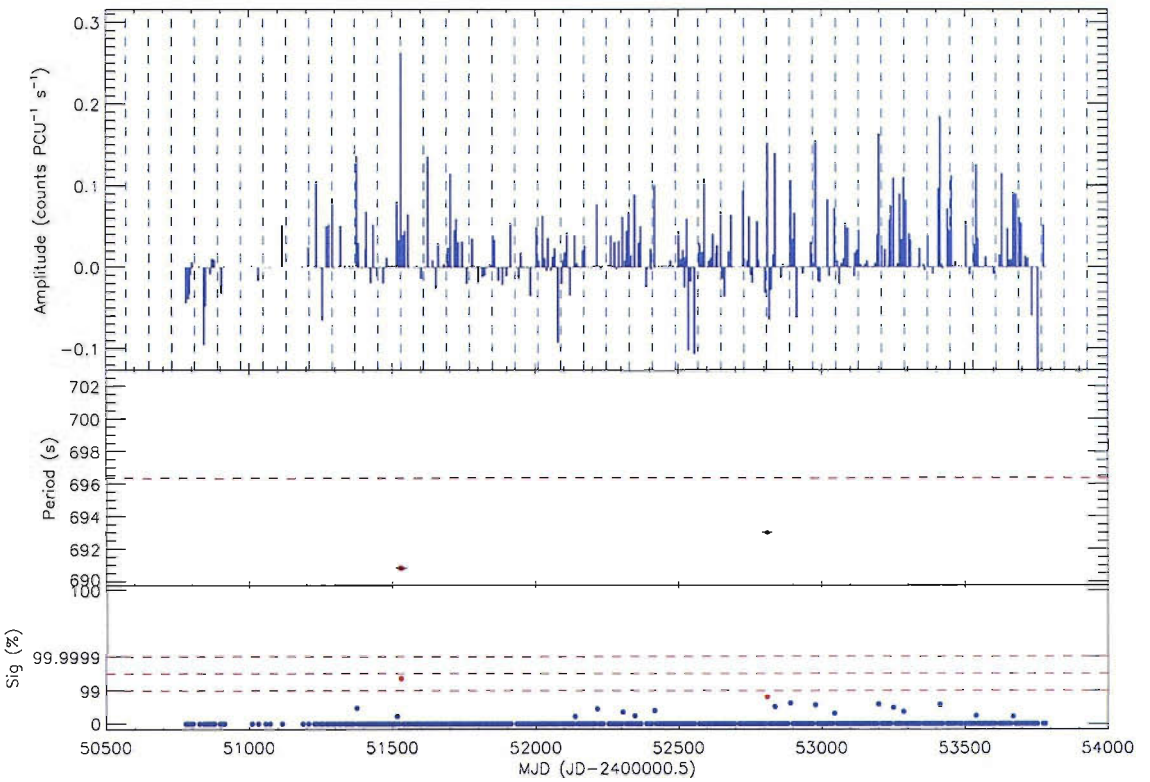

(a) X-ray amplitude light curve.

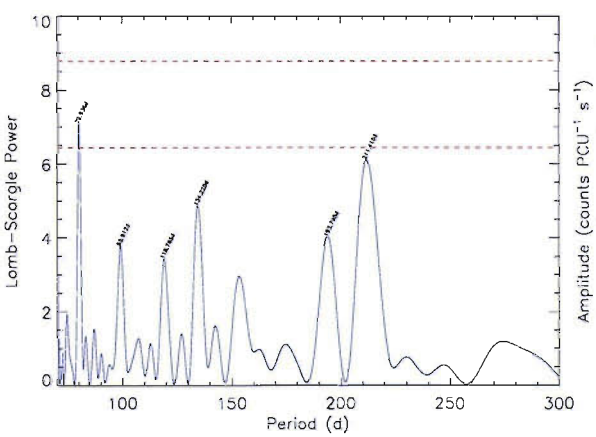

(b) Lomb-Scargle power spectrum.

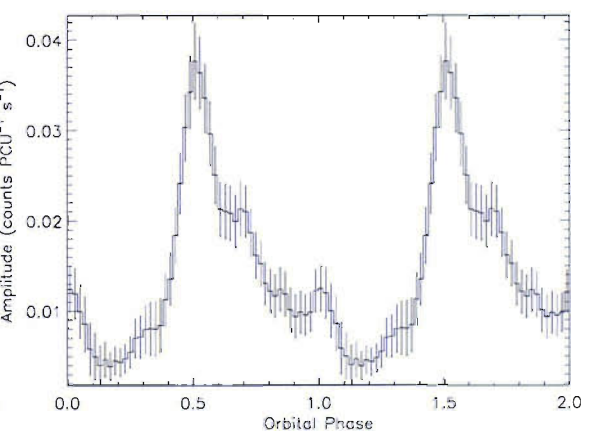

(c) Orbital profile folded at 79.9 d.

Figure 4.52: SXP701.

observation of the SMC in April 2000, the source was detected at a luminosity of $L_x = 5 \times 10^{35}\,\mathrm{erg\,s^{-1}}$ (Yokogawa et al. 2000a). The optical counterpart was later established as a V = 15 Be star (Edge and Coe 2003). Laycock (2002); Laycock et al. (2005) find an X-ray period of 396 ± 5 d while Cowley and Schmidtke (2003) report recurring outbursts at ~ 394 d intervals in R and V MACHO data.

Survey Results: This seems to be a low luminosity pulsar, so we would expect to detect it only when at its brightest. Coverage has been sparse due to its southern location, only visible to observations of Positions 4 and 5. Despite this, it has been detected 4 times in outburst, the brightest of which lasted 4 weeks. The periodogram show two periods: the main one at 196.9 d and a second, very broad one at 383 d. We believe the first is a harmonic of the second, that happens to be stronger due to the poor coverage. Also, looking at the light curve it is evident that the bright detections are spaced ~ 400 d apart. Moreover, this is exactly the optical period of the system, thus, the orbital ephemeris we derive from the X-ray data is MJD $51805.1 \pm 11.8 + \mathrm{n} \times 393.7 \pm 3.1$ d. This ephemeris places the first outburst in the data at MJD 51411, which is consistent with the last optical outburst available in the MACHO data reported by Cowley and Schmidtke (2003). Fig. 4.53(c) may show evidence of X-ray emission at apastron.

4.1.45 SXP1323

RX J0103.6−7201
RA 01 03 37.5, dec −72 01 33.2

History: The confirmed pulsar with the longest pulse period in the SMC, SXP1323 was reported by Haberl and Pietsch (2005) in a number of archival *XMM* observations. The authors identify the emission line star [MA93] 1393 (V $\simeq$ 14.6) as the optical counterpart.

Survey Results: This source is difficult to detect due to its long period (requiring observations with a baseline longer than ~ 4 ks) and its location near the edge of Position 1/A. Despite these limitations, a number of bright outbursts have been

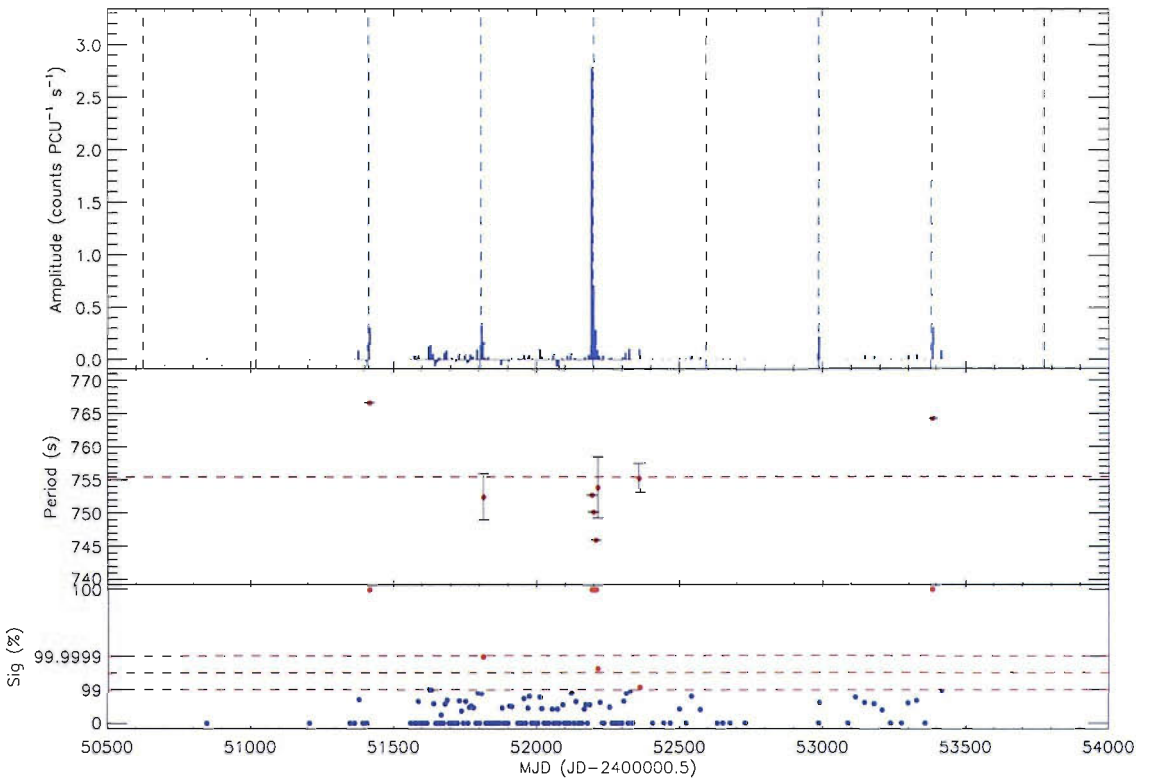

(a) X-ray amplitude light curve.

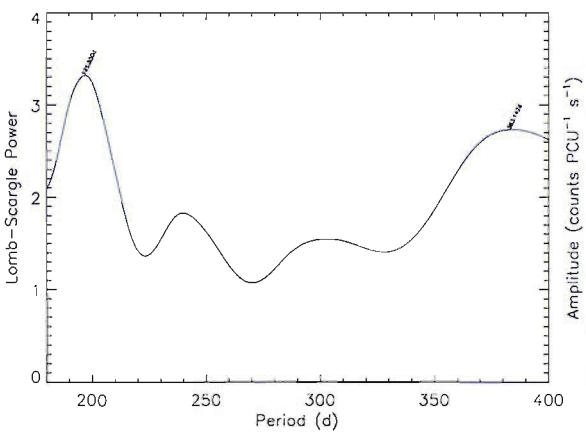

(b) Lomb-Scargle power spectrum.

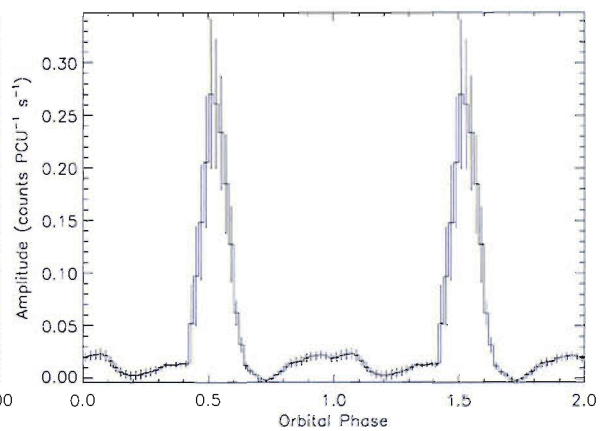

(c) Orbital profile folded at 393.7 d.

Figure 4.53: SXP756.

detected. When searching for periodicities, only data for MJD > 52300 were used, and a very weak period of 324 d is found. This value is within the normal variance of the Corbet diagram and is probably the orbital period of the system. SXP1323 is close to the centre of Position X, which will be monitored in AO11 with observation baselines in excess of 10 ks. Thanks to this it should be possible to detect it easily during the next major outburst, which is expected in late November 2006. The ephemeris we derive is MJD $52765 \pm 10 + \mathrm{n} \times 323 \pm 11$ d.

4.2 Pulse profiles

Change alone is eternal,
perpetual, immortal.

—Arthur Schopenhauer

As was mentioned earlier in § 1.3.5, pulse profiles have been observed to change over time and energy bands. As such, the following profiles are not necessarily representative of the particular pulsar, but rather of the particular moment in time at which the observation took place. For some of those pulsars that underwent long outbursts, or have been outbursting regularly, we show the evolution of their pulse profiles over time and comment on the possible reasons why these changes in shape occurred. For other pulsars we show simply a selection of profiles from the strongest detections.

For every plot, the date of the observation is noted under each profile. The Y axis is the count-rate, in counts $\mathrm{PCU}^{-1}\,\mathrm{s}^{-1}$, obtained from folding of the actual light curve of the observation, and then scaling the counts such that the mean pulsed flux is zero. Under each profile is A, the collimator-corrected amplitude of the pulsed flux as estimated from the power of the pulsations in the power spectrum. For those systems where the orbital period is known, the orbital phase, ϕ, at which the observation was made is also printed.

The characteristic that is common to all pulsar profiles is their uniqueness. Although there are certain trends at the higher luminosities associated with the brighter

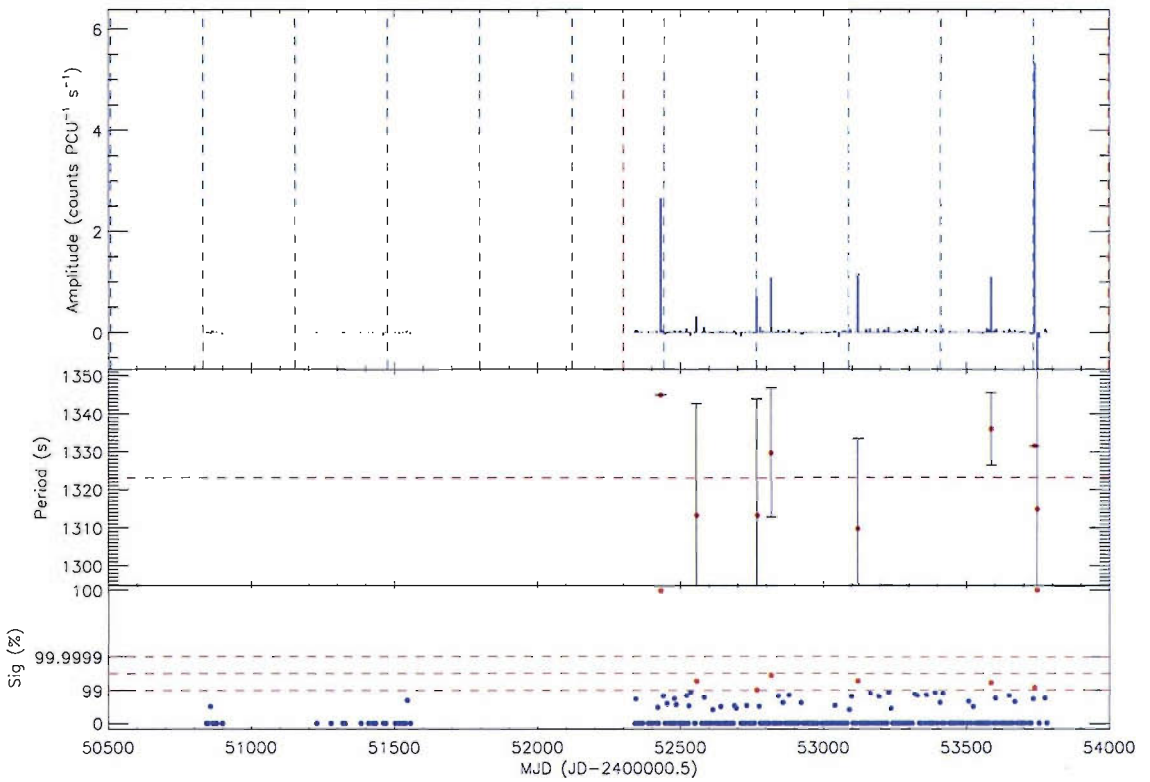

(a) X-ray amplitude light curve.

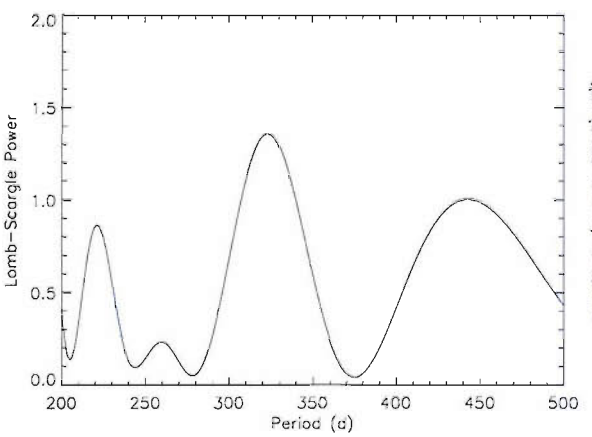

(b) Lomb-Scargle power spectrum.

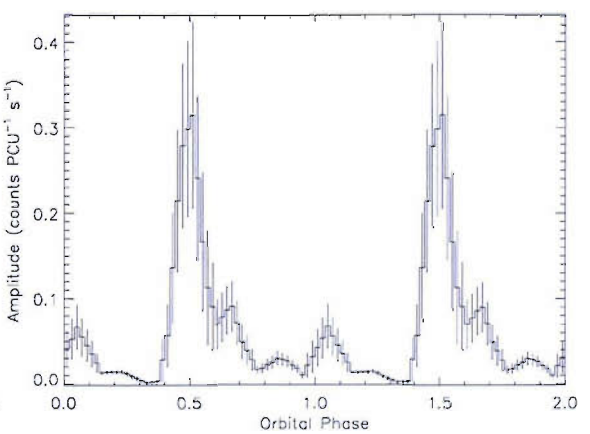

(c) Orbital profile folded at 323 d.

Figure 4.54: SXP1323.

outbursts, at the average level of luminosity (which varies for each pulsar) we find complicated profiles composed of various peaks, of which sometimes one is dominant. In view of this we discuss each in a different section.

4.2.1 Pulse profiles at low luminosities

These show complicated structure and appear to be the sum of 3 or 4 components, as these are most often the number of peaks observed. See MJD 52778.87 in Fig. A.7 for an example of 3-peak structure, and MJD 52078.15 in Fig. A.6 for a 4-peak. A smaller number of observations show a 2-peak structure (MJD 52360.05 in Fig. A.18; MJD 52508.49 in Fig. A.22) or even a single peak (MJD 52988.20 in Fig. A.25 shows a narrow upper peak while MJD 52890.77 in Fig. A.26 has a broad peak; MJD 53359.64 in Fig. A.14 shows an almost symmetrical triangular profile).

Although many of these shapes could be disregarded as being inaccurate representations of the actual pulse profile due to low S/N, we find that some of them reappear at different times. For example, the profiles of SXP504 on MJDs 51898.85 and 53725.33 are very similar, despite having been observed 5 years apart! Even at a slightly higher amplitude, the profile on MJD 52438.72 is similar (Fig. A.39). SMC X-3 shows practically identical profiles on MJDs 52499.86 (Fig. A.9) and MJD 53417.34 (Fig. A.10). SXP16.1 has similar profiles on MJDs 50897.28 and 52171.31 (Fig. A.13). SXP140 has almost identical profiles on MJDs 52572.51 and 52841.82 (Fig. A.26). The list could continue, and we encourage the reader to find more examples, but what these reappearing profiles show is that the shapes we see in all these plots are likely accurate representations of the true pulsar profile, even at low luminosities.

4.2.2 Pulse profiles at high luminosities

At high luminosities the S/N is increased and the profiles become smoother, with smaller error bars. Their shape also changes when compared to their low luminosity brethren, generally becoming simpler in structure. Following are some comments on

a number of pulsars exhibiting bright profiles.

SMC X-2 has a wide peak profile at low luminosities (MJDs 51974.00 and 51997.72 in Fig. A.3) but shows all type of different profiles in outburst. The profile on MJD 51586.27 has two pencil beam-like peaks separated by $\phi = 0.4$, but 4 days later on MJD 51592.23 the peaks are wider, reminiscent of a fan beam, and $\phi = 0.6$ apart. This behaviour could actually be explained the pulsar having non symmetrical magnetic poles; if one pole were $\sim 36°$ away (on the plane of rotation) from the antipodal point, you would expect to see the peaks from pencil beams $\phi = 0.4$ apart, which would become $\phi = 0.6$ apart when the emission changed to fan beam as the luminosity increased. Different opening angles of the fan beams could explain other profiles, such as MJDs 51580.15, 51611.12, 51616.12 or 51651.96; but explaining the broad, single-peaked profiles on MJDs 51624.15 – 51646.97 is trickier unless one of the poles is emitting a pencil beam while the other has a fan beam.

SXP4.78 exhibits a similar behaviour to SMC X-2. Profiles during MJD 51905.15 – 51933.35 suggest two pencil beams from symmetrical magnetic poles, but profiles from MJD 53738.12 – 53753.67 appear to have 3 components of varying strength which are difficult to explain with this beam/pole configuration (see Fig. A.6). It is possible that the first 3 profiles are of fan beams, which would mean that the others would be fan beams plus a pencil beam from one of the poles.

SXP8.80 also shows a 3-component profile, which could be explained if only one of the poles were visible, and both a fan and a pencil beam were present. In this scenario, we would see pencil beam emission from only one pole, but fan beam emission from both, leading to 3 peaks in the profile (see Fig. A.11).

SXP15.3 is likely to be exhibiting fan beams in its double profiles, which are all at high luminosities. Fig. A.14 shows the evolution of the pulse profile throughout the MJD 53600 outburst. At the beginning and ending of the series, when the luminosities are lower, the profile reverts to a single peak, so it is likely that only one of the magnetic poles is visible. The difference in height between the two peaks at high luminosities could be due to non-symmetrical poles or the geometric configuration of the system with respect to our line of sight.

SXP46.6 probably also shows a pencil beam from one pole coupled with a fan beam from both (Fig. A.17). The relative intensities of each vary throughout the outbursts although it would appear that, in general, they are all of similar magnitude, giving rise to the single, wide peak that is the most common shape.

SXP51.0 is slightly puzzling, as two profiles at different amplitudes (which we expect to imply different luminosities) appear almost identical (see MJDs 52318.99 and 52360.05 in Fig. A.18). They seem like a double-peaked profile coming from the pencil beams of two poles, yet the profile of MJD 51640.05 shows a single-peaked profile.

SXP74.7 exhibits both double-peaked (likely fan beams) and single-peaked (pencil beam from single pole) profiles at different times (Fig. A.19).

SXP59.0 has some difficult to explain profiles (Fig. A.20). The most common shape is one resembling MJD 50841.57, which would appear to be a single-peaked, pencil beam profile, were it not for the "hump" shortly after the peak. This feature increases in strength to equal that of the main peak on MJD 52541.72, but seems to disappear completely on MJD 52573.44. We estimate it to be $\sim\frac{1}{4}$ of a phase away from the main peak. A small bump seen $\sim\frac{1}{2}$ a phase away from the main peak in a number of profiles might imply a pencil beam from the opposite pole that just barely comes within our line of sight. If this is the case, then we would expect to see the pencil beam at a small angle (hence very bright), which could be brighter than the fan beams emitted from the poles. It would still be necessary to explain why the pencil beam is closer to one of the fan beam peaks than the other; this might be due to relativistic light-bending effects.

SXP82.4 is another interesting pulsar (see Fig. A.21). The profiles on MJDs 50779.39 and 52823.71 would be consistent with fan beam emission from two poles, one of which is offset $\sim 18°$. However, the bright detection on MJD 52451.86 shows emission consisting (at least in part) of a pencil beam. We would expect pencil beams at lower luminosities and fan beams at higher luminosities, not the other way around.

SXP91.1 has the broadest peak of any of the SMC pulsar profiles, spanning up to ~ 0.65 of a phase and often appearing completely flat on top (Fig. A.23).

It seems to be formed of 3 components of similar intensities, which could be explained by one pencil beam and two fan beams.

SXP144 shows a single-peak profile in most observations (Fig. A.27), although in some the peak is split in two (e.g., MJDs 52730.95 and 53738.12), which could be due to the pencil beam widening out to become conical, leaving a semi-hollow centre.

SXP169 presents a wide variety of profiles (Fig. A.30). There are a number of fan beam profiles (e.g., MJDs 50799.97 and 51277.23), some 3-component profiles (e.g., MJDs 51488.69 and 52515.41), and even 4-component profiles (e.g., MJDs 52745.94 and 53422.19). All this suggests that emission from only one pole is seen most of the time, or that the emission from the second pole is so weak (in our line of sight) that it is washed out at high luminosities.

SXP323 was remarkably consistent during 3 outbursts presenting similar profiles at almost equal amplitude (MJDs 51651.96, 51982.09 and 52120.52 in Fig. A.36). They appear to be 3-component profiles.

SXP452 shows almost identical profiles during two outbursts of similar amplitude separated by almost 3000 days! (See profiles on MJDs 50777.42 and 53738.12 in Fig. A.38.) There may be evidence in some of the other profiles to suggest that one of the magnetic poles is offset.

SXP756 seems to show fan beam emission on MJD 52199.47 (Fig. A.42), but judging from the other profiles it would seem that it is a double-peaked pulsar with different shaped peaks from each of its poles; it would also seem that one of them is offset $\sim 18°$. To produce the profile on MJD 52193.62 would likely require one pole to emit more X-rays than the other.

SXP1323 has one bright profile, and it is difficult to explain (MJD 53738.12 in Fig. A.43). One possibility are two pencil beam peaks of unequal height sumperimposed on a weak fan beam profile.

4.3 Relating physical parameters of Be/X-ray binaries

Since the discovery of a relationship between a pulsar's spin period and its orbital period around its high-mass companion (Corbet 1986) it became clear that the orbit of a system influenced some of the characteristics of the pulsar. With a large sample of Be/X-ray systems at our disposal we set out to determine whether other properties of the systems were influenced by, or depended on, the orbit. To begin we show the spin/orbit relation derived for the SMC sample of systems in Fig. 4.55.

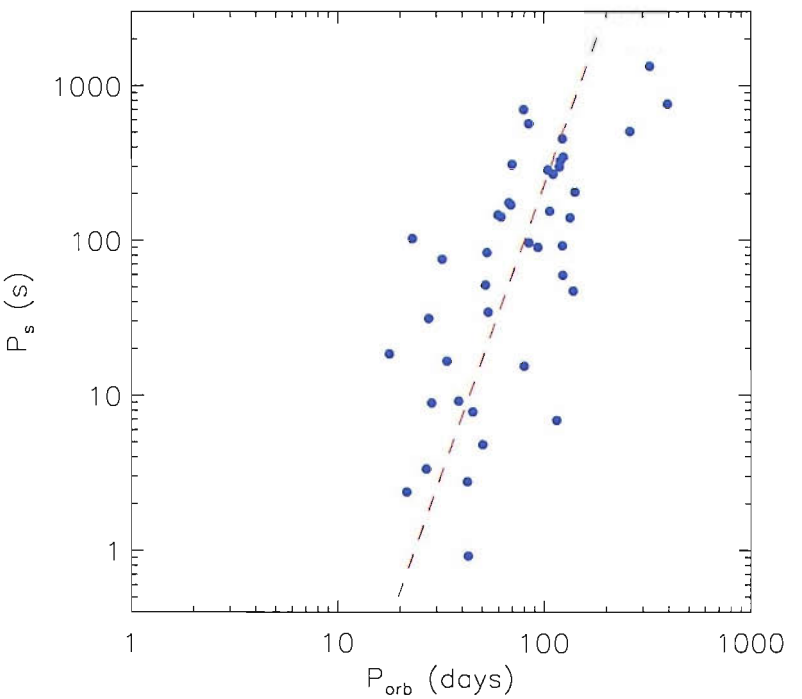

Figure 4.55: P_s vs P_{orb} for the SMC systems. The dashed line represents the fit to P_{orb} vs P_s, and has $r = 0.760$.

Although we plot P_{orb} as the independent variable, it is usually more useful to predict an orbital period given a known pulse period. To this end we have calculated P_{orb} as a function of P_s, which is the line that has been fitted to the data. The relationship between the two periods is

$$P_{\rm orb} = 23.45\, P_{\rm s}^{0.2670} \tag{4.1}$$

where $P_{\rm orb}$ is in days and $P_{\rm s}$ in seconds. The linear correlation coefficient of the fit is $r = 0.76047$. Compare to the values obtained in Eq. (1.2) by Corbet (2006, private communication) using a smaller sample of 17 systems.

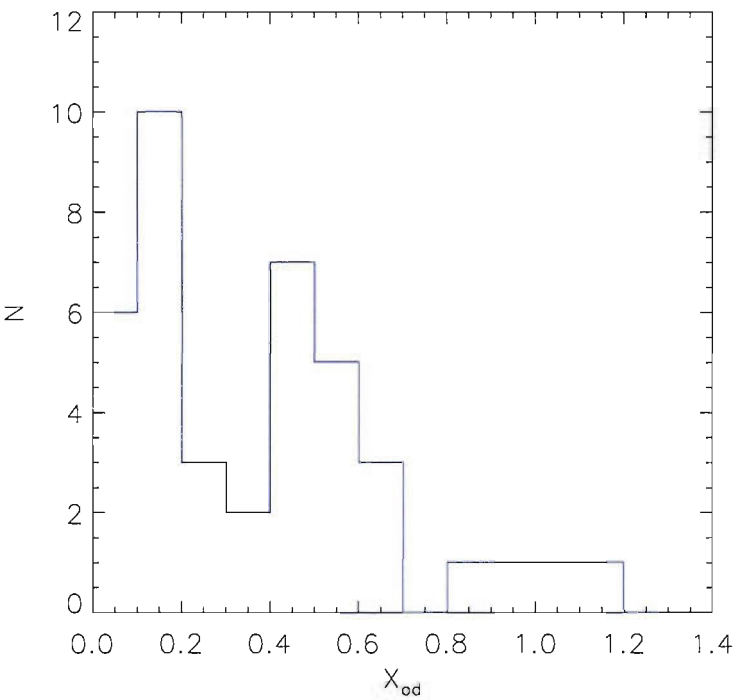

Figure 4.56: Histogram of $X_{\rm od}$ values for SMC systems.

Given the tentative (and qualitative) classification of systems into 3 classes proposed in § 1.3.1, it would be desirable to establish a quantitative base for this grouping. To this end the value of $X_{\rm od}$ was calculated for all systems with a likely orbital period, and a histogram produced of the results (see Fig. 4.56). The first thing that becomes apparent is how large the number of systems with low $X_{\rm od}$ really is, which highlights the transient nature of the Be/X-ray phenomenon; $\sim$53% of the SMC population has $X_{\rm od} < 0.4$. The distribution whithin the histogram corroborates the 3-group theory, with the first group residing in the $X_{\rm od} \gtrsim 0.75$ region, the second in $0.3 \lesssim X_{\rm od} \lesssim 0.75$, with the third having $X_{\rm od} \lesssim 0.3$. These groups would

be, respectively, the Class Ia, Class Ib and Class II systems proposed in § 1.3.1.

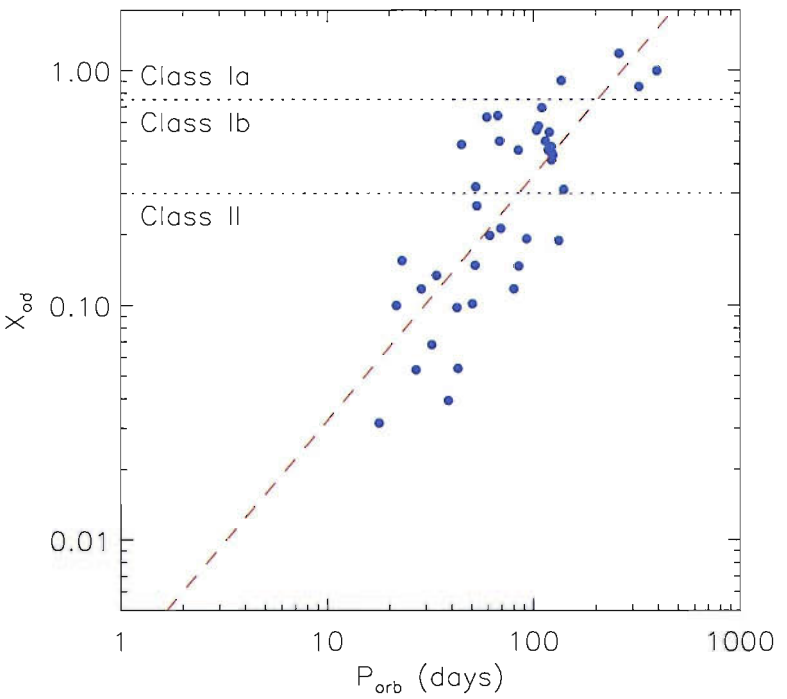

Figure 4.57: X_{od} vs P_{orb} for SMC systems. The straight-line fit has $r = 0.786$. The two horizontal dotted lines separate the regions of each of the three classes of systems.

The next question we might ask is what particular systems populate each of these classes and whether they share any characteristics. To that end we show the relationship between the the spin and orbital periods of these systems and their values of X_{od}. Although the points in Fig. 4.57 have a certain amount of scatter, there is a definite relationship between the orbital period of the systems and the frequency of their outbursts, with longer period binaries undergoing outbursts more often (per number of orbits) than shorter period systems. This relationship does not exist to the same degree between X_{od} and the spin period (Fig. 4.58), as might have been expected given the scatter in the Corbet diagram. The empirical equation we derive to relate X_{od} to the orbital period, P_{orb}, is

$$X_{od} = \frac{1}{336.90} P_{orb}^{1.0406} \tag{4.2}$$

where $P_{\rm orb}$ is in days and $X_{\rm od}$ is in outbursts per orbit. The linear correlation coefficient of the fit is $r = 0.78599$.

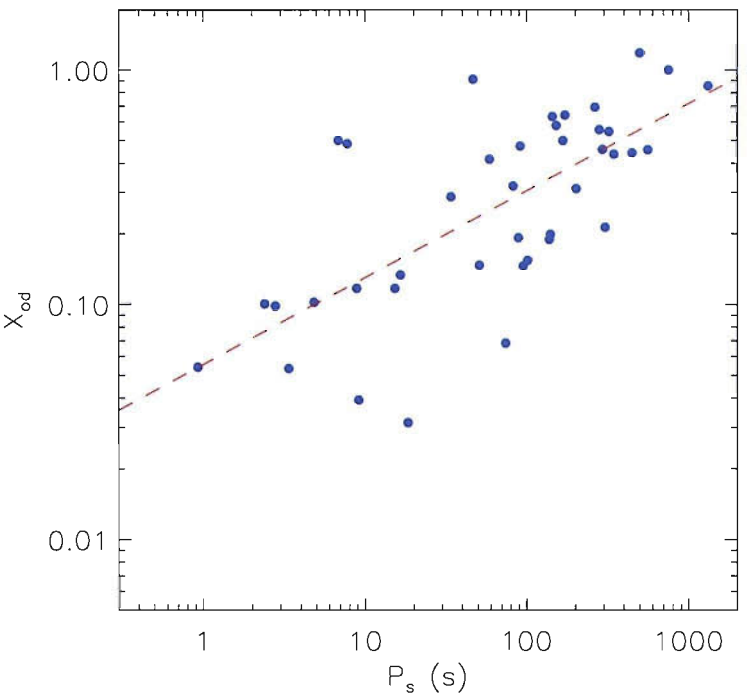

Figure 4.58: $X_{\rm od}$ vs $P_{\rm s}$ for SMC systems. The straight-line fit has $r = 0.699$.

It is unlikely that the orbital period is the only variable responsible for the outburst behaviour of a system; the eccentricity of the orbit should also be expected to play a role as it determines the shape of the orbit and how close the neutron star will be to its companion at periastron. Okazaki and Negueruela (2001) explain the outburst behaviour of Be/X-ray systems based on the eccentricity and size of the orbits, and Fig. 4.57 would imply that the duration (size) of the orbit is indeed a factor. It would be desireable to see if a similar relationship exists between $X_{\rm od}$ and e, but no SMC Be system has had any orbital parameters, beyond the period, calculated for it. We venture a guess that high eccentricity systems will have high values of $X_{\rm od}$ and probably belong to Class Ia; medium eccentricity systems with medium orbital periods will belong to Class Ib; and finally low eccentricity systems with short orbital periods will belong to Class II. A low eccentricity system with a medium orbit would probably be Class Ib, while a high eccentricity coupled with

a small or medium orbit would likely be Class II. The values to determine what constitutes a low/medium/high eccentricity or a small/medium/large orbit cannot yet be unequivocally established. From Fig. 4.57 we would propose medium-sized orbits are within the range $40-150$ days, and when moving along a line of isoperiod the eccentricity increases with $X_{\rm od}$. When moving along a line of iso$X_{\rm od}$, the eccentricity should remain approximately constant.

Another factor in explaining outburst behaviour is the neutron star's magnetic field strength. While a number of accretion-powered pulsars in the Milky Way have had magnetic fields measured for them through cyclotron features, this has not been possible for SMC systems given the low fluxes available from this distance in the $\sim 10-40\,$keV energy range where we expect to find cyclotron lines.

Thanks to the observed changes in spin period of a number of SMC pulsars, it has been possible to obtain a rough estimate of the magnetic field for 9 of them, together with luminosity estimates. Although we know the amplitude of the pulsations of each pulsar, these can not be directly compared as the pulse fraction of each one is unknown[4].

Given the orbital period of a system, a quantity can be derived to express the discrepancy between the observed value, $P_{\rm orb}$, and the expected value, $P_{\rm pred}$ (obtained through Eq. (4.1)), given the pulse period:

$$\delta_{\rm orb} = 100 \times \frac{|P_{\rm orb} - P_{\rm pred}|}{P_{\rm pred}} \tag{4.3}$$

where $P_{\rm pred}$ and $P_{\rm orb}$ are in days and the orbital discrepancy, $\delta_{\rm orb}$, is a percentage.

Fig. 4.59 shows how B varies with $\delta_{\rm orb}$. Given this distribution, it would seem that neutron stars with weaker magnetic fields tend to be in orbits either much larger or much smaller than the predicted size. In fact, what is probably happening

[4]Even for a single pulsar, the pulse fraction has been seen to vary with luminosity (White et al. 1983; Nagase 1989; Bildsten et al. 1997) so it would be necessary to know the pulse fraction for each observation in order to convert pulsed fluxes to total luminosities.

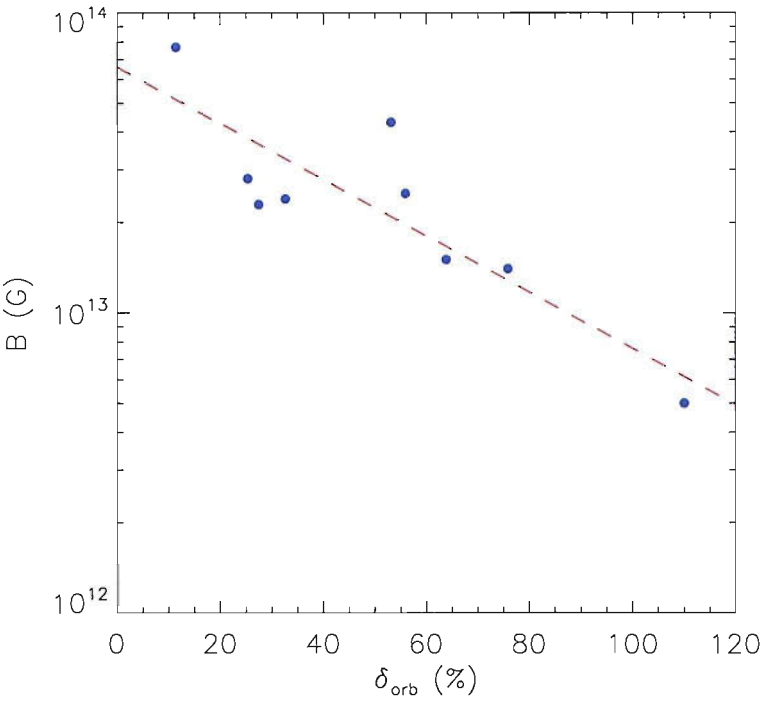

Figure 4.59: B vs δ_{orb} for the 9 SMC systems for which a magnetic field has been estimated. The straight-line fit has $r = -0.863$.

is that neutron stars with weaker magnetic fields have spin periods that are shorter or longer than the values required to predict the actual orbital periods. A simple interpretation would be that higher magnetic fields are more efficient at funnelling material onto the neutron star and should therefore also be more efficient at regulating the pulsar's spin period to bring it closer to the expected value. However, there are certain systems that defy this interpretation, as a number of them, undergoing frequent outbursts, suffer from torques that are spinning them further *away* from the spin/orbit relationship. Examples of such systems are SXP46.6 (Fig. 4.19(a)), with $P_{orb} = 137.4\,d$ ($P_{pred} = 65.4\,d$) which is spinning *up* $\sim 2.4 \times 10^{-2}\,s\,yr^{-1}$, and SXP144 (Fig. 4.34(a)), with $P_{orb} = 59.5\,d$ ($P_{pred} = 88.5\,d$) which is spinning *down* $\sim 0.50\,s\,yr^{-1}$. If the principles on which the Corbet diagram is based on are correct (that the orbital period regulates the spin period) then both these systems should have a $\dot{P}$ of opposite sign to that which they actually have.

There is no apparent relationship between δ_{orb} and X_{od}, or B and X_{od}, so it would

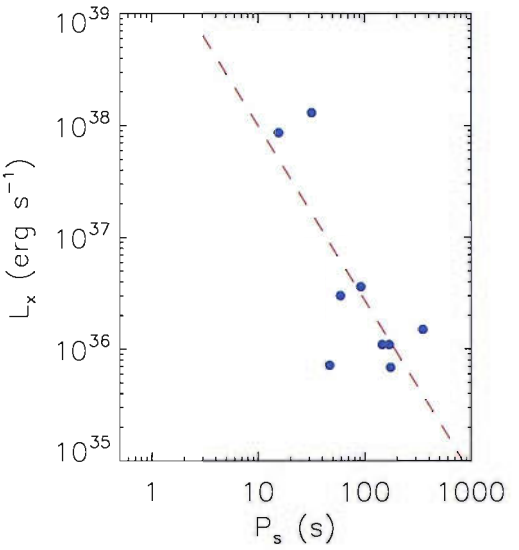

Figure 4.60: L_x vs P_s for SMC systems. The straight-line fit has $r = -0.759$.

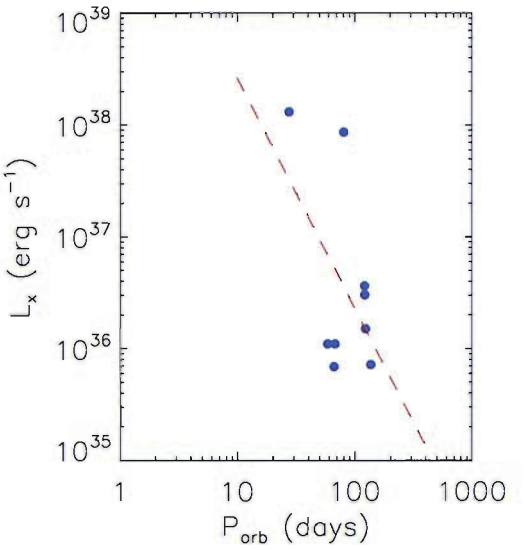

Figure 4.61: L_x vs P_{orb} for SMC systems. The straight-line fit has $r = -0.530$.

seem that the frequency of outbursts is not a determining factor in how far from P_{pred} systems are, and neither is the magnetic field a factor in how often outbursts occur.

We show the dependence of the estimated L_x on P_s and P_{orb} in Figs. 4.61 and 4.60. L_x is not independent of P_s (as it was calculated using Eq. (1.14), which depends on both P_s and $\dot{P}$), but was calculated independently of P_{orb}, and shows no strong dependence on it. We found no relation between B and P_{orb}.

A strong relation is found between L_x and X_{od}. The linear correlation coefficient in Fig. 4.62 is $r = -0.96092$ and the empirical relation for the fitted line is given in an approximate form by

$$L_{x37} = \frac{1}{31} X_{od}^{-\frac{5}{2}} \tag{4.4}$$

where the luminosity will be in units of $10^{37}\,\mathrm{erg\,s^{-1}}$.

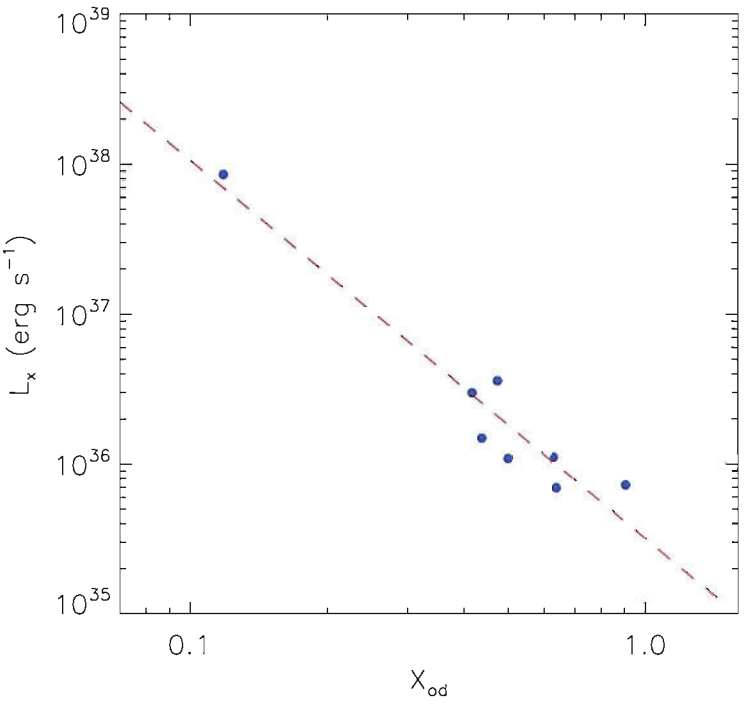

Figure 4.62: L_x vs X_{od} for the 8 SMC systems for which the luminosity and the orbital period have been estimated. The straight-line fit has $r = -0.961$.

This inverse relationship between the luminosity of outbursts and their frequency can be interpreted as a difference between the amount of matter available for accretion during frequent and infrequent outbursts. If matter is accreted from the circumstellar disc of the companion Be star, it is plausible to think that frequent outbursts will not allow the build up of a substantial disc as the neutron star will deplete it periodically. On the other hand, if outbursts are infrequent (due to a long orbital period and/or a large orbit), the Be star will be able to "store" more gas in the disc in between outbursts, which will then provide larger amounts of material for the neutron star to accrete, thus increasing the luminosity of the outburst.

4.4 Searching for new pulsars

As soon as an observation is made by *RXTE* the quick-look data is searched for periodicities; any bright pulsars within the field of view will be seen at a high level of significance and their detection noted down. If a new one is found, it is entered into the list of pulsars and a search can be made for fainter outbursts in the past. For this to happen, a period is required around which to base the search.

It is likely that a number of pulsars exist that have never been detected at a high enough significance to stand out in the global power spectrum, and have thus not been identified. This could be for a number of reasons: they could lie at the edge of the field of view, not be bright enough to stand out, have a very low pulse fraction, or be heavily obscured. It could also be a combination of these factors.

Occasionally, pulsations are detected slightly above 90% in the global power spectrum at a period not belonging to a known pulsar. These ambiguous detections are treated with caution, and it is not until further detections are made at the same, or similar period that a new pulsar is announced. If other detections are not forthcoming, these orphan periods are discarded as spurious peaks. One case in point is SXP452; it was present at a high significance in the first observation of this survey, together with a number of other pulsars (SXP91.1, SXP74.7, SXP46.6, etc.), but was never recognised as a new pulsar. It was later "discovered" in archival *Chandra* data.

When PUMA finds a peak in the global power spectrum above 90% significance that it cannot assing to a known pulsar, it will file it away with information on its period, flux and the observation it was found in. This file has been revised to look for unknown periods that are recurring, or periods that were relatively strong in their observation. The most promising ones were then added to the list of known pulsars, to be searched for by PUMA in the same way a known pulsar is.

After the first run of PUMA, the amplitude light curve was examined to see at what positions each of these candidate pulsars were detected, and from this information coordinates were estimated in order to apply a collimator correction

on the next run of PUMA. It is important to collimator correct these detections in order to bring them above the noise level because we are dealing with faint pulsars. If they were not faint, they would have been spotted and recognised already.

4.4.1 Candidate pulsars – Light curves

Table 4.2 lists a number of candidate pulsars that have been detected frequently enough to suggest they may be real. Most of them have also been detected periodically such that an orbital period has been estimated. The light curves of these pulsars are also shown, with vertical, dashed lines denoting the expected times of outburst (where applicable). The column titled FAP lists the false alarm probability for the pulsar, which estimates the probability that the data points above our detection threshold ($Sig_{\min}$) are due to chance.

The method used to estimate the FAP is as follows: For a given observation, the probability that a peak in the periodogram is due to chance is $100-Sig_{\text{peak}}$. If we set a minimum threshold $Sig_{\min}$, then the probability of detecting a peak due to noise, within a specified period range, above this threshold is $p \equiv (100 - Sig_{\min})/100$. Let us extend this to our survey, where we have a large number of observations: given n observations, the probability P that we will find m peaks above $Sig_{\min}$ will be given by the Binomial Distribution Function:

$$BDF(n, m, p) = C_m^n \, p^m (1-p)^{n-m} = \frac{n!}{m!\,(n-m)!} \, p^m (1-p)^{n-m} \tag{4.5}$$

To obtain the FAP we must consider another factor: the detections are not randomly spaced, but lie at distances from each other that are multiples of the orbital period P_{orb}. The way in which the detections are organised in time is therefore important; in how many different ways could m significant detections appear in n observations? The answer is the combination

$$C_m^n = \frac{n!}{m!\,(n-m)!} \tag{4.6}$$

A subset of these will be the number of detections that would fall on dates predicted by the outburst ephemeris. Given an orbital period, there are only a certain number of dates when the outbursts should occur; we will call this number o. So the number of ways that detections can occur and be consistent with an orbital period $P_{\rm orb}$ is

$$N_m^o = \frac{o!}{m!\,(o-m)!}\,\frac{P_{\rm orb}}{t_{\rm s}} \tag{4.7}$$

where $t_{\rm s}$ is the sampling interval of the observations (~ 7 d). Therefore, the probability that, given m detections in n observation, these will be consistent with an orbital period is obtained by dividing Eq. (4.7) by Eq. (4.6). Multiplying the result by Eq. (4.5) will give us our estimate of the FAP. Because the C_m^n cancel out, we are left with

$$\mathrm{FAP} \simeq N_m^o\, p^m (1-p)^{n-m} = \frac{P_{\rm orb}}{t_{\rm s}}\,\frac{o!}{m!\,(o-m)!}\, p^m (1-p)^{n-m} \tag{4.8}$$

Why do we consider this only an *estimate* of the FAP? In order to simplify the problem we have adopted the following strategies: a) assumed that $t_{\rm s}$ is 7 days, when in reality it is only 7 on average; b) detections do not always fall exactly on the predicted date; c) we have used the number of outbursts for m (as given in the Outburst column of Table 4.2, which is not necessarily the same as the number of significant detections; and lastly, d) we over estimated N_m^o as some of the dates included in this number fall during times when there are no observations, but multiplying by the factor $P_{\rm orb}/t_{\rm s}$ to obtain the required number was more convenient (and quicker!) that analysing each case separately.

Given these caveats, we still believe the estimation to be worthwhile and necessary as it provides a ballpark figure with which to judge these findings objectively. A better way to calculate the FAP would be to simulate all the observations using Monte-Carlo techniques and then analyse them with PUMA. Repeating this process a few hundred times would give us the required statistics to correctly calculate the FAP. Unfortunately, the computer burden of executing a single run of simulations is estimated at ~ 10 hours; to conduct even 100 such runs would require ~ 42 days,

Table 4.2:

Possible New X-Ray Pulsars in the SMC

$P_{\rm spin}$ (s)	$T_{\rm P}$ (MJD)	$P_{\rm orbital}$ (days)	Outbursts	$Sig_{\rm min}$ (%)	FAP (%)
0.61	52264.0 ± 0.7	22.34 ± 0.03	7	95	2.28×10^{-5}
0.68	52238.0 ± 0.9	29.78 ± 0.05	10	95	8.11×10^{-7}
0.77	52270.6 ± 1.0	34.06 ± 0.06	10	95	2.09×10^{-7}
2.02	52242.9 ± 1.5	48.95 ± 0.13	7	95	3.15×10^{-5}
5.06	52255.5 ± 0.8	25.69 ± 0.04	5	95	5.60×10^{-3}
8.28	52280.7 ± 1.7	34.40 ± 0.07	9	95	5.14×10^{-7}
10.7	52298.8 ± 0.8	15.96 ± 0.01	8	90	7.90×10^{-6}
19.4	52269.3 ± 2.9	57.87 ± 0.16	7	95	3.88×10^{-8}
19.7	52238.8 ± 1.9	38.10 ± 0.07	9	95	1.73×10^{-7}
27.7	52279.0 ± 1.9	27.50 ± 0.05	7	95	1.28×10^{-3}
55.9	52254.0 ± 3.6	71.12 ± 0.24	12	98	5.14×10^{-12}
57.6 [5]	52182.4 ± 5.1	73.10 ± 0.28	12	96	6.53×10^{-12}
61.0	52175.7 ± 4.9	97.37 ± 0.65	9	99	2.43×10^{-10}
93.1	52268.7 ± 1.0	32.15 ± 0.05	8	96	1.97×10^{-5}
126	52261.0 ± 6.1	123.0 ± 0.9	3	99	7.59×10^{-2}
287	52306.9 ± 2.7	88.81 ± 0.44	11?	97	2.04×10^{-12}
401	52081.6 ± 14.3	285.7 ± 5.4	4	98.5	1.56×10^{-4}
708	52281.5 ± 2.2	73.7 ± 0.4	8	99	1.37×10^{-8}
779	52049.3 ± 7.3	242.7 ± 4.7	8?	99	7.85×10^{-12}
2460	52636.7 ± 6.3	126.7 ± 0.9	8	97	1.29×10^{-8}
2790	–	–	4	99	3.33×10^{-3} [6]

which is not feasible.

[5]This could be the same pulsar as 55.9, given the similar orbital epochs and periods, although it would require large changes in the spin period in short amounts of time. A high inclination of the orbit with respect to our line of sight would be able to account for this, but would also require the pulsar's magnetic field to be similarly inclined in order for pulsations to be detected.

[6]Because there is no orbital period proposed for this candidate system, this is the FAP of detecting 4 signals above 99% significance in the available observations.

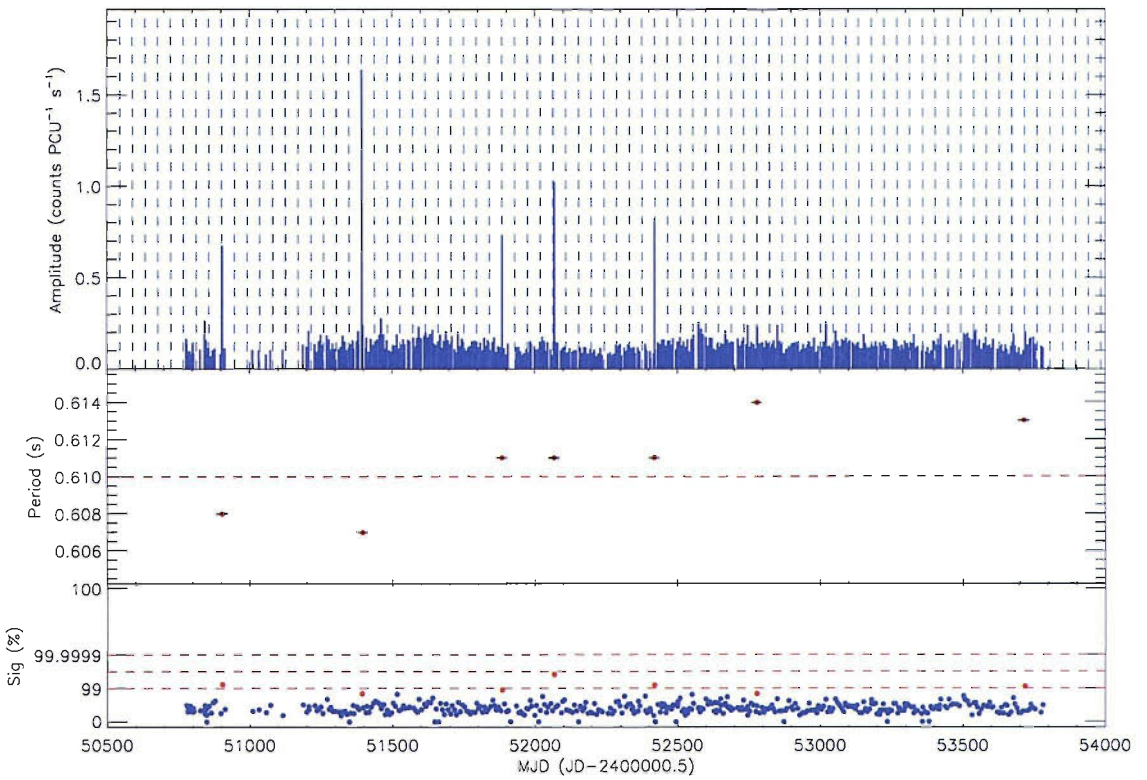

Figure 4.63: Light curve of candidate pulsar SXP0.61. For clarity, only every other ephemeris line has been plotted.

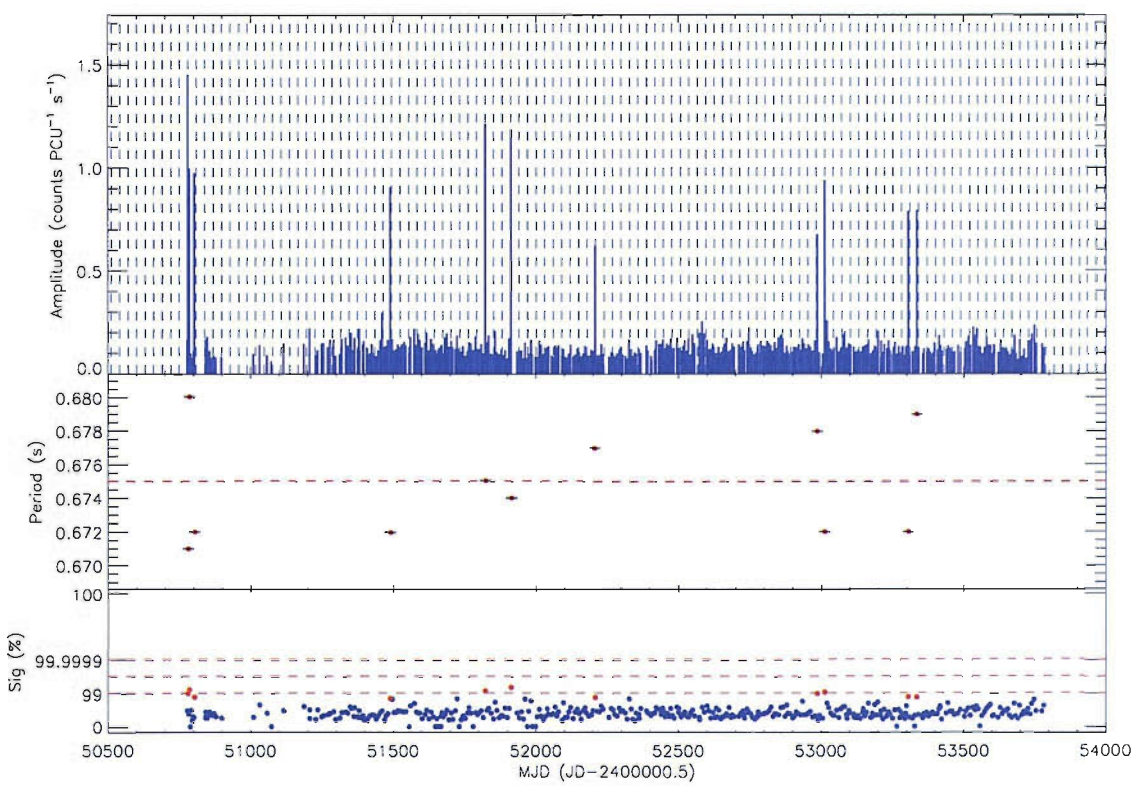

Figure 4.64: Light curve of candidate pulsar SXP0.68.

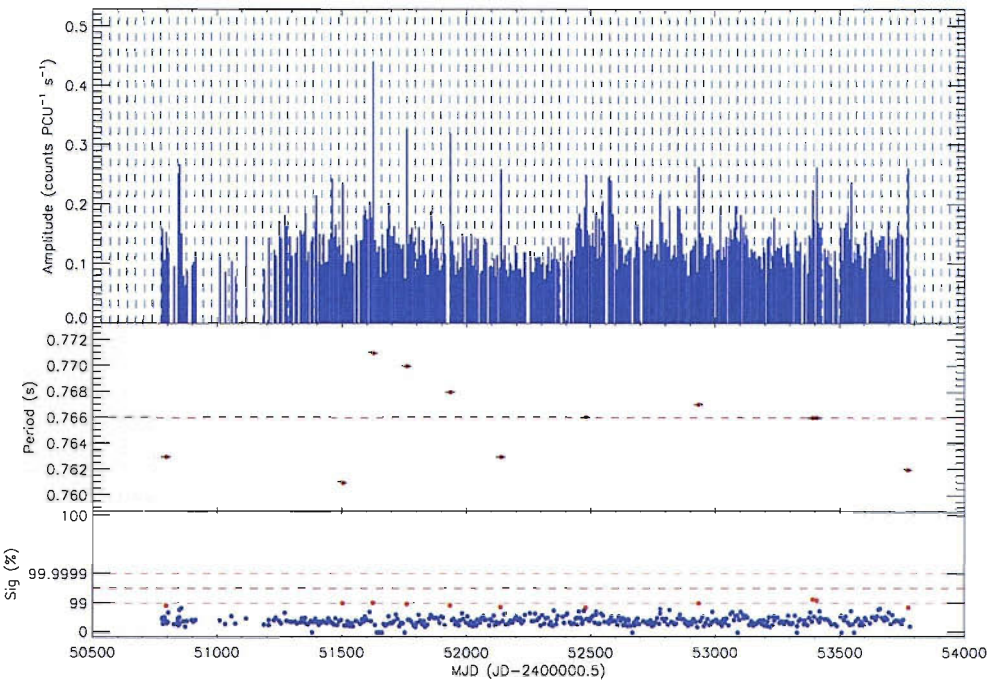

Figure 4.65: Light curve of candidate pulsar SXP0.77.

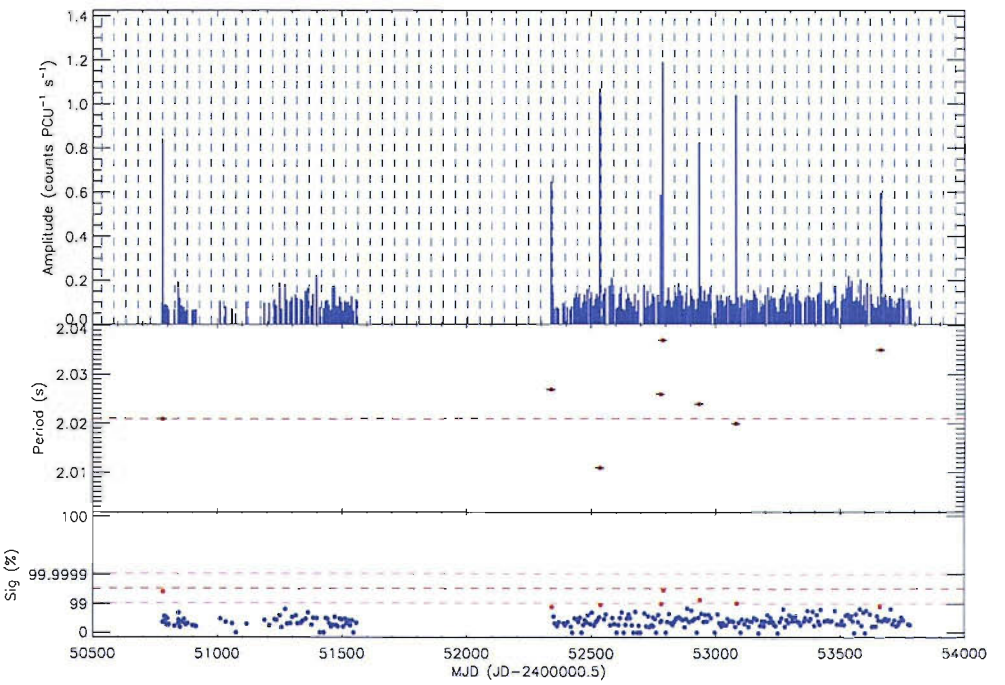

Figure 4.66: Light curve of candidate pulsar SXP2.02.

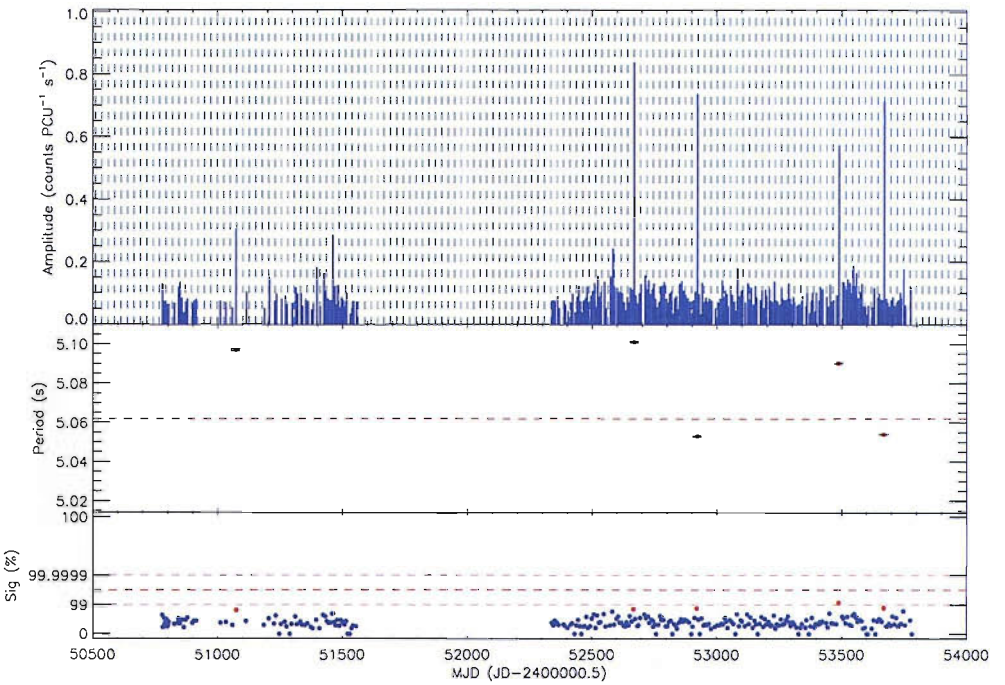

Figure 4.67: Light curve of candidate pulsar SXP5.06.

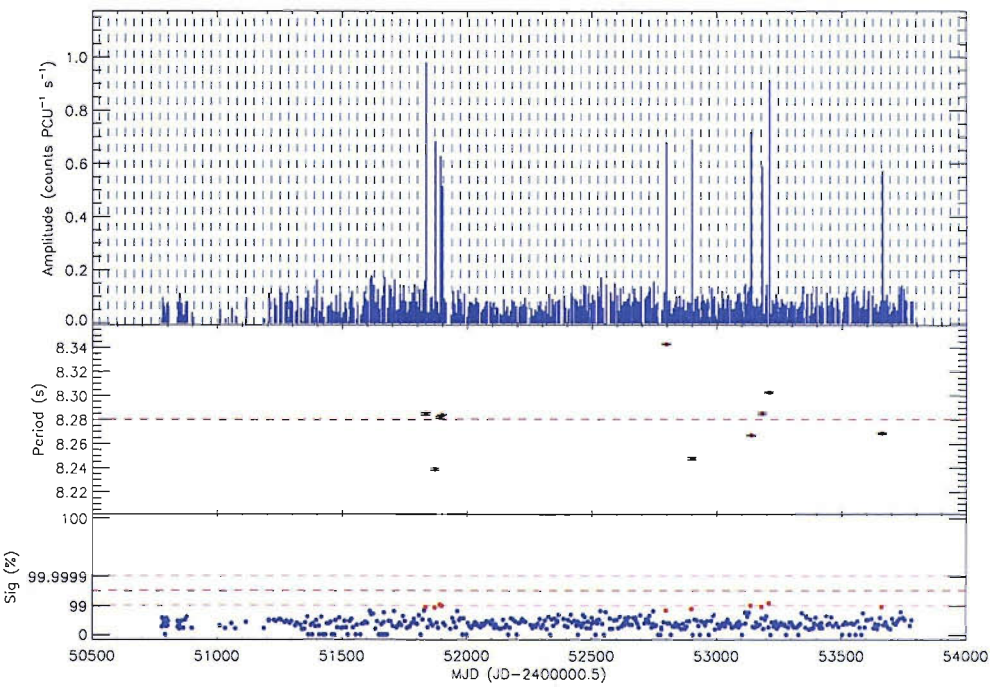

Figure 4.68: Light curve of candidate pulsar SXP8.28.

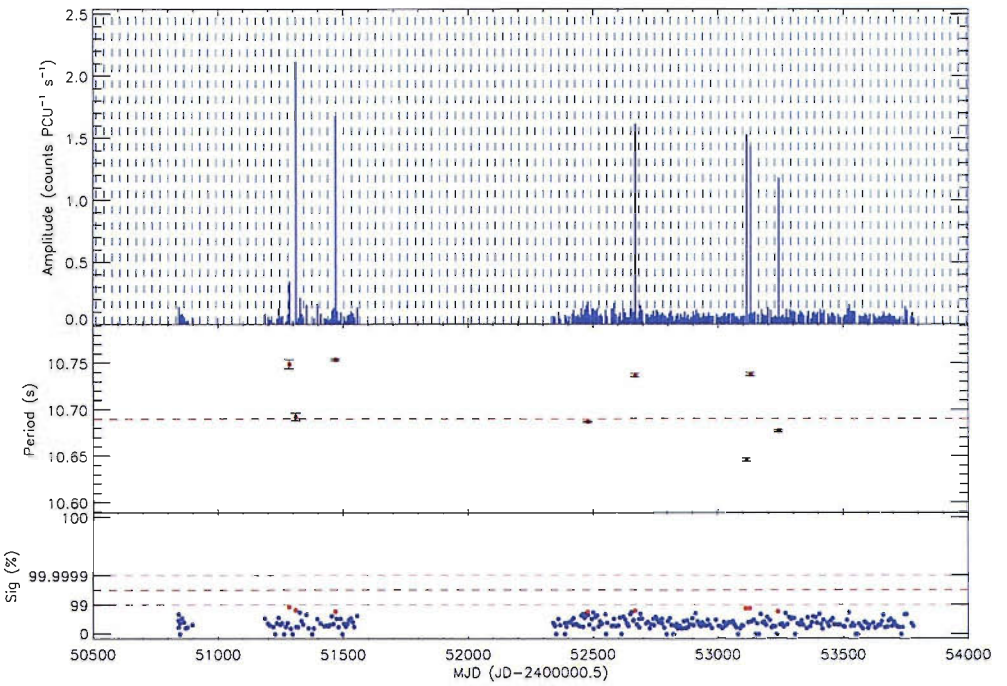

Figure 4.69: Light curve of candidate pulsar SXP10.7. For clarity, only every other ephemeris line has been plotted.

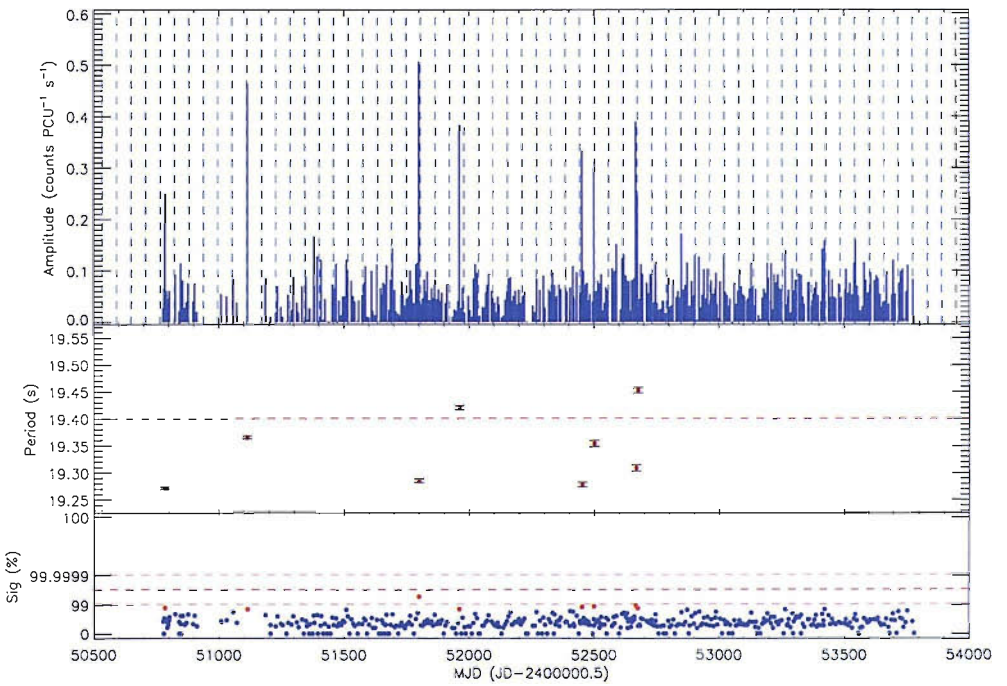

Figure 4.70: Light curve of candidate pulsar SXP19.4.

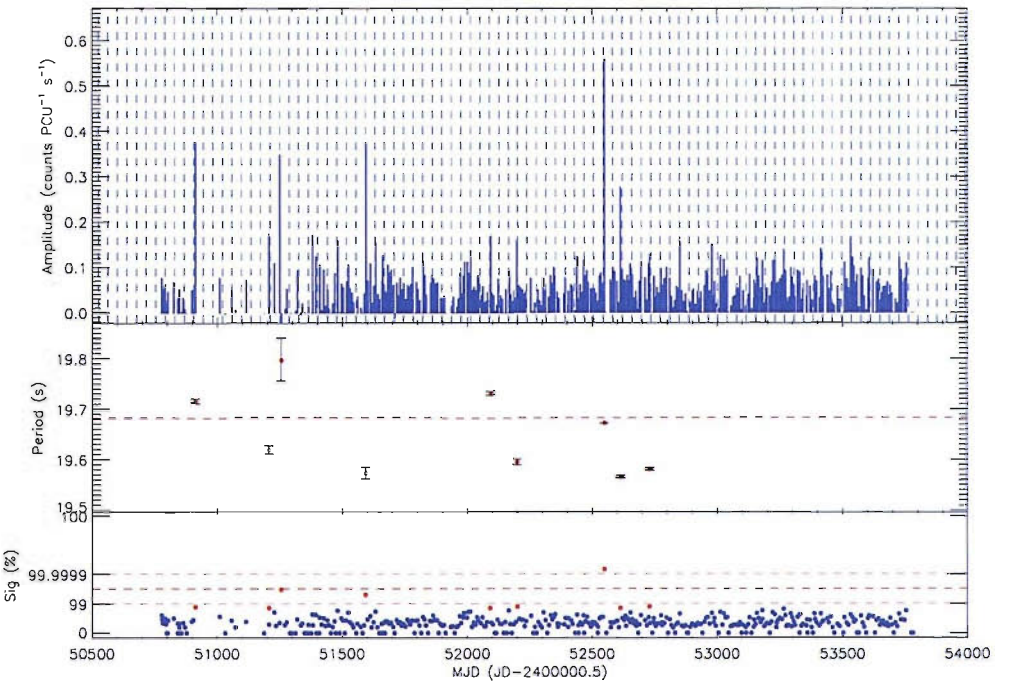

Figure 4.71: Light curve of candidate pulsar SXP19.7.

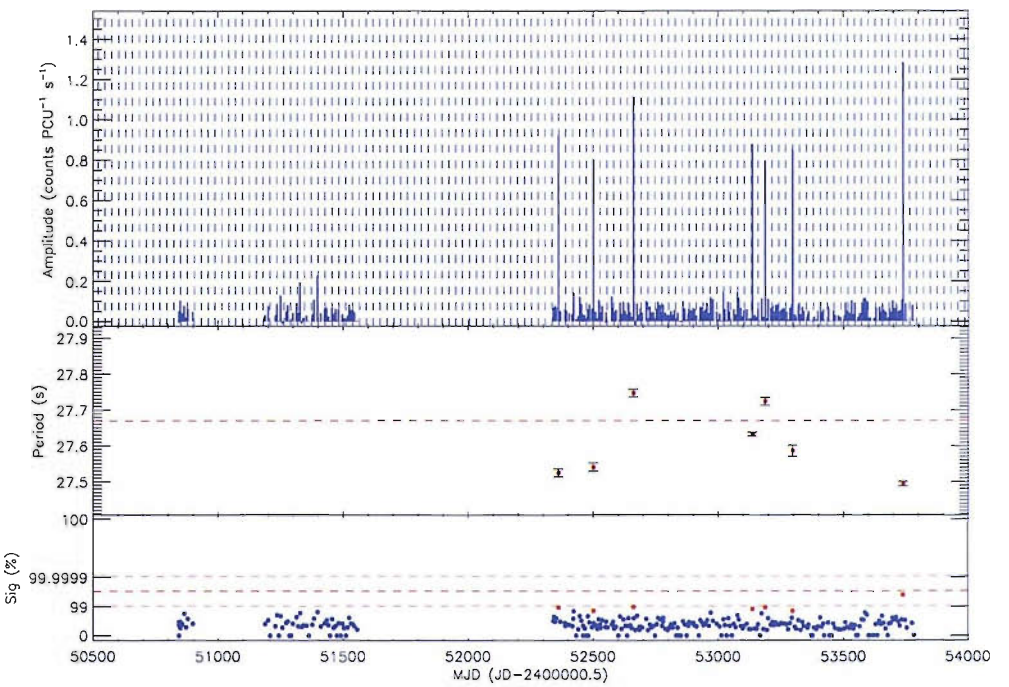

Figure 4.72: Light curve of candidate pulsar SXP27.7.

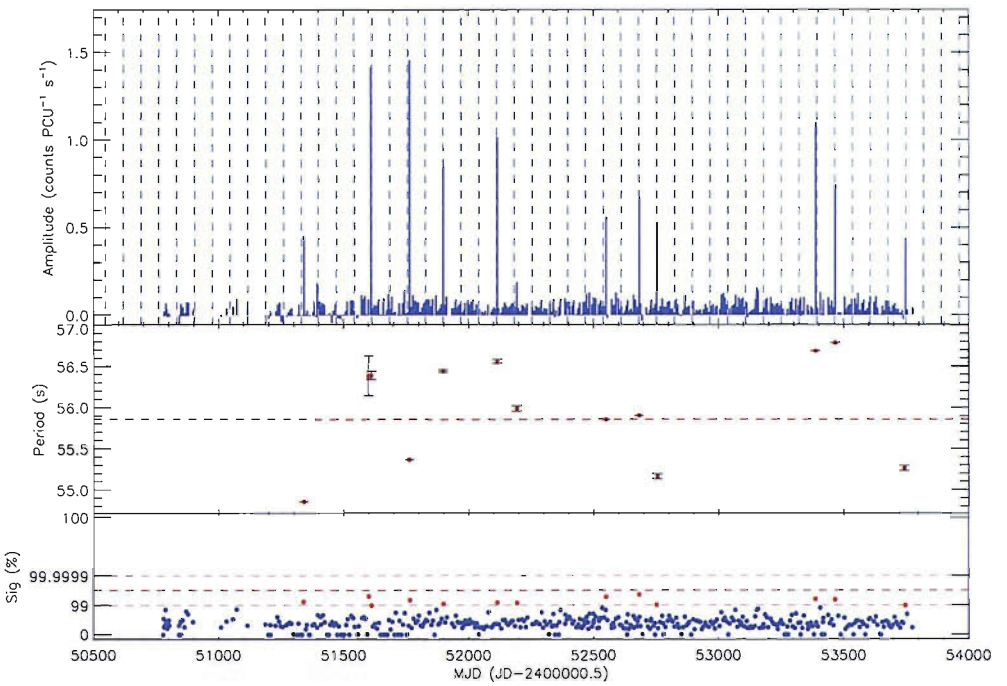

Figure 4.73: Light curve of candidate pulsar SXP55.9.

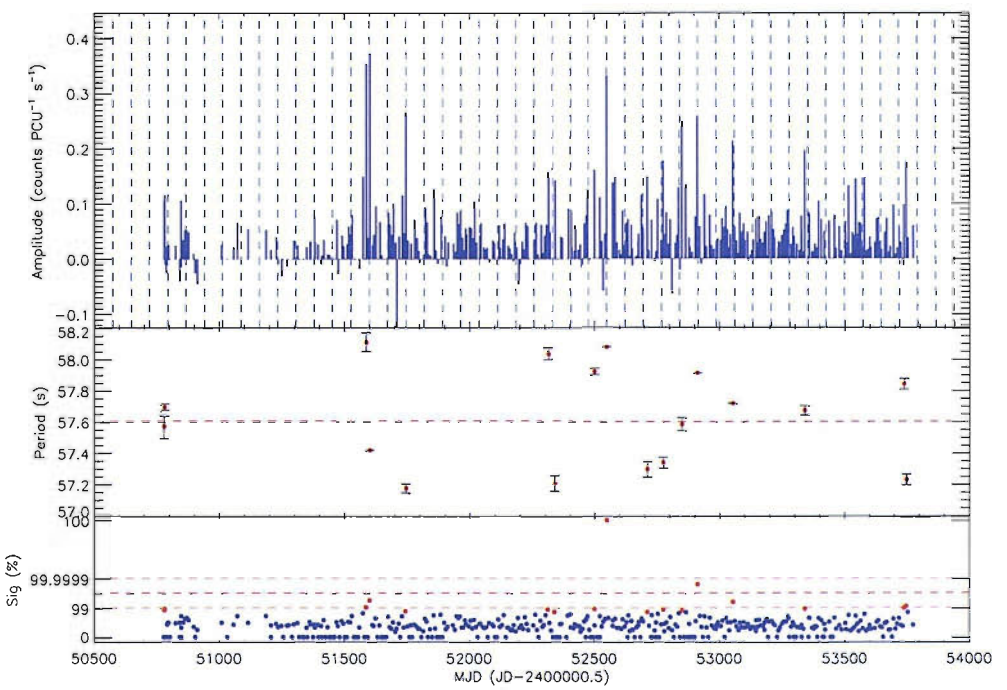

Figure 4.74: Light curve of candidate pulsar SXP57.6.

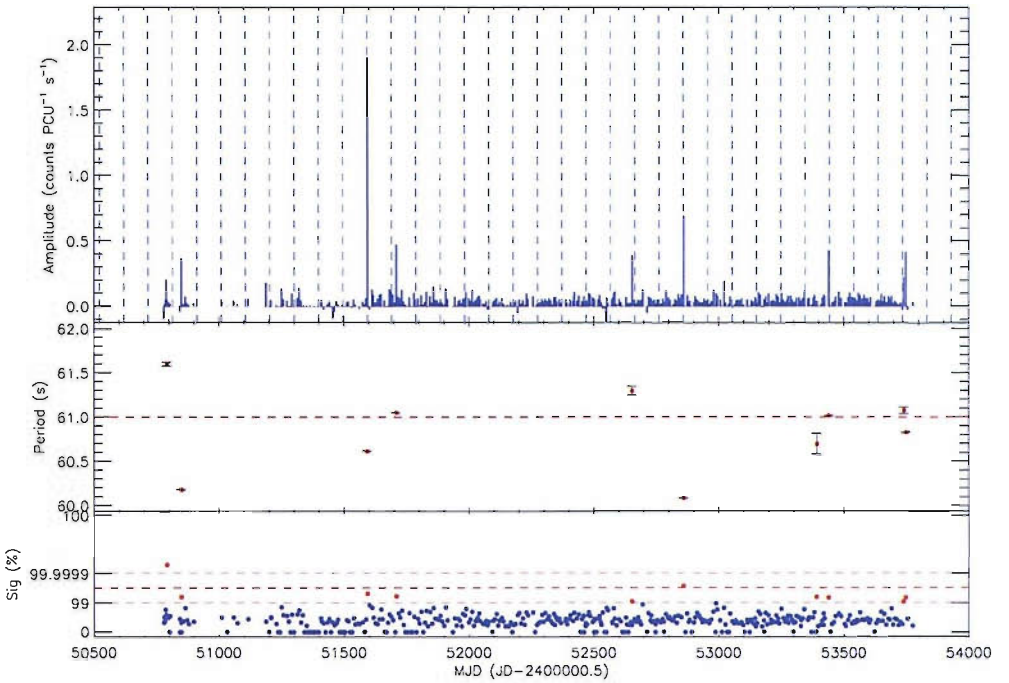

Figure 4.75: Light curve of candidate pulsar SXP61.0.

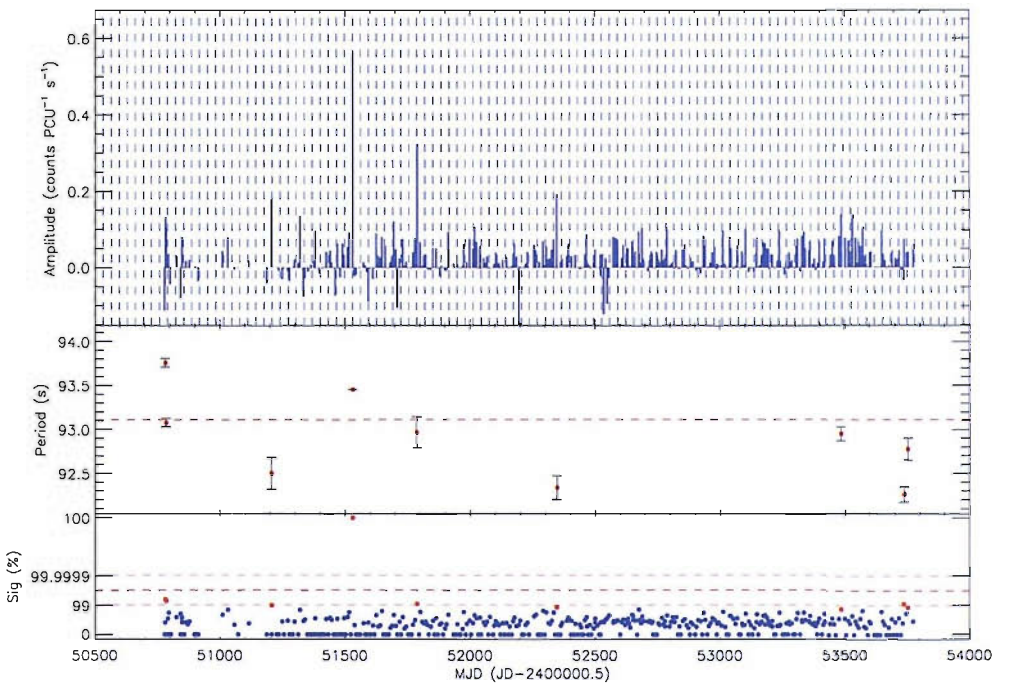

Figure 4.76: Light curve of candidate pulsar SXP93.1.

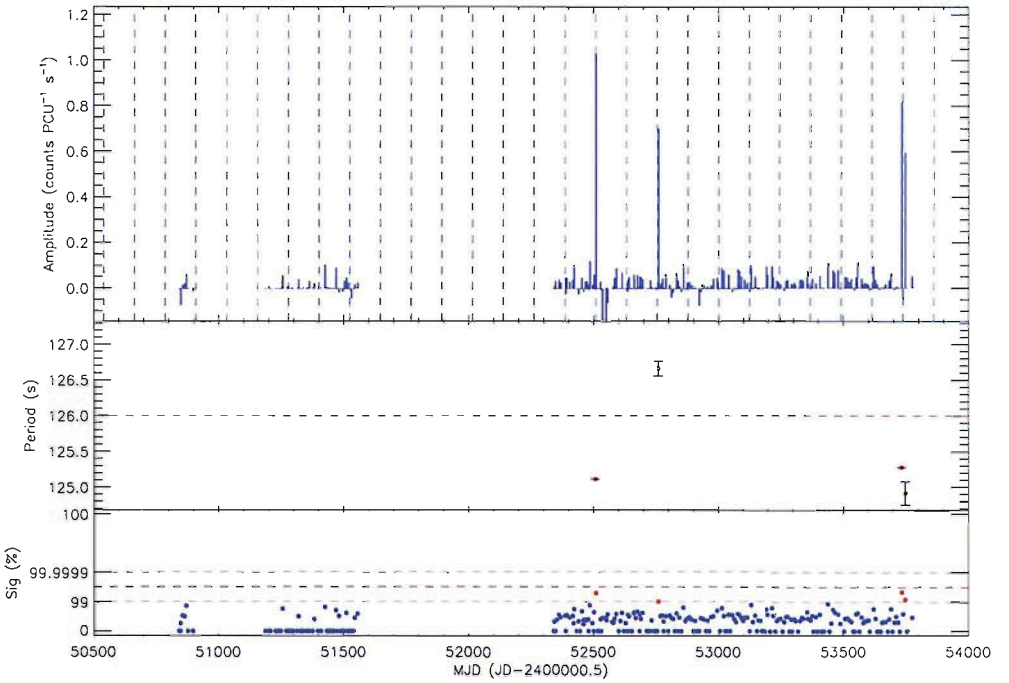

Figure 4.77: Light curve of candidate pulsar SXP126.

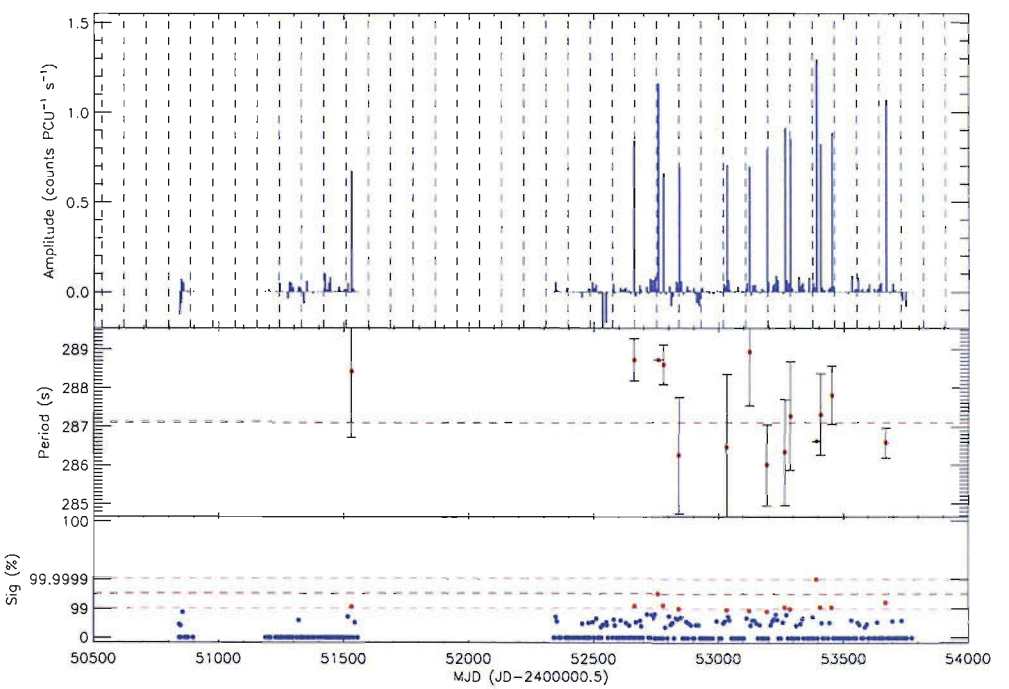

Figure 4.78: Light curve of candidate pulsar SXP287.

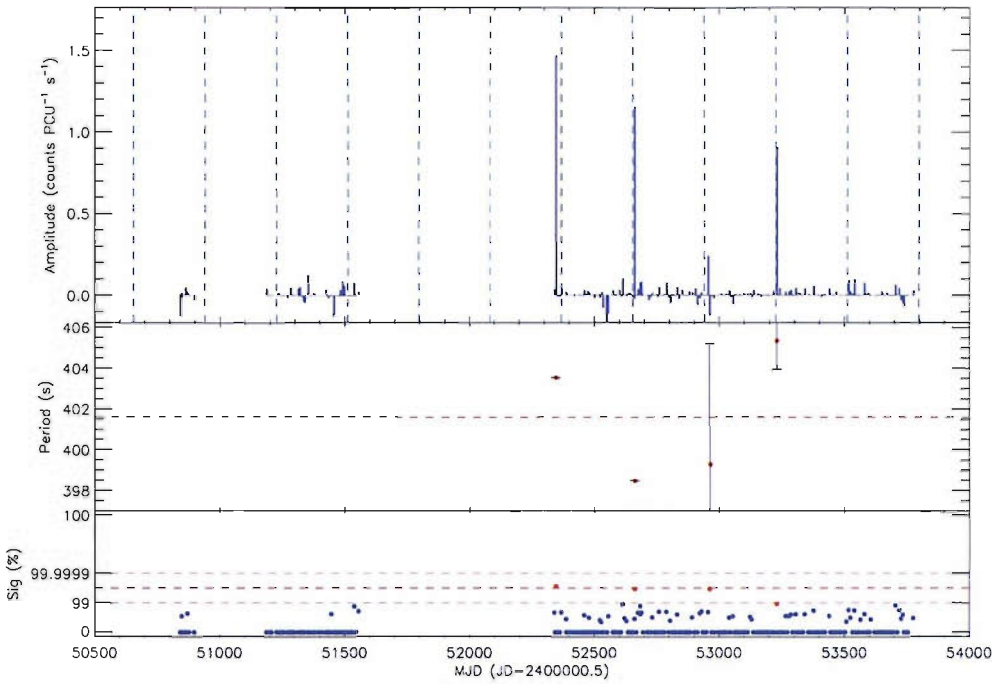

Figure 4.79: Light curve of candidate pulsar SXP401.

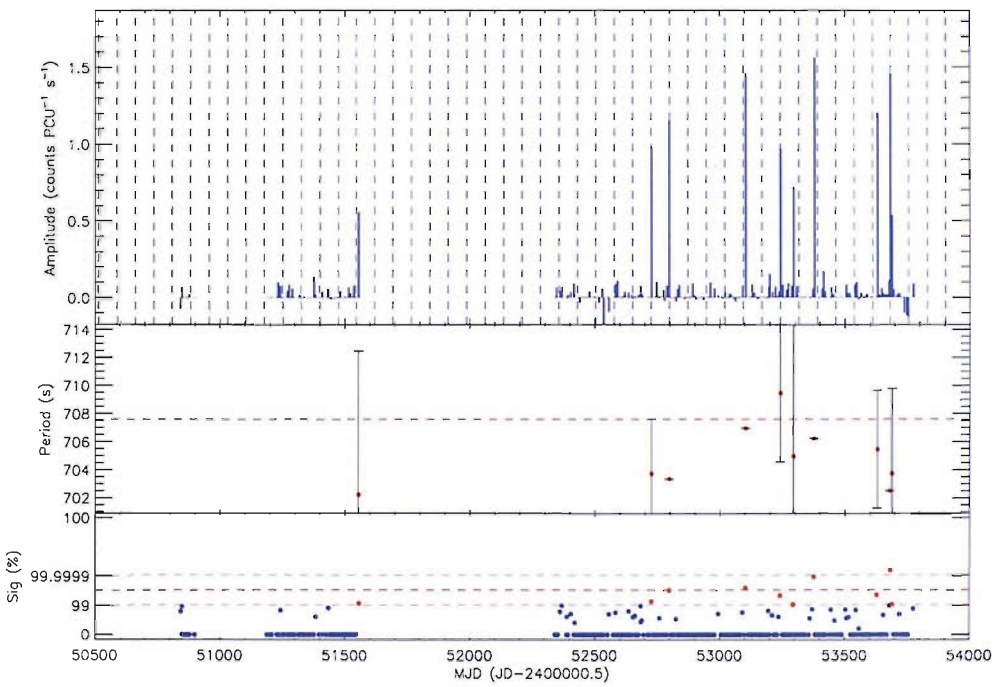

Figure 4.80: Light curve of candidate pulsar SXP708.

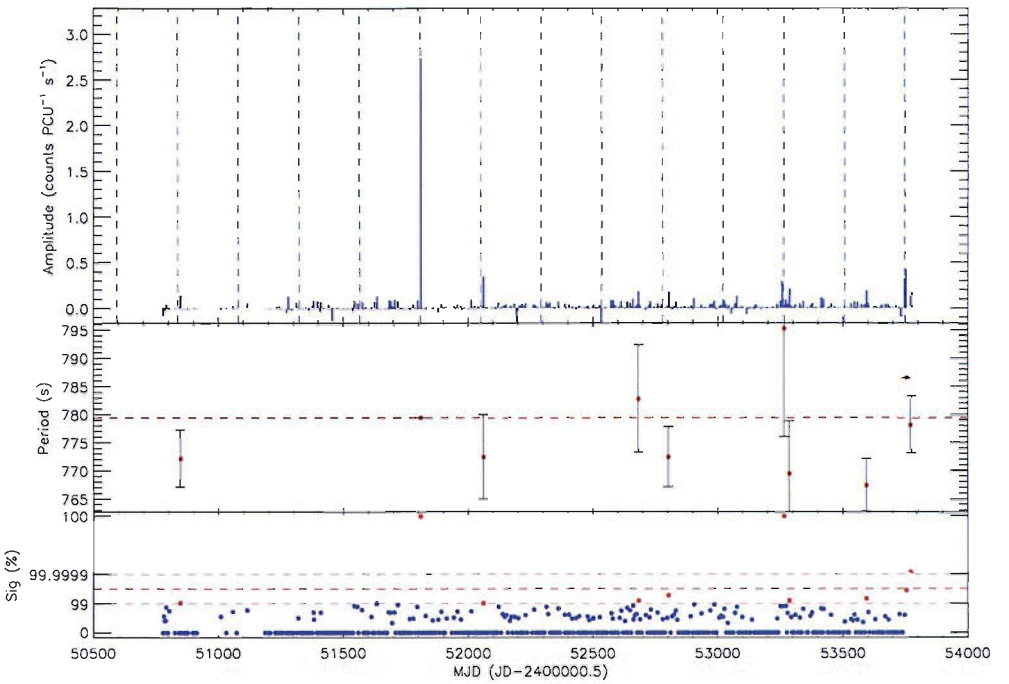

Figure 4.81: Light curve of candidate pulsar SXP779.

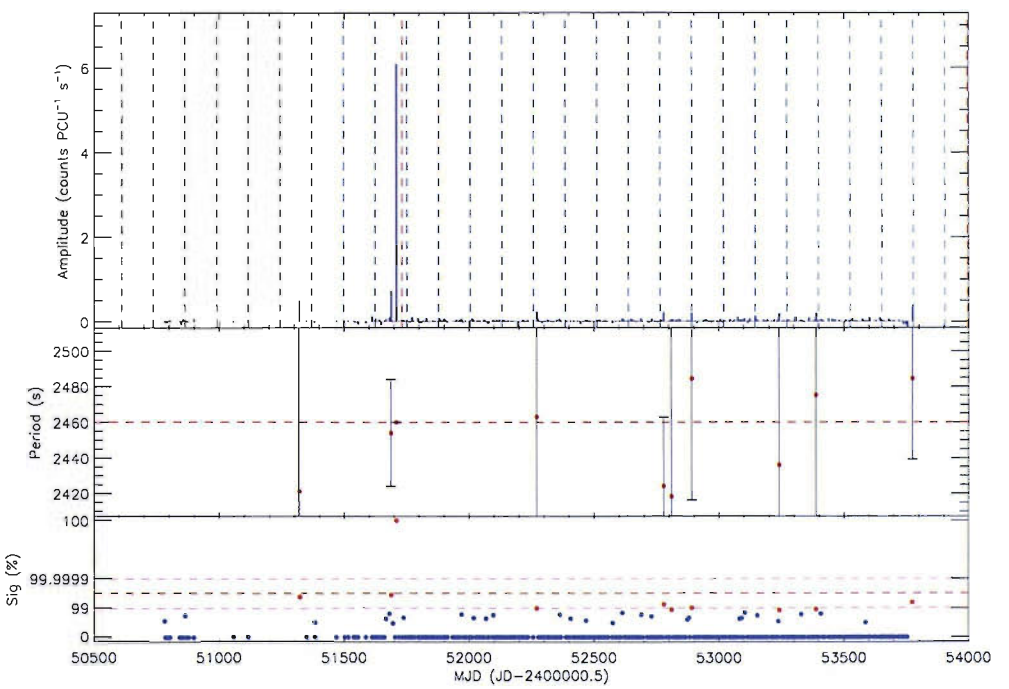

Figure 4.82: Light curve of candidate pulsar SXP2460.

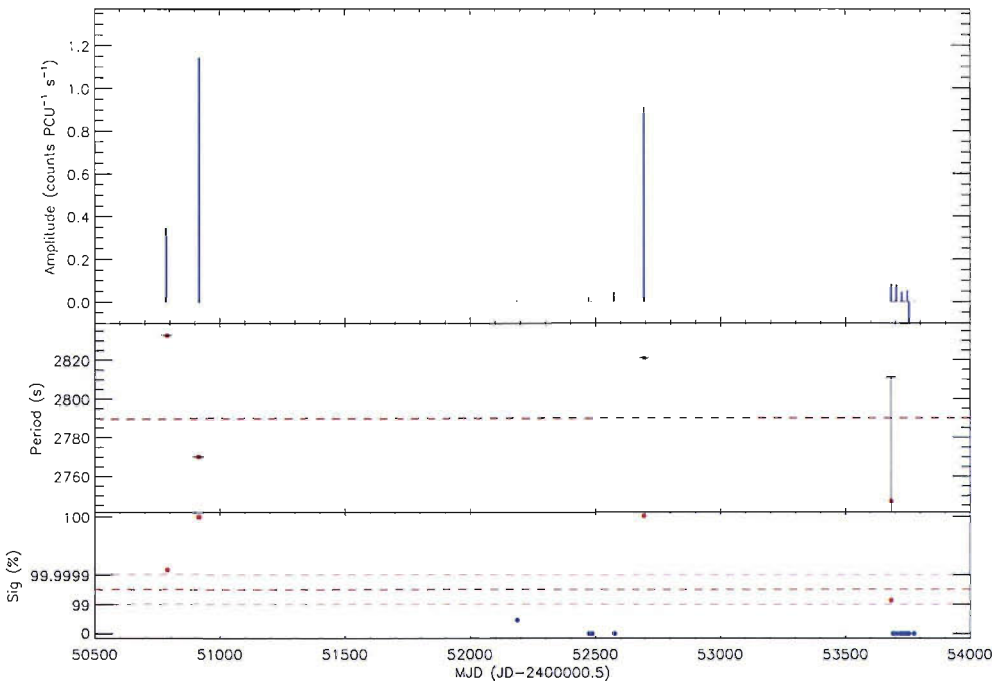

Figure 4.83: Light curve of candidate pulsar SXP2790.

4.4.2 Candidate pulsars – Pulse profiles

In the following pages the reader will find a selection of pulse profiles from the candidate pulsars. All light curves where an unknown pulsar was detected were folded and inspected by eye. Whenever possible, the observation where the pulsar was detected at the highest level of significance was the one chosen to be folded. However, on some occasions a pulsar displayed a greater pulse amplitude in an observation where it was detected at a lower significance, in which case this light curve was chosen. In general, the folded profile exhibiting the lowest dispersion within each bin is shown.

It should be noted that these are not necessarily representative profiles of each pulsar. As has been shown, pulse profiles can vary greatly from one observation to another and never has a pulsar displayed a characteristic pulse shape throughout the present survey.

The profiles are plotted with respect to the average amplitude, which is then set to zero.

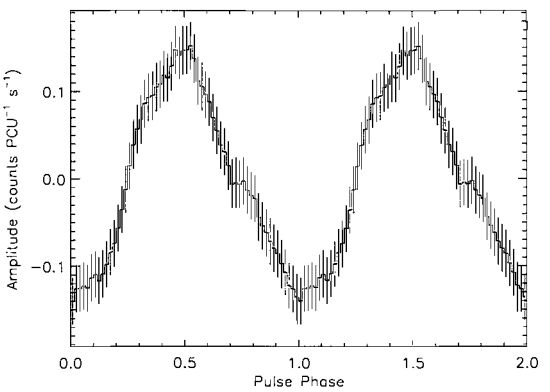

Figure 4.84: Pulse profile of candidate pulsar SXP0.61 on MJD 51856.4.

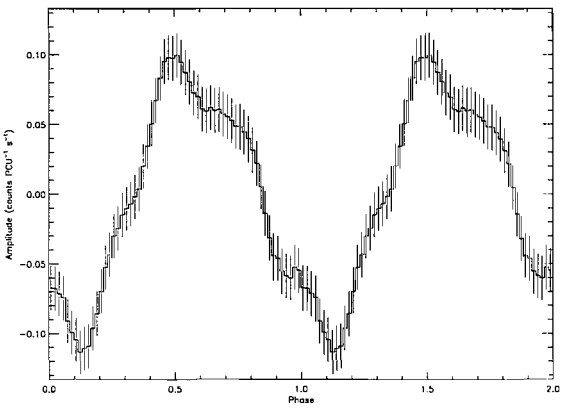

Figure 4.85: Pulse profile of candidate pulsar SXP0.68 on MJD 50784.2.

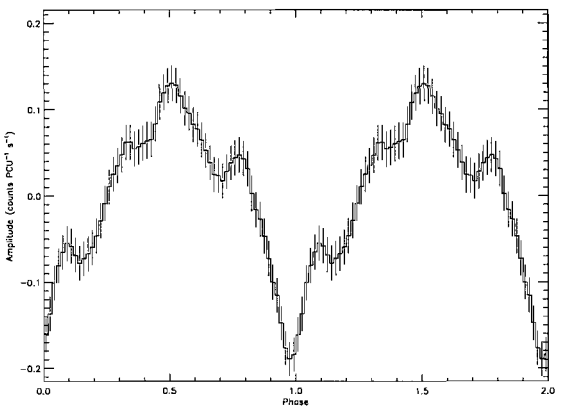

Figure 4.86: Pulse profile of candidate pulsar SXP0.77 on MJD 53390.6.

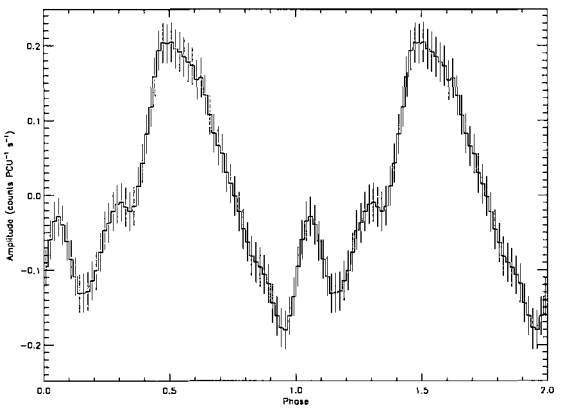

Figure 4.87: Pulse profile of candidate pulsar SXP2.02 on MJD 50779.4.

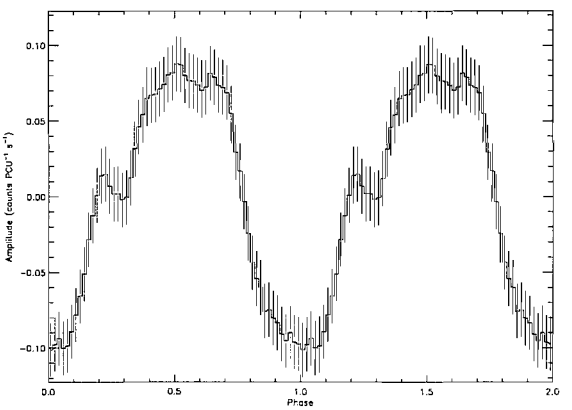

Figure 4.88: Pulse profile of candidate pulsar SXP5.06 on MJD 53488.0.

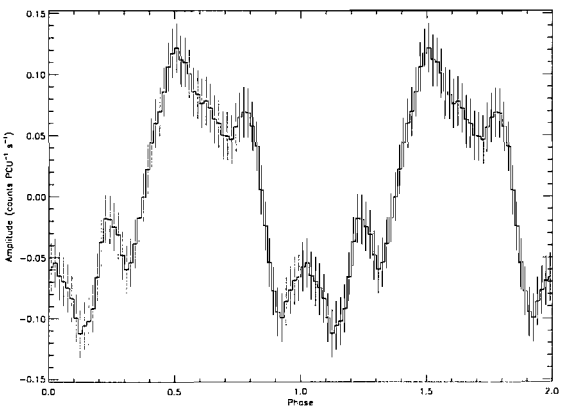

Figure 4.89: Pulse profile of candidate pulsar SXP8.28 on MJD 51891.3.

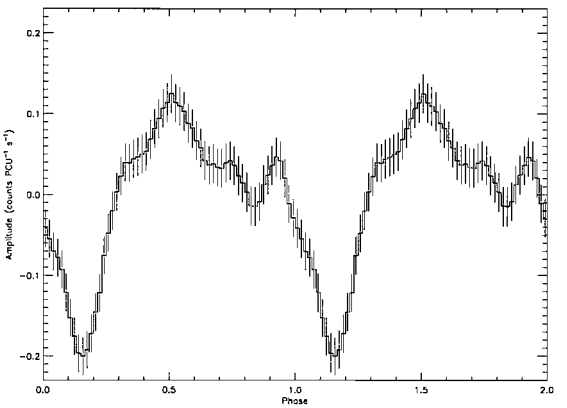

Figure 4.90: Pulse profile of candidate pulsar SXP10.7 on MJD 51283.3.

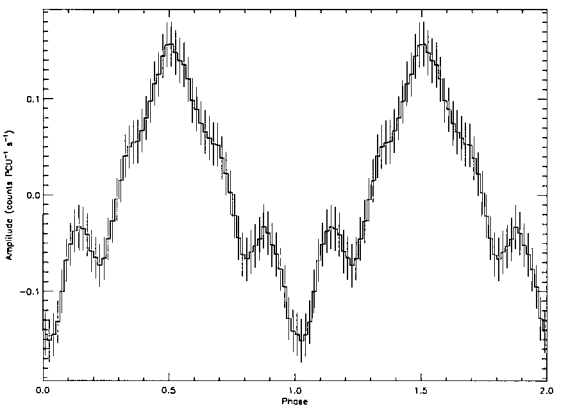

Figure 4.91: Pulse profile of candidate pulsar SXP19.4 on MJD 51800.0.

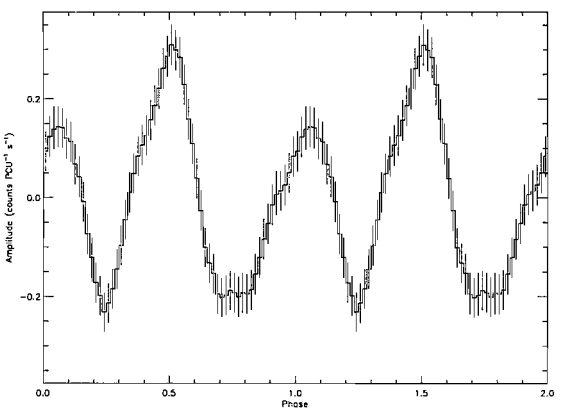

Figure 4.92: Pulse profile of candidate pulsar SXP19.7 on MJD 51248.1.

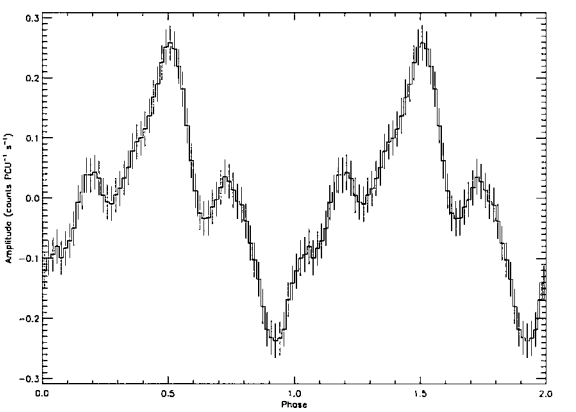

Figure 4.93: Pulse profile of candidate pulsar SXP27.7 on MJD 53738.1.

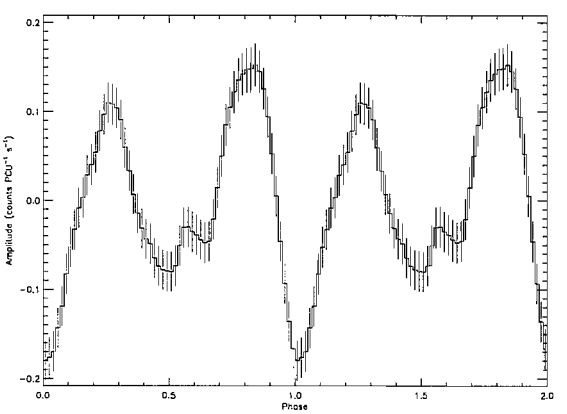

Figure 4.94: Pulse profile of candidate pulsar SXP55.9 on MJD 51647.0.

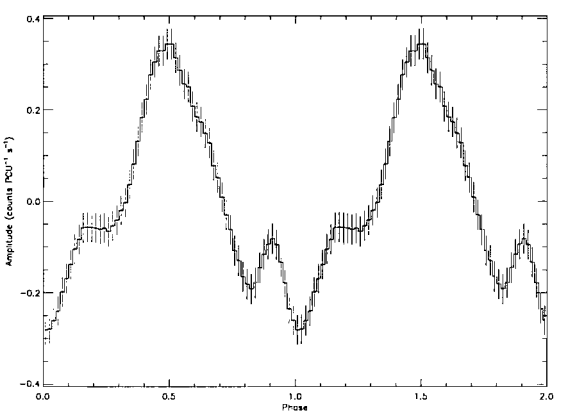

Figure 4.95: Pulse profile of candidate pulsar SXP57.6 on MJD 52548.6.

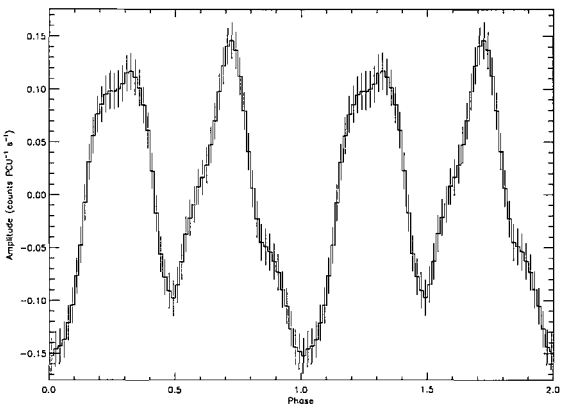

Figure 4.96: Pulse profile of candidate pulsar SXP61.0 on MJD 50787.4.

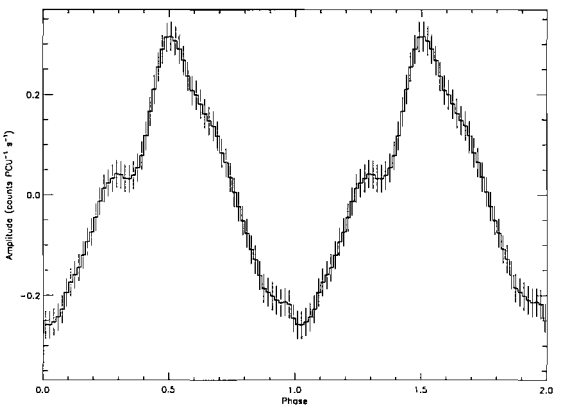

Figure 4.97: Pulse profile of candidate pulsar SXP93.1 on MJD 51529.8.

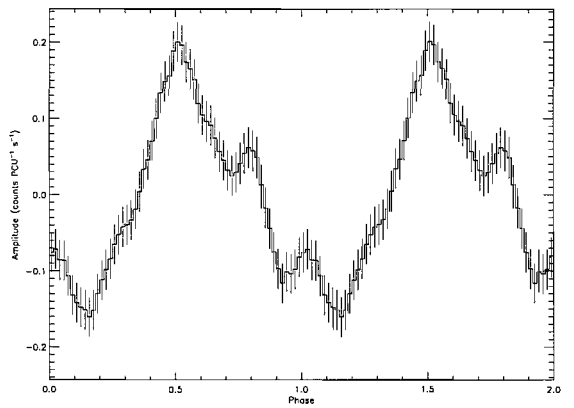

Figure 4.98: Pulse profile of candidate pulsar SXP126 on MJD 50779.4.

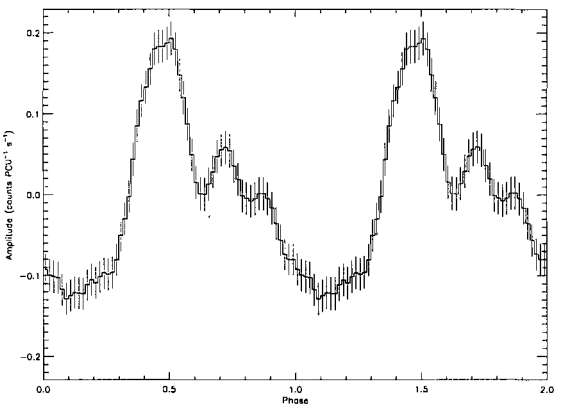

Figure 4.99: Pulse profile of candidate pulsar SXP287 on MJD 553390.6.

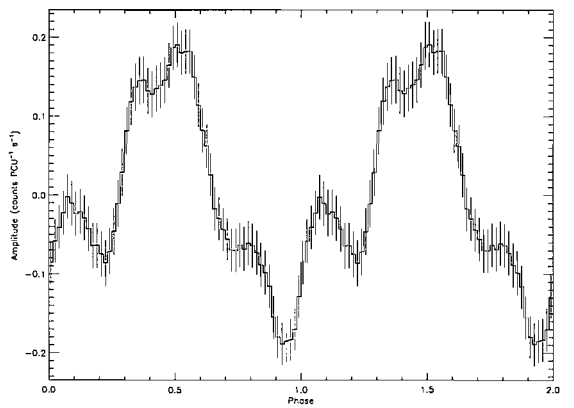

Figure 4.100: Pulse profile of candidate pulsar SXP401 on MJD 52346.1.

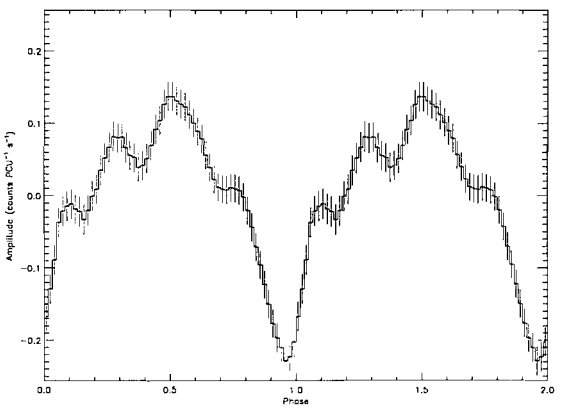

Figure 4.101: Pulse profile of candidate pulsar SXP708 on MJD 53682.5.

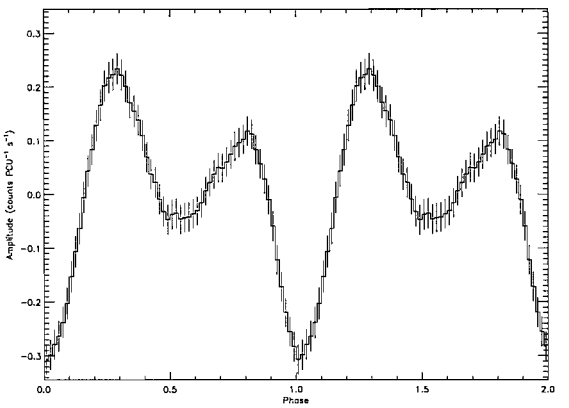

Figure 4.102: Pulse profile of candidate pulsar SXP779 on MJD 53257.8.

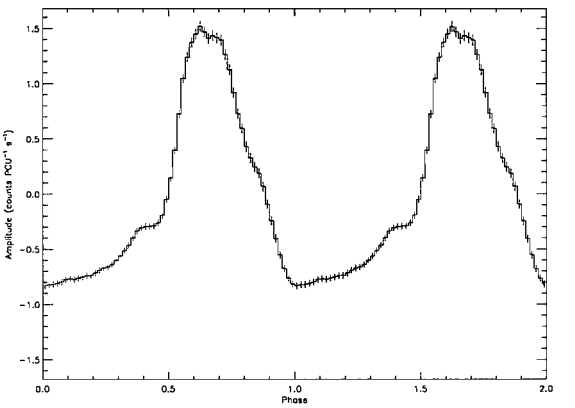

Figure 4.103: Pulse profile of candidate pulsar SXP2460 on MJD 51708.0.

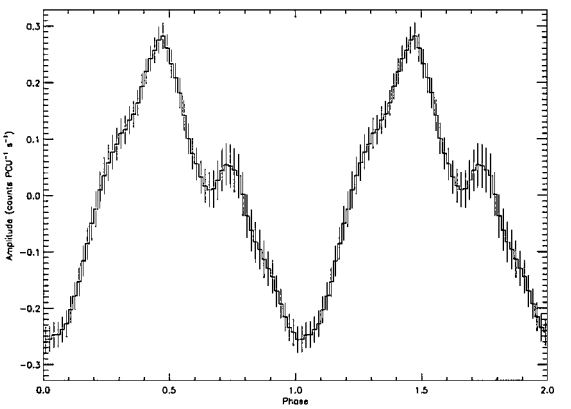

Figure 4.104: Pulse profile of candidate pulsar SXP2790 on MJD 52694.4.

Chapter 5

Conclusions and Future Work

Do you believe in tomorrow? I don't even believe in today.

—Pete Steele

We demand rigidly defined areas of doubt and uncertainty!

—Vroomfondel *(in The Hitchhiker's Guide to the Galaxy)*

5.1 Overview

In the present work we have used two extended data sets to study the long-term behaviour of Be/X-ray binary systems. Chapter 2 contains the results of monitoring a sample of 14 Galactic systems in the $20-50\,\mathrm{keV}$ band with *BATSE* over ~ 9 years. We calculated the orbital parameters of two of these systems using a piece-wise orbit fitting technique and attempted (but failed) to calculate the orbital period of two other systems using timing analysis on the pulsed flux light curves. The spin up/down rate of 12 systems was measured, from which an estimate of the luminosity was obtained, and from these values an approximate upper limit was placed on the

magnetic field of their pulsars.

Chapter 3 contains the light curve analysis and cleaning techniques (coded into the PUMA and ORCA programs) by which pulsars were "subtracted" from the data and their harmonic content recorded. The benefits of this method are twofold, it allows bright pulsars and their harmonics to be taken out of the power spectra, thus reducing contamination due to harmonics and aliases; it also gives us a P^2S^2, a pulsar-specific power spectrum, which tells us how much power is associated with the fundamental and all of the harmonics. The P^2S^2 should allow a theoretical pulse profile to be constructed for each pulsar in an observation, but we have postponed the implementation of this option until an upgraded version of PUMA is produced.

The practical application of these analysis techniques is reported in Chapter 4, which presents the results of monitoring a sample of 46 SMC systems in the $3-10\,\mathrm{keV}$ band with *RXTE* for varying amounts of time, depending on their locations, over the course of ~ 8 years. A history of the amplitude of the pulsed flux was constructed for each pulsar and a value for the orbital periods of all but 4 of these systems was obtained via Lomb-Scargle analysis. In total, we were able to confirm, refine and/or refute the orbital periods of 17 systems with previously known orbital periods, while proposing 25 periods for the remaining systems with no previously published orbital period. The spin up/down rates, luminosities and magnetic fields of 9 pulsars were estimated. We used this large sample of orbital periods to confirm the validity of the spin/orbit relation, obtaining new values for its parameters that differ slightly from the original values given by Corbet (2006, private communication). Two systems were also "taken off the map": SXP46.4 was found to be detections of SXP46.6 which had spun up, largely undetected over a 2 year period; due to similar circumstances, SXP165 was determined to be SXP169.

We have provided a representative sample of pulse profiles for all pulsars and offer some qualitative views on the nature and geometry of the emission regions. A number of pulsars have sequences of profiles covering a long outburst and the evolution of the profiles is discussed. We find that certain shapes appear at different times during the survey of each pulsar and that profiles depend strongly on luminosity. Most systems are found to exhibit both pencil and fan beams at the same time; some evolve to only pencil beams at higher luminosities, while others to only fan

beams.

Using the predicted values for the orbital period of each system, we defined the quantity $\delta_{\rm orb}$ as the difference between the predicted and actual orbital periods expressed as a percentage, and found that the magnetic fields of the pulsars were inversely proportional to $\delta_{\rm orb}$. We explain this result as the spin period being either too short or too long to predict the correct observed orbital period, and the reason the spin period has not been "guided" towards the appropriate value is because weaker magnetic fields are less efficient at spinning pulsars up or down.

We defined the X-ray outburst density, $X_{\rm od}$, as the number of outbursts per orbit, and find that it is correlated with the orbital period, suggesting that, in general, longer orbit systems are more efficient at outbursting, and thus exhibit outbursts more often *per orbit*. We also found that the estimated luminosity of outbursts was higher for systems with lower values of $X_{\rm od}$.

Based on the distribution of values of the outburst density we propose a classification for Be/X-ray systems (which could maybe be extended to other types of systems) into Class Ia, Ib and II, which undergo very frequent, semi-frequent and very infrequent outbursts, respectively.

Using the analysis code developed for the present work we searched for new faint, pulsars in the data and present a list of 21 candidate pulsars, complete with their amplitude lightcurves and a sample pulse profile. The calculated orbital periods for all but one of these systems are also provided.

5.2 Comparing results across galaxies and groups

It would be interesting to know if the results obtained for the SMC systems would be similar in the Milky Way population. Fig. 5.1 shows the Corbet diagram for the systems studied, with the red dashed line showing the fit to the data, and the blue dotted line being the fit using all 23 known orbital periods (provided by Corbet (2006, private communication)). In order to calculate $\delta_{\rm orb}$ we used the expected

$P_{\rm orb}$ given by this last fit, given the brevity of our sample and poor quality of the fit (with a value of $r = 0.22241$).

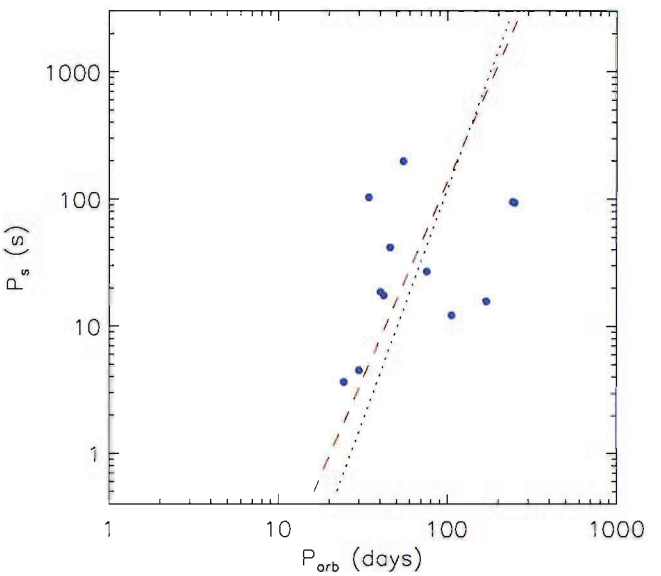

Figure 5.1: $P_{\rm s}$ vs $P_{\rm orb}$ for the Milky Way systems. The red dashed line represents the fit to $P_{\rm orb}$ vs $P_{\rm s}$ for the plotted data (and has $r = 0.222$), while the blue dotted line is the fit given by Corbet (2006, private communication).

Fig. 5.2 shows the relationship between B and $\delta_{\rm orb}$ for the Milky Way pulsars. It is clear that we do not see the same relationship as in the SMC (Fig. 4.59).

Fig. 5.3 shows $L_{\rm x}$ vs $X_{\rm od}$ for the Milky Way pulsars. There is a weaker fit to the data than for the SMC ($r = -0.81433$ vs -0.96092), and the lines differ substantially.

We now compare the values of $X_{\rm od}$ vs $P_{\rm orb}$ in Fig. 5.4. The lines deviate from each other, but it should be noted that the slope of the Milky Way fit is driven largely by the 3 pulsars with very low values of $X_{\rm od}$. Nevertheless, there does appear to be a certain degree of dependence between the two variables.

For the candidate pulsars there are no estimates available of the luminosity or magnetic field. However, we can plot them on a corbet diagram to see if they show a similar spin/orbit relation to the confirmed SMC pulsars. Fig. 5.5 shows that although the linear correlation coefficient is poor ($r = 0.42766$), the fit itself is very close to that of the confirmed SMC systems. Furthermore, a K-S test comparing

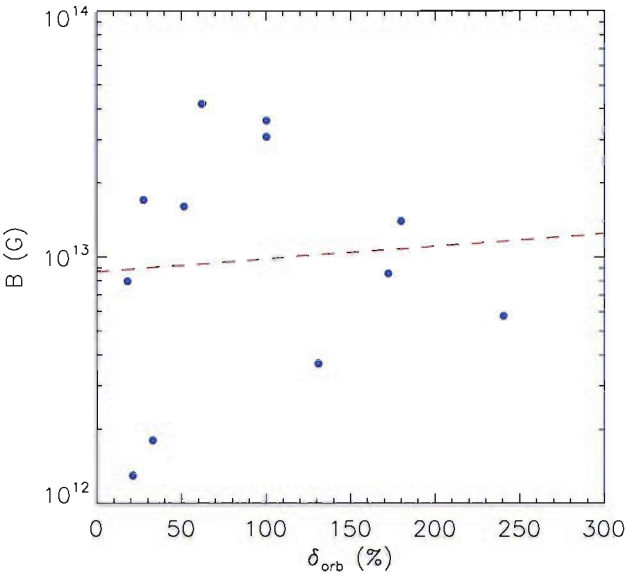

Figure 5.2: B vs $\delta_{\rm orb}$ for the 12 Milky Way systems for which a magnetic field has been estimated. The straight-line fit has $r = 0.095$.

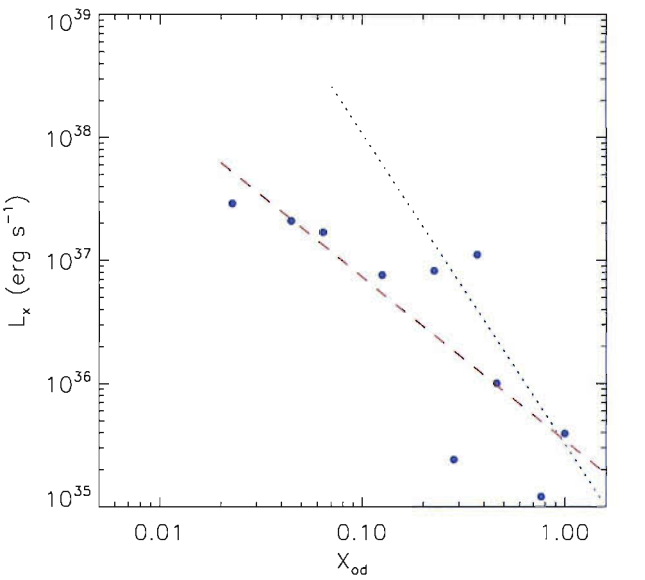

Figure 5.3: $L_{\rm x}$ vs $X_{\rm od}$ for the 12 Milky Way systems for which the luminosity and the orbital period have been estimated. The straight-line fit has $r = -0.814$ and is shown by the red dashed line; the blue dashed line shows the fit to the SMC data.

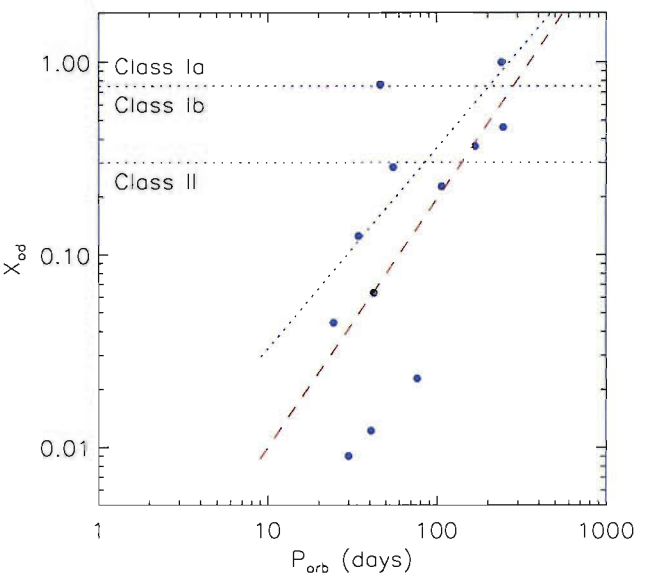

Figure 5.4: X_{od} vs P_{orb} for Milky Way systems. The straight-line fit has $r = 0.650$. The two horizontal dotted lines separate the regions of each of the three classes of systems. The red dashed line is the fit to the data while the blue dotted line is the fit to the SMC data.

the pulse period distribution of the candidate and SMC populations shows that the probablity of them belonging to the same distribution is 61%.

Fig. 5.6 shows the relation between X_{od} and P_{orb} for the candidate SMC systems. The fit is strong ($r = 0.92047$) and in close agreement with the SMC fit. As might have been expected, there are no Class Ia systems.

Lastly, we show the histograms of X_{od} for both the Milky Way and the candidate SMC pulsars. It is difficult to make comparisons with such little numbers as we have for the Milky Way systems, however there would seem to also be 3 groups in the histogram (Fig. 5.7), albeit with different limits to that of the SMC. It could be that due to differences in the behaviour of the Be stars in each galaxy (brought about by the different metalicities), the classes would have different limits. As it stands now, there appear to be a larger proportion of infrequent outbursters (Class II) in the Milky Way than in the SMC. The candidate SMC systems, on the other hand, do appear to divide themselves into two groups (if we ignore the fact that there are no systems with X_{od} in the range $0.4-0.5$) following the limits established in the

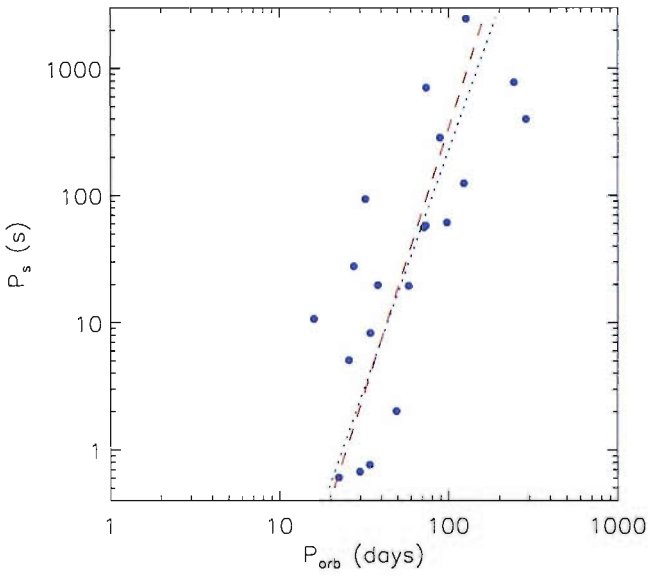

Figure 5.5: P_s vs P_{orb} for the candidate SMC systems. The red dashed line represents the fit to P_{orb} vs P_s for the plotted data (and has $r = 0.428$), while the blue dotted line is the fit to the confirmed pulsars.

previous chapter; the division into classes appears clearer in Fig. 5.6. As was noted earlier, there are no Class Ia systems; given the variations in brightness normally associated with regular outbursters, and the loss of sensitivity when the pulsar is further away from the centre of the field of view, we would expect a faint source, with regular outbursts, to dip in and out of the detection window and not be visible at every outburst.

5.3 Future opportunities

Given the wealth of pulse profiles obtained during this survey, much could be learnt about the geometric position of the neutron star with respect to us by fitting the profiles using a computer model. With a large set of profiles available for each pulsar, the possible degeneracy of solutions would likely not be an issue. Unfortunately, this was beyond the scope of the present work but is something we hope to carry out in the near future.

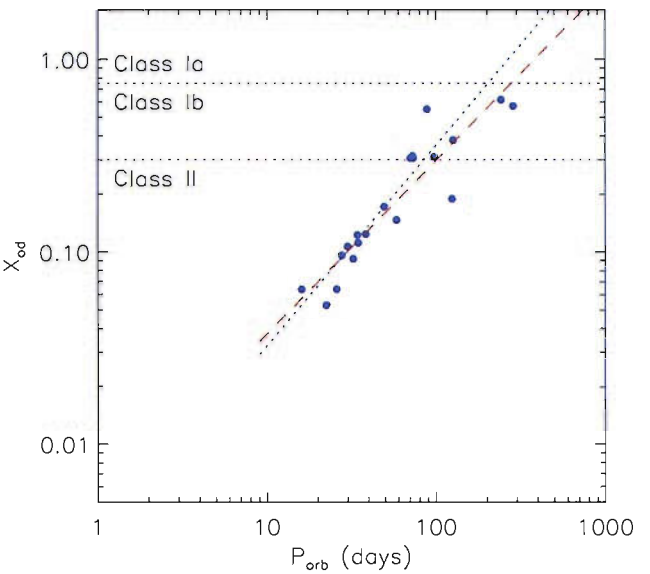

Figure 5.6: X_{od} vs P_{orb} for candidate SMC systems. The straight-line fit has $r = 0.920$. The two horizontal dotted lines separate the regions of each of the three classes of systems. The red dashed line is the fit to the data while the blue dotted line is the fit to the SMC data.

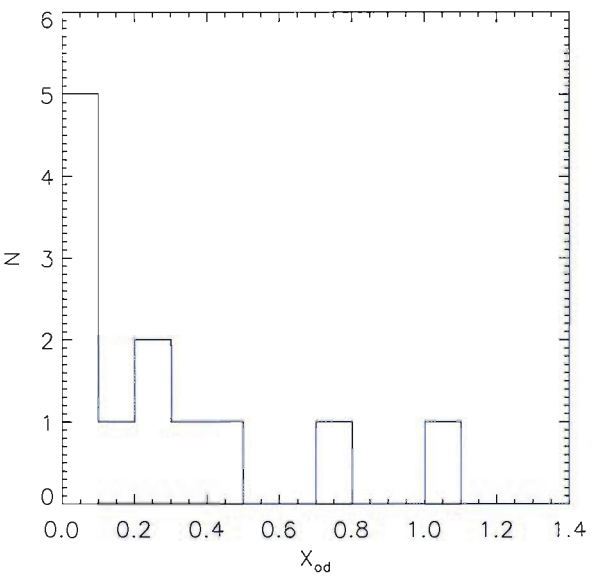

Figure 5.7: Histogram of X_{od} values for Milky Way systems.

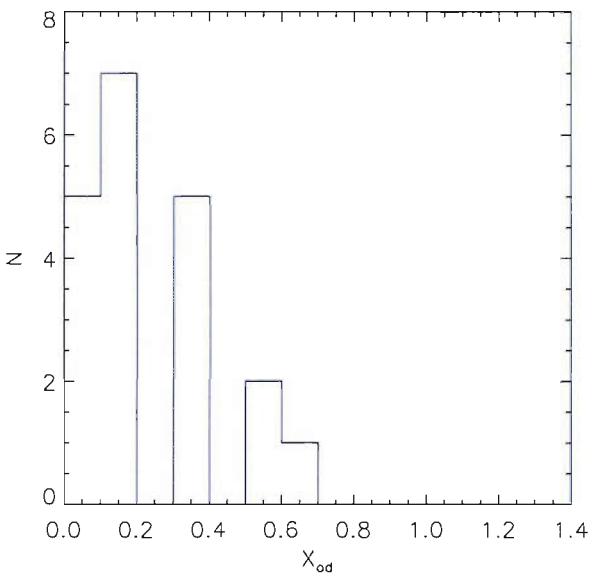

Figure 5.8: Histogram of $X_{\rm od}$ values for candidate SMC systems.

By using phase matching techniques to calculate time delays in pulse arrivals, we believe it would be possible to determine the orbital parameters of a number of SMC systems using the techniques outlined in § 2.1.4 (e.g., SXP46.6, SXP59.0, etc.). It is an important next step in the study of SMC systems that we find values for the eccentricities and compare them with the Galactic values that are known so far. We also believe the eccentricity plays an important role in determining where on the outburst-per-orbit diagram each system will fall.

A larger sample of SMC pulsar magnetic field and luminosity estimates are required to further explore their relationship with $\delta_{\rm orb}$ and $X_{\rm od}$, respectively. If there is a real connection between these quantities, and it is not present in Galactic systems, this would provide an important clue as to how these galaxies differ.

Lastly, we plan to further explore the relationship between $X_{\rm od}$ and $P_{\rm orb}$ for other types of X-ray binaries, such as low-mass systems and other non-persistent high-mass systems. Firstly, we would like to use all the available orbital periods for Galactic systems (23 at time of writing) to obtain better statistics for the Milky Way. Another interesting possibility is calculating an optical outburst density ($O_{\rm od}$) for both Galactic and SMC systems. Given the relatively long baseline of the MACHO

and OGLE data archives, this could be accomplished for the SMC with relative ease. The only problem we forsee with many systems is the lack of clear outbursts in the optical, so maybe a different, but related, definition for the $O_{\rm od}$ should be found.

Appendices

Appendix A

Pulse Profiles of SMC Pulsars

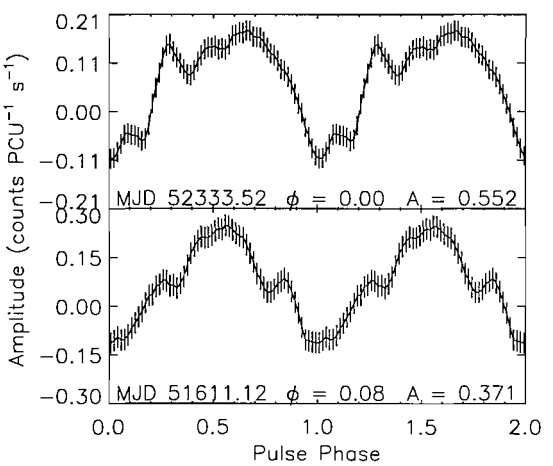

Figure A.1: Pulse profiles of SXP0.92.

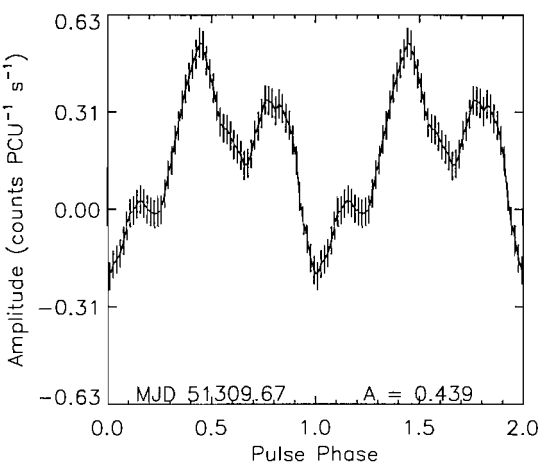

Figure A.2: Pulse profile of SXP2.16.

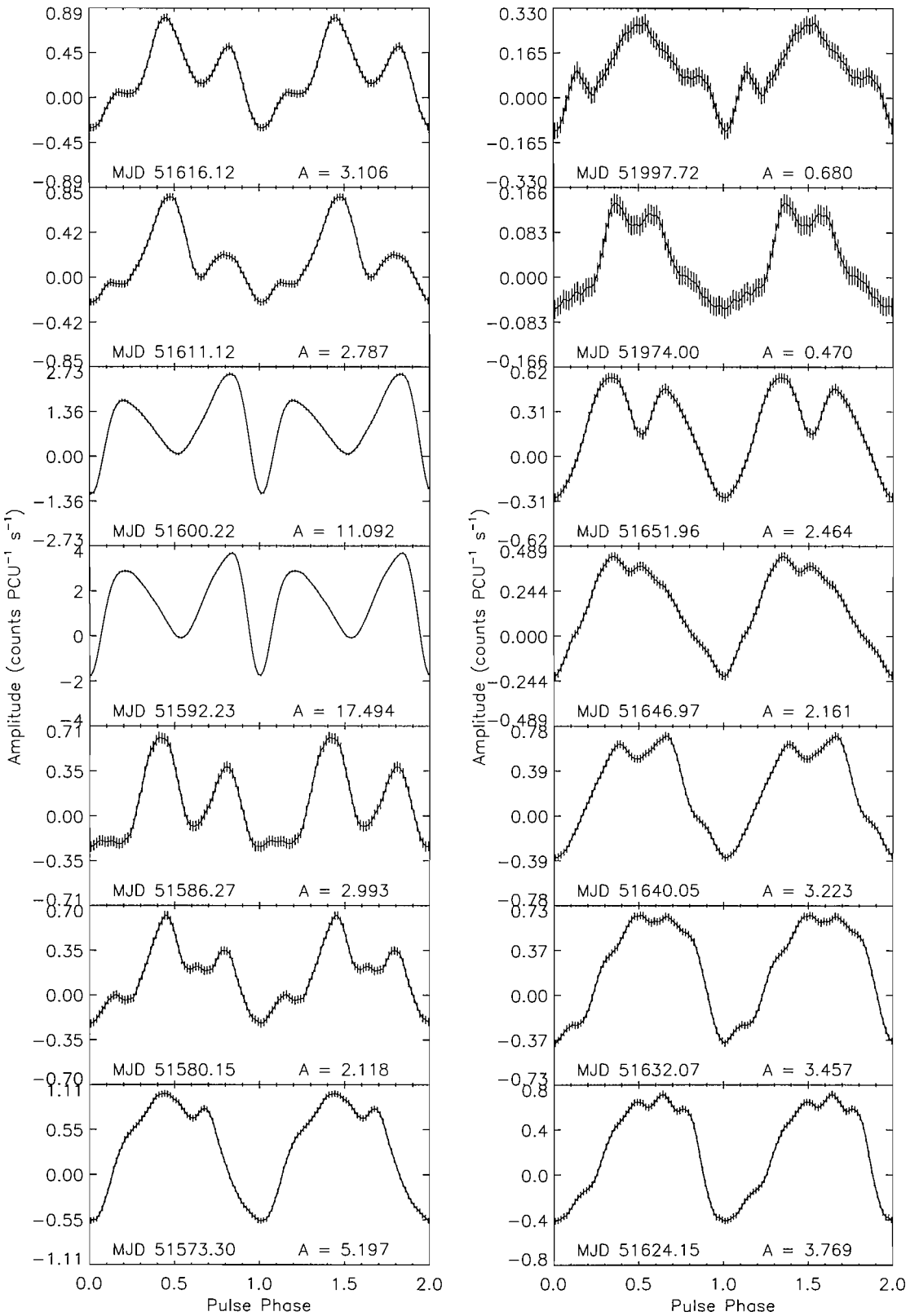

Figure A.3: Pulse profiles of SMC X-2 during the MJD 51600 outburst.

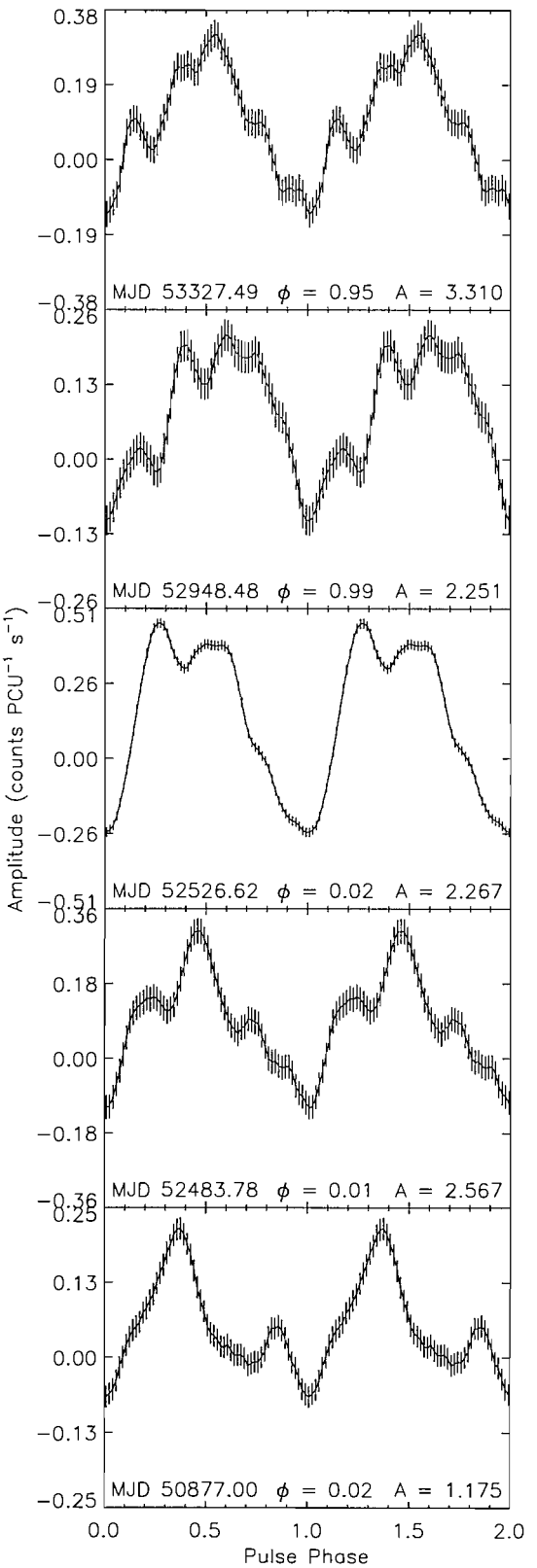

Figure A.4: Pulse profiles of SXP2.76.

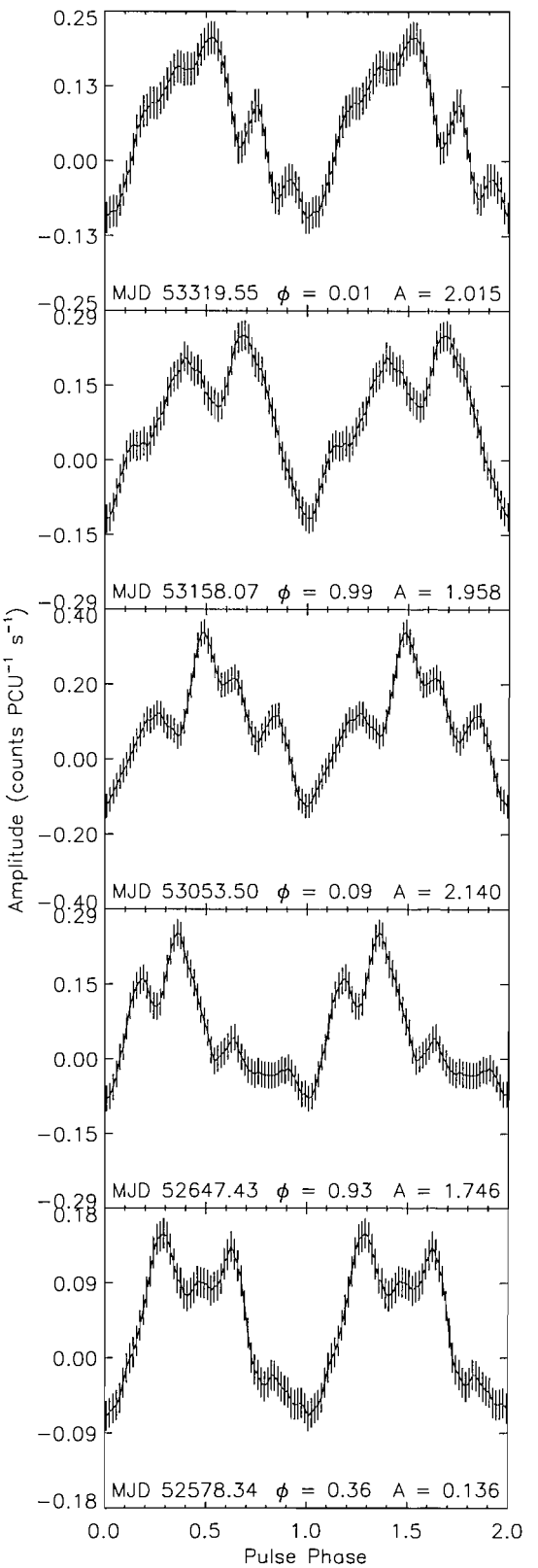

Figure A.5: Pulse profiles of SXP3.34.

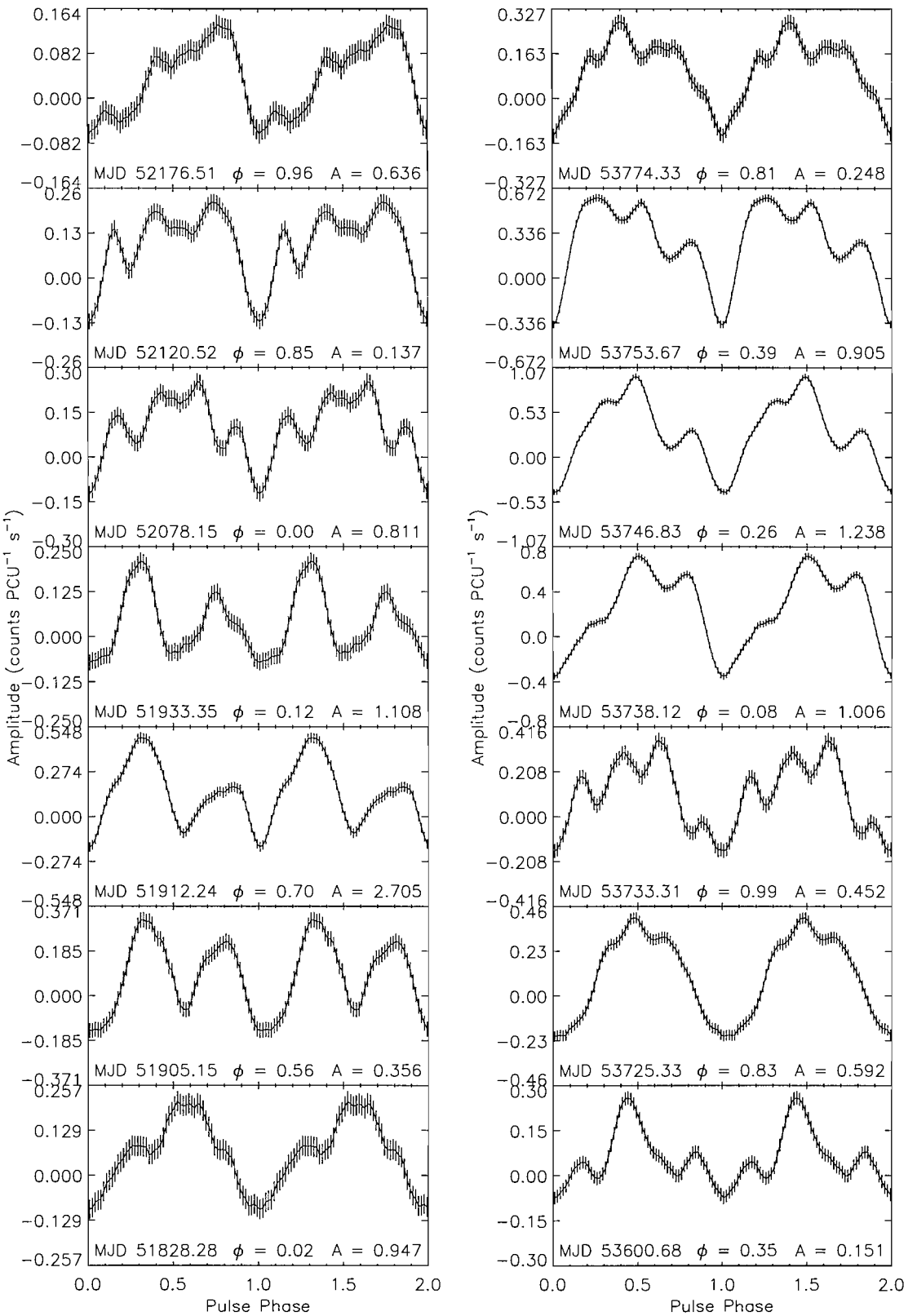

Figure A.6: Pulse profiles of SXP4.78. *Left*: during the MJD 51925, and surrounding outbursts. *Right*: during the MJD 53750 outburst.

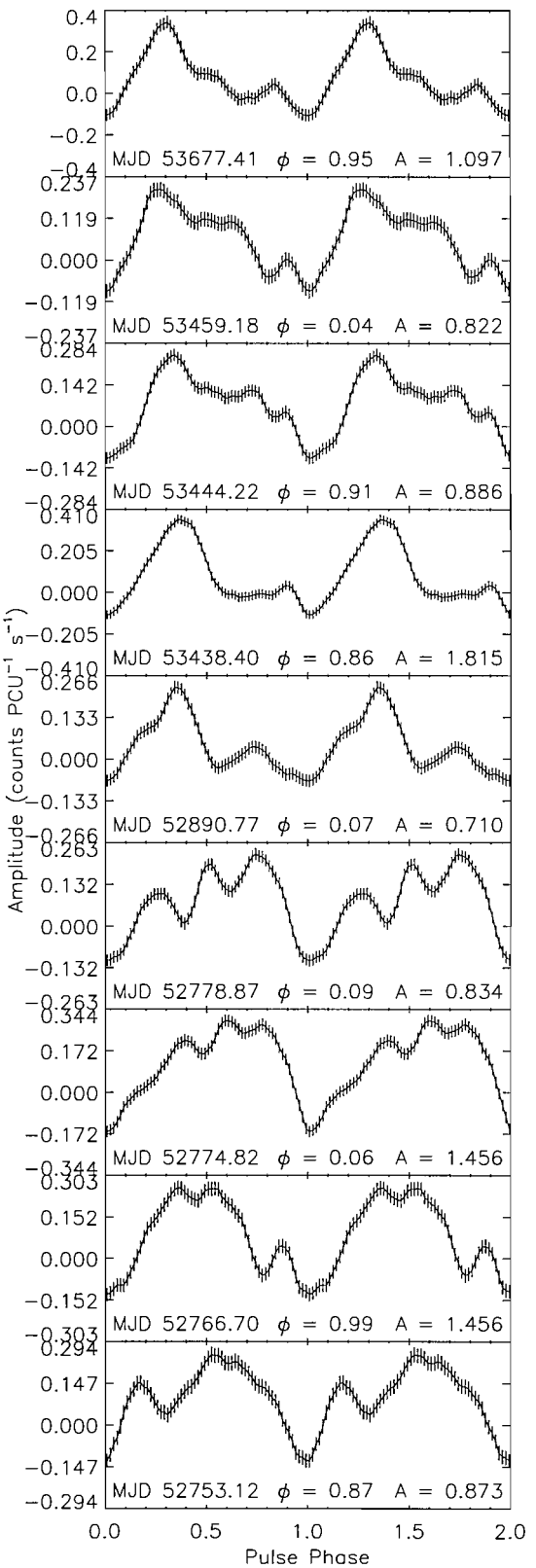

Figure A.7: Pulse profiles of SXP6.85.

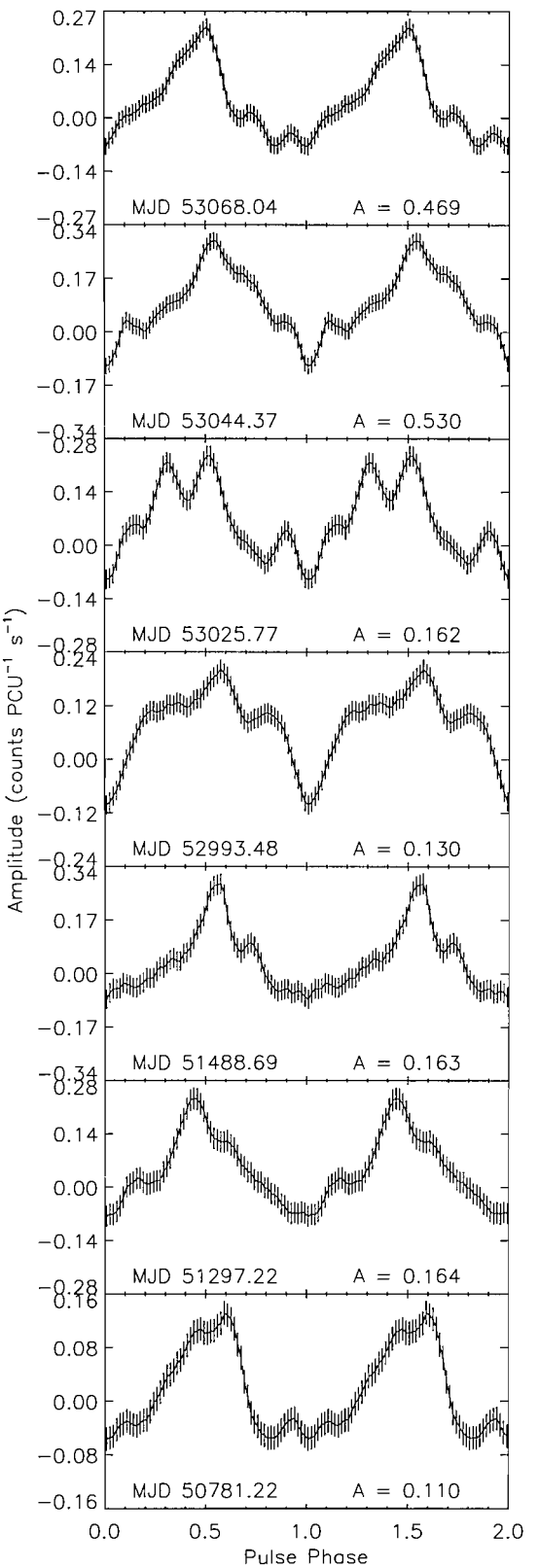

Figure A.8: Pulse profiles of SXP8.02.

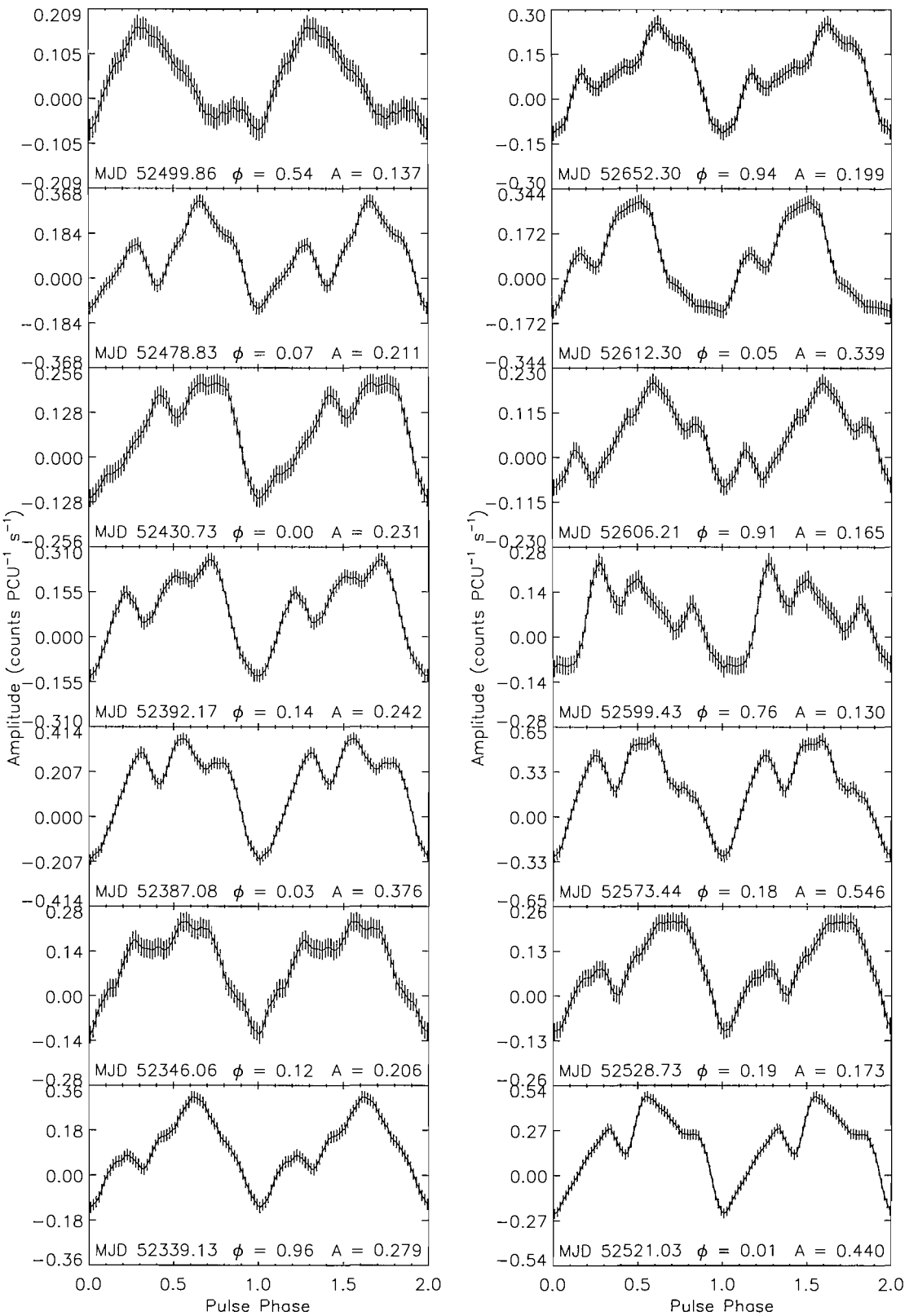

Figure A.9: Pulse profiles of SMC X-3 during the period of outbursts MJD 52330 – 52660.

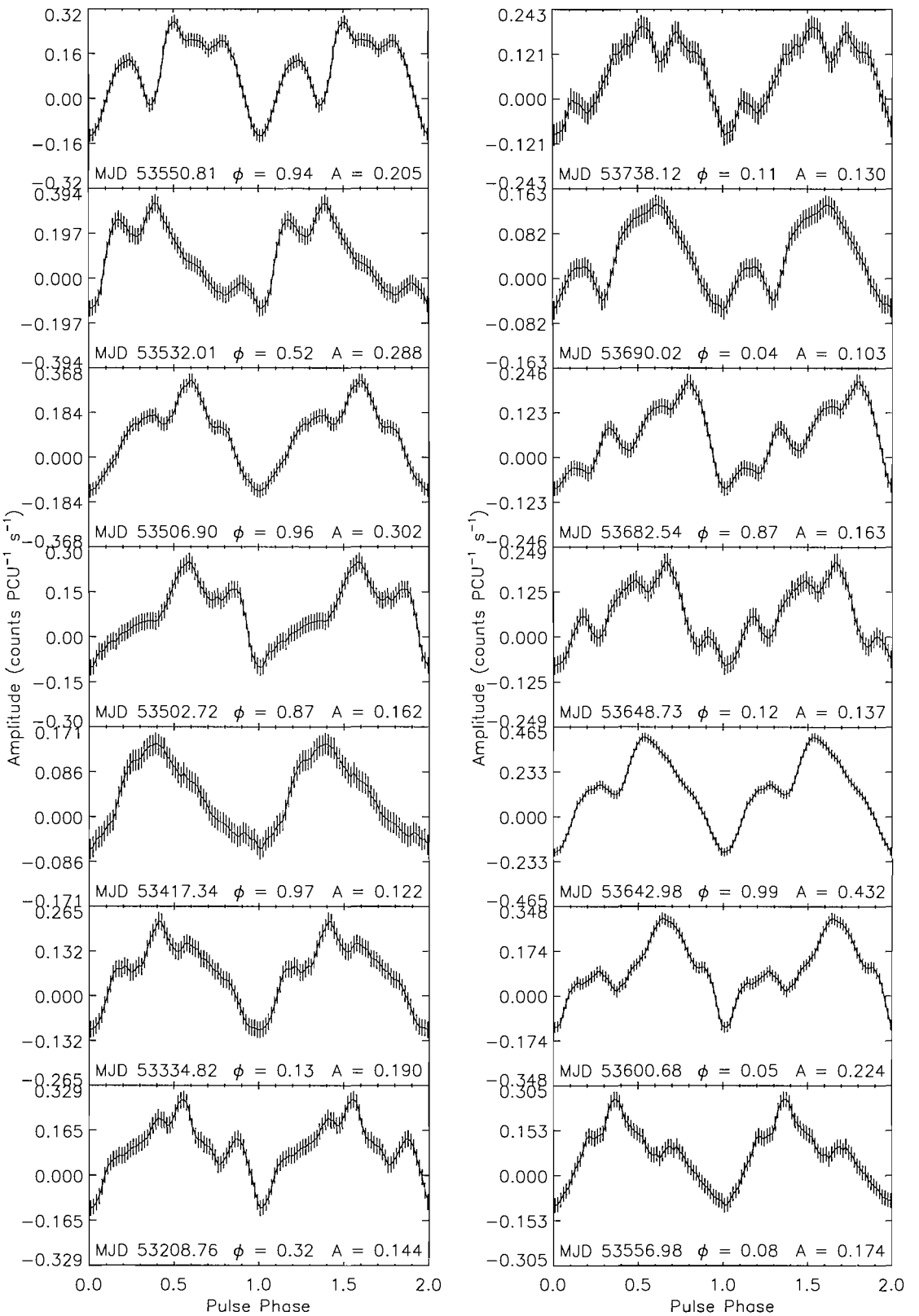

Figure A.10: Pulse profiles of SMC X-3 during the period of outbursts MJD 53200 – 53740.

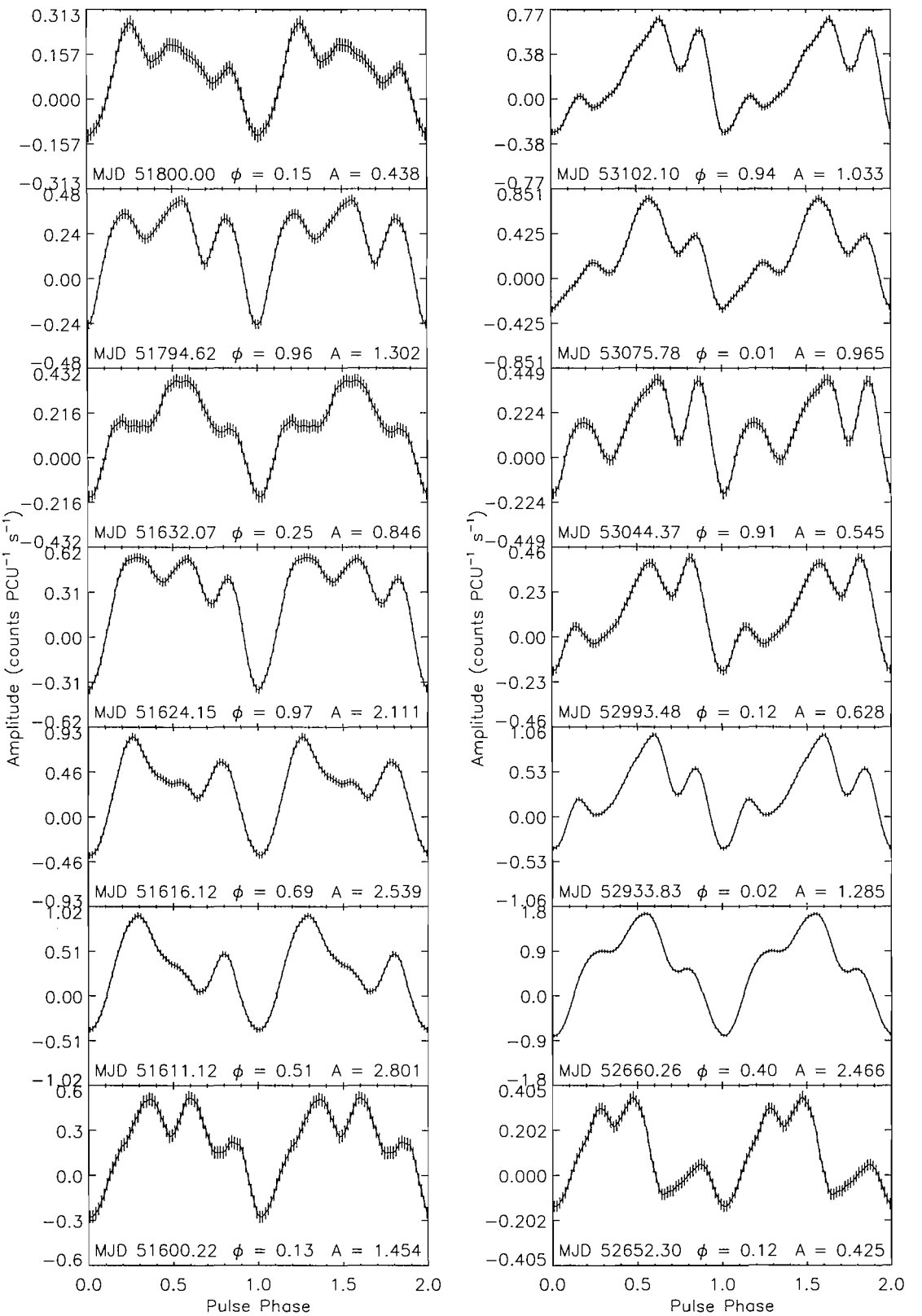

Figure A.11: Pulse profiles of SXP8.80. *Left*: during the MJD 51600 outburst. *Right*: at various other times during outburst.

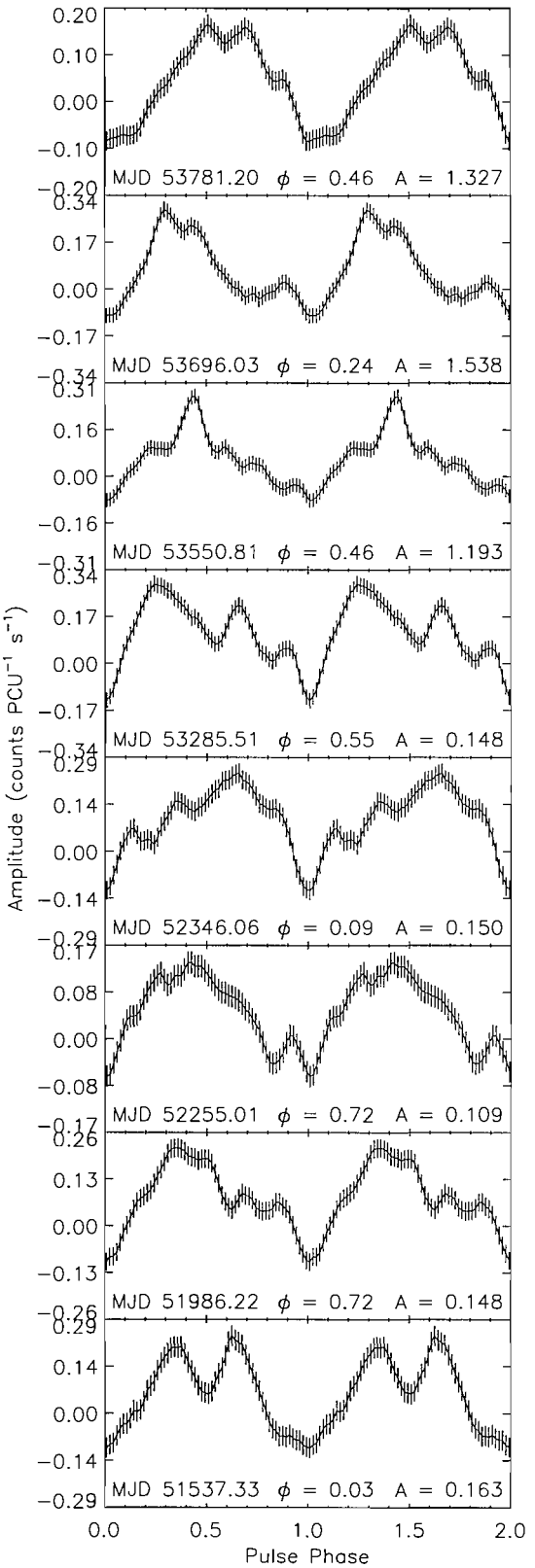

Figure A.12: Pulse profiles of SXP9.13.

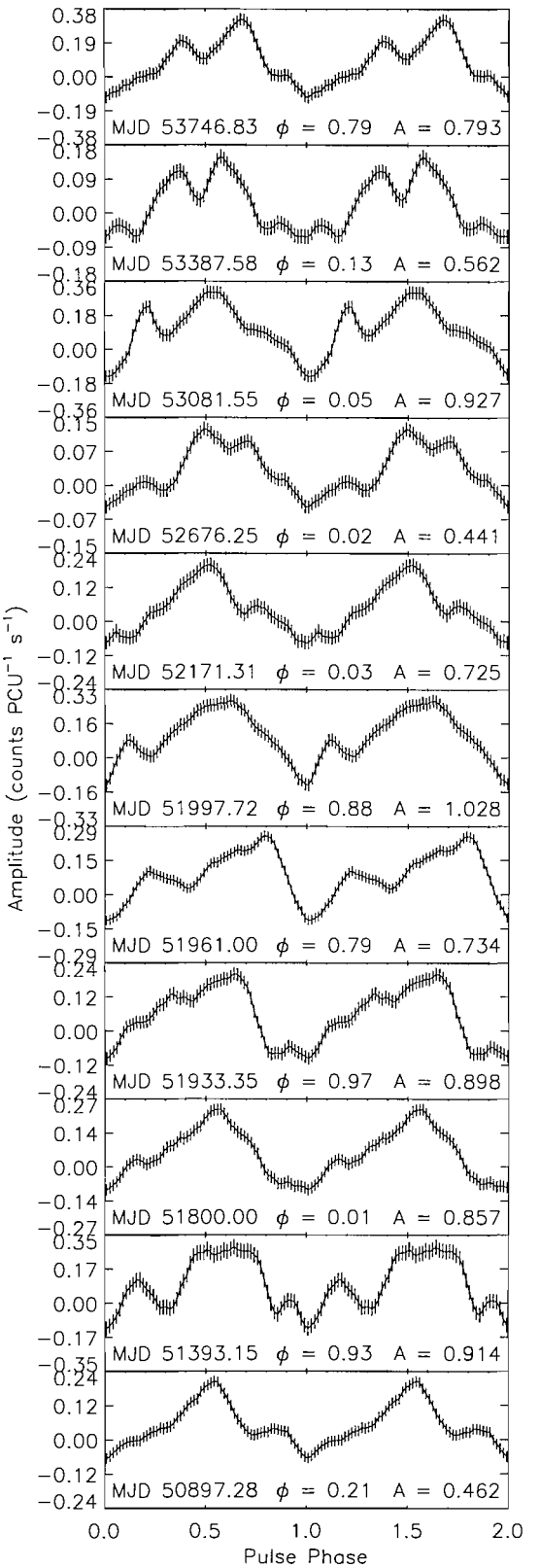

Figure A.13: Pulse profiles of SXP16.6.

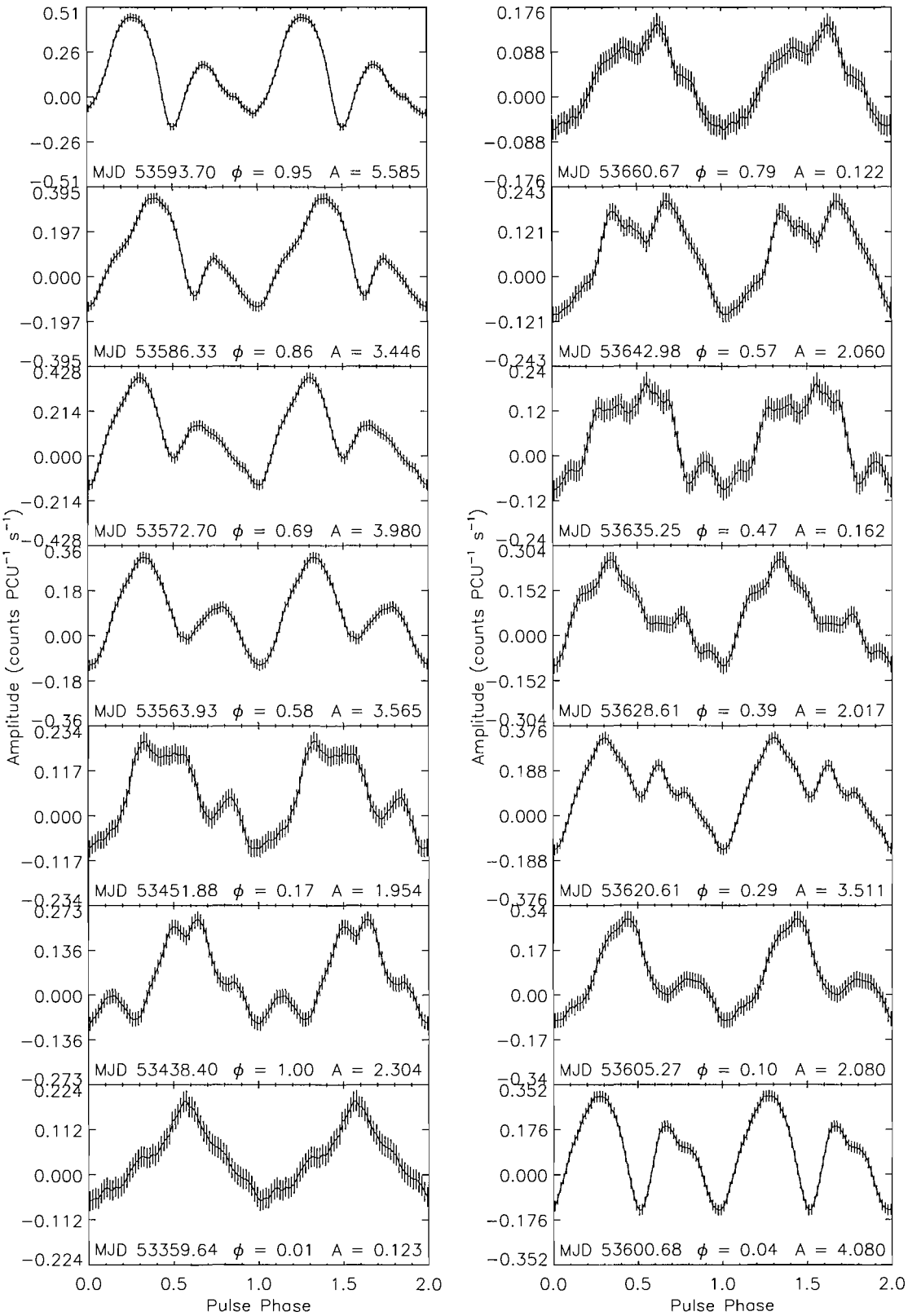

Figure A.14: Pulse profiles of SXP15.3 during the MJD 53600 outburst.

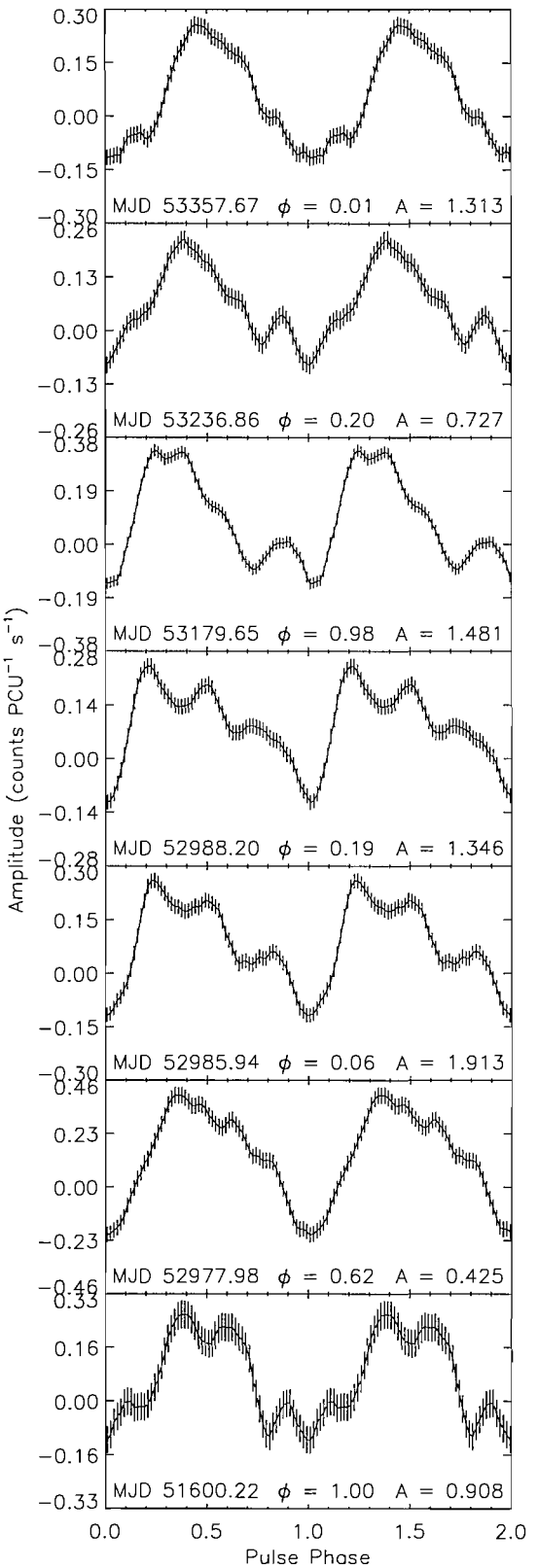

Figure A.15: Pulse profiles of SXP18.3.

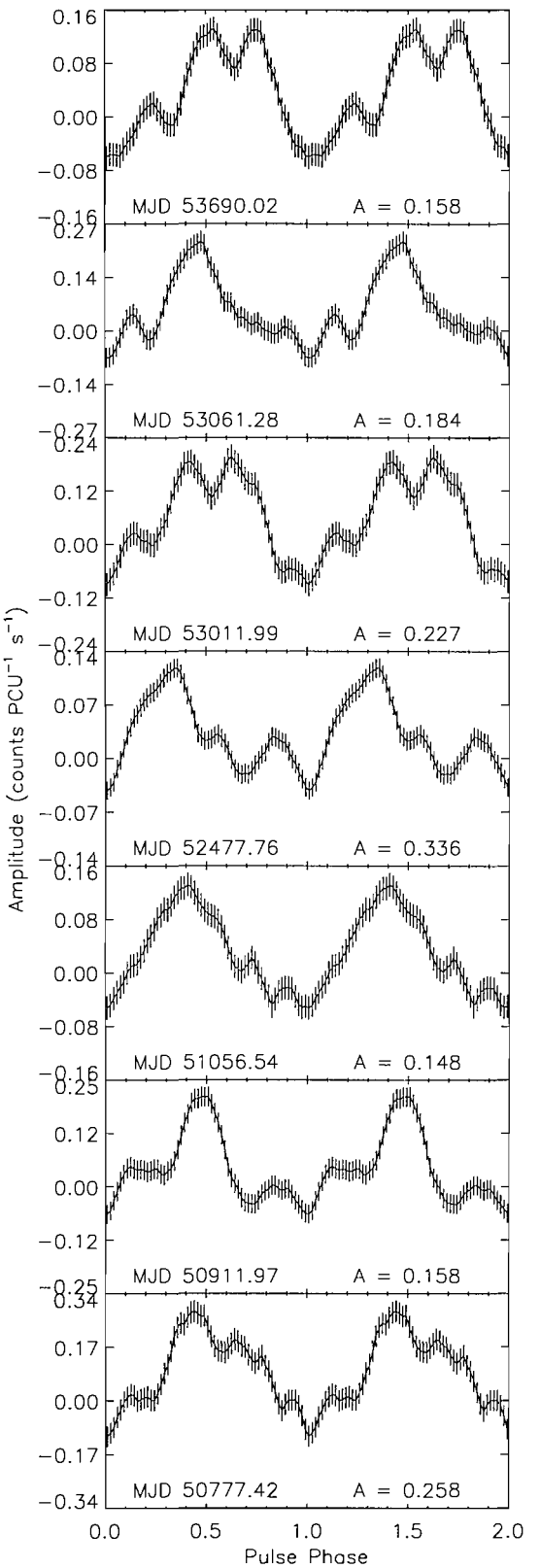

Figure A.16: Pulse profiles of SXP34.1.

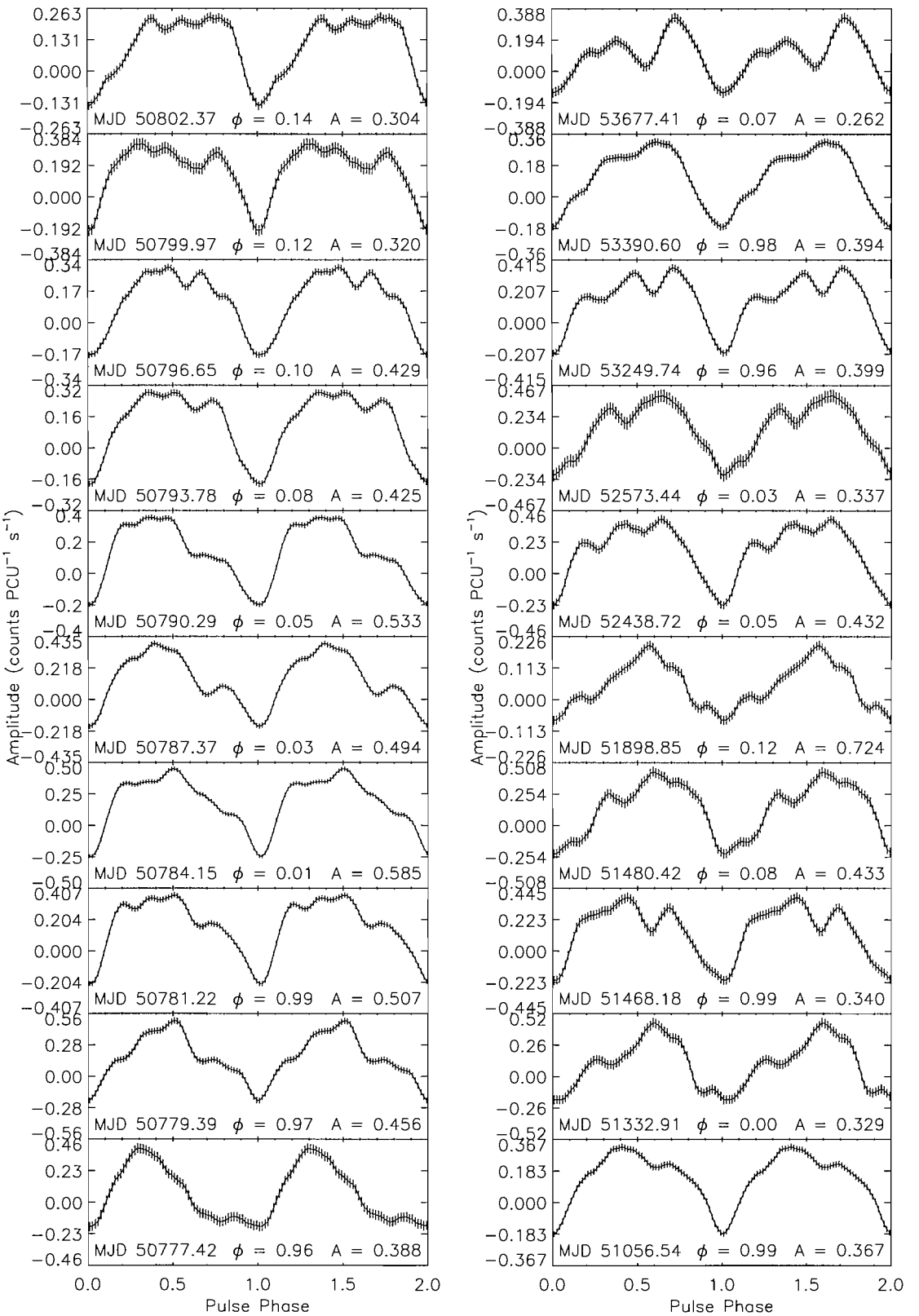

Figure A.17: Pulse profiles of SXP46.6. *Left*: during the MJD 50790 outburst. *Right*: at various other times during outburst.

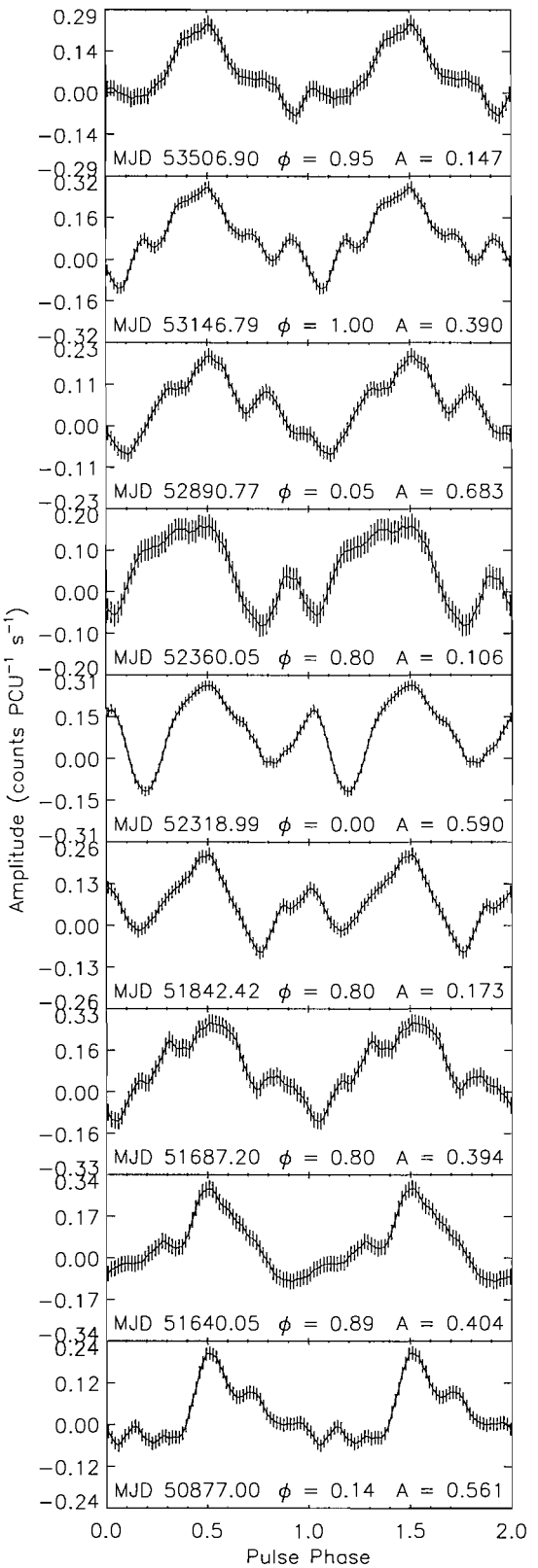

Figure A.18: Pulse profiles of SXP51.0.

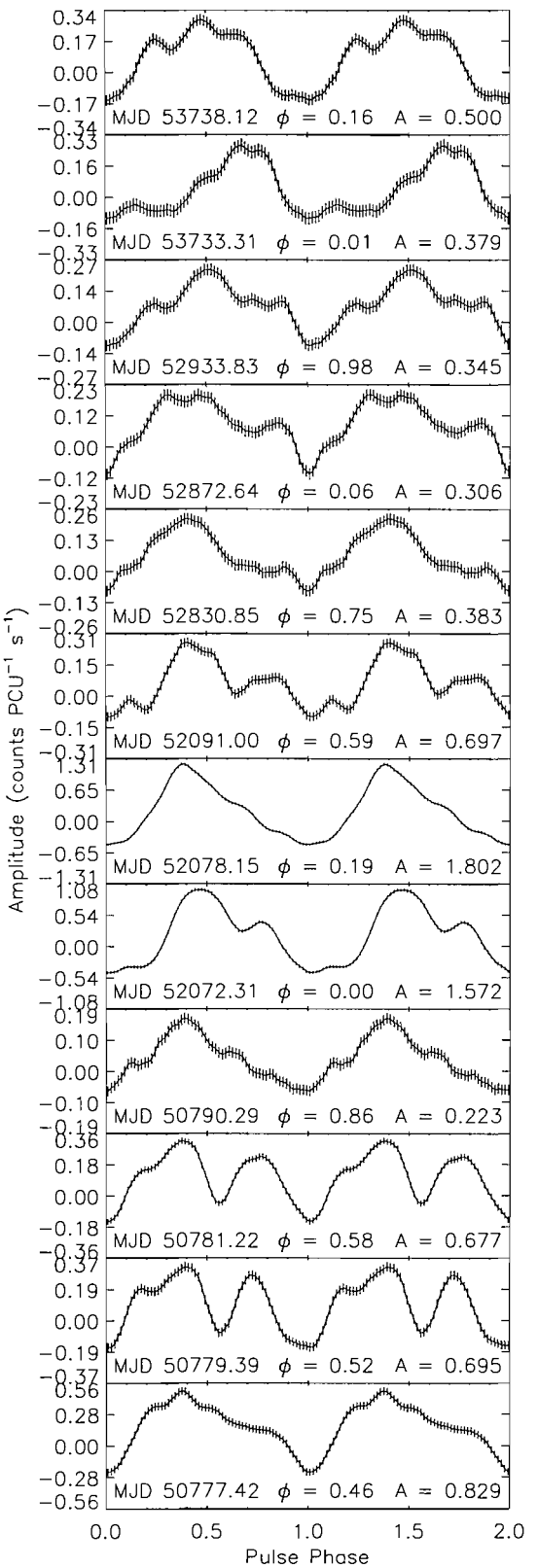

Figure A.19: Pulse profiles of SXP74.7.

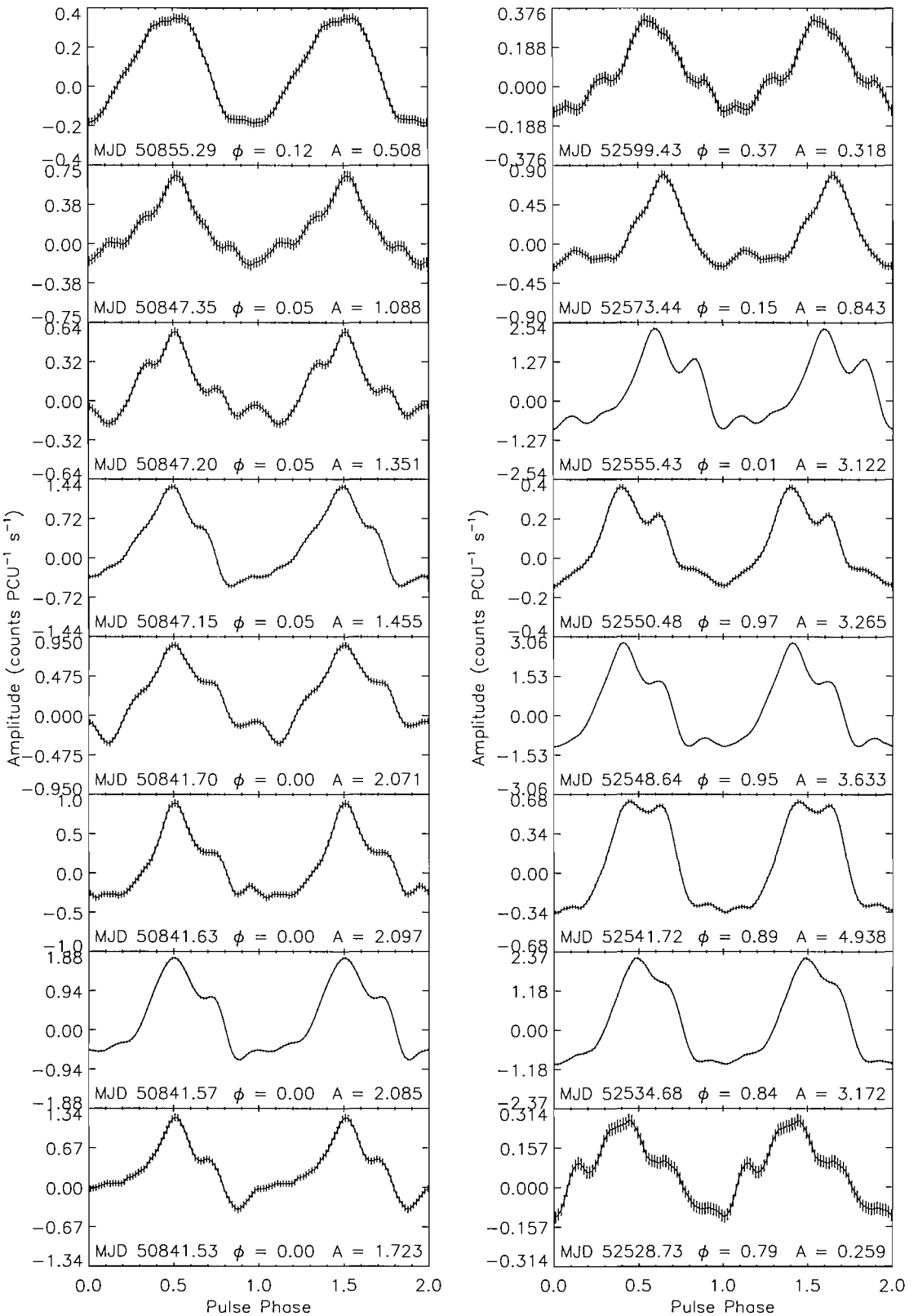

Figure A.20: Pulse profiles of SXP59.0. *Left*: during the MJD 50845 outburst. *Right*: during the MJD 52565 outburst.

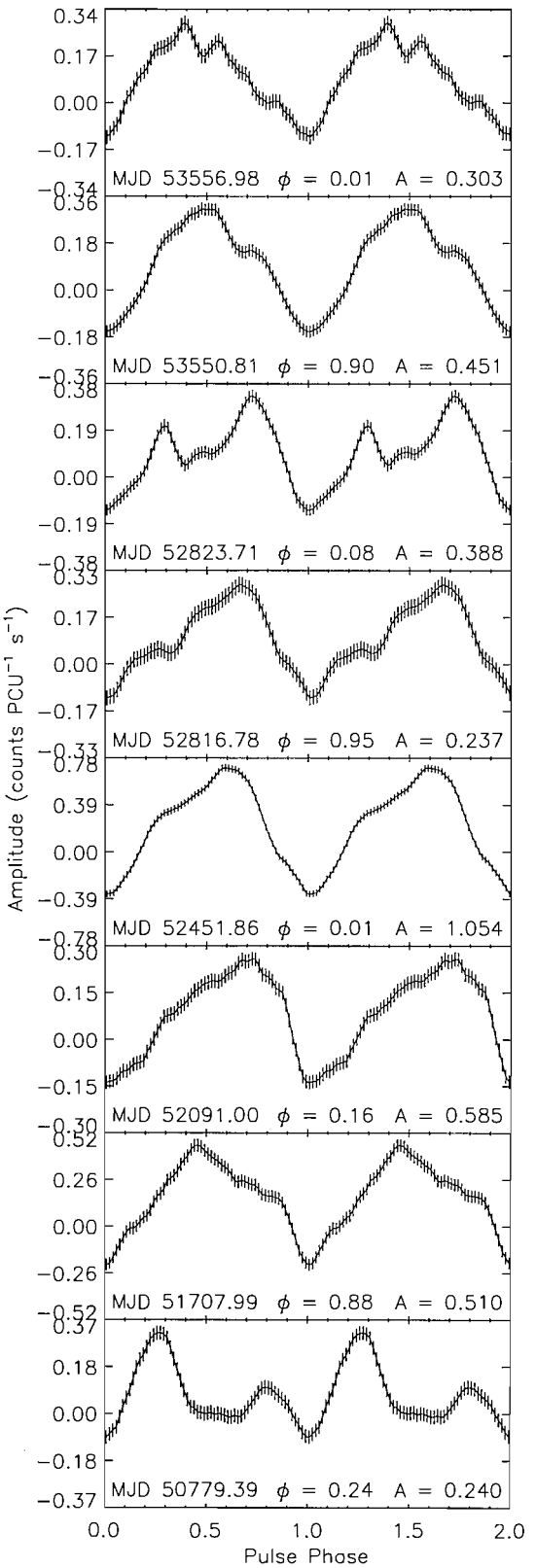

Figure A.21: Pulse profiles of SXP82.4.

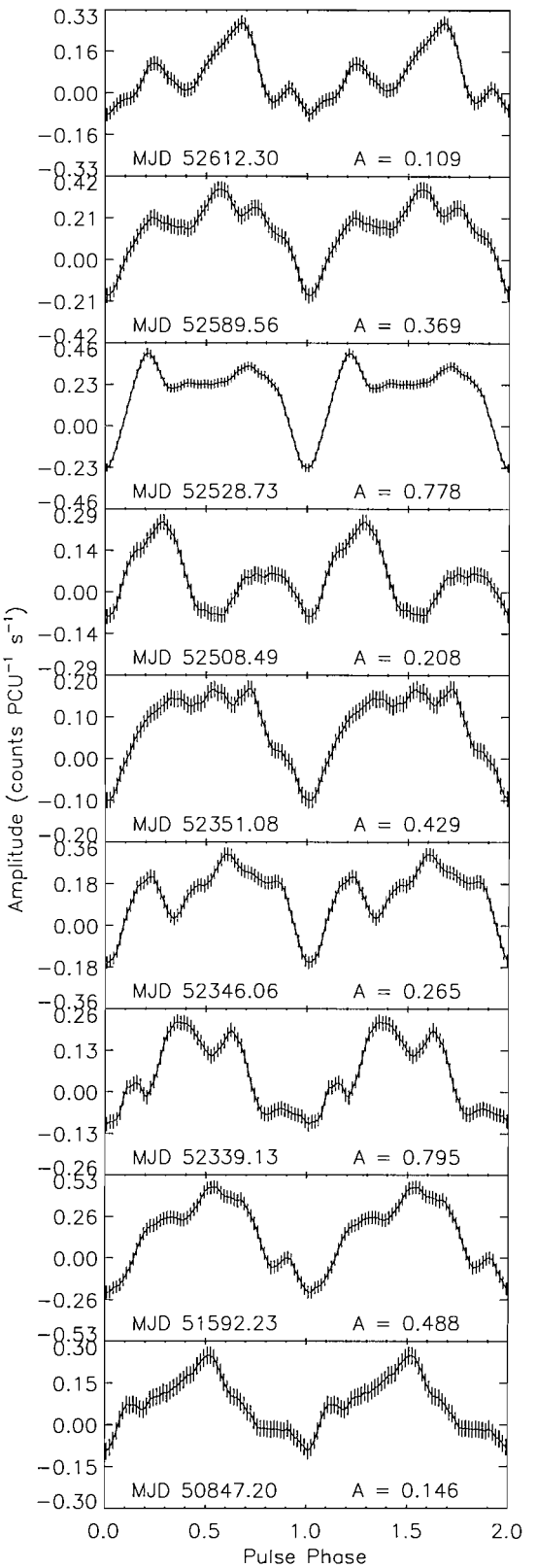

Figure A.22: Pulse profiles of SXP89.0.

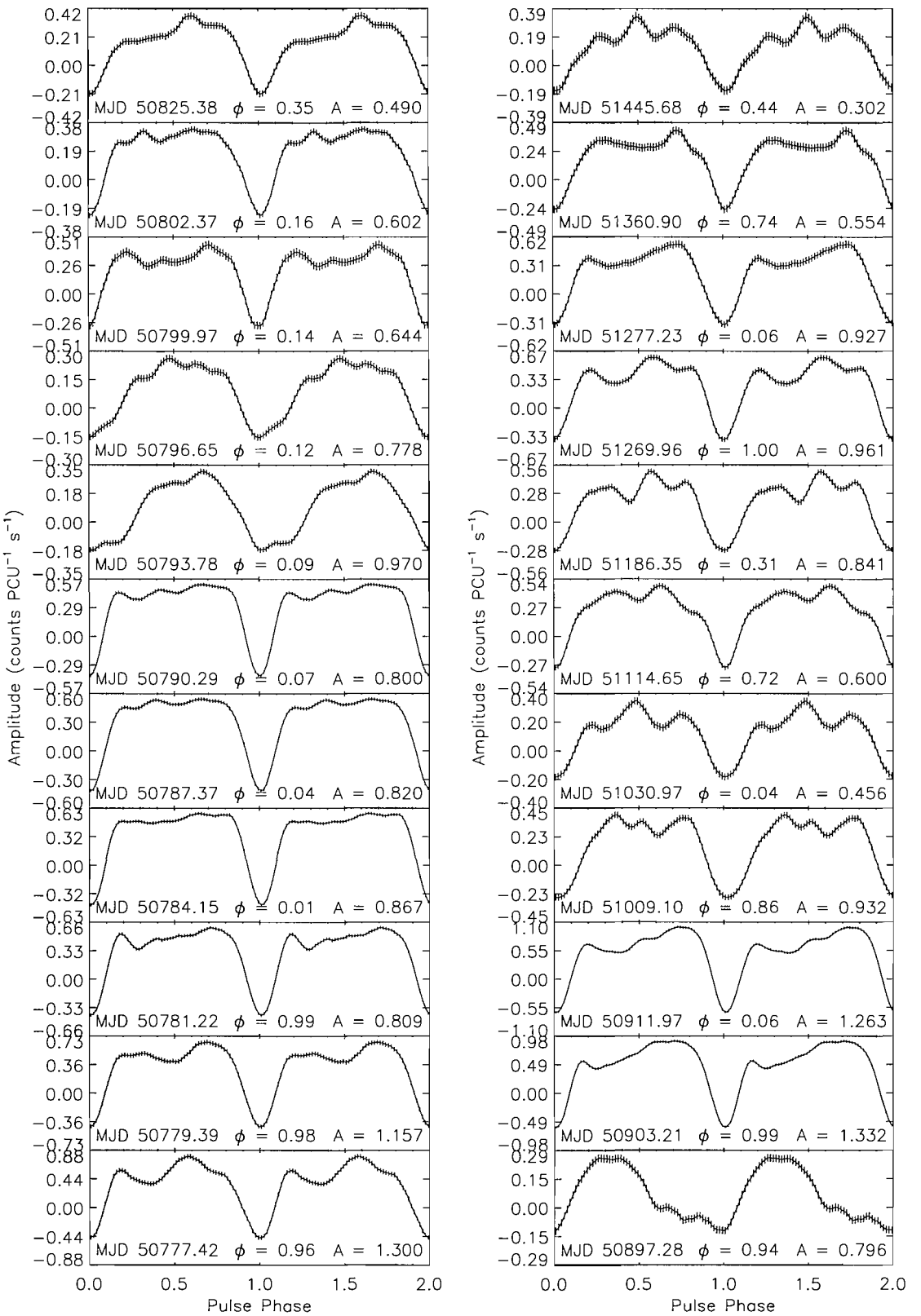

Figure A.23: Pulse profiles of SXP91.1. *Left*: during the MJD 50800 outburst. *Right*: at various other times during outburst.

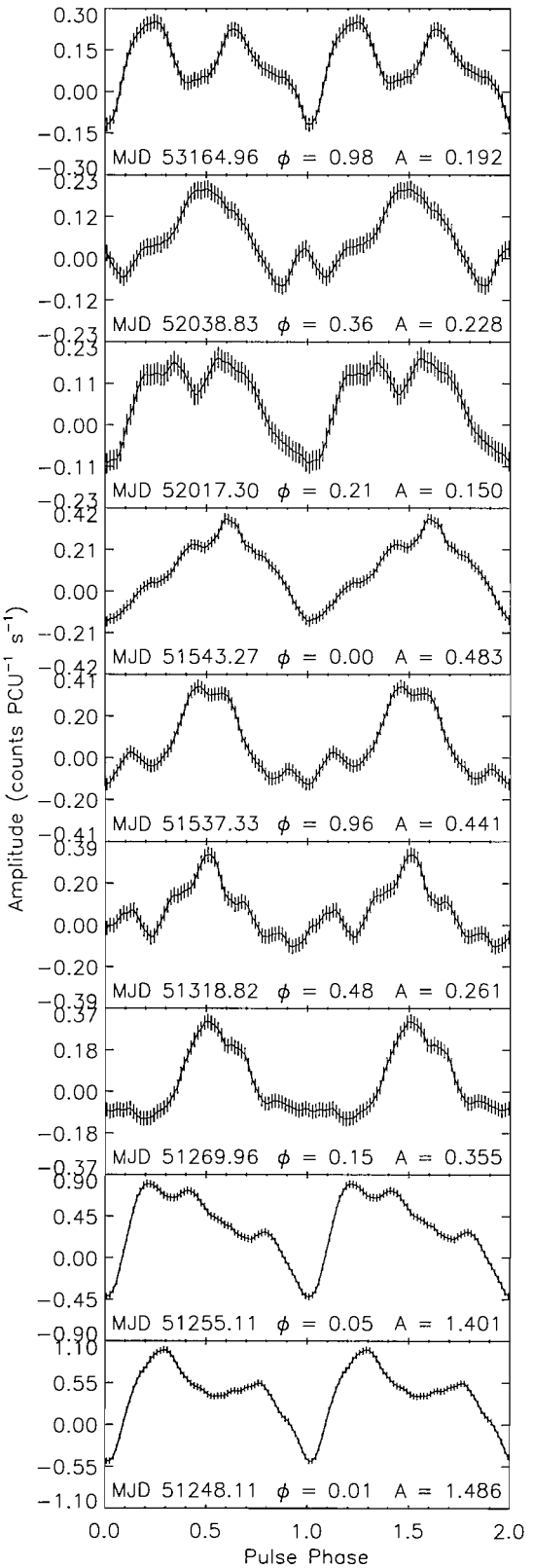

Figure A.24: Pulse profiles of SXP95.2.

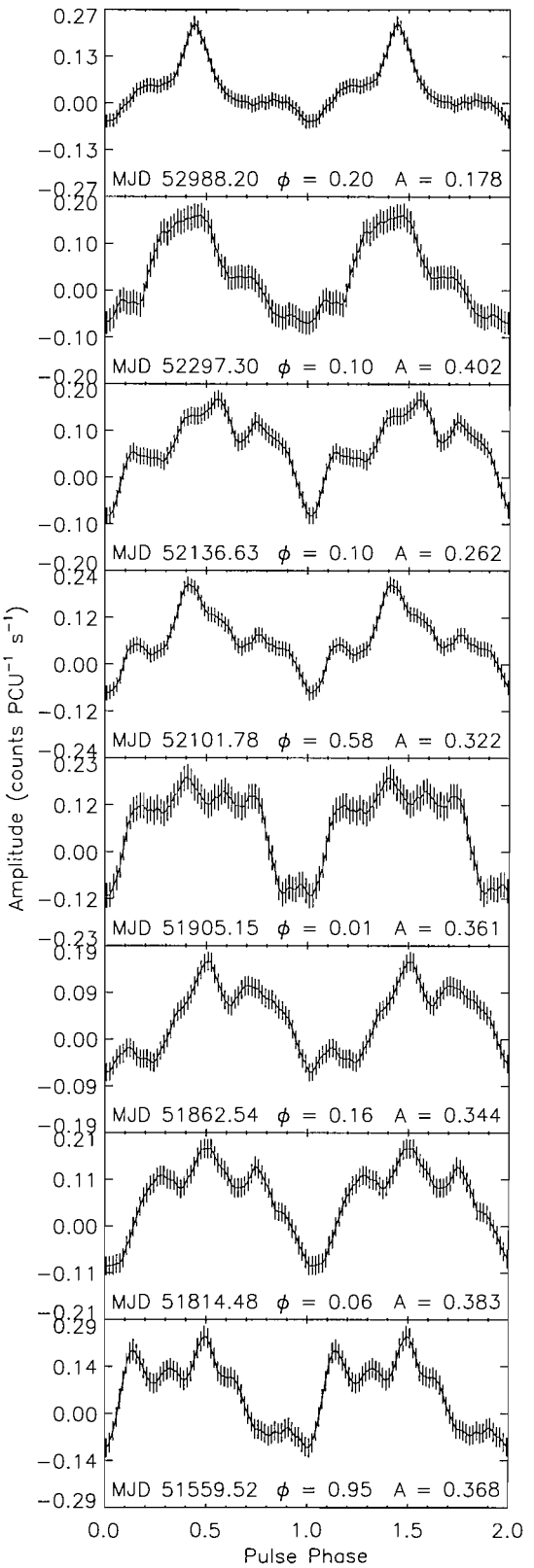

Figure A.25: Pulse profiles of SXP101.

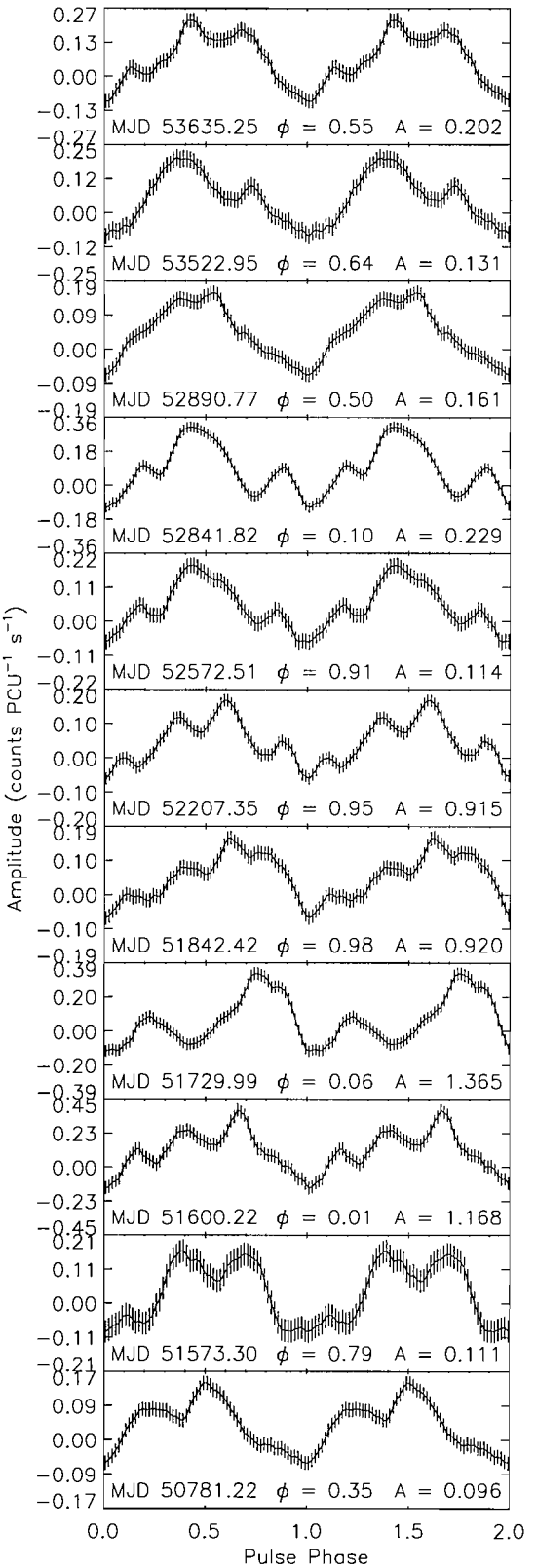

Figure A.26: Pulse profiles of SXP140.

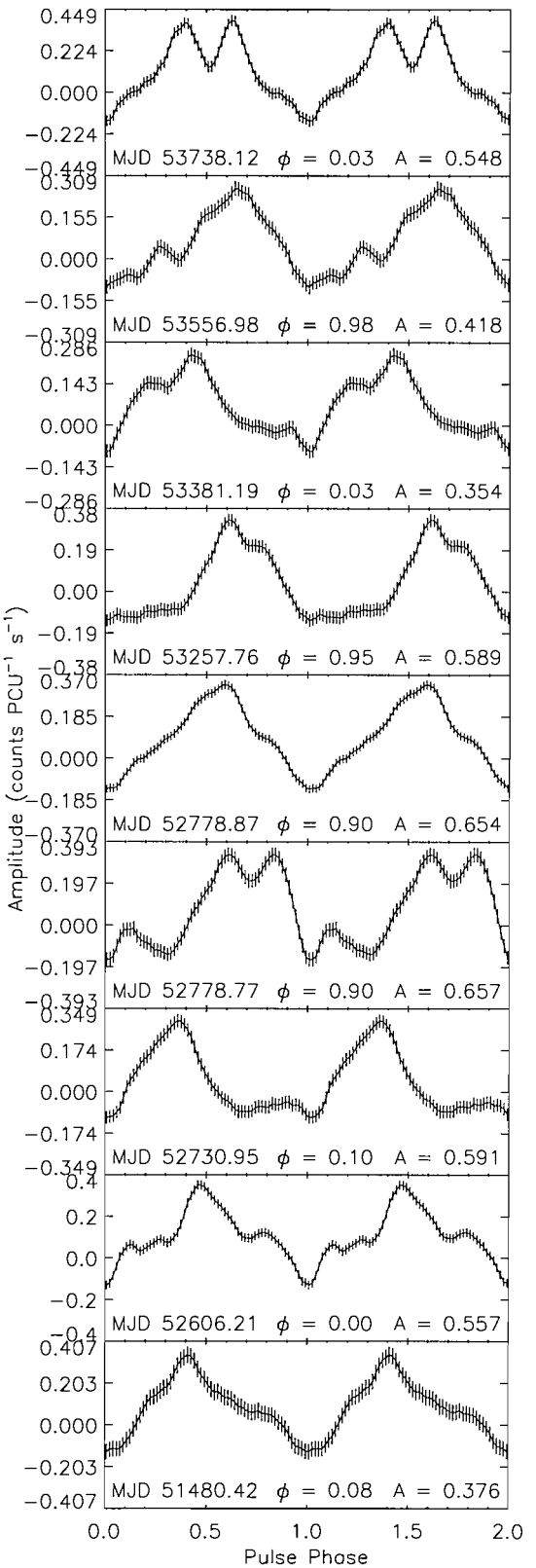

Figure A.27: Pulse profiles of SXP144.

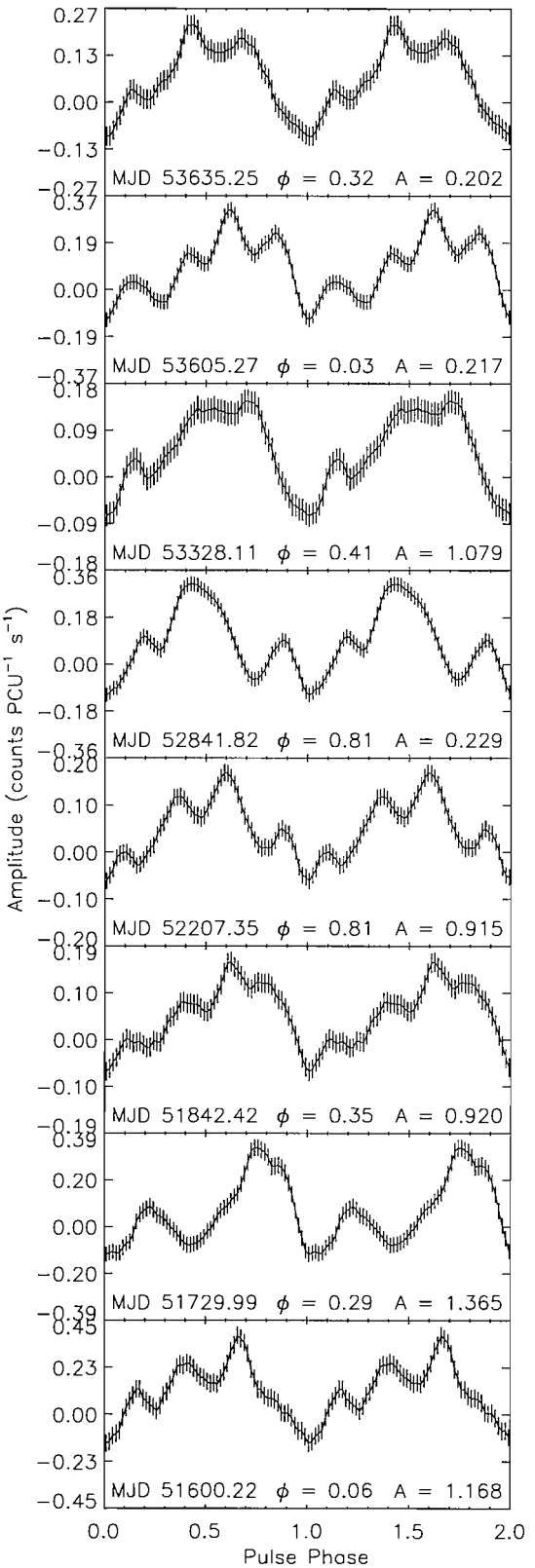

Figure A.28: Pulse profiles of SXP152.

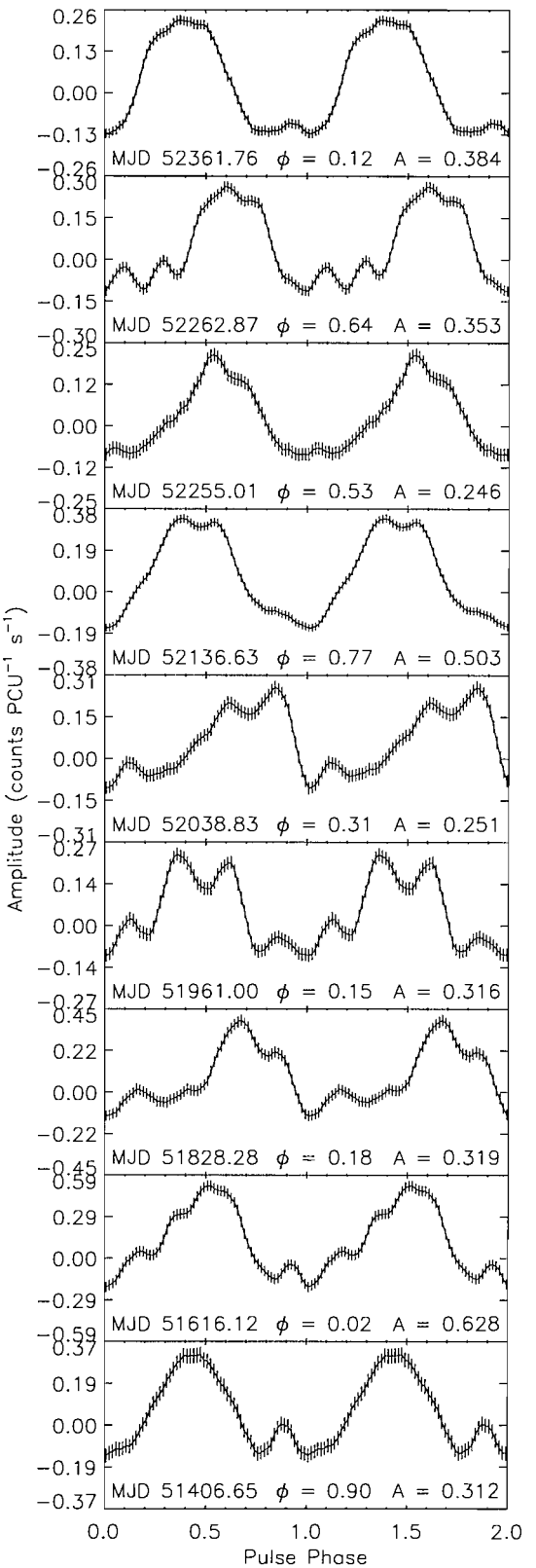

Figure A.29: Pulse profiles of SXP172.

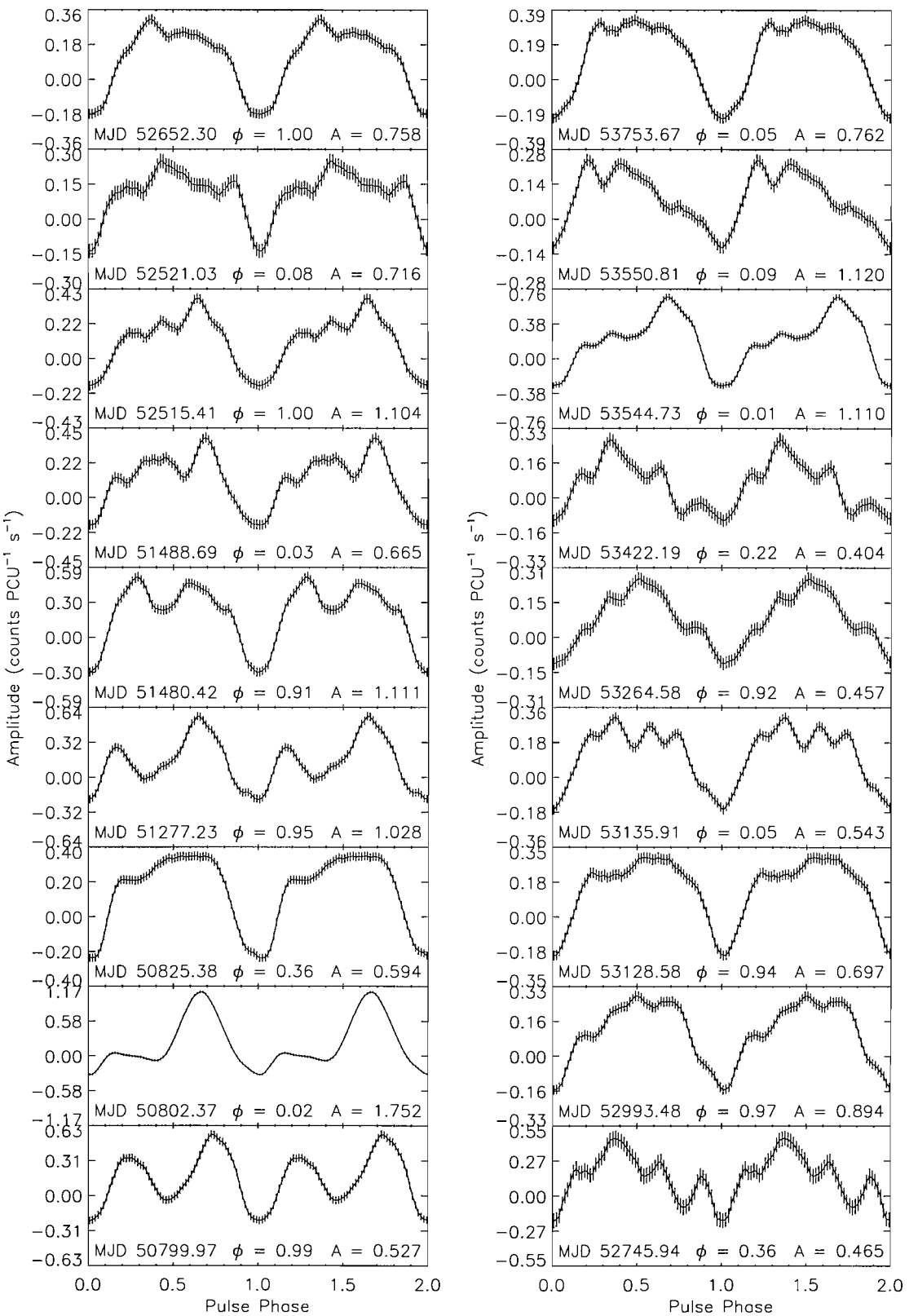

Figure A.30: Pulse profiles of SXP169 at various times during outburst.

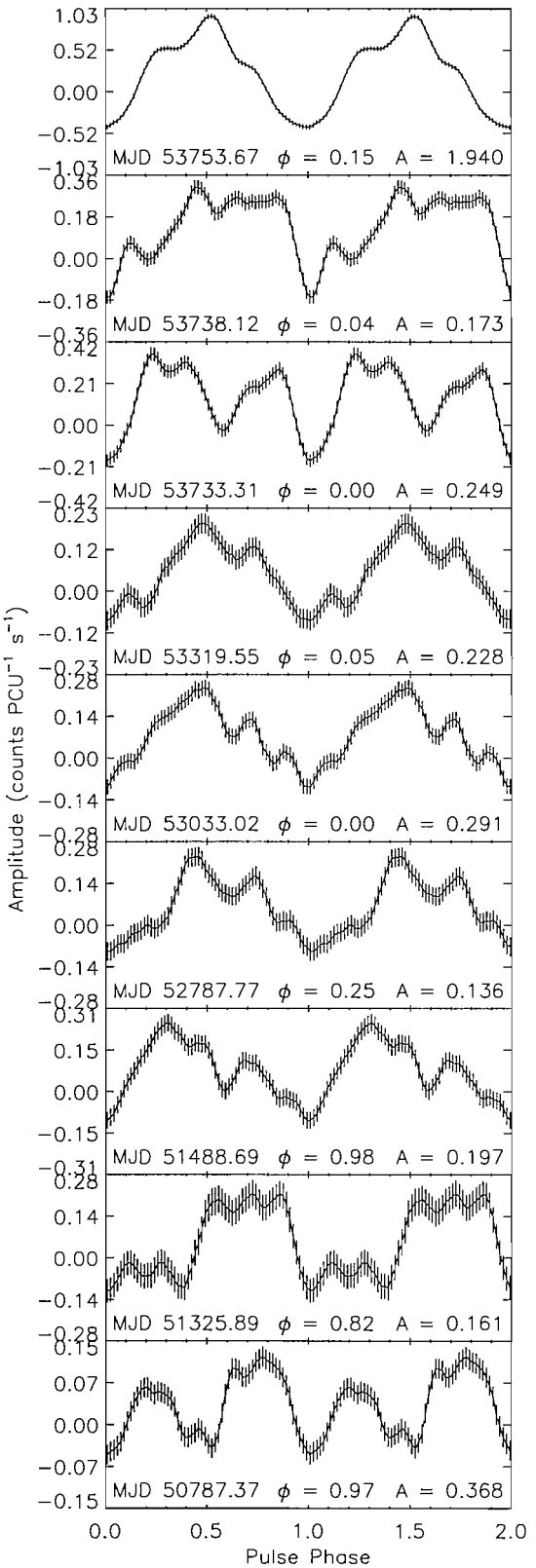

Figure A.31: Pulse profiles of SXP202.

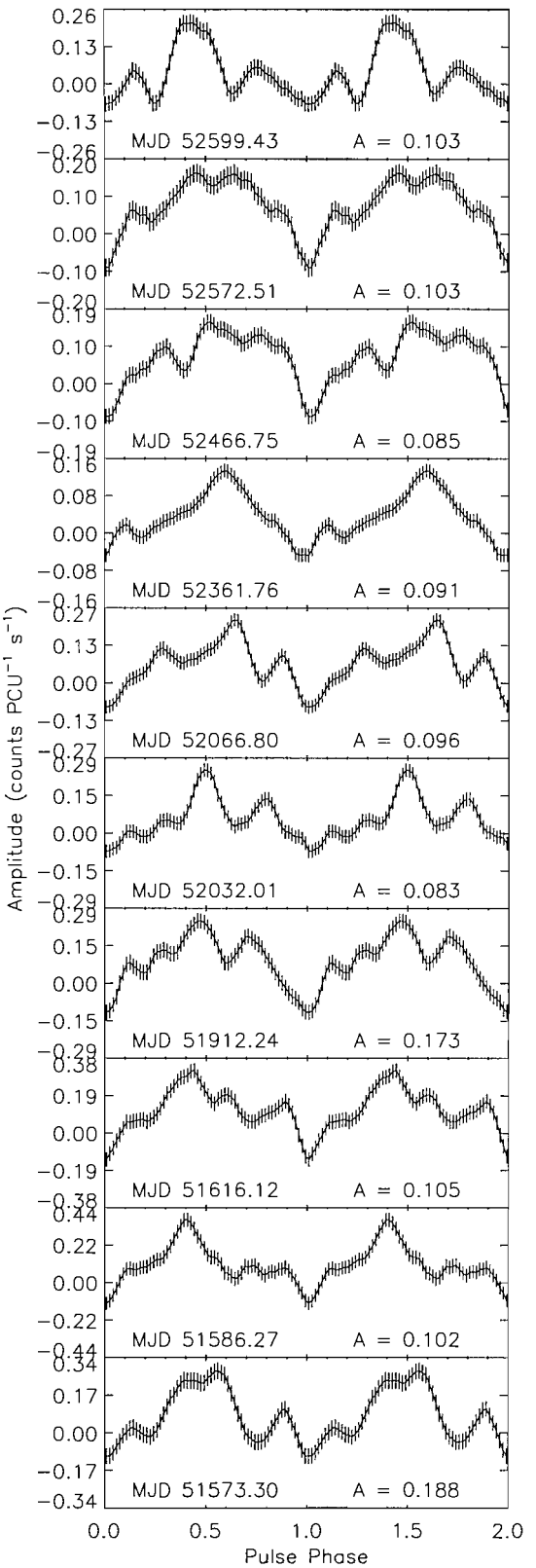

Figure A.32: Pulse profiles of SXP264.

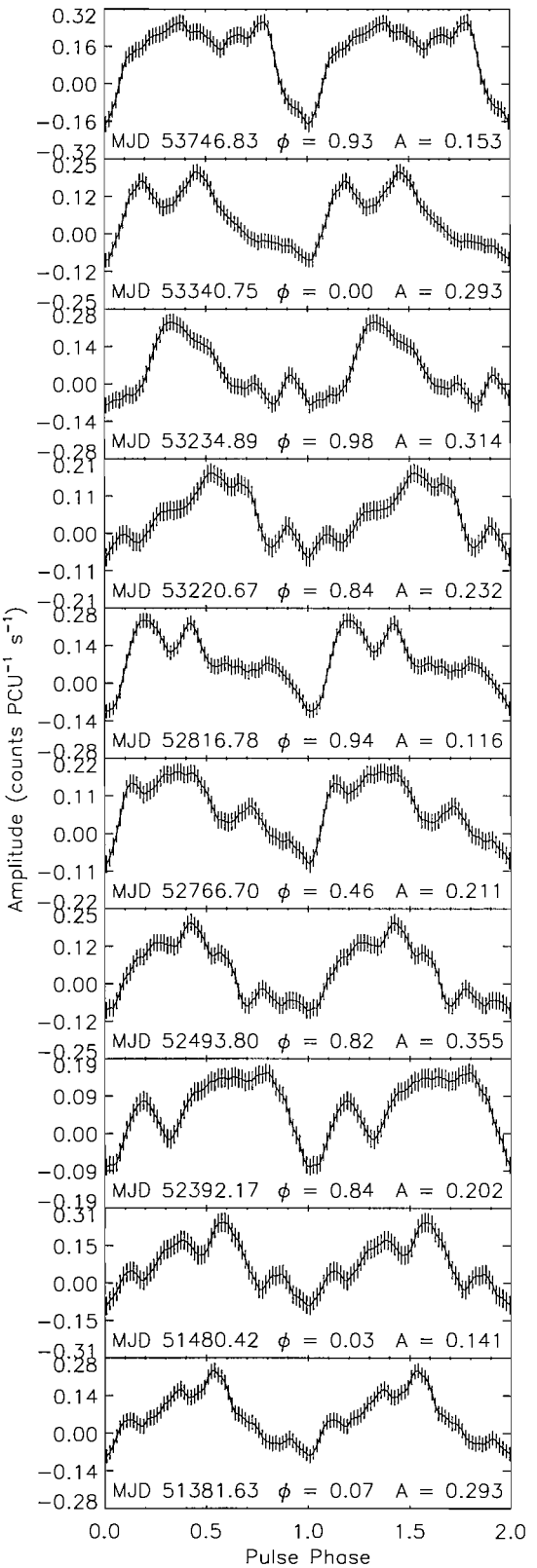

Figure A.33: Pulse profiles of SXP280.

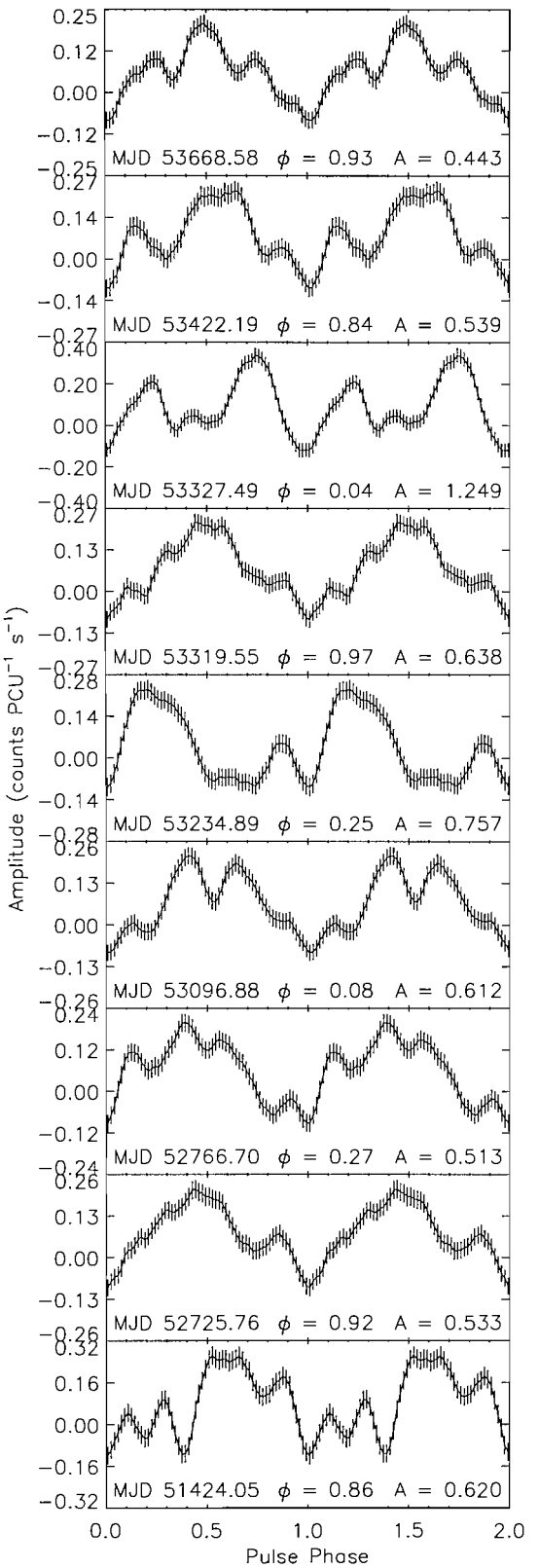

Figure A.34: Pulse profiles of SXP293.

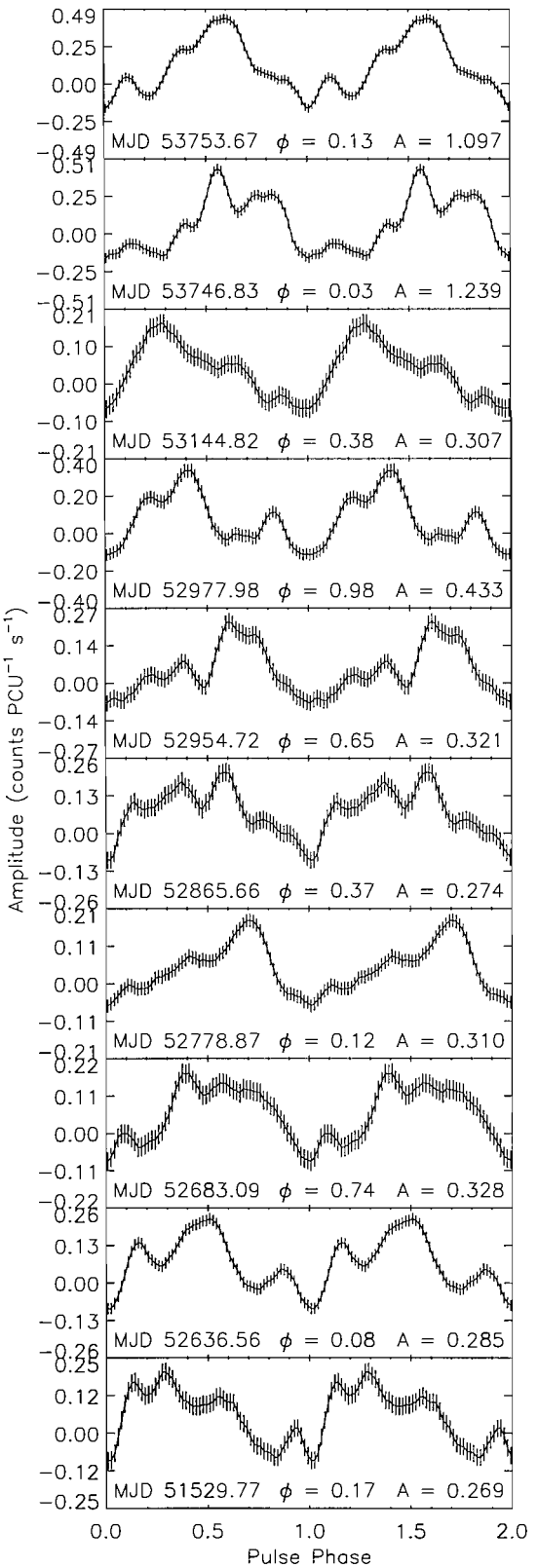

Figure A.35: Pulse profiles of SXP304.

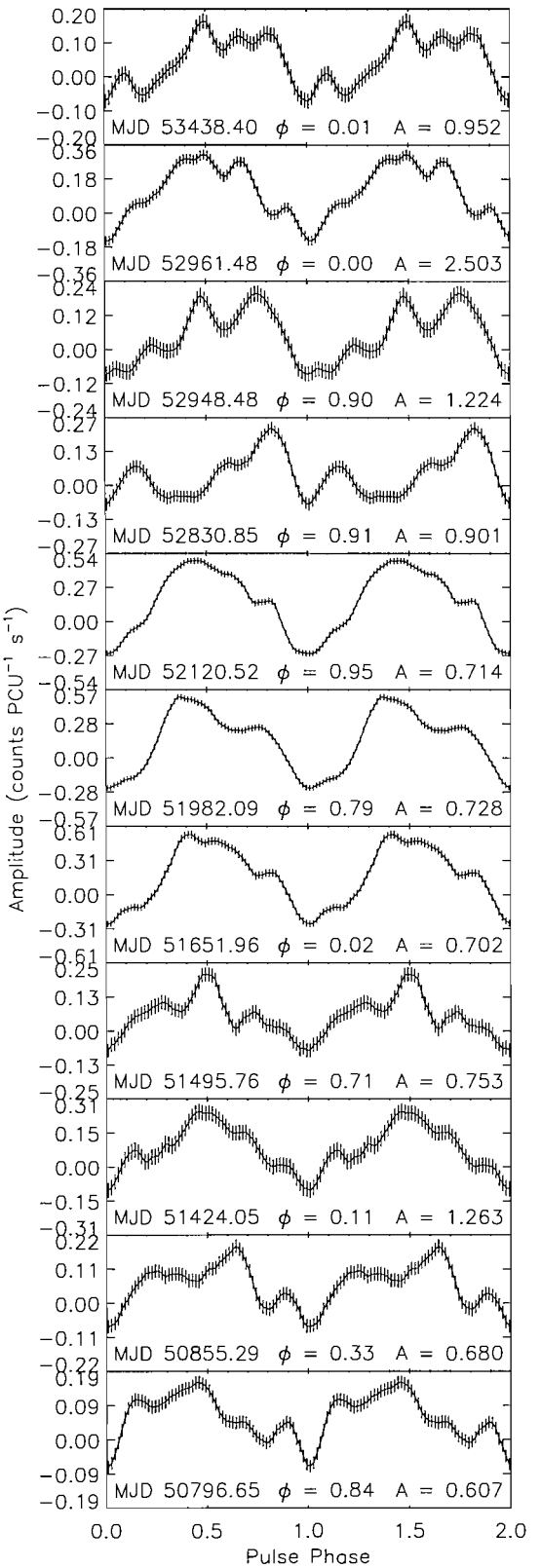

Figure A.36: Pulse profiles of SXP323.

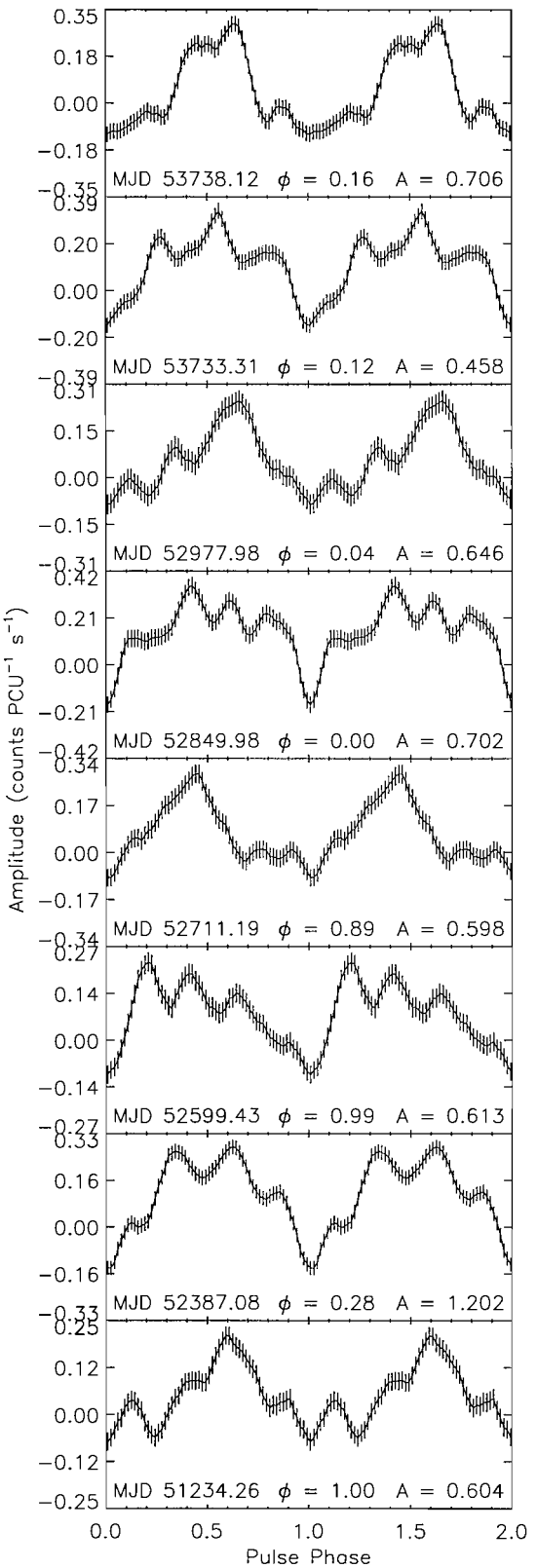

Figure A.37: Pulse profiles of SXP348.

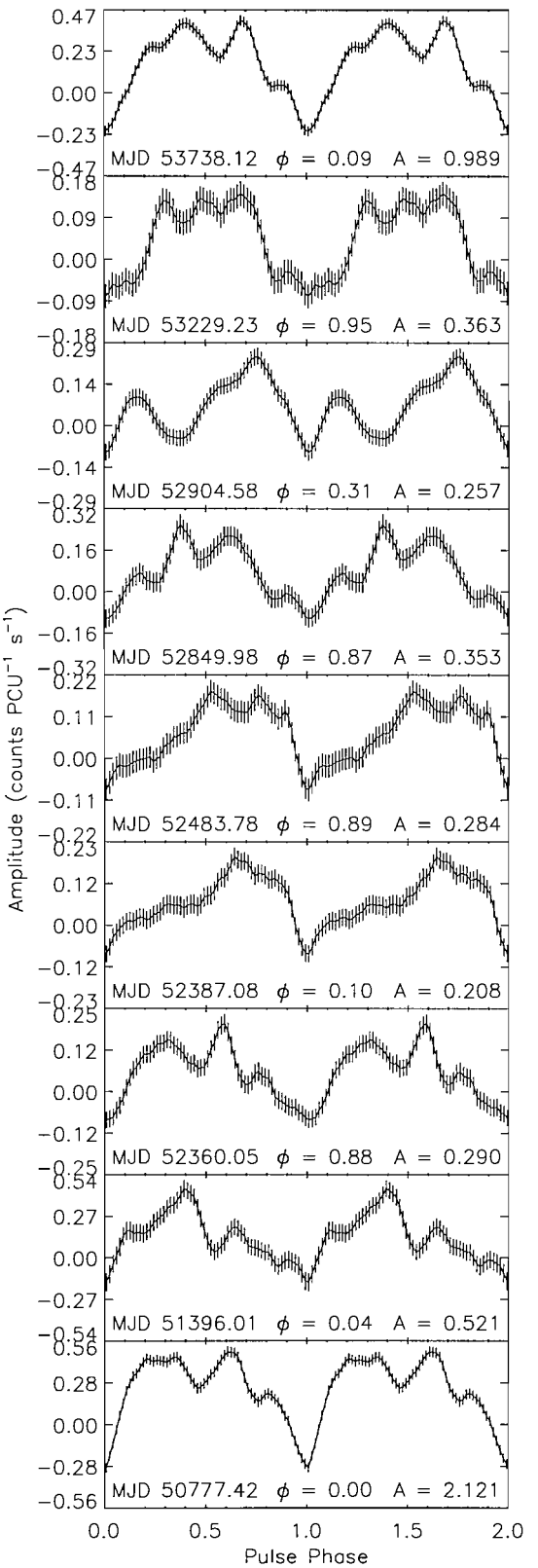

Figure A.38: Pulse profiles of SXP452.

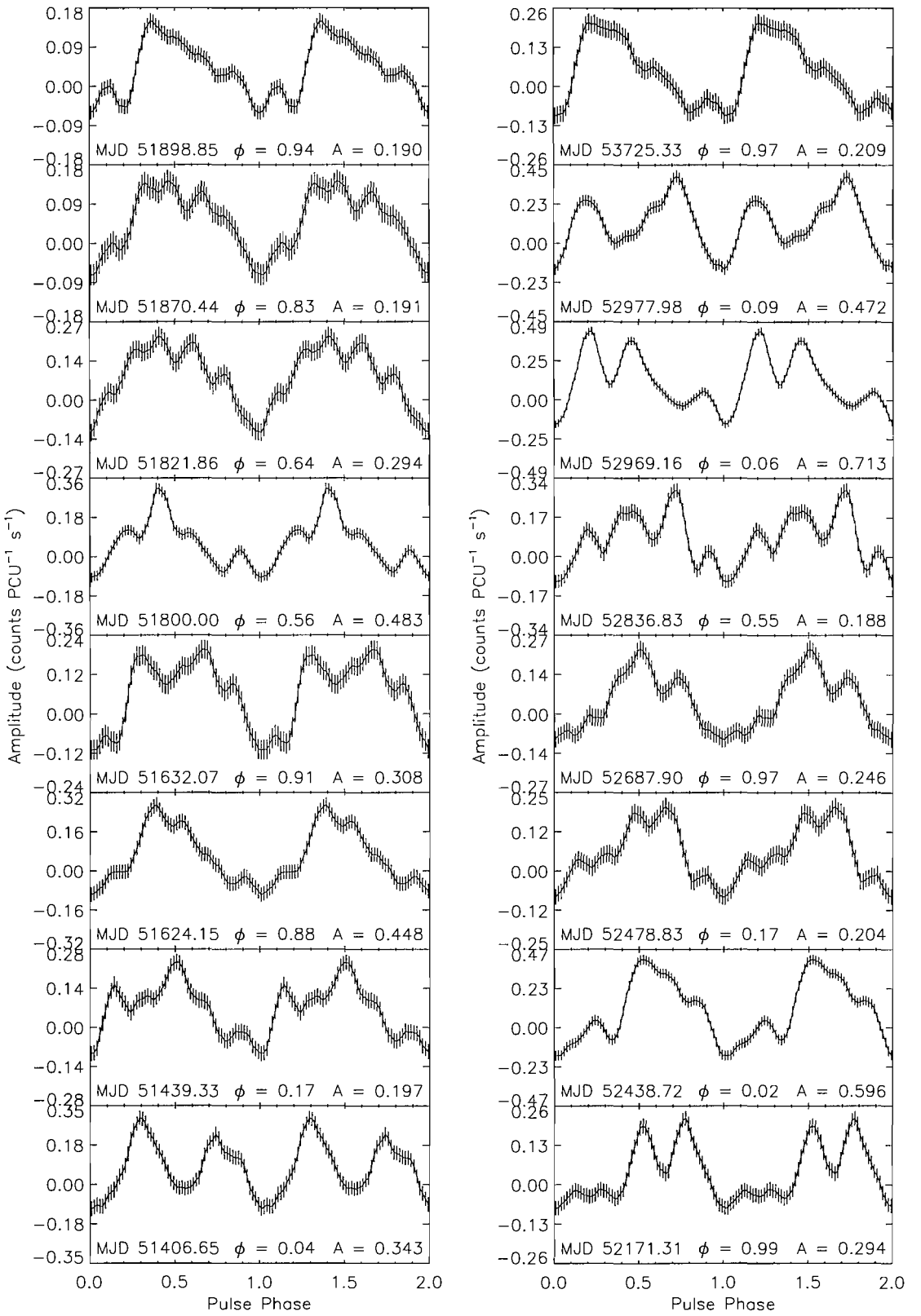

Figure A.39: Pulse profiles of SXP504 at various times during outburst.

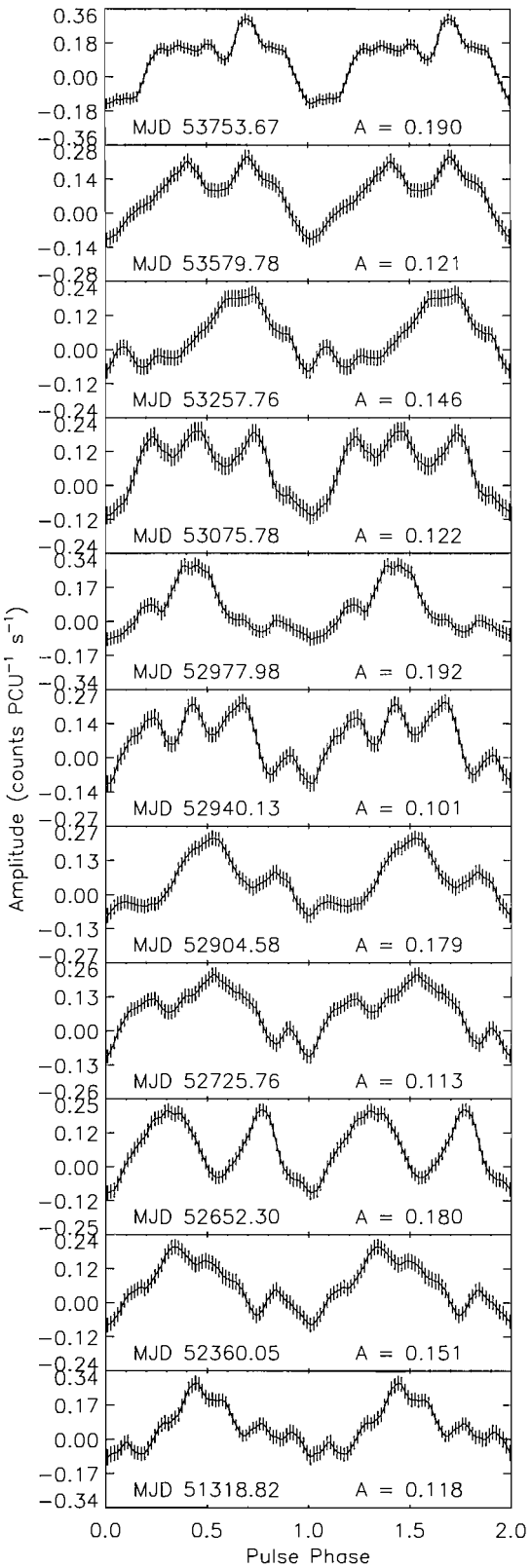

Figure A.40: Pulse profiles of SXP565.

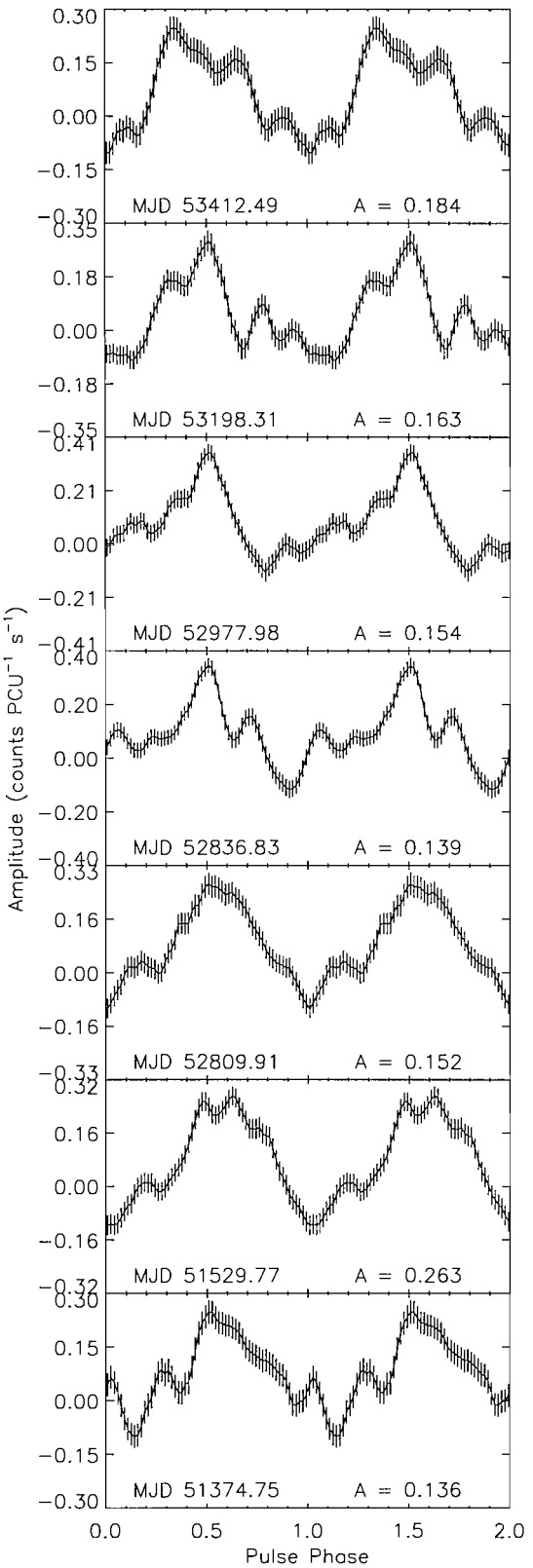

Figure A.41: Pulse profiles of SXP701.

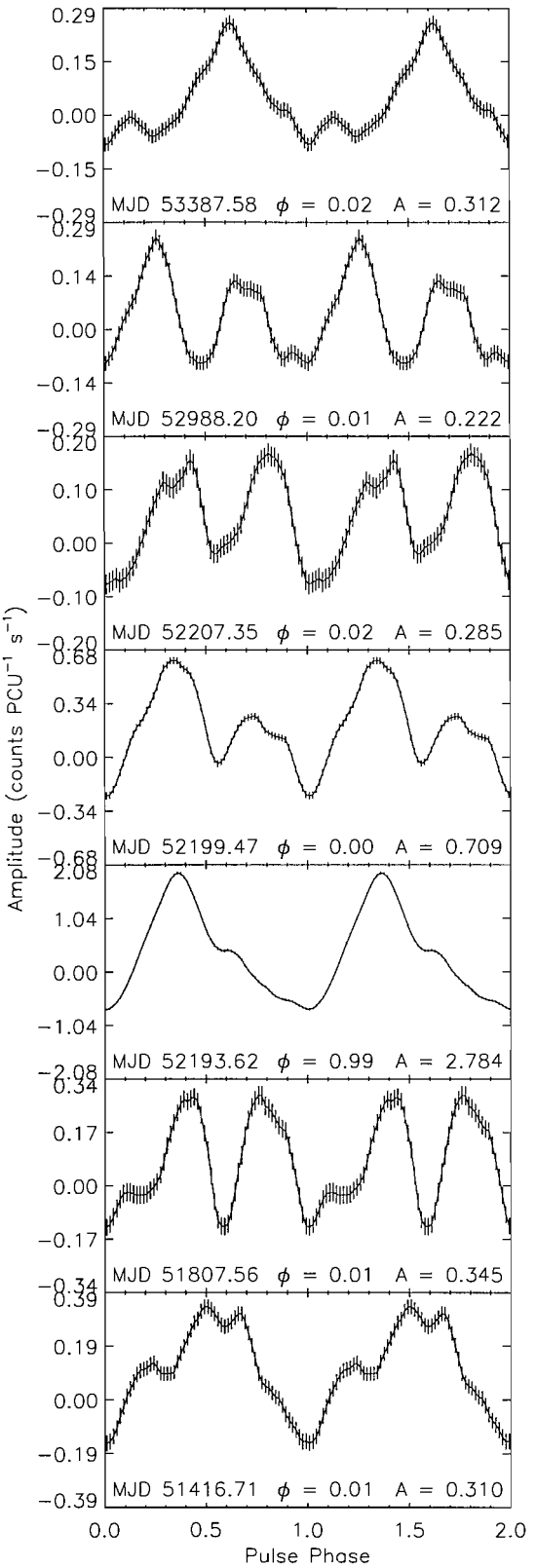

Figure A.42: Pulse profiles of SXP756.

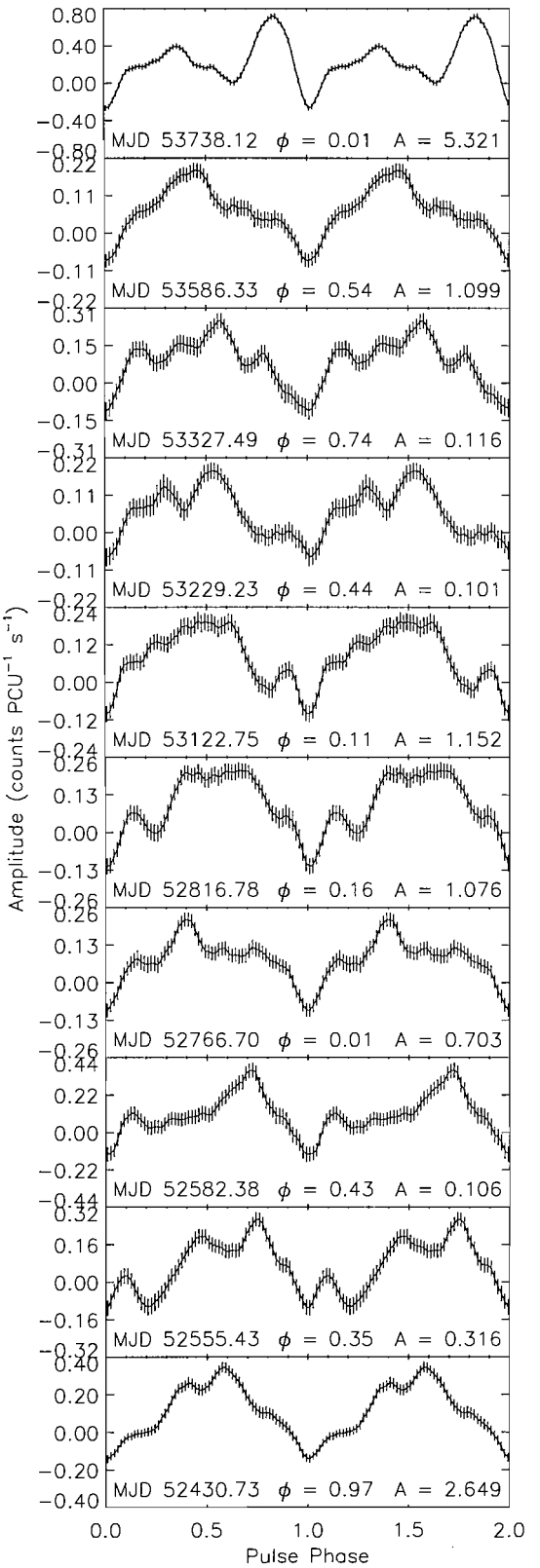

Figure A.43: Pulse profiles of SXP1323.

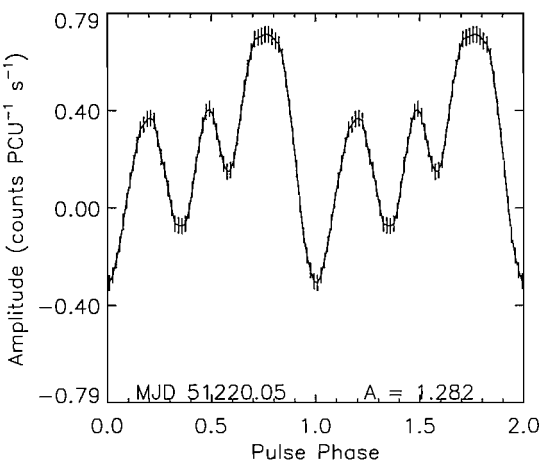

Figure A.44: Pulse profiles of SXP31.0.

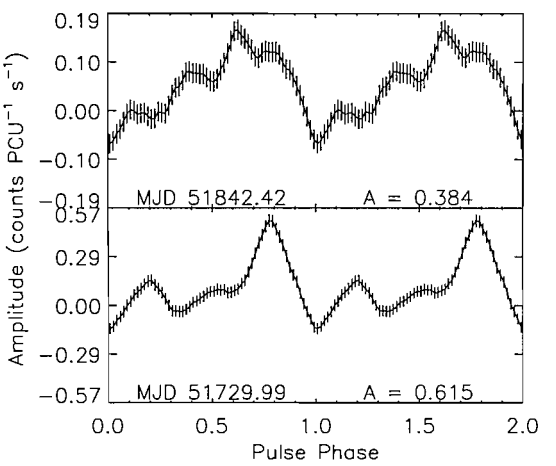

Figure A.45: Pulse profile of SXP138.

Bibliography

Ables, J. G., Jacka, C. E., Hall, P. J., Hamilton, P. A., McConnell, D., and McCulloch, P. M.: 1987, *IAU Circ.* **4422**, 1

Aoki, T., Dotani, T., Ebisawa, K., Itoh, M., Makino, F., Nagase, F., Takeshima, T., Mihara, T., and Kitamoto, S.: 1992, *Publ. Astron. Soc. Jpn.* **44**, 641

Baan, W. A. and Treves, A.: 1973, *Astron. Astrophys.* **22**, 421

Bell, J. F.: 1994, *Proceedings of the Astronomical Society of Australia* **11**, 81

Bildsten, L., Chakrabarty, D., Chiu, J., Finger, M. H., Koh, D. T., Nelson, R. W., Prince, T. A., Rubin, B. C., Scott, D. M., Stollberg, M., Vaughan, B. A., Wilson, C. A., and Wilson, R. B.: 1997, *Astrophys. J., Suppl. Ser.* **113**, 367

Blum, S. and Kraus, U.: 2000, *Astrophys. J.* **529**, 968

Bradt, H. V., Rothschild, R. E., and Swank, J. H.: 1993, *Astron. Astrophys. Suppl. Ser.* **97**, 355

Buccheri, R., Bennett, K., Bignami, G. F., Bloemen, J. B. G. M., Boriakoff, V., Caraveo, P. A., Hermsen, W., Kanbach, G., Manchester, R. N., Masnou, J. L., Mayer-Hasselwander, H. A., Ozel, M. E., Paul, J. A., Sacco, B., Scarsi, L., and Strong, A. W.: 1983, *Astron. Astrophys.* **128**, 245

Bulik, T., Gondek-Rosińska, D., Santangelo, A., Mihara, T., Finger, M., and Cemeljic, M.: 2003, *Astron. Astrophys.* **404**, 1023

Burnard, D. J., Arons, J., and Klein, R. I.: 1991, *Astrophys. J.* **367**, 575

Carstairs, I. R.: 1992, *Ph.D. Thesis, University of Southampton*

Chakrabarty, D., Koh, T., Bildsten, L., Prince, T. A., Finger, M. H., Wilson, R. B., Pendleton, G. N., and Rubin, B. C.: 1995, *Astrophys. J.* **446**, 826

Chakrabarty, D., Levine, A., Clark, G., Takeshima, T., Wilson, C., and Finger, M.: 1998, *IAU Circ.* **7048**, 1

Charles, P. A. and Seward, F. D.: 1995, *Exploring the X-ray universe*, Cambridge, New York: Cambridge University Press, —c1995, ISBN 0521261821

Charles, P. A., Southwell, K. A., and O'Donoghue, D.: 1996, *IAU Circ.* **6305**, 2

Clark, G., Doxsey, R., Li, F., Jernigan, J. G., and van Paradijs, J.: 1978, *Astrophys. J., Lett.* **221**, L37

Clark, G., Remillard, R., and Woo, J.: 1996, *IAU Circ.* **6282**, 1

Clark, G. W., Remillard, R. A., and Woo, J. W.: 1997, *Astrophys. J., Lett.* **474**, L111+

Coburn, W.: 2001, *Ph.D. Thesis, University of California San Diego*

Coe, M., Haigh, N., and Reig, P.: 2000, *Mon. Not. R. Astron. Soc.* **314**, 290

Coe, M., Reig, P., McBride, V., Galache, J., and Fabregat, J.: 2006, *Mon. Not. R. Astron. Soc.* **368**, 447

Coe, M. J., Edge, W. R. T., Galache, J. L., and McBride, V. A.: 2005, *Mon. Not. R. Astron. Soc.* **356**, 502

Coe, M. J., Haigh, N. J., Laycock, S. G. T., Negueruela, I., and Kaiser, C. R.: 2002, *Mon. Not. R. Astron. Soc.* **332**, 473

Coe, M. J., Roche, P., Everall, C., Fishman, G. J., Hagedon, K. S., Finger, M., Wilson, R. B., Buckley, D. A. H., Shrader, C., Fabregat, J., Polcaro, V. F., Giovannelli, F., and Villada, M.: 1994, *Astron. Astrophys.* **289**, 784

Coe, M. J., Stevens, J. B., Buckley, D. A. H., Charles, P. A., and Southwell, K. A.: 1998, *Mon. Not. R. Astron. Soc.* **293**, 43

Collins, G. W.: 1987, in *IAU Colloq. 92: Physics of Be Stars*, pp 3–19

Cominsky, L., Clark, G. W., Li, F., Mayer, W., and Rappaport, S.: 1978, *Nature* **273**, 367

Cook, M. C. and Warwick, R. S.: 1987, *Mon. Not. R. Astron. Soc.* **225**, 369

Corbet, R., Markwardt, C. B., Marshall, F. E., Coe, M. J., Edge, W. R. T., and Laycock, S.: 2003a, *IAU Circ.* **8064**, 4

Corbet, R., Markwardt, C. B., Marshall, F. E., Laycock, S., and Coe, M.: 2002, *IAU Circ.* **7932**, 2

Corbet, R., Marshall, F. E., Lochner, J. C., Ozaki, M., and Ueda, Y.: 1998, *IAU Circ.* **6803**, 1

Corbet, R. H. D.: 1984, *Astron. Astrophys.* **141**, 91

Corbet, R. H. D.: 1986, *Mon. Not. R. Astron. Soc.* **220**, 1047

Corbet, R. H. D., Coe, M. J., Edge, W. R. T., Laycock, S., Markwardt, C. B., and Marshall, F. E.: 2004a, *The Astronomer's Telegram* **277**, 1

Corbet, R. H. D., Edge, W. R. T., Laycock, S., Coe, M. J., Markwardt, C. B., and Marshall, F. E.: 2003b, *AAS/High Energy Astrophysics Division* **7**, 1

Corbet, R. H. D., Laycock, S., Coe, M. J., Marshall, F. E., and Markwardt, C. B.: 2004b, in *AIP Conf. Proc. 714: X-ray Timing 2003: Rossi and Beyond*, pp 337–341

Corbet, R. H. D., Laycock, S., Marshall, F. E., Markwardt, C. B., and Coe, M. J.: 2003c, *The Astronomer's Telegram* **209**, 1

Corbet, R. H. D., Markwardt, C. B., Coe, M. J., Edge, W. R. T., Laycock, S., and Marshall, F. E.: 2003d, *The Astronomer's Telegram* **214**, 1

Corbet, R. H. D., Markwardt, C. B., Coe, M. J., Edge, W. R. T., Laycock, S., and Marshall, F. E.: 2004c, *The Astronomer's Telegram* **273**, 1

Corbet, R. H. D., Markwardt, C. B., Marshall, F. E., Coe, M. J., Edge, W. R. T., Galache, J. L., and Laycock, S.: 2004d, *The Astronomer's Telegram* **347**, 1

Corbet, R. H. D., Markwardt, C. B., Marshall, F. E., Coe, M. J., Edge, W. R. T., and Laycock, S.: 2003e, *The Astronomer's Telegram* **163**, 1

Corbet, R. H. D., Marshall, F. E., Coe, M. J., Laycock, S., and Handler, G.: 2001, *Astrophys. J., Lett.* **548**, L41

Corbet, R. H. D. and Peele, A. G.: 1997, *Astrophys. J., Lett.* **489**, L83+

Cowley, A. P. and Schmidtke, P. C.: 2003, *Astrophys. J.* **126**, 2949

Cowley, A. P., Schmidtke, P. C., McGrath, T. K., Ponder, A. L., Fertig, M. R., Hutchings, J. B., and Crampton, D.: 1997, *Publ. Astron. Soc. Pac.* **109**, 21

Dachs, J., Hanuschik, R., Kaiser, D., and Rohe, D.: 1986, *Astron. Astrophys.* **159**, 276

Davidson, K. and Ostriker, J. P.: 1973, *Astrophys. J.* **179**, 585

de Jager, O. C., Raubenheimer, B. C., North, A. R., Nel, H. I., and van Urk, G.: 1988, *Astrophys. J.* **329**, 831

Doazan, V., Thomas, R. N., and Barylak, M.: 1986, *Astron. Astrophys.* **159**, 75

Edge, W. R. T.: 2005, *Ph.D. Thesis, University of Southampton*

Edge, W. R. T. and Coe, M. J.: 2003, *Mon. Not. R. Astron. Soc.* **338**, 428

Edge, W. R. T., Coe, M. J., Corbet, R. H. D., Markwardt, C. B., and Laycock, S.: 2004a, *The Astronomer's Telegram* **225**, 1

Edge, W. R. T., Coe, M. J., Corbet, R. H. D., Markwardt, C. B., Laycock, S., and Marshall, F. E.: 2004b, *The Astronomer's Telegram* **216**, 1

Edge, W. R. T., Coe, M. J., and Galache, J. L.: 2005a, *The Astronomer's Telegram* **405**, 1

Edge, W. R. T., Coe, M. J., Galache, J. L., McBride, V. A., Corbet, R. H. D., Markwardt, C. B., and Laycock, S.: 2004c, *Mon. Not. R. Astron. Soc.* **353**, 1286

Edge, W. R. T., Coe, M. J., Galache, J. L., McBride, V. A., Corbet, R. H. D., Markwardt, C. B., Laycock, S., and Marshall, F. E.: 2005b, *The Astronomer's Telegram* **426**, 1

Edge, W. R. T., Coe, M. J., Galache, J. L., McBride, V. A., Corbet, R. H. D., Okazaki, A. T., Laycock, S., Markwardt, C. B., Marshall, F. E., and Udalski, A.: 2005c, *Mon. Not. R. Astron. Soc.* **361**, 743

Edge, W. R. T., Coe, M. J., and McBride, V. A.: 2004d, *The Astronomer's Telegram* **217**, 1

Eyles, C. J., Skinner, G. K., Willmore, A. P., and Rosenberg, F. D.: 1975, *Nature* **254**, 577

Fabrycky, D.: 2005, *Mon. Not. R. Astron. Soc.* **359**, 117

Filipović, M. D., Haberl, F., Pietsch, W., and Morgan, D. H.: 2000, *Astron. Astrophys.* **353**, 129

Finger, M. H., Bildsten, L., Chakrabarty, D., Prince, T. A., Scott, D. M., Wilson, C. A., Wilson, R. B., and Zhang, S. N.: 1999, *Astrophys. J.* **517**, 449

Finger, M. H. and Wilson, C. A.: 2000, *IAU Circ.* **7366**, 2

Finger, M. H., Wilson, R. B., and Chakrabarty, D.: 1996, *Astron. Astrophys. Suppl. Ser.* **120**, C209+

Finger, M. H., Wilson, R. B., Scott, M., Stollberg, M., and Prince, T. A.: 1994, *IAU Circ.* **5959**, 2

Fishman, G. J., Meegan, C. A., Wilson, R. B., Parnell, T. A., Paciesas, W. S., Pendleton, G. N., Hudson, H. S., Matteson, J. L., Peterson, L. E., Cline, T. L., Teegarden, B. J., and Schaefer, B. E.: 1989, *Bull. Am. Astron. Soc.* **21**, 860

Frank, J., King, A., and Raine, D. J.: 2002, *Accretion Power in Astrophysics: Third Edition*, Cambridge University Press

Galache, J. L., Corbet, R. H. D., Coe, M. J., Laycock, S., Markwardt, C. B., and Marshall, F. E.: 2005, *The Astronomer's Telegram* **674**, 1

Giacconi, R., Branduardi, G., Briel, U., Epstein, A., Fabricant, D., Feigelson, E., Forman, W., Gorenstein, P., Grindlay, J., Gursky, H., Harnden, F. R., Henry, J. P., Jones, C., Kellogg, E., Koch, D., Murray, S., Schreier, E., Seward, F., Tananbaum, H., Topka, K., Van Speybroeck, L., Holt, S. S., Becker, R. H., Boldt, E. A.,

Serlemitsos, P. J., Clark, G., Canizares, C., Markert, T., Novick, R., Helfand, D., and Long, K.: 1979, *Astrophys. J.* **230**, 540

Giacconi, R. and Gursky, H.: 1965, *Space Science Reviews* **4**, 151

Haberl, F., Filipović, M. D., Pietsch, W., and Kahabka, P.: 2000, *Astron. Astrophys. Suppl. Ser.* **142**, 41

Haberl, F. and Pietsch, W.: 2004, *Astron. Astrophys.* **414**, 667

Haberl, F. and Pietsch, W.: 2005, *Astron. Astrophys.* **438**, 211

Haberl, F., Pietsch, W., Schartel, N., Rodriguez, P., and Corbet, R. H. D.: 2004, *The Astronomer's Telegram* **219**, 1

Haberl, F. and Sasaki, M.: 2000, *Astron. Astrophys.* **359**, 573

Hanuschik, R. W., Dachs, J., Baudzus, M., and Thimm, G.: 1993, *Astron. Astrophys.* **274**, 356

Harmon, B. A., Fishman, G. J., Wilson, C. A., Paciesas, W. S., Zhang, S. N., Finger, M. H., Koshut, T. M., McCollough, M. L., Robinson, C. R., and Rubin, B. C.: 2002, *Astrophys. J., Suppl. Ser.* **138**, 149

Hayasaki, K. and Okazaki, A. T.: 2004, *Mon. Not. R. Astron. Soc.* **350**, 971

Hayasaki, K. and Okazaki, A. T.: 2005, *Mon. Not. R. Astron. Soc.* **360**, L15

Heindl, W. A., Coburn, W., Gruber, D. E., Rothschild, R. E., Kreykenbohm, I., Wilms, J., and Staubert, R.: 2001, *Astrophys. J., Lett.* **563**, L35

Heindl, W. A., Rothschild, R. E., Coburn, W., Staubert, R., Wilms, J., Kreykenbohm, I., and Kretschmar, P.: 2004, in *AIP Conf. Proc. 714: X-ray Timing 2003: Rossi and Beyond*, pp 323–330

Horne, J. H. and Baliunas, S. L.: 1986, *Astrophys. J.* **302**, 757

Howells, L., Steele, I. A., Porter, J. M., and Etherton, J.: 2001, *Astron. Astrophys.* **369**, 99

Hughes, J. P.: 1994, *Astrophys. J., Lett.* **427**, L25

Illarionov, A. F. and Sunyaev, R. A.: 1975, *Astron. Astrophys.* **39**, 185

Imanishi, K., Yokogawa, J., and Koyama, K.: 1998, *IAU Circ.* **7040**, 2

in't Zand, J. J. M., Corbet, R. H. D., and Marshall, F. E.: 2001, *Astrophys. J., Lett.* **553**, L165

Israel, G. L., Covino, S., Campana, S., Polcaro, V. F., Roche, P., Stella, L., Di Paola, A., Lazzati, D., Mereghetti, S., Giallongo, E., Fontana, A., and Verrecchia, F.: 2000, *Mon. Not. R. Astron. Soc.* **314**, 87

Israel, G. L., Negueruela, I., Campana, S., Covino, S., Di Paola, A., Maxwell, D. H., Norton, A. J., Speziali, R., Verrecchia, F., and Stella, L.: 2001, *Astron. Astrophys.* **371**, 1018

Israel, G. L., Stella, L., Angelini, L., White, N. E., Giommi, P., and Covino, S.: 1997, *Astrophys. J., Lett.* **484**, L141+

Israel, G. L., Stella, L., Campana, S., Covino, S., Ricci, D., and Oosterbroek, T.: 1998, *IAU Circ.* **6999**, 1

Ives, J. C., Sanford, P. W., and Burnell, S. J. B.: 1975, *Nature* **254**, 578

Jahoda, K., Markwardt, C. B., Radeva, Y., Rots, A., Stark, M. J., Swank, J. H., Strohmayer, T. E., and Zhang, W.: 2005, *ArXiv Astrophysics e-prints* astro-ph/0511531

Jahoda, K., Swank, J. H., Giles, A. B., Stark, M. J., Strohmayer, T., Zhang, W., and Morgan, E. H.: 1996, in *Proc. SPIE Vol. 2808, p. 59-70, EUV, X-Ray, and Gamma-Ray Instrumentation for Astronomy VII, Oswald H. Siegmund; Mark A. Gummin; Eds.*, pp 59–70

Jaschek, C. and Jaschek, M.: 1990, *The Classification of Stars*, Cambridge University Press

Kahabka, P. and Pietsch, W.: 1998, *IAU Circ.* **6840**, 1

Kaspi, V. M., Johnston, S., Manchester, R. N., Bailes, M., Bell, J. F., Bessell, M., Lyne, A. G., and D'Amico, N.: 1993, *Bulletin of the American Astronomical Society* **25**, 1434

Kelley, R. L., Doxsey, R. E., Jernigan, J. G., Rappaport, S., Apparao, K. M. V., and Naranan, S.: 1981, *Astrophys. J.* **243**, 251

Lamb, F. K., Pethick, C. J., and Pines, D.: 1973, *Astrophys. J.* **184**, 271

Lamb, R. C., Fox, D. W., Macomb, D. J., and Prince, T. A.: 2002a, *Astrophys. J., Lett.* **574**, L29

Lamb, R. C., Macomb, D. J., Prince, T. A., and Majid, W. A.: 2002b, *Astrophys. J., Lett.* **567**, L129

Lamb, R. C., Prince, T. A., Macomb, D. J., and Finger, M. H.: 1999, *IAU Circ.* **7081**, 4

Lamers, H. J. G. L. M. and Waters, L. B. F. M.: 1987, *Astron. Astrophys.* **182**, 80

Lapshov, I. Y., Dremin, V. V., Syunyaev, R. A., Brandt, S., and Lund, N.: 1992, *Soviet Astronomy Letters* **18**, 12

Laycock, S., Coe, M. J., Wilson, C. A., Harmon, B. A., and Finger, M.: 2003a, *Mon. Not. R. Astron. Soc.* **338**, 211

Laycock, S., Corbet, R. H. D., Coe, M. J., Marshall, F. E., Markwardt, C., and Edge, W.: 2003b, *Mon. Not. R. Astron. Soc.* **339**, 435

Laycock, S., Corbet, R. H. D., Coe, M. J., Marshall, F. E., Markwardt, C., and Lochner, J.: 2005, *Astrophys. J., Suppl. Ser.* **161**, 96

Laycock, S., Corbet, R. H. D., Perrodin, D., Coe, M. J., Marshall, F. E., and Markwardt, C.: 2002, *Astron. Astrophys.* **385**, 464

Laycock, S. G. T.: 2002, *Ph.D. Thesis, University of Southampton*

Lee, U., Saio, H., and Osaki, Y.: 1993, in K.-C. Leung and I.-S. Nha (eds.), *ASP Conf. Ser. 38: New Frontiers in Binary Star Research*, pp 225–+

Lewin, W. H. G., van Paradijs, J., and van der Heuvel, P. J.: 1997, *X-Ray Binaries*, Cambridge University Press

Liu, Q. Z., van Paradijs, J., and van den Heuvel, E. P. J.: 2000, *Astron. Astrophys. Suppl. Ser.* **147**, 25

Liu, Q. Z., van Paradijs, J., and van den Heuvel, E. P. J.: 2006, *to appear in Astron. Astrophys.*

Lochner, J. C., Marshall, F. E., Whitlock, L. A., and Brandt, N.: 1998, *IAU Circ.* **6814**, 1

Lochner, J. C., Whitlock, L. A., Corbet, R. H. D., and Marshall, F. E.: 1999a, *American Astronomical Society Meeting Abstracts, 194$^{\rm th}$ Meeting*

Lochner, J. C., Whitlock, L. A., Corbet, R. H. D., and Marshall, F. E.: 1999b, *Bulletin of the American Astronomical Society* **31**, 742

Lomb, N. R.: 1976, *Astrophys. Space. Sci.* **39**, 447

Macomb, D. J., Finger, M. H., Harmon, B. A., Lamb, R. C., and Prince, T. A.: 1999, *Astrophys. J., Lett.* **518**, L99

Macomb, D. J., Fox, D. W., Lamb, R. C., and Prince, T. A.: 2003, *Astrophys. J., Lett.* **584**, L79

Maeder, A., Grebel, E. K., and Mermilliod, J.-C.: 1999, *Astron. Astrophys.* **346**, 459

Majid, W. A., Lamb, R. C., and Macomb, D. J.: 2004, *Astrophys. J.* **609**, 133

Makino, F.: 1988a, *IAU Circ.* **4661**, 2

Makino, F.: 1988b, *IAU Circ.* **4583**, 1

Makino, F.: 1988c, *IAU Circ.* **4587**, 1

Makishima, K., Ohashi, T., Sakao, T., Dotani, T., Inoue, H., Koyama, H., Makino, F., Mitsuda, K., Nagase, F., Thomas, H. D., Turner, M. J. L., Kii, T., and Tawara, Y.: 1988, *Nature* **333**, 746

Marshall, F. E., Lochner, J. C., Santangelo, A., Cusumano, G., Israel, G. L., dal Fiume, D., Orlandini, M., Frontera, F., Parmar, A. N., and Corbet, R. H. D.: 1998, *IAU Circ.* **6818**, 1

Marshall, F. E., Lochner, J. C., and Takeshima, T.: 1997, *IAU Circ.* **6777**, 2

Marshall, F. E., Takeshima, T., and in 't Zand, J.: 2000, *IAU Circ.* **7363**, 2

Nagase, F.: 1989, *Publ. Astron. Soc. Jpn.* **41**, 1

Okazaki, A. T.: 1998, in *IAU Symp. 188: The Hot Universe*, Vol. 188, p. 362

Okazaki, A. T. and Negueruela, I.: 2001, *Astron. Astrophys.* **377**, 161

Paciesas, W. S., Pendleton, G. N., Lestrade, J. P., Fishman, G. J., Meegan, C. A., Wilson, R. B., Parnell, T. A., Austin, R. W., Berry, F. A., and Horack, J. M.: 1989, in *EUV, X-ray, and gamma-ray instrumentation for astronomy and atomic physics; Proceedings of the Meeting, San Diego, CA, Aug. 7-11, 1989 (A90-50251 23-35). Bellingham, WA, Society of Photo-Optical Instrumentation Engineers, 1989, p. 156-164.*, pp 156–164

Parmar, A. N., White, N. E., and Stella, L.: 1989a, *Astrophys. J.* **338**, 373

Parmar, A. N., White, N. E., Stella, L., Izzo, C., and Ferri, P.: 1989b, *Astrophys. J.* **338**, 359

Porter, J. M.: 1996, *Mon. Not. R. Astron. Soc.* **280**, L31

Porter, J. M.: 1999, *Astron. Astrophys.* **348**, 512

Press, W. H. and Rybicki, G. B.: 1989, *Astrophys. J.* **338**, 277

Raguzova, N. V. and Popov, S. B.: 2005, *ArXiv Astrophysics e-prints*

Rappaport, S., Clark, G. W., Cominsky, L., Li, F., and Joss, P. C.: 1978, *Astrophys. J., Lett.* **224**, L1

Sasaki, M., Haberl, F., Keller, S., and Pietsch, W.: 2001, *Astron. Astrophys.* **369**, L29

Sasaki, M., Pietsch, W., and Haberl, F.: 2003, *Astron. Astrophys.* **403**, 901

Scargle, J. D.: 1982, *Astrophys. J.* **263**, 835

Schmidtke, P. C. and Cowley, A. P.: 2005a, *The Astronomer's Telegram* **648**, 1

Schmidtke, P. C. and Cowley, A. P.: 2005b, *Astron. J.* **130**, 2220

Schmidtke, P. C., Cowley, A. P., Levenson, L., and Sweet, K.: 2004, *Astron. J.* **127**, 3388

Scott, D. M., Finger, M. H., Wilson, R. B., Koh, D. T., Prince, T. A., Vaughan, B. A., and Chakrabarty, D.: 1997, *Astrophys. J.* **488**, 831

Shakura, N. I. and Sunyaev, R. A.: 1973, *Astron. Astrophys.* **24**, 337

Shrader, C. R., Sutaria, F. K., Singh, K. P., and Macomb, D. J.: 1999, *Astrophys. J.* **512**, 920

Slettebak, A.: 1982, *Astrophys. J., Suppl. Ser.* **50**, 55

Slettebak, A.: 1988, *Publ. Astron. Soc. Pac.* **100**, 770

Smith, D. A. and Takeshima, T.: 1998, *The Astronomer's Telegram* **36**, 1

Smith, M. A. and Robinson, R. D.: 1998, *Bulletin of the American Astronomical Society* **30**, 1395

Smith, M. A., Robinson, R. D., and Hatzes, A. P.: 1998, *Astrophys. J.* **507**, 945

Soffitta, P., Tomsick, J. A., Harmon, B. A., Costa, E., Ford, E. C., Tavani, M., Zhang, S. N., and Kaaret, P.: 1998, *Astrophys. J., Lett.* **494**, L203+

Southwell, K. A. and Charles, P. A.: 1996, *Mon. Not. R. Astron. Soc.* **281**, L63

Stanimirovic, S., Staveley-Smith, L., Dickey, J. M., Sault, R. J., and Snowden, S. L.: 1999, *Mon. Not. R. Astron. Soc.* **302**, 417

Staveley-Smith, L., Kim, S., Calabretta, M. R., Haynes, R. F., and Kesteven, M. J.: 2003, *Mon. Not. R. Astron. Soc.* **339**, 87

Stella, L., White, N. E., and Rosner, R.: 1986, *Astrophys. J.* **308**, 669

Stevens, J. B., Coe, M. J., and Buckley, D. A. H.: 1999, *Mon. Not. R. Astron. Soc.* **309**, 421

Stollberg, M. T., Finger, M. H., Wilson, R. B., Harmon, B. A., Rubin, B. C., Zhang, N. S., and Fishman, G. J.: 1993, *IAU Circ.* **5836**, 1

The HEASARC *BATSE* webpage: 2005, *The BATSE Instrument*, http://cossc.gsfc.nasa.gov/docs/cgro/batse/BATSE-desc.html

Torii, K., Yokogawa, J., Imanishi, K., and Koyama, K.: 2000, *IAU Circ.* **7428**, 3

Toropina, O. D., Romanova, M. M., Toropin, Y. M., and Lovelace, R. V. E.: 2003, *Astrophys. J.* **593**, 472

Townsend, R. H. D., Owocki, S. P., and Howarth, I. D.: 2004, *Mon. Not. R. Astron. Soc.* **350**, 189

Udalski, A.: 1998, *Acta Astronomica* **48**, 113

Ueno, M., Yamaguchi, H., Takagi, S.-I., Yokogawa, J., and Koyama, K.: 2004, *Publ. Astron. Soc. Jpn.* **56**, 175

Ventura, J. and Pines, D. (eds.): 1991, *Neutron stars: Theory and Observation*

White, N. E., Parkes, G. E., Sanford, P. W., Mason, K. O., and Murdin, P. G.: 1978, *Nature* **274**, 664

White, N. E., Swank, J. H., and Holt, S. S.: 1983, *Astrophys. J.* **270**, 711

Wilson, C. and Finger, M.: 1998, *IAU Circ.* **7048**, 1

Wilson, C. A., Fabregat, J., and Coburn, W.: 2005a, *Astrophys. J., Lett.* **620**, L99

Wilson, C. A., Finger, M. H., Coe, M. J., Laycock, S., and Fabregat, J.: 2002, *Astrophys. J.* **570**, 287

Wilson, C. A., Finger, M. H., Coe, M. J., and Negueruela, I.: 2003, *Astrophys. J.* **584**, 996

Wilson, C. A., Finger, M. H., Harmon, B. A., Chakrabarty, D., and Strohmayer, T.: 1998a, *Astrophys. J.* **499**, 820

Wilson, C. A., Finger, M. H., Harmon, B. A., Scott, D. M., Wilson, R. B., Bildsten, L., Chakrabarty, D., and Prince, T. A.: 1997a, *Astrophys. J.* **479**, 388

Wilson, C. A., Finger, M. H., and Scott, D. M.: 2000, in M. L. McConnell and J. M. Ryan (eds.), *American Institute of Physics Conference Series*, pp 208–+

Wilson, C. A., Finger, M. H., Wilson, R. B., and Scott, D. M.: 1998b, *IAU Circ.* **7014**, 2

Wilson, C. A., Weisskopf, M. C., Finger, M. H., Coe, M. J., Greiner, J., Reig, P., and Papamastorakis, G.: 2005b, *Astrophys. J.* **622**, 1024

Wilson, C. A., Zhang, S. N., Finger, M. H., Wilson, R. B., Scott, M., Koh, T., Chakrabarty, D., Vaughan, B., and Prince, T. A.: 1995, *IAU Circ.* **6238**, 1

Wilson, R. B., Harmon, B. A., Scott, D. M., Finger, M. H., Robinson, C. R., Chakrabarty, D., and Prince, T. A.: 1997b, *IAU Circ.* **6586**, 2

Yokogawa, J., Imanishi, K., Koyama, K., Nishiuchi, M., and Mizuno, N.: 2002, *Publ. Astron. Soc. Jpn.* **54**, 53

Yokogawa, J., Imanishi, K., Tsujimoto, M., Koyama, K., and Nishiuchi, M.: 2003, *Publ. Astron. Soc. Jpn.* **55**, 161

Yokogawa, J., Imanishi, K., Ueno, M., and Koyama, K.: 2000a, *Publ. Astron. Soc. Jpn.* **52**, L73

Yokogawa, J. and Koyama, K.: 1998a, *IAU Circ.* **6853**, 2

Yokogawa, J. and Koyama, K.: 1998b, *IAU Circ.* **7009**, 3

Yokogawa, J. and Koyama, K.: 1998c, *IAU Circ.* **7028**, 1

Yokogawa, J., Torii, K., Kohmura, T., Imanishi, K., and Koyama, K.: 2000b, *Publ. Astron. Soc. Jpn.* **52**, L53

Yoshizawa, A. M. and Noguchi, M.: 2003, *Mon. Not. R. Astron. Soc.* **339**, 1135

Though here at journey's end
I lie in darkness buried deep,
beyond all towers strong and high,
beyond all mountains steep,
above all shadows rides the Sun
and Stars forever dwell:
I will not say the Day is done,
nor bid the Stars farewell.

—Sam Gamgee (in *The Return of the King*)